INJURY MECHANISMS, TISSUE PROPERTIES, AND RESPONSE OF THE POST-MORTEM HUMAN ABDOMEN IN FRONTAL IMPACT

MEGHAN KATHLEEN HOWES

Dissertation submitted to the faculty of the
Virginia Polytechnic Institute and State University
in partial fulfillment of the requirements for the degree of

Doctor of Philosophy

in

Biomedical Engineering

Warren N. Hardy, Chair
Philippe Beillas
Stephen W. Rouhana
Stefan M. Duma
Joel D. Stitzel
F. Scott Gayzik

24 October 2013

Blacksburg, Virginia

Keywords: Abdomen, Injury, Biomechanics, Cadaver, Impact, Stress, Strain

INJURY MECHANISMS, TISSUE PROPERTIES, AND RESPONSE OF THE POST-MORTEM HUMAN ABDOMEN IN FRONTAL IMPACT

Meghan Kathleen Howes

ABSTRACT

Motor vehicle collisions (MVCs) are a leading cause of injuries and injury-related fatalities in the United States. The National Highway Traffic Safety Administration (NHTSA) reported over 21,250 vehicle occupant fatalities in 2011, with 1,240,000 injuries sustained by passenger car occupants alone[1]. MVCs are a common cause of blunt abdominal injuries. It has been reported that approximately 9,000 front seat occupants sustain moderate to severe abdominal injuries in frontal MVCs in the United States each year[2]. A detailed understanding of the occurrence and mechanisms of abdominal injuries, as well as knowledge of the biomechanical response and tolerance of the abdomen in crash-specific loading modes, could benefit the reduction of abdominal organ injury incidence in MVCs. Therefore, the objective of the research presented in this dissertation was to characterize abdominal injury mechanisms, tissue failure thresholds, and internal organ response to blunt impacts of the abdomen. Field accident data from the Crash Injury Research and Engineering Network (CIREN) database were analyzed to determine the occupant and crash characteristics associated with crash-induced hollow abdominal organ injuries. Dynamic equibiaxial tension tests were conducted on tissue samples obtained from the human post-mortem stomach, small intestine, and colon to characterize the material properties and failure tolerance of these tissues. The effects of cadaver orientation on the relative position of the abdominal organs of two cadavers were quantified, and high-speed biplane x-ray imaging was used to investigate the relative kinematics of the thoracic and abdominal organs of four cadavers in response to crash-specific loading modes. Test configurations included blunt abdominal and thoracic impacts and driver-shoulder seatbelt loading. The motivation for this research was to advance efforts toward abdominal organ injury mitigation in MVCs, with each aspect of this research generating novel injury biomechanics data with applications for future experimental testing and finite element modeling.

[1]NHTSA. (2013). Traffic safety facts: a compilation of motor vehicle crash data from the fatality analysis reporting system and the general estimates system. U.S. Department of Transportation, Washington, D.C.

[2]Klinich, K. D., Flannagan, C. A. C., Nicholson, K., Schneider, L. W., and Rupp, J. D. (2010). Factors associated with abdominal injury in frontal, farside, and nearside crashes. *Stapp Car Crash Journal,* 54, 73-91.

ACKNOWLEDGMENTS

I would like to express my sincerest appreciation to my advisor, Warren Hardy, for his support and guidance, and especially for imparting his unparalleled knowledge of experimental methods and biomechanics research throughout my graduate studies. I am fortunate to have had the opportunity to learn from such a distinguished mentor. I would also like to gratefully acknowledge the guidance and contributions of my doctoral committee members: Philippe Beillas, Stephen Rouhana, Stefan Duma, Joel Stitzel, and Scott Gayzik. Their advice and technical input have contributed immensely to the merit of this research.

In addition to my committee members, I would like to thank all of the individuals who have mentored me throughout this process, particularly Eric Kennedy, who supported my interest in pursuing graduate studies in injury biomechanics from the beginning. I cannot fully express my gratitude to my friends and family for providing endless encouragement, support, and motivation. I would like to especially thank my parents, brothers, and uncle for their unwavering support as I worked to achieve each of my goals.

Finally, I would like to acknowledge all of the organizations and individuals who have contributed to the completion of the research in this dissertation. This research was funded in part by the Global Human Body Models Consortium, LLC, Toyota Motor Corporation, and Toyota Motor Engineering & Manufacturing North America, Inc. I would like to gratefully acknowledge the contributions of Philippe Beillas, Jason Hallman, and my colleagues in the Center for Injury Biomechanics at Virginia Tech and Wake Forest University. I would also like to acknowledge the Stapp Association for graciously granting reprint permission for material in this dissertation.

TABLE OF CONTENTS

LIST OF FIGURES

§ Reprinted by permission of the Stapp Association.

LIST OF TABLES

CHAPTER 1

Introduction to Abdominal Injury Biomechanics

Motor vehicle collisions (MVCs) result in approximately 45,000 injury-related deaths and 357,000 hospitalizations in the United States each year (MacKenzie and Fowler, 2008). MVCs are a common cause of blunt abdominal injuries. An estimated 9,000 front seat occupants sustain moderate to severe abdominal injuries in frontal MVCs annually in the United States (Klinich et al., 2010). As injury incidence for the head and thorax in MVCs is reduced with the implementation of improved occupant safety systems, increased importance has been placed on injury mitigation efforts for the abdominal organs in an attempt to improve overall occupant protection (Lamielle et al., 2006; Frampton and Lenard, 2009; Yaguchi et al., 2011). A detailed understanding of the occurrence and mechanisms of abdominal injuries and the biomechanical response and tolerance of the abdomen in crash-specific loading modes could benefit abdominal organ injury mitigation in MVCs. This chapter provides a summary of the epidemiological data and biomechanical response data available in the literature for the abdomen and sets forth the objectives of this research to address gaps in the literature regarding abdominal injury mechanisms, component-level tolerance data, and regional response data for crash-specific impacts.

EPIDEMIOLOGY

In general, studies examining occupant injuries in frontal crashes have indicated that abdominal injuries account for a greater percentage of all injuries in MVCs when higher injury severity levels are considered (Bondy, 1980; Elhagediab and Rouhana, 1998; Lee and Yang, 2002). Injury distribution within the abdominal region has been reported with varying percentages of injury for each organ depending on the inclusion criteria for data analysis. However, the liver and the spleen are often cited as the most frequently injured abdominal organs in MVCs (Bondy, 1980; Elhagediab and Rouhana, 1998; Yoganandan et al., 2000; Lee and Yang, 2002; Klinich et al., 2010; Frampton et al., 2012). Although the prevalence of hollow organ injury is less frequent overall, field accident analysis and clinical data have associated an increase in the occurrence of injury to the hollow organs of the digestive tract with seatbelt use (Rutledge et al., 1991; Lamielle et al., 2006).

A number of studies have investigated abdominal injury patterns with field accident data from 1980-2000. The datasets typically contained a limited number of vehicles equipped with airbags (not depowered) and included a higher percentage of unbelted occupants compared to the current rate of seatbelt use in the United States. Elhagediab and Rouhana (1998) analyzed abdominal injuries in front seat occupants in frontal MVCs using the National Automotive Sampling System (NASS) database for years 1988 through 1994. Rollovers and ejected drivers and right front passengers were excluded from the analysis. Both

belted and unbelted occupants were included. The most frequently injured abdominal organs were the liver (38%), spleen (23%), and digestive system (17%). The vehicle components associated with abdominal injuries were the steering wheel (68%), seatbelt (17%), and other interior components including the airbag (14%). Yoganandan et al. (2000) examined abdominal injury frequency and severity in MVCs using the National Automotive Sampling System/Crashworthiness Data System (NASS/CDS) database for the years 1993 through 1998. The dataset included belted and unbelted drivers and right front passengers. Injuries were classified using the Abbreviated Injury Scale (AIS). Injury to the digestive tract comprised a greater percentage of all injuries in frontal impacts when AIS2+ abdominal injuries were included compared to injuries that were AIS3+ in severity. The organs injured most frequently in frontal crashes were the liver (39%), spleen (29%), and digestive organs (11%) for AIS2+ injuries and the liver (35%), spleen (28%), and arteries (14%) for AIS3+ injuries. These studies provide useful data on abdominal injury patterns and frequency; however, it is likely that the types and distributions of abdominal injuries have since varied with changes in occupant restraint use and the implementation of current safety technologies.

Lamielle et al. (2006) investigated abdominal injury patterns for front and rear seat occupants in frontal crashes occurring in France from 1970 to 2005. Occupants that sustained AIS3+ abdominal injuries were significantly older than occupants without AIS3+ abdominal injuries. The likelihood of sustaining an AIS3+ abdominal organ injury increased with increasing crash severity. Overall, the use of seatbelts with retractors reduced abdominal injury risk. The likelihood of sustaining an abdominal injury varied with occupant seating position. For example, belted rear seat occupants were identified as more likely to sustain abdominal injury compared to belted front seat occupants. For all occupants, the organs injured most frequently (AIS3+) were the spleen (22%), jejunum (16%), and the liver (16%). For belted occupants, hollow abdominal organ injury occurred more frequently (59%) than solid organ injury, whereas solid organ injury occurred more frequently for unbelted occupants (77%). This study was a comprehensive review of French accident analysis spanning multiple decades. Variations in restraint type and use in the United States may result in differing distributions for a US-specific population.

Klinich et al. (2010) analyzed abdominal injuries occurring in frontal, farside, and nearside crashes using the NASS/CDS (1998-2008) and Crash Injury Research and Engineering Network (CIREN) databases. This study expanded on previous analyses by examining a population in which 85% of the occupants were belted and 68% were travelling in airbag-equipped vehicles. The analysis therefore emphasized characterizing injury for occupants utilizing current safety technologies. Compared to unbelted occupants, belted occupants had a significant reduction in the risk of AIS2+ and AIS3+ abdominal organ injuries in all crash modes. No difference in abdominal organ injury incidence was found in frontal crashes with and

without airbag deployment. The percentage of occupants sustaining AIS2+ abdominal organ injuries increased with increasing crash severity. This was also true for the percentage of occupants sustaining rib fractures. Controlling for crash severity, the authors found that the likelihood of sustaining AIS2+ and AIS3+ injuries to the solid abdominal organs (liver, spleen, and kidneys) increased considerably when the occupant also sustained AIS2+ rib fractures. The study also reported an increase in rib fracture incidence with age, but no increase in abdominal injury incidence with age. Therefore, it is not likely that abdominal injuries were caused by fractured ribs; it is more probable that the solid abdominal organs and the ribs are injured under similar loading conditions.

Compared to the results of Elhagediab and Rouhana (1998), Klinich et al. (2010) reported increased spleen injury incidence in frontal collisions (40% compared to 23%) with little change in liver injury incidence at the AIS3+ severity level (40% compared to 38%). Component contacts associated with abdominal injury also varied compared to previous studies. Klinich et al. (2010) reported that the most common contacts associated with AIS3+ abdominal injury were the steering wheel (50%), seatbelt (30%), and vehicle interior (12%). Klinich et al. (2010) also identified the seatbelt as the injury source for the majority of other abdominal organ injuries not including injures to the liver and the spleen. These injuries were not further categorized by organ or injury type. No association was found between the incidence of abdominal organ injury and occupant age.

Yaguchi et al. (2011) identified the abdominal region as an area requiring injury mitigation efforts in order to improve overall occupant protection in frontal crashes for belted drivers in Japan. The study data included all traffic accidents in Japan from 2004 to 2008 with one or more injured occupants. The patterns of serious and fatal injuries were investigated by body region and injury type. The results were not parsed by specific internal organ. For belted drivers in frontal crashes, Yaguchi et al. (2011) reported that fatalities that were attributed to head and thoracic injuries generally decreased from 2005 to 2008, whereas fatalities attributed to abdominal injuries maintained a fairly constant trend from 2004 to 2008. This difference in trend by body region highlighted the abdomen as an area for future focus for injury mitigation. For belted drivers, the ratio of serious injuries to total injuries by body region was greater for the abdomen than any other region. The analyses also suggested that increased age was associated with fatality resulting from injury to the abdomen, though it was not clear that this trend was significant.

Frampton et al. (2012) investigated abdominal injury risk factors for belted front and rear seat occupants in frontal crashes (± 30°) in the United Kingdom (UK). The dataset was obtained from the UK Co-operative Crash Injury Study (CCIS) for the years 1998 to 2010. The analysis included both injured and non-injured belted occupants ≥ 10 years old in passenger cars equipped with driver airbags. In general,

abdominal injury risk increased with age for both AIS2+ and AIS3+ severity levels; however, the injury incidence was also high for occupants less than 19 years of age. The authors identified an increased risk of AIS2+ and AIS3+ abdominal injuries for rear seat passengers compared to right front passengers and drivers. These results were consistent with the results of Lamielle et al. (2006). The liver and the spleen were the most frequently injured organs for drivers, while the most frequently injured organs for right front passengers were the liver, the jejunum-ileum, and the spleen. The injury pattern for rear seat passengers differed from front seat occupants with the jejunum-ileum, the mesentery, and the colon injured more frequently than the solid organs. However, the liver and spleen injury incidence also remained high for rear seat occupants.

Frampton et al. (2012) also assessed the association between abdominal organ injuries and rib fractures for all occupants. Similar to the results of Klinich et al. (2010), Frampton et al. (2012) reported an increased occurrence of AIS2+ liver and spleen injuries when the occupant also sustained two or more rib fractures. The majority of liver, spleen, and mesentery injuries were sustained in association with two or more rib fractures, whereas the majority of the colon, duodenum, and jejunum-ileum injuries were associated with one or no rib fractures. The incidence of rib fractures did not differ significantly between seating positions while the distributions of organ injury varied considerably for front and rear seat occupants.

ANATOMY

An understanding of human abdominal anatomy and basic tissue functionality is necessary for the development of appropriate testing methodologies and for the interpretation of experimental results. Therefore, abdominal anatomy relevant to the biomechanics of blunt trauma is summarized in this section, with additional detail provided for organs and structures pertinent to this research.

The abdominal cavity is the largest of the body cavities, bounded superiorly by the diaphragm and extending into the pelvis. The anterolateral boundary consists of the abdominal muscles – the internal and external oblique muscles and the transverse and rectus abdominus muscles – and the posterior boundary includes the vertebral column, the psoas muscles, and the quadratus lumborum muscles. The abdomen is traditionally divided into nine regions: the right and left hypochondriac, right and left lumbar, right and left iliac (or inguinal), and the epigastric, umbilical, and hypogastric (or suprapubic) regions (Figure 1). Four planes section the abdomen to define the nine regions: the subcostal and transtubercular planes extending horizontally and two vertical midclavicular planes (Moore and Agur, 2002). Alternatively, the median plane and the transumbilical plane divide the abdomen into four quadrants (Figure 1).

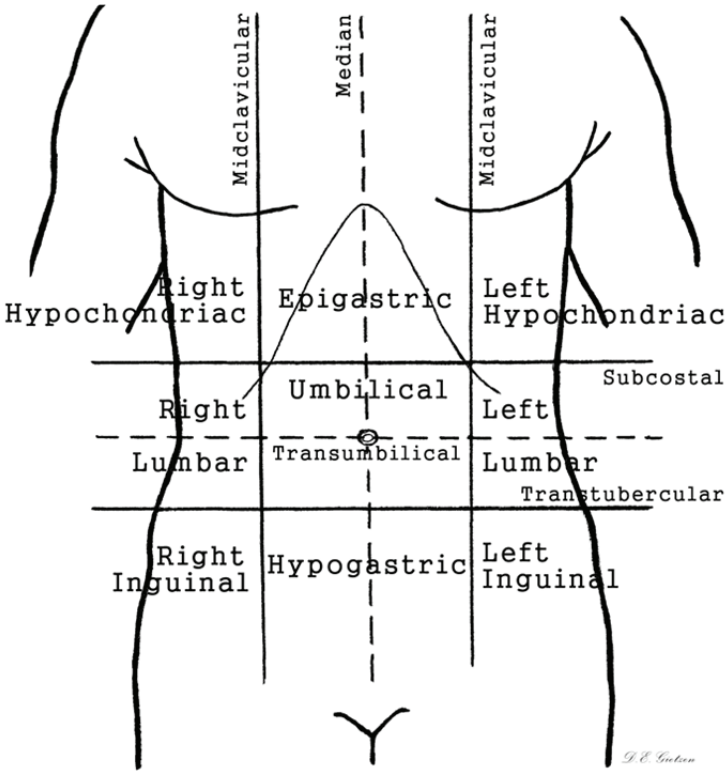

Figure 1: Regions and quadrants of the human abdomen.

The abdominal cavity consists of the peritoneal cavity and the abdominal viscera (Figure 2). In general, the abdomen is essentially unprotected by bony structures; however, the upper abdomen is afforded some protection from blunt trauma by the lower rib cage. Additional protection is provided to the abdominal viscera by the muscles and fasciae of the anterolateral abdominal wall. The abdominal wall consists of skin, subcutaneous tissue, musculature, fascia, and parietal peritoneum (Moore and Agur, 2002). Parietal peritoneum is a serous membrane lining the interior abdominal wall, and visceral peritoneum surrounds the abdominal viscera. The thin space between the parietal and visceral peritoneum forms the peritoneal cavity. The abdominal viscera are positioned within the peritoneal cavity (i.e. intraperitoneal) with the exception of the pancreas, most of the duodenum, and the kidneys, which are located external and posterior to the peritoneal cavity (i.e. retroperitoneal).

Mesentery consists of two layers of peritoneum that suspend the organs within the peritoneal cavity and connect underlying viscera to the abdominal wall (Moore and Agur, 2002). Mesentery provides vascular and neural connections to the abdominal organs and is essential to the mobility of the viscera within the abdominal cavity. The length of the tethering mesentery permits or restricts the relative motion of the organs. Subdivisions of mesentery include the peritoneal ligaments extending between organs, and the omentum, which connects the stomach to the surrounding viscera. The lesser omentum extends between

the lesser curvature of the stomach and the liver, consisting of the gastrohepatic and gastroduodenal ligaments. The greater omentum spans from the greater curvature of the stomach to cover the majority of the abdominal viscera and folds over to connect to the transverse colon. The greater omentum separates the viscera from the parietal peritoneum and the abdominal wall, which adds to the protection of the abdominal organs during frontal blunt impact.

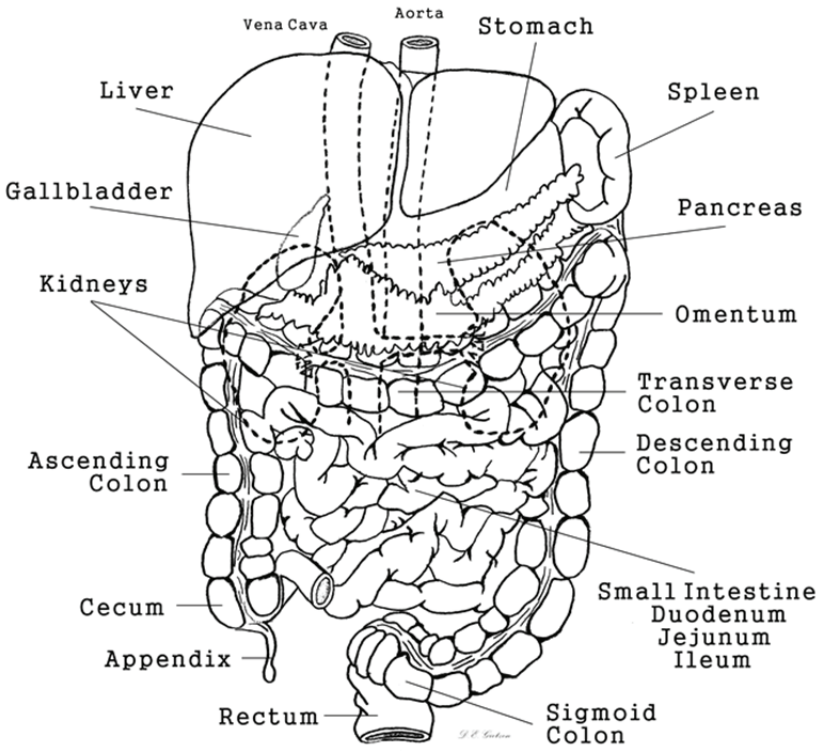

Figure 2: Gross anatomy of the abdominal cavity.

The abdominal viscera are classified into two groups based on composition: the hollow or membranous abdominal organs and the solid abdominal organs. The hollow organs mainly consist of the organs of the gastrointestinal tract, and the solid organs include the liver, spleen, kidneys, and pancreas. The variations in organ composition result in differences in injury type and outcome for each classification, such as perforation of the hollow organs or laceration and extensive blood loss from the solid organs. Further, the asymmetric positioning of the organs within the abdominal cavity leads to differences in injury patterns dependent on loading mode and impact location. Defining characteristics of the hollow and solid abdominal organs are detailed herein.

Hollow or Membranous Abdominal Organs

The hollow abdominal organs are typically thin-walled organs including the stomach, small intestine, large intestine, and gallbladder. The urinary bladder, a hollow, muscular organ, is commonly included in this classification. The diaphragm, mesentery, and vasculature are also categorized with the hollow organs as membranous soft tissues with similar biomechanical test protocols. The most common crash-induced injuries of the hollow abdominal organs are serosal tears, or lacerations, and perforations, or rupture-type injuries (Rutledge et al., 1991; Munns et al., 1995; Carrillo et al., 1996; Shinkawa et al., 2004). Based on these injury types, an understanding of the structure and response of the intact wall is essential to the biomechanical assessment of failure tolerances for accurately predicting hollow abdominal organ injury in blunt trauma.

Together the esophagus, stomach, and the small and large intestines make up the gastrointestinal tract and perform the various aspects of digestion. In general, the wall structure of the gastrointestinal tract has a consistent layered organization throughout its length. The four wall layers, described from the lumen to the outer layer, consist of the mucosa, submucosa, muscularis externa, and serosa or adventitia (Gartner and Hiatt, 2006). The mucosa is organized in three concentric layers: an epithelial lining, a layer of connective tissue known as the lamina propria, and a smooth muscle layer, the muscularis mucosae. The greatest variations in wall structure between organs of the digestive tract exist in the mucosal layer. Nervous, vascular, and lymphatic connections reach the mucosa through the connective tissue of the submucosal layer. The muscularis externa is comprised of an inner circular smooth muscle layer and an outer longitudinal smooth muscle layer. The outer layer of the wall structure varies throughout the gastrointestinal tract. Structures suspended by peritoneum have an outer serous membrane known as serosa that consists of connective tissue and mesothelium. Structures attached to the abdominal or pelvic wall have an outer layer of connective tissue known as adventitia. Variations in the wall structure of specific organs are described in the respective sections.

The Stomach. The stomach is positioned in the left upper quadrant of the abdomen, continuous superiorly with the esophagus and inferiorly with the proximal duodenum of the small intestine. The organ is a hollow reservoir mainly responsible for storage and the mechanical and chemical breakdown of food. The stomach is classified into four gross anatomic regions: the cardia, adjacent to the esophageal opening, the fundus which lies superior to the esophageal opening (cardiac orifice), the corpus or body of the stomach inferior to the orifice, and the pyloric antrum. The lesser curvature of the stomach extends from the cardia to the pyloric region on the medial side, and the greater curvature forms the lateral and inferior borders of the stomach.

Histologically, the stomach is divided into only three regions: the cardia, fundus, and pylorus, based on the composition of glands within the gastric mucosal layer (Ross and Pawlina, 2011). The gastric mucosal layer forms longitudinal folds, or rugae, that permit the extension of the stomach during filling (Figure 3). Rugae are less prominent in the upper region of the stomach, where the gastric wall generally appears thin and smooth. Other features of the gastric mucosa include mamillated areas that increase surface area for secretion, and openings known as gastric pits, or foveolae. Opening into the gastric pits are the gastric glands of the fundus that produce gastric juice comprised of water, electrolytes, and additional substances to aid in digestion.

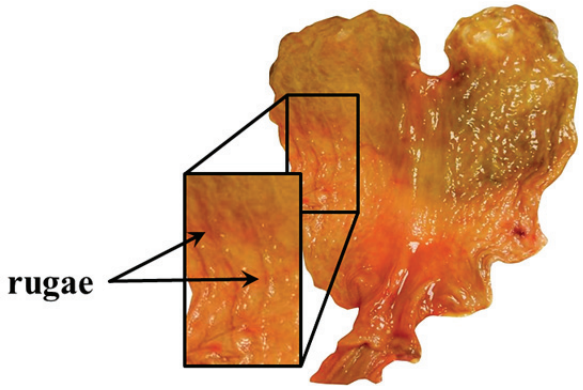

Figure 3: Rugae shown in an *ex vivo* cadaveric stomach opened along the greater curvature.

The stomach can accommodate a volume of up to 1.0 or 1.5 liters of food or fluid (Guyton and Hall, 2000). Although the position and shape of the stomach change with the stages of digestion, the stomach generally extends from the level of the 5th left rib to the level of the 9th costal cartilage or the first lumbar vertebra (Moore and Agur, 2002). The pyloric region typically crosses the midline of the body, where it is continuous with the duodenum to the right of the midline. The stomach is adjacent to the diaphragm, spleen, left kidney, left adrenal gland, and pancreas, and is positioned posterior to the transverse colon.

The Small Intestine. The small intestine is divided into three anatomic regions: the duodenum, the jejunum, and the ileum. The duodenum is approximately 23 cm to 28 cm in length, extending from the pylorus of the stomach to the duodenojejunal flexure, and wrapping around the head of the pancreas (Moore and Agur, 2002). The duodenum is the widest and most fixed portion of the small intestine and is mostly retroperitoneal in position. This portion of the small intestine receives partially digested matter from the stomach, as well as secretions from the stomach, pancreas, and gallbladder.

The remainder of the intestine is approximately six meters in length, extending from the duodenojejunal junction to the ileocecal junction (Moore and Agur, 2002). The jejunum and ileum are continuous but can be distinguished visually by a decrease in diameter and a change in wall thickness at the ileum. The

jejunum and ileum are extremely mobile within the abdominal cavity. Mesentery connects these regions, providing the blood and lymphatic supply, and links the jejunum and the ileum to the posterior abdominal wall.

The wall structure of the small intestine is continuous throughout its length and consistent with the remainder of the gastrointestinal tract. The distinguishing characteristics of the small intestine are the presence of plicae circulares, visible transverse folds comprised of submucosa (Figure 4), and villi that line the entire mucosa of the small intestine (Ross and Pawlina, 2011). Villi and microvilli increase surface area for absorption. The jejunum is the primary location for nutrient absorption and the ileum is the primary site for the reabsorption of water and electrolytes in the small intestine.

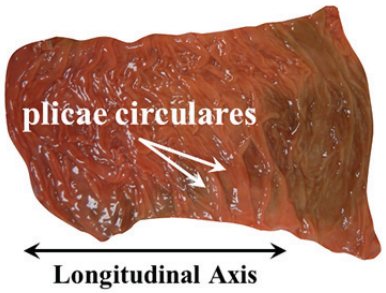

Figure 4: Mucosal folds of the excised cadaveric intestine.

The Large Intestine. The cecum, colon, rectum, and anal canal make up the large intestine. The colon is divided into four anatomic regions arcing around the border of the abdomen: the ascending, transverse, descending, and sigmoid colon. Both the ascending and descending portions of the colon are retroperitoneal in position. The transverse colon is fairly mobile and extends between the ascending and descending colon from the right to the left colic flexures. The sigmoid colon curves from the descending colon, adjacent to the iliac fossa, to the rectum (Moore and Agur, 2002).

The wall structure of the large intestine matches the general four-layered structure of the gastrointestinal tract. The distinguishing characteristics of the large intestine are teniae coli and haustra (Figure 5). Teniae coli are thin bands of muscle fibers extending axially throughout the cecum and colon to the rectum, and haustra coli are sections of tissue between the bands of teniae (Ross and Pawlina, 2011). The inner mucosal surface of the large intestine is smooth; however, mucosal folds appear during digestion as a result of contractions of the muscularis mucosae. During digestion, the function of the proximal portion of the large intestine is absorption, and the distal portion functions for storage (Guyton and Hall, 2000). Therefore, the contents of the colon tend to be more fluid in the proximal portion and more solid in the distal regions.

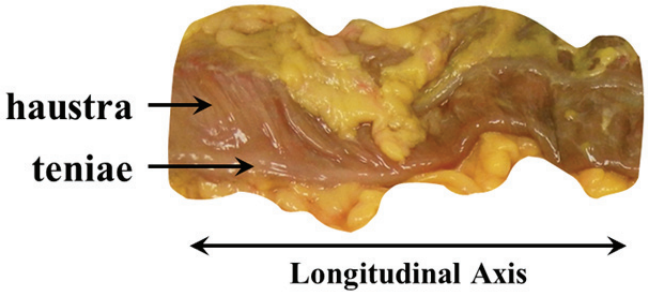

Figure 5: Teniae coli and haustra identified on excised cadaveric colon tissue.

The Diaphragm. The diaphragm is a sheet of muscle and tendon that forms the superior border of the abdominal cavity. The structure is mobile in the central region and fixed on the outer margins to the rib cage and the lumbar spine with ligamentous attachments. The diaphragm arcs superiorly on either side of the midline to form right and left domes. The central tendon of the diaphragm is formed by the convergence of the surrounding muscle fibers that extend radially toward the sternum, ribs (costal fibers), and the lumbar vertebrae (Moore and Agur, 2002). Three major diaphragmatic openings connect the thorax and the abdomen: the caval opening typically located at the level of T8, the esophageal hiatus (T10), and the aortic hiatus (T12).

The Gallbladder. The gallbladder is a hollow reservoir that stores and concentrates the bile that is produced in the liver. The structure is surrounded by peritoneum, which fixes the body and neck of the gallbladder to the visceral surface of the liver (Moore and Agur, 2002). The gallbladder can distend to accommodate approximately 50 mL of bile (Ross and Pawlina, 2011). Contractions of the smooth muscle cells in the muscularis externa empty the contents of the gallbladder into the cystic duct. Concentrated bile is secreted through the cystic duct to the common bile duct and into the duodenum of the small intestine.

The Urinary Bladder. The urinary bladder is a hollow organ with thick, muscular walls located within the lesser pelvis when empty and extending toward the umbilicus during filling (Moore and Agur, 2002). Two ureters empty into the bladder from the kidneys, and the urethra extends from the bladder to the external urethral orifice. The three orifices of the bladder form the trigone, a triangular region of consistent wall thickness (Ross and Pawlina, 2011). The remainder of the bladder wall is comprised of thick, muscular folds arranged to direct urine toward the urethra during contraction.

The Uterus. The uterus is a thick-walled hollow organ positioned within the female lower pelvis between the bladder and the rectum. The uterus is divided into two regions: the body and the cervix. The wall of the body consists of three layers: an outer perimetrium, a thick, muscular layer known as myometrium,

and an internal mucosal lining of endometrium (Moore and Agur, 2002). The histology of the uterus varies throughout the menstrual cycle, and the position and structure alter considerably during pregnancy.

Solid Abdominal Organs

The solid abdominal organs include the liver, spleen, kidneys, and pancreas and are frequent contributors to increased injury severity in automobile collisions. The liver and the spleen are the most commonly injured abdominal organs in frontal MVCs (Bondy, 1980; Elhagediab and Rouhana, 1998; Klinich et al., 2010), and lacerations are the most common injury mode (Lee and Yang, 2002; Holbrook et al., 2007). Injuries to the solid abdominal organs can be associated with high morbidity and mortality, particularly if surgical intervention is necessary or the vasculature is involved (Christmas et al., 2005; Hurtuk et al., 2006; Ball et al., 2010).

The Liver. The liver is the largest internal organ in the body, weighing up to 1500 g and occupying the majority of the right upper quadrant of the abdomen (Moore and Agur, 2002). The size and location of the liver result in an increased vulnerability to injury compared to the other abdominal organs (Fabian and Bee, 2003). The liver is partially protected by the rib cage; however, fractured ribs have the potential to result in penetrating trauma. The liver is a highly vascular organ, and blunt liver injuries range in severity from contusions and hematomas to lacerations, burst or rupture-type injuries with a high degree of parenchymal disruption, and hepatic avulsions.

Anatomically, the liver is divided into two surfaces and four lobes. The diaphragmatic surface of the liver is the anterior, superior surface located inferior to the diaphragm, and the visceral surface is the posterior, inferior surface adjacent to the stomach, duodenum, colon, and right kidney (Moore and Agur, 2002). The liver is separated into right and left lobes by the line of attachment of the falciform ligament that connects the diaphragmatic surface to the anterior abdominal wall. Superiorly, the falciform ligament gives rise to the coronary ligament and the right and left triangular ligaments suspending the liver from the diaphragm and extending posteriorly. The round ligament, or ligamentum teres, extends from the inferior margin of the falciform ligament. From the posterior aspect of the liver, the left, right, caudate, and quadrate lobes are visible, as well as a bare area without peritoneum where the liver connects to the diaphragm. The porta hepatis is the opening between the caudate and quadrate lobes where the portal vein and hepatic artery enter into the liver. The inferior vena cava and the gallbladder are also visible from the posterior aspect of the liver.

The liver is comprised of an outer fibrous capsule known as Glisson's capsule and internal parenchyma consisting of hepatocytes (Ross and Pawlina, 2011). Hepatic lobules are the functional units of the liver. Lobules are hexagonal in shape, with a central vein running through the long axis and hepatic sinusoids

radiating outward to portal triads at each of the angles at the periphery of the hexagon. The portal triads consist of a bile duct, portal vein, and hepatic artery. The amount of connective tissue between the lobules is limited, and therefore, the boundaries of adjacent lobules are not clearly defined.

The Spleen. The spleen is positioned in the left upper quadrant of the abdomen, inferior to the diaphragm and adjacent to the left colic flexure (Moore and Agur, 2002). The splenic artery and vein exit through the hilum of the spleen, located at the medial aspect where the spleen borders the tail of the pancreas. The gastrosplenic ligament and the splenorenal ligament connect the spleen to the greater curvature of the stomach and to the left kidney, respectively. The average spleen is approximately 12 cm in length and 7 cm in width, and does not extend below the rib cage, which offers some protection from blunt impact.

The spleen is a lymphatic organ also responsible for the breakdown of red blood cells. The parenchyma of the spleen is comprised of white and red pulp and is protected by a thin capsule of connective tissue (Ross and Pawlina, 2011). The spleen receives a high percentage of the blood supply through segmental arterial branches into the parenchyma. Motor vehicle collisions are the most common cause of splenic injuries, which range in severity from subcapsular hematomas to lacerations and ruptures with considerable blood loss (Peitzman et al., 2001).

The Kidneys. The kidneys are part of the urinary system, which also includes the ureters, bladder, and urethra. The kidneys are retroperitoneal organs located on either side of the vertebral column, posterior to the parietal peritoneum and bordering the posterior abdominal wall (Moore and Agur, 2002). Each kidney is positioned within the retroperitoneal space and encased in both adipose and connective tissues. These two attributes result in the kidneys remaining well protected from frontal blunt impact. In general, the kidneys extend from T12 to L3, with the right kidney positioned lower than the left due to the expanse of the liver. The suprarenal glands are positioned adjacent to the superior aspect of each kidney.

The kidneys are enclosed in a capsule of connective tissue. The renal artery, renal vein, and renal pelvis of the ureter enter and exit the kidney at the renal hilum, located on the medial aspect where the capsule passes inward (Ross and Pawlina, 2011). Within the kidney, the vasculature and renal pelvis lie in the renal sinus. The renal pelvis separates into major and minor calyces. The parenchyma of the kidney is divided into an outer cortex and inner medulla. The medulla is further divided into renal pyramids that extend into the calyces of the renal pelvis. Located within the cortex and the medulla are the nephrons, which are the functional units of the kidney responsible for urine production.

The Pancreas. The pancreas is a digestive gland positioned posterior to the transverse colon in the retroperitoneal space between the spleen and the duodenum. The pancreas is classified into four regions,

ordered from medial to lateral as the head, neck, body, and tail (Moore and Agur, 2002). The length of the pancreas extends across the midline, with the potential for compression injuries due to interaction with the vertebral column during loading. Rupture of the pancreas is rare in blunt trauma but can result in the release of pancreatic enzymes into the abdominal cavity.

Vasculature

The major vessels within the abdominal region are positioned adjacent to the vertebral column and are retroperitoneal in location. The arteries are efferent vessels, resistant to blood pressure with a muscular and elastic composition. The veins are afferent, thin-walled vessels with a high expansion capacity for containing blood volume.

The Arteries. The aorta enters into the abdominal cavity through the aortic hiatus, located at the posterior aspect of the diaphragm at the level of the T12 vertebra. The abdominal aorta extends anterior to the vertebral column to L4, where the aortic bifurcation into the common iliac arteries occurs at the left of the midline (Moore and Agur, 2002). The left and right common iliac arteries branch into the internal and external iliac arteries before exiting the abdominal region. The branches of the abdominal aorta are paired, extending into visceral or parietal branches to the left and right of the midline, or unpaired, dividing into the celiac trunk, superior and inferior mesenteric arteries, and the median sacral artery.

The superior mesenteric artery branches from the anterior surface of the abdominal aorta and extends through layers of mesentery to supply the majority of the intestines. The divisions reach the length of the jejunum and ileum, cecum, ascending colon, and the proximal portion of the transverse colon (Saladin, 2008). The inferior mesenteric artery branches from the inferior region of the abdominal aorta and supplies the distal colon and the proximal length of the rectum.

The Veins. Blood from the abdominal viscera is transported back to the heart via the portal venous system entering into the inferior vena cava (IVC) through the hepatic veins. The common iliac veins combine to form the IVC at the level of L5, posterior to the right common iliac artery (Moore and Agur, 2002). The IVC extends to the right of the vertebral column and aorta, entering into the thorax through the caval opening in the diaphragm. In addition to draining the hepatic portal system through the hepatic veins, other tributaries to the IVC include the iliac, lumbar, renal, suprarenal, and phrenic veins (Saladin, 2008).

BIOMECHANICAL RESPONSE

Material Properties

The complex nature of soft biological tissues confounds the ability to characterize and model the response of the material to mechanical loading. Biological tissues are inhomogeneous and anisotropic, typically exhibiting a non-linear, viscoelastic deformation response. To simplify experimental conditions, material tests are often conducted and analyzed assuming incompressibility, homogeneity, and isotropy. Further, many of the applications of constitutive modeling of biological tissues are physiologic or surgical. Therefore, biomechanical response data are often obtained using sub-failure (non-injurious) loading mechanisms at quasi-static loading rates.

High-rate global deformation of the abdominal region can occur in MVCs, often resulting in injuries to the abdominal organs. The local material properties and failure response of the abdomen have only recently been investigated using high deformation rates, with the literature largely concentrated on the solid abdominal organs. No data exist characterizing the dynamic material and failure properties of the human post-mortem stomach, small intestine, or colon, though these tissues have been investigated using quasi-static loading rates. This section summarizes the biomechanical literature available for tests conducted to failure on the human post-mortem abdominal tissues.

Membranous Abdominal Tissues. Material properties data for the human post-mortem stomach, small intestine, and large intestine have been investigated in uniaxial tension. Yamada (1970) cited the studies of Nonogaki (1960) and Fukuyama (1961) reporting the tensile response of the human gastric wall of 43 fresh, unembalmed cadavers. The tissue samples were rectangular strips with a reduced central region 10 mm in length and 2 to 3 mm in width. Although strain rates were not reported for these tests, it can be assumed that the tests were conducted using quasi-static loading rates based on the testing machines used in these studies. A higher ultimate elongation (1.2 times greater) was reported in the transverse direction for all regions of the stomach. In both the longitudinal and transverse directions, the greatest ultimate strength and greatest percent elongation were reported for the fundus, followed by the corpus and the antrum regions.

Yamada (1970), citing Iwasaki (1953), reported directional and regional differences in tensile response for the small and large intestinal tissues of 71 fresh, unembalmed human cadavers. The methodologies used in this study were identical to the studies of Nonogaki (1960) and Fukuyama (1961). For all regions of the small intestine, the ultimate percent elongation was lower in the longitudinal direction compared to the transverse direction. The ultimate tensile strength was greater in the longitudinal direction for the duodenum and the jejunum. In both the longitudinal and transverse directions, the greatest ultimate

strength and the greatest ultimate elongation were reported for the ileum, followed by the jejunum and the duodenum. Similarly, for all regions of the large intestine, the ultimate percent elongation in the transverse direction was greater than in the longitudinal direction. Regional differences were also identified for the large intestine. In the transverse direction, the greatest tensile strength was reported for the ascending colon, followed by the transverse colon and the descending colon. No significant regional differences were reported for the ultimate strength in the longitudinal direction. In both directions, the ultimate elongation for the descending colon was lower than for the other regions of the large intestine.

Egorov et al. (2002) tested longitudinal and transverse tissue samples from the human cadaveric stomach, small intestine, and large intestine in uniaxial tension at a constant, quasi-static loading rate of 50 mm/min. Rectangular tissue samples 60 to 65 mm in length and 10 mm in width were tested. The results indicated directional response variations for the small and large intestines, with a greater peak stress occurring in the longitudinal direction. The results were reported as engineering stress and percent engineering strain. The small intestine samples had a peak stress and failure strain of 0.8 MPa and 139% in the transverse direction and 1.5 MPa and 153% in the longitudinal direction. The large intestine samples were obtained from the transverse colon and had a peak stress and failure strain of 0.8 MPa and 177% for the transverse direction. The peak stress and failure strain were 1.2 MPa and 205% for teniae samples in the longitudinal direction and 0.5 MPa and 206% for haustra samples in the longitudinal direction. No directional differences were reported for the stomach. The peak stress and failure strain were 0.5 MPa and 190% for the transverse direction and 0.7 MPa and 189% for the axial direction.

In each of these studies, an anisotropic material response was identified for uniaxial tension testing conducted using samples obtained in multiple orientations. Despite the anisotropic nature of the membranous abdominal tissues reported in these studies, no data are available that characterize the material response of these tissues in multi-axial loading modes.

Solid Abdominal Organs. Local failure response data have been quantified at both the material and structural levels for the human liver, spleen, and kidneys. For soft biological tissues such as the liver and the spleen, material properties data are often obtained using isolated samples tested in uniaxial tension or unconfined compression. Brunon et al. (2010) reported the tensile material properties of fresh human liver capsule and parenchyma samples tested to failure using quasi-static rates of 0.001-0.01 s^{-1}. The average true stress at failure was 1.85 MPa and the average Green-Lagrange failure strain was 32.6% for all samples. Kemper et al. (2010; 2013) characterized the uniaxial tensile and compressive response of fresh human liver parenchyma samples using loading rates of 0.01, 0.1, 1.0, and 10.0 s^{-1}. The response was non-linear and rate dependent in both tension and compression, with a significant increase in failure stress

and a significant decrease in failure strain reported with increased loading rate. In uniaxial tension, the average 2nd Piola Kirchhoff stress at failure ranged from 40.2 to 61.0 kPa, and the average Green-Lagrange failure strain ranged from 0.34 to 0.24 for loading rates of 0.01 to 10.0 s^{-1}. In unconfined compression, the average true stress at failure ranged from 63.7 to 110.5 kPa, and the average true strain at failure ranged from 0.94 to 0.60 for loading rates of 0.01 to 10.0 s^{-1}.

Kemper et al. (2012) characterized the uniaxial tensile response of fresh human spleen parenchyma samples and combined capsule and parenchyma samples using loading rates of 0.01, 0.1, 1.0, and 10.0 s^{-1}. The response of both types of samples was non-linear and rate dependent with a significant increase in failure stress and a significant decrease in failure strain with increased loading rate. For the spleen parenchyma samples, the average 2nd Piola Kirchhoff stress at failure ranged from 16.5 to 33.8 kPa, and the average Green-Lagrange strain at failure ranged from 0.26 to 0.18 for loading rates of 0.01 to 10.0 s^{-1}. For the spleen capsule/parenchyma samples, the average 2nd Piola Kirchhoff stress at failure ranged from 43.6 to 65.3 kPa, and the average Green-Lagrange failure strain ranged from 0.23 to 0.17. The failure stress reported for the combined capsule/parenchyma samples was significantly greater than the response reported for the parenchyma samples. Failure strain was not significantly different between sample types.

At the structural level, studies have investigated the direct blunt impact response of the human solid abdominal organs. Schmitt et al. (2006) reported the response of five isolated, perfused human kidneys to pendulum impacts with energies of 2.5, 4.0, and 7.0 J. The organs were suspended such that the setup represented a standing or seated posture with gravity perpendicular to the loading direction. Viscoelastic behavior was reported for the increasing energy impacts, and the 4.0 J impact condition, associated with clinical grade III injuries in the porcine model (Schmitt and Snedeker, 2006), resulted in an average maximum load of 500 N. Sparks et al. (2007) characterized the response of the perfused human liver to direct falling-weight impacts. This study was designed to investigate pressure as a predictor for blunt liver injury. The importance of organ turgor has been shown in previous studies for the generation of realistic injuries in *ex vivo* impacts (Mays, 1966) and maintaining the viscoelastic tissue response representative of *in vivo* behavior (Kerdok et al., 2006). The results of Sparks et al. (2007) indicated that pressure-based metrics were the best predictors for the injuries that were generated in the study, and these injuries were consistent with liver injuries occurring in field accidents. However, in general the load distribution across the non-uniform organ geometry is difficult to quantify for isolated *ex vivo* tests. This confounds the ability to translate the results of these impacts to the load distribution occurring *in vivo* during blunt impact. Further, the mechanisms of organ motion and interaction leading to injury *in vivo* are unknown. This is an area for future research in the investigation of solid abdominal organ injuries resulting from blunt impact.

Regional Response

A number of regional experimental studies have been conducted using post-mortem human surrogates (PMHS) to investigate the impact and injury response of the abdomen to crash-specific loading modes. Typically, these tests are designed to simulate the interaction of a vehicle occupant with components of the vehicle interior. Experimental configurations are often simplified to improve the repeatability of the tests and designed to measure parameters of interest. For example, surrogates are often positioned in a rigid fixture to avoid the complications of dynamic testing, and often the loading is conducted with a simplified impactor representative of a component of the vehicle interior, such as a rigid-bar impactor that represents the steering wheel rim. Additionally, human cadaver testing is limited by post-mortem changes in the cadaver, including a lack of active musculature, respiration, organ turgor, and physiologic response. Various procedures are typically implemented during PMHS preparation and testing to improve the biofidelity of the test surrogates including perfusion of the vasculature and ventilation of the lungs. Response data from these impacts are often scaled to a common basis to develop corridors and identify metrics for injury prediction. This section summarizes studies that characterized the response of the human cadaver abdomen to rigid-bar and rigid-disk impact, seatbelt loading, and airbag interaction.

Frontal Rigid Impact Studies. Cavanaugh et al. (1986) reported the abdominal response of 12 unembalmed human cadavers impacted at the level of L3 using a 2.5-cm diameter rigid-bar attached to linear impactors of 31.5 kg and 63.5 kg. Cadavers were positioned in an upright, seated posture, with the spine of the cadaver unrestrained (free-back), which allowed translation to occur during the impact. Impact speeds ranged from 4.9 to 13.0 m/s, and the response data were divided into two groups with average speeds of 6.1 m/s and 10.4 m/s. The response of the abdomen was reported to be proportional to impact speed and impactor mass, suggesting a rate sensitive mechanical response. Load-penetration curves indicated an initial rise to the peak loading response followed by a sudden unloading.

Viano et al. (1989) conducted impacts using unembalmed, re-pressurized human cadavers positioned in a free-back, upright posture. The impactor was a 15.2-cm diameter rigid-disk attached to a 23.4-kg pendulum. Tests were conducted with the impactor face centered 7.5 cm below the xiphoid process and aligned at an angle of 60 degrees to the right or left of the midline of the cadaver. Three impact speed ranges were used, with average speeds of 4.5, 6.7, and 9.4 m/s for each group. The load-penetration response curves showed an initial rise to peak loading, followed by a force plateau and a restorative unloading response. This response differed from the sudden unloading response reported by Cavanaugh et al. (1986) and can be attributed to impactor contact with the rib cage resulting in more restorative forces compared to impacts that do not engage the ribs.

Nusholtz and Kaiker (1994) reported the abdominal response of six unembalmed, re-pressurized human cadavers impacted at the level of L2 using an impactor that simulated the lower rim of a steering wheel. The impacts were conducted using an angled semi-circular tube attached to an 18-kg pendulum impactor. The cadavers were positioned in a free-back, seated posture, and the impactor was aligned halfway between the lower aspects of the tenth ribs and the iliac crests. Tests were conducted at nominal speeds of 6 and 10 m/s; however, no rate sensitivity was reported for the load-penetration response of these impacts.

Hardy et al. (2001a) reanalyzed the rigid-bar impact response data reported by Cavanaugh et al. (1986), Viano et al. (1989), and Nusholtz and Kaiker (1994), as well as data reported by Stalnaker et al. (1985) for free-back, seated primate impacts conducted using rigid-bar and wedge-shaped impactors at speeds ranging from 8.4 to 17.0 m/s. The load-penetration response for the primate impacts showed a three-stage rise-plateau-rise response. Data from each of these studies were scaled using equal-stress/equal-velocity scaling (Eppinger, 1976) and velocity scaling where appropriate. Data were grouped as high-speed (10 m/s) and mid-speed (6 m/s) responses and compared to corridors generated from the data reported by Cavanaugh et al. (1986) for 6 and 10 m/s impacts. General agreement between studies was found for the stiffness of the 10 m/s impacts; however, for the 6 m/s impacts, response variations were identified in the curve shapes and by loading rate. The discrepancies suggested that the rate effects observed in these studies were dependent on the relative impactor-to-subject mass ratios for the different conditions, with increased rate sensitivity reported for impacts with higher ratios. Additionally, the characteristics of the load-penetration response varied with impactor shape. The more distributed loading of the rigid-disk impactor resulted in a steeper rise and load plateau compared to the response of the rigid-bar impactors.

Hardy et al. (2001a) also conducted free-back and fixed-back impacts to the human cadaver abdomen to address variations in the response data reported for previous rigid impact studies. Tests were conducted with cadavers re-pressurized and positioned in an upright, seated posture. The free-back impacts were conducted at the level of L3 or T11 using a 48-kg pendulum impactor with a 2.5-cm diameter rigid-bar applied at 6 and 9 m/s. New response corridors were developed for these impacts with an average dynamic stiffness of 27 kN/m for the mid-speed tests and 63 kN/m for the high-speed tests. Fixed-back tests were also conducted at 3, 6, and 9 m/s using one male cadaver. The motion of the pendulum was arrested following 200 mm of penetration into the abdomen to avoid damaging the cadaver during the repeated impacts. The load-penetration responses of the fixed-back tests matched the free-back response initially, but subsequently fell below the free-back corridors. This variation in response for the fixed-back tests was attributed to the elimination of the inertial component of whole-body motion present in the free-back response.

Seatbelt Loading. Initial investigations of the abdominal response to seatbelt loading used swine cadavers (Rouhana et al., 1989) and anesthetized swine (Miller, 1989) to characterize the load-penetration response. The response of the human cadaver abdomen to seatbelt loading has been investigated in a number of studies (Hardy et al., 2001a; Trosseille et al., 2002; Foster et al., 2006; Lamielle et al., 2008). Hardy et al. (2001a) conducted six seatbelt tests using three human cadavers loaded at the level of the mid-umbilicus. Five tests were conducted in a free-back configuration, and one test was conducted in a fixed-back configuration. The peak loading rate was approximately 3 m/s using a haversine penetration speed-time history. The seatbelt webbing was routed around the anterior and lateral aspects of the cadaver and fastened to a pneumatic driving mechanism positioned behind the cadaver. The tests were designed to optimize abdominal interaction with the seatbelt and resulted in a distributed and consistent application of load to the abdomen. The seatbelt webbing at the lateral aspects of the cadaver restricted the lateral expansion of the abdomen during loading. The high abdominal stiffness value of 120 kN/m reported by Hardy et al. (2001a) was attributed to these factors. The only injuries reported for these cadavers were rib fractures.

Trosseille et al. (2002) reported the results of high-power pretensioner tests using six human cadavers. Seatbelt penetration rates ranged from 8.2 to 11.7 m/s with the belt applied out-of-position in a fixed-back test configuration. The seatbelt webbing was routed around the abdomen above the iliac crests, similar to the configuration used by Hardy et al. (2001a). Trosseille et al. (2002) reported abdominal compression that ranged from 25 to 32 percent; however, seatbelt penetration was measured at the lateral aspect of the belt and not at the umbilicus. The injuries reported for these tests were mostly minor or moderate mesenteric tears, with the exception of one cadaver that sustained spleen, liver, and omentum injuries. No correlation was found between abdominal injury and measured response parameters for these tests.

Foster et al. (2006) reported the response of the re-pressurized human cadaver abdomen to high-speed seatbelt loading applied using pyrotechnic pretensioners. Tests were conducted in an upright, seated, fixed-back configuration using a custom loading apparatus designed to maximize the interaction between the seatbelt and the abdomen in controlled, repeatable tests. Eight cadavers were tested in out-of-position conditions with the seatbelt aligned at the level of the mid-umbilicus and routed along the lateral aspects of the cadaver, similar to the configurations of Hardy et al. (2001a) and Trosseille et al. (2002). Three pretensioner systems of varying energy were used: two systems with single pretensioners and one system with two pretensioners of the same type. Peak abdominal penetration ranged from 49 mm to 138 mm, and peak penetration speed ranged from 4.0 m/s to 13.3 m/s. The initial slope reported for the load-penetration response was 3500 kN/m for the most severe system and 3000 kN/m for the lower energy system. The high initial stiffness was attributed to the compression of the lateral aspects of the cadaver during

pretensioner deployment, prior to penetration of the belt into the abdomen. In addition, differences were reported between the motion of the seatbelt at the umbilicus compared to belt motion at the lateral aspects of the cadaver. This suggested that seatbelt deflection measured at the lateral aspects of the cadaver, such as in the results reported by Trosseille et al. (2002), results in an underestimation of abdominal penetration and an overestimation of penetration rate.

Foster et al. (2006) reported liver injuries in response to high-speed seatbelt loading for three of the cadavers tested in this study, and spleen injuries were reported for one cadaver. Considering all of the tests, the proposed Injury Assessment Reference Values (IARVs) showed similar trends with no overlap in the distinction between the non-injury and the injury responses. This included the product of maximum penetration speed and maximum compression (Vmax*Cmax) (Rouhana et al., 1985) and the product of maximum load and maximum compression (Fmax*Cmax) (Rouhana et al., 1987). There was overlap in the peak aortic pressure for injurious and non-injurious responses. Additional tests would be necessary to assess the predictive capability of each of the proposed IARVs. This would be a valuable investigation as currently there is no widely accepted metric for abdominal organ injury prediction.

Lamielle et al. (2008) conducted tests using eight human cadavers and two different conditions that represented occupant submarining and out-of-position seatbelt loading. Lamielle et al. (2008) used test configurations similar to Trosseille et al. (2002) and Foster et al. (2006). The submarining condition was simulated using a lower seatbelt penetration speed of approximately 4 m/s and a higher peak compression of approximately 40% compared to the out-of-position conditions of approximately 8 m/s and 30% compression. The primary objective of this study was to characterize the dynamic three-dimensional deformation of the abdomen in multiple configurations to aid in the development or validation of human computational models. This was achieved through the three-dimensional reconstruction of the position of 900 targets glued to the abdomen and imaged using four high-speed video cameras. Additionally, static stiffness values were reported as approximately 30 kN/m for the submarining tests and 7 to 12 kN/m for the out-of-position tests, determined using abdominal penetration and belt displacement, respectively. In addition to solid abdominal organ injuries, multiple small bowel contusions were reported for both test conditions. These injury patterns differed from those reported by Trosseille et al. (2002) and Foster et al. (2006). The effects of boundary conditions and test conditions on hollow abdominal organ injury outcomes therefore warrant further investigation.

Airbag Tests. The cadaver response to airbag loading was investigated by Hardy et al. (2001a) for out-of-position occupants, and a surrogate airbag loading device was developed to improve repeatability and reduce measurement issues during low-mass, high-rate, distributed loading. Tests were conducted using

passenger airbags aligned with the umbilicus of the human cadaver abdomen. Tests were conducted in a free-back configuration. Based on the results of these tests, the surrogate airbag device was designed to penetrate the cadaver abdomen at a peak speed of approximately 13 m/s with a peak load between 3.8 and 4.6 kN. A new corridor was generated for the response to surrogate airbag loading. The lower bound of the initial rise in stiffness was 500 kN/m, and the upper bound was 2000 kN/m. The airbag tests resulted in injuries to the ribs, colon, liver, mesentery, peritoneum, and diaphragm. This was one of the few studies that generated colon tears in the cadaver.

RESEARCH OBJECTIVES

The objective of this research was to characterize moderate and serious abdominal injury mechanisms, tissue failure thresholds, and internal organ response to blunt loading. This research had three primary components, which are addressed in subsequent chapters of this dissertation:

1. In-depth examination of field accident data to investigate the mechanisms of hollow abdominal organ (e.g. intestinal) injuries in MVCs,
2. High-rate tissue testing to quantify the material properties and failure thresholds of the abdominal tissues,
3. Impact testing using whole post-mortem human surrogates (PMHS) and high-speed biplane x-ray imaging to quantify the relative position and kinematics of the internal organs in response to blunt loading.

The overall motivation for this research was to advance efforts toward abdominal organ injury mitigation in MVCs. To that end, each aspect of this research generated novel injury biomechanics data with applications for future experimental testing and finite element modeling.

A portion of this dissertation was presented by Howes and Hardy (2012), Howes et al. (2012), Howes and Hardy (2013), and Howes et al. (2013). Some figures are reprinted by permission of the Stapp Association. Each of these figures is labeled with a § symbol in the caption.

CHAPTER 2

Abdominal Injury Patterns and Mechanisms

Case data from the Crash Injury Research and Engineering Network (CIREN) database were analyzed to determine the occupant and crash characteristics associated with moderate and serious hollow abdominal organ injuries occurring in motor vehicle collisions (MVCs). In frontal crashes with adult occupants, no clear association was found between hollow organ injury and age or anthropometry. Hollow organ injuries were associated with high crash severity, with 58% of occupants with these injuries involved in crashes above 50 kmph. The percentage of injuries attributed to the hollow abdominal organs was higher for rear seat occupants compared to right front passengers or drivers. Lap-shoulder belt interaction was found to be a common factor associated with hollow organ injury. All occupants in the CIREN database with abdominal injuries to only the hollow organs were restrained with a lap-shoulder belt, whereas only 52% of occupants with only solid organ injuries were restrained. This suggests that the primary mechanism of injury may be different for the hollow and solid organs. The majority of occupants with abdominal injuries to the jejunum-ileum also sustained abdominal skin contusions attributed to the seatbelt. Occupants with seatbelt contusions high on the abdomen, suggesting improper seatbelt routing or submarining, typically sustained injuries to the proximal jejunum, whereas occupants with lower abdominal contusions sustained injuries to the distal jejunum and ileum. The association between injury location and seatbelt routing found in this analysis supports a localized mechanism for hollow organ injury of combined tension and compression due to lap-belt loading of the abdomen.

INTRODUCTION

A number of studies have investigated abdominal injury patterns in field accident data, but few studies have applied real-world crash data analysis to investigate abdominal organ injury mechanisms. The injury analysis in this study was largely driven by variations in the results from field accident data investigations in the United States, Europe, and Japan. For example, European and Japanese studies have shown trends indicating an increased rate of abdominal injury in older occupants (Lamielle et al., 2006; Yaguchi et al., 2011; Frampton et al., 2012), whereas Klinich et al. (2010) showed no increase in abdominal injuries for older age groups in the United States. Additionally, belted rear seat occupants in European studies were found to have a higher rate of AIS2+ abdominal injuries compared to front seat occupants (Lamielle et al., 2006; Frampton et al. 2012). The majority of the studies in the United States have focused on front seat adult occupants, and abdominal injuries in rear seat occupants have not been investigated specifically.

In addition to these differences, the analysis of Yaguchi et al. (2011) suggested that increased age was associated with fatality resulting from injury to the abdominal region, though it was not clear that this

trend was significant. The fatality rate reported for belted drivers age 65+ was considerably greater for the abdomen compared to any other region. The analysis also suggested that for belted drivers of any age, the rate of fatalities and the rate of serious injuries were greater for the abdomen compared to all other regions. Rate was determined as the number of fatalities (or serious injuries) for a given region divided by the sum of all fatalities and injuries for that region. Therefore, these values did not reflect the actual rate of injury or fatality as the data were not normalized to the injuries and fatalities from the entire dataset. Additionally, it was unclear in this analysis how fatalities (death within 24 hours of MVCs) were attributed to a given body region, and whether comorbidities, other indirect causes of death such as surgical complications and infection, or multiple serious injuries from different regions contributed to the fatalities. Fatalities occurring after 24 hours were excluded from this analysis. Further, the scale used to categorize injuries as slight or serious was not described; therefore, the relationship between these injuries and those classified using the Abbreviated Injury Scale (AIS) is unknown. The issues that arose with this analysis warranted further investigation with field accident data to characterize the factors influencing abdominal injury distributions and to identify potential local injury mechanisms.

The analysis detailed herein was conducted in conjunction with a separate National Automotive Sampling System/Crashworthiness Data System (NASS/CDS) database analysis (Gabler, 2013). The objective of the NASS/CDS analysis was to identify trends in the type and occurrence of abdominal injuries in MVCs. Data for the NASS/CDS analysis included case years spanning from 1998 through 2008 and were compiled using the following filters: AIS2+ abdominal injuries, front seat occupants, age of 12+ years, belted and unbelted occupants, airbag equipped vehicles, and frontal crash modes as the most harmful event. These criteria were selected to give emphasis to occupants with the advantage of the current safety technologies. Rollovers were excluded from this analysis. The study also reported trends in abdominal injuries for rear seat occupants. Data for this portion of the analysis included case years spanning from 1997 through 2008 with model year 1997+ vehicles, rear seat occupants of all ages, and all crash modes excluding rollovers.

The results of the NASS/CDS analysis identified an increased risk of AIS2+ abdominal injuries for occupants $\geq$ 60 years old. These occupants accounted for 10% of vehicle occupants; however, 20% of occupants that sustained AIS2+ abdominal injuries were $\geq$ 60 years old. The 20-29 year old age group was also overrepresented in terms of abdominal injury incidence. A similar trend with age was identified for occupants sustaining abdominal injuries in the rear seat. No correlation was found between abdominal injury occurrence and occupant gender, height, weight, or seating position. The distribution of AIS2+ abdominal injuries by frequency for all occupants was the liver (36%), spleen (31%), and digestive organs (20%). Considering AIS2+ abdominal injuries for rear seat occupants only, the injury distribution by

order of frequency was digestive (56%), kidneys (15%), and spleen (15%). The most common injury sources for AIS2+ abdominal injuries in frontal impacts were the steering wheel (41%) and seatbelt system (28%). The restraint system was the most common injury source for abdominal injuries sustained in the rear seat (75%). The analysis of rear seat occupants also indicated that approximately equal proportions of belted and unbelted occupants sustained abdominal injuries. The median speed for occupants with AIS2+ abdominal injuries (39 kmph) was 2.3 times greater than the median speed for all occupants, with and without abdominal injury (17 kmph). The injured population was skewed toward occupants in fixed-object collisions, which accounted for 20% of crashes and 40% of abdominal injuries. The results of the NASS/CDS analysis were used to tailor the analysis in this study to capture injury characteristics representative of those occurring in the field.

The objective of this study was to supplement the data in the literature regarding abdominal injury patterns by investigating the characteristics and mechanisms of moderate and serious hollow abdominal organ injuries occurring in frontal MVCs. The analysis was carried out with an in-depth examination of field accident data using the CIREN database. The CIREN database combines accident data from detailed crash investigations with occupant data from medical examinations and imaging to allow for a multidisciplinary analysis of real-world crashes. The database includes cases in which at least one vehicle occupant was transported to a Level 1 trauma center. For inclusion in the dataset, adult occupants in frontal and side crashes must sustain at least one AIS3+ injury or sustain two or more AIS2+ injuries in different body regions (Loftis et al., 2011, citing NHTSA, 2010). By design, the CIREN database includes an overrepresentation of occupants with serious injuries. Therefore, results from the NASS/CDS database analysis were used to provide a context to guide case selection using the CIREN database. Occupants with abdominal injury to the hollow organs only or to the solid organs only were characterized by occupant and crash characteristics. Based on this analysis, cases of jejunum-ileum injury in the CIREN database were analyzed in detail to further examine potential hollow organ injury mechanisms related to occupant anthropometry, seating location and posture, seatbelt routing, and the resulting injuries.

METHODOLOGY

Injury Characterization

Selection Criteria. The CIREN dataset that was analyzed contained completed cases in the database as of August 2012. The case selection criteria mirrored the NASS/CDS criteria with preference given to AIS3+ abdominal injury cases. Both front and rear seat occupants, 12 years old or older, were included in the CIREN analysis. For categories specific to solid and hollow abdominal organ injuries, impacts were limited to frontal crash modes with a principal direction of force (PDOF) of ± 20°. Pregnant occupants were excluded from this analysis due to the interest in associating occupant anthropometry with injury type, as variations in the stage of pregnancy could affect this comparison.

Analysis. Occupants 12 years old or older in frontal crashes (PDOF ± 20°) with serious abdominal organ injuries were categorized as sustaining only solid abdominal organ injuries (denoted: Solid): including occupants with AIS3+ injuries to the liver, spleen, kidney, or pancreas, or occupants were categorized as sustaining only hollow abdominal organ injuries (denoted: Hollow): including AIS3+ injuries to the colon, jejunum-ileum, duodenum, or stomach. These groups were compared to the characteristics of case occupants 12 years old or older in the CIREN database sustaining any injuries in all crash modes (denoted: CIREN), as well as to case occupants 12 years old or older in all crash modes sustaining one or more abdominal injury of any type or severity (denoted: Abdomen). The purpose of this analysis was to gain an indication of the different occupant and crash characteristics associated with serious solid and hollow abdominal organ injuries in frontal collisions. The four groups were compared to identify any differing characteristics between gender, age, height, weight, occupant position, restraint use, delta-V or Barrier Equivalent Speed (BES), and object struck. For the Hollow and Solid categories, injury severity and injury source were also assessed. Occupants sustaining jejunum-ileum injuries were further analyzed to identify the occupant and crash characteristics associated with these injuries in the database.

Case Analysis

Selection Criteria. Detailed case analysis was used to further examine cases in which occupants sustained jejunum-ileum injuries. Jejunum-ileum injuries are classified as AIS2+ injuries (Table 1), ranging in severity from I to V on the Organ Injury Scale (OIS) (Moore et al., 1990). Only belted occupants 12+ years old in frontal crashes (PDOF ± 20°) were included in this analysis. From the dataset of 58 cases fitting these inclusion criteria, 19 unique cases were selected for further analysis based on an approximate distribution within anthropometry bins centered on the national estimates of the median height and weight for males and females in the United States (McDowell et al., 2008) (Table 2-Table 3). Emphasis was placed on bins in which the dataset characterization indicated a higher likelihood of injury. Multiple

impact or chaotic crash events were avoided based on an assessment of the collision summary for each case. Only cases with a known delta-V or BES were included.

Table 1: Small intestine (jejunum-ileum) injury description and scale.

OIS Grade *	Injury Type	Description	AIS 2005 §
I	Hematoma/Laceration	No devascularization; No perforation	2
II	Laceration	<50% of circumference	2
III	Laceration	>50% of circumference	3
IV	Laceration	Transection	4
V	Laceration/Vascular	Transection with tissue loss; Devascularization	4

*Moore et al., 1990

§Gennarelli and Wodzin (Eds.), 2005

Table 2: Median national estimates for height and weight*.

Median Height			Median Weight		
	cm	in		kg	lb
Male	176	69	Male	86	190
Female	162	64	Female	71	157

*McDowell et al., 2008

Table 3: Anthropometry bins for case analysis.

		Height (cm)			Weight (kg)		
Female	Range	150-159	160-169	170-180	50-69	70-79	80+
	N	3	4	3	5	2	3
Male	Range	160-169	170-179	180-190	60-79	80-89	90+
	N	1	3	5	4	2	3

Analysis. For each selected case, the following details were identified: crash characteristics including vehicle type, object struck, speed, PDOF, collision deformation classification, and maximum crush; occupant characteristics including gender, age, height, weight, body mass index (BMI), seating position, restraint use, occupant posture, and belt routing; injury characteristics including Injury Severity Score (ISS), MAIS, abdominal injury type and the associated OIS, AIS, rank, and source, additional occupant injuries, and the presence of rib fractures. Of particular interest were the associations between occupant anthropometry, seating location and posture, seatbelt routing, and the resulting injuries. Operative data and medical films were used to identify the specific location of the injury along the length of the jejunum or ileum. Seatbelt routing in the final position was identified based on abdominal skin contusions, CT evidence, and operative notes. Cases were first summarized based on the relevant characteristics, then the variations between occupant and injury characteristics were assessed to compare case occupants with differing seatbelt routing as evidenced by abdominal contusions.

RESULTS

Within the CIREN database (August 2012), the total number of all abdominal injuries was 4894. This included occupants of any age involved in all crash modes. Figure 6 shows the distribution of injuries by organ, excluding abdominal skin contusions, which accounted for 2188 injuries. Injuries to the liver and the spleen were the most common abdominal organ injuries in the CIREN database, accounting for 734 and 714 injuries, respectively. There were 227 injuries to the kidneys. Injury to the mesentery was the most common hollow organ or membranous tissue injury, accounting for 212 injuries. There were 130 case occupants with a total of 146 colon injuries, and there were 109 occupants that sustained a total of 124 injuries to the jejunum or ileum. Injuries to other hollow abdominal organs such as the duodenum, omentum, and stomach were less common, with 28, 20, and 19 injuries, respectively.

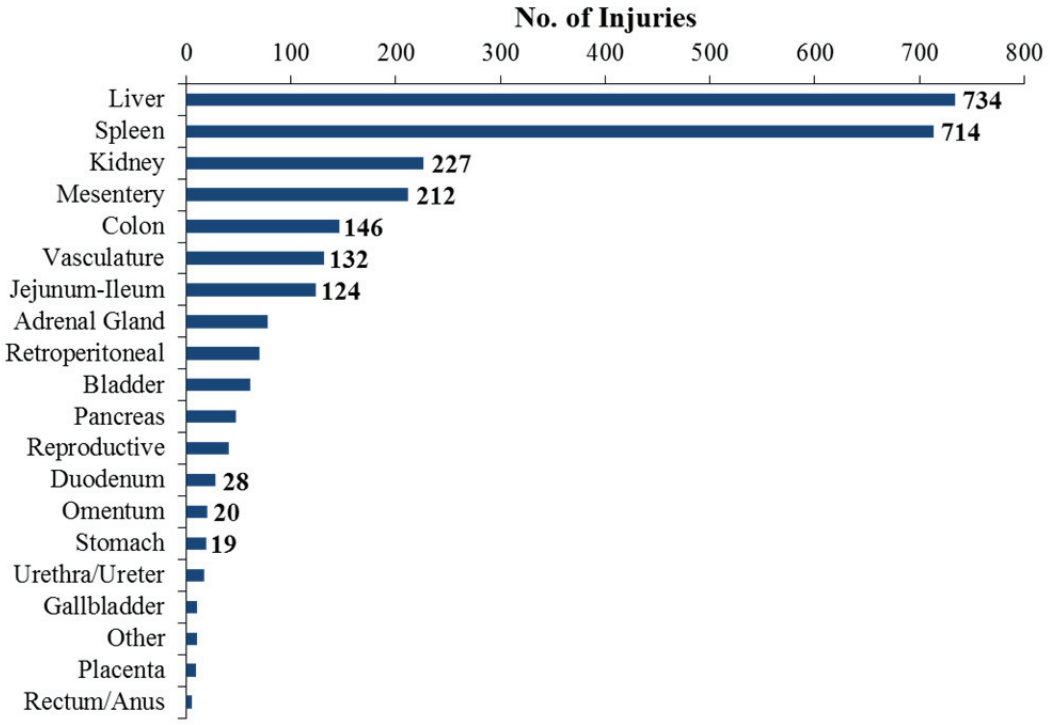

Figure 6: Abdominal organ injury distribution in the CIREN database (N=2706).

Injury Characterization

Hollow and Solid Organ Injuries. The characteristics of four occupant categories were compared to identify mechanistic differences between hollow organ trauma and solid abdominal organ trauma. Differences in occupant and crash characteristics were assessed for all occupants in the CIREN database (N=4150), occupants with abdominal injuries (N=1892), and occupants in frontal crashes (± 20°) with

serious abdominal organ injuries to either the solid organs only (N=229) or the hollow organs only (N=36). The number of occupants in each category ≥ 12 years old (yo) is summarized in Table 4.

The Collision Deformation Classification, or CDC, (SAE, 1980) was used to assess the area of vehicle damage for cases in the Solid and Hollow categories. For the cases with occupants sustaining AIS3+ abdominal injuries to the hollow organs only in collisions with a PDOF of ± 20° (N=36), all case vehicles sustained front end vehicle damage. Damage was classified as distributed across the front end, or across the right front, center front, left front, left and center, or right and center of the vehicle. For the cases with occupants sustaining AIS3+ abdominal injuries to the solid organs only in collisions with a PDOF of ± 20° (N=229), eight case vehicles had a CDC indicating damage to the right or left lateral side of the vehicle. Of these cases, five had lateral damage areas between the front end of the vehicle and the rear seat, one had lateral damage between the windshield and rear of the vehicle, and two cases had distributed lateral damage. The remainder of the cases in the Solid category had front end vehicle damage (N=221). All cases with a PDOF of ± 20° were included in the analysis.

Table 4: The number of occupants by category, with pregnant occupants excluded.

Category	No. Occupants ≥ 12 yo
CIREN: All Injuries	4150
Abdomen: Abdominal Injuries	1892
Solid Organ Injuries	1045
Solid Organ Injuries Only	958
Solid: AIS3+ Solid Organ Injuries Only & PDOF ± 20°	229
Hollow Organ Injuries	178
Hollow Organ Injuries Only	91
Hollow: AIS3+ Hollow Organ Injuries Only & PDOF ± 20°	36

The distribution of occupant gender by category is shown in Figure 7. The distribution of occupant gender was similar for the CIREN, Abdomen, and Solid categories. Male occupants that sustained serious abdominal injuries (AIS3+) to the hollow organs only in frontal crashes comprised a greater percentage of occupants in that category compared to the distribution of occupant gender in the CIREN database and for occupants with abdominal injuries or solid organ injuries only. However, a chi-square test for independence (α=0.05) was performed to assess the differences between the Abdomen, Hollow, and Solid categories, and there was not a significant relationship between gender and injury category (p=0.15).

No clear trends existed with respect to occupant age (Figure 8). Compared to the distribution of age in the CIREN database, a slightly greater percentage of occupants in the Solid and Hollow categories were less than 40 years old. The median age for occupants with hollow abdominal organ injuries only was 36 years, and the median age for occupants with solid abdominal organ injuries only was 32 years. No statistically

significant difference in age was identified between the Hollow and Solid categories (p=0.34) using the Mann-Whitney test (α=0.05). The Mann-Whitney test was selected because the data in each category were not normally distributed.

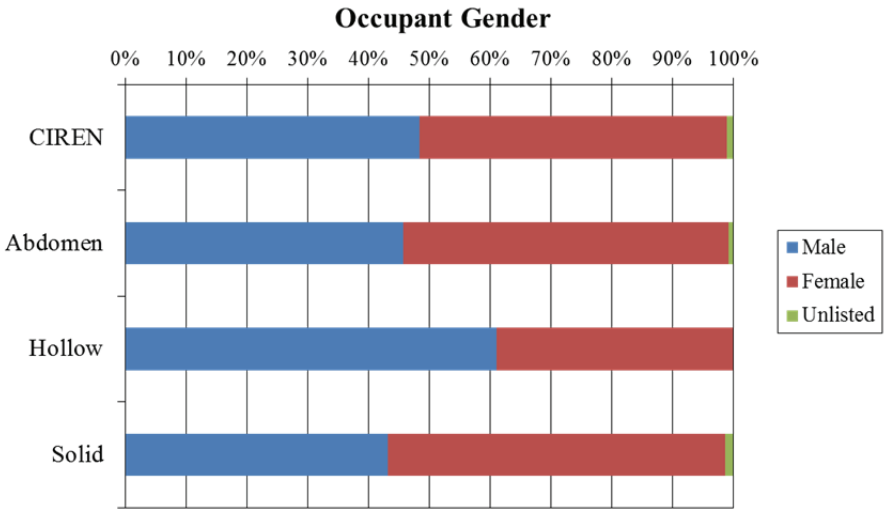

Figure 7: Occupant gender distribution by category.

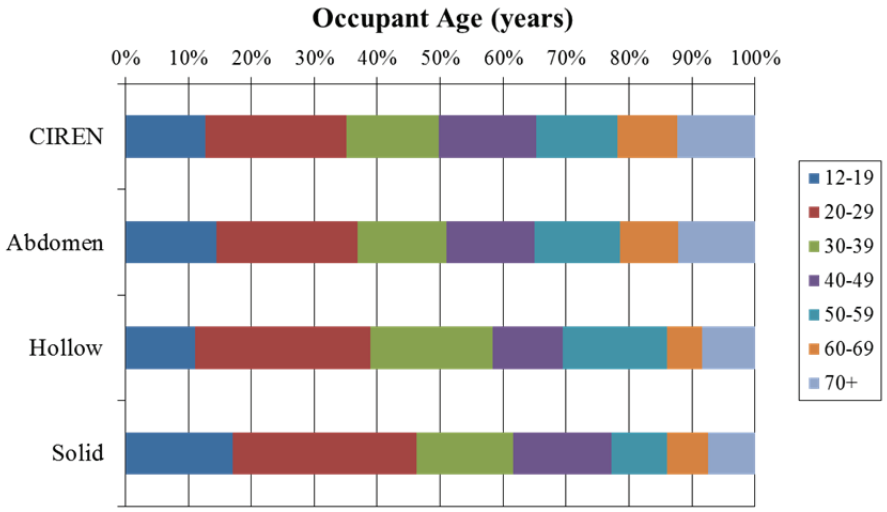

Figure 8: Occupant age distribution by category.

Occupant height and weight for males and females were directly compared for the Solid and Hollow categories. Occupants with either an unknown height or an unknown weight were excluded, and pregnant occupants were excluded. Overall trends with respect to occupant anthropometry were not particularly evident. However, assuming a normal distribution of occupants in each category centered around the median national estimates, Figure 9 potentially indicates a greater likelihood of serious hollow only injury

for females less than 160 cm and for male occupants in the height range of 180-189 cm. Considering occupant weight, the distribution of female occupants in both the Solid and Hollow categories was skewed relative to the median national estimate of 71 kg, indicating a greater likelihood of both injury types for occupants with a weight less than the median national estimate (Figure 10). Injury incidence by male occupant weight was a roughly normal distribution around the median national estimate of 86 kg, with a peak in serious hollow only injury incidence for occupants in the 70-79 kg range and the 100-109 kg range. Figure 11 and Figure 12 show these trends as the percent of occupants that sustained injury within each respective category (serious hollow only or solid only injuries by gender). Table 5 summarizes the median BMI by gender in each category, which was below the median national estimate for both genders.

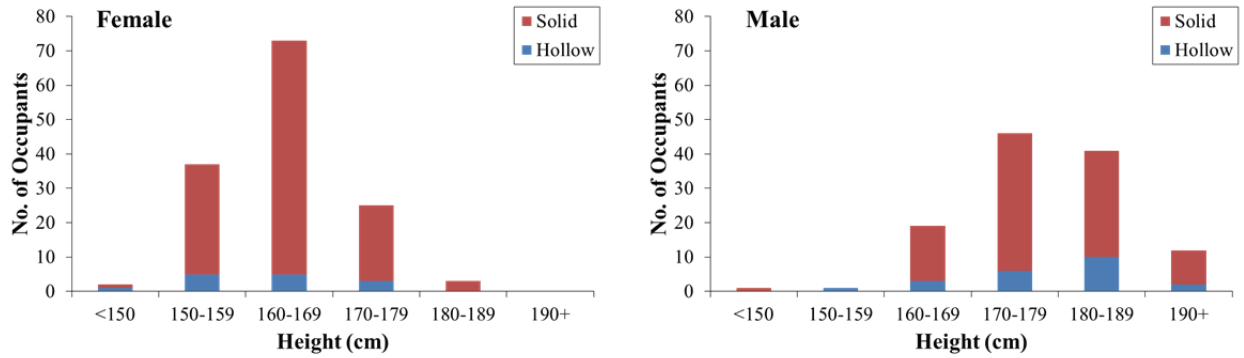

Figure 9: Height distributions for females (left) and males (right) in the Hollow and Solid categories.

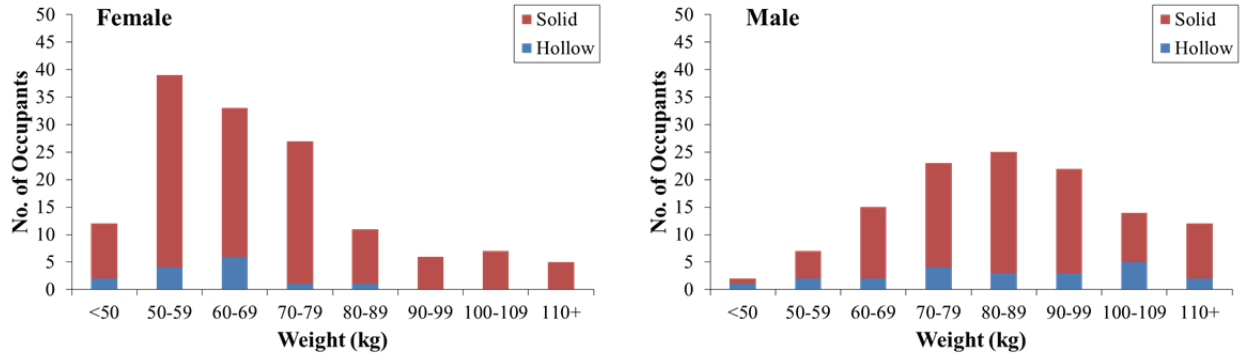

Figure 10: Weight distributions for females (left) and males (right) in the Hollow and Solid categories.

Table 5: Median BMI for males and females.

Category	Female Median BMI	Male Median BMI
Hollow Only	22.7	26.2
Solid Only	23.8	26.3
Median Nat'l Estimate (McDowell et al., 2008)	26.9	27.7

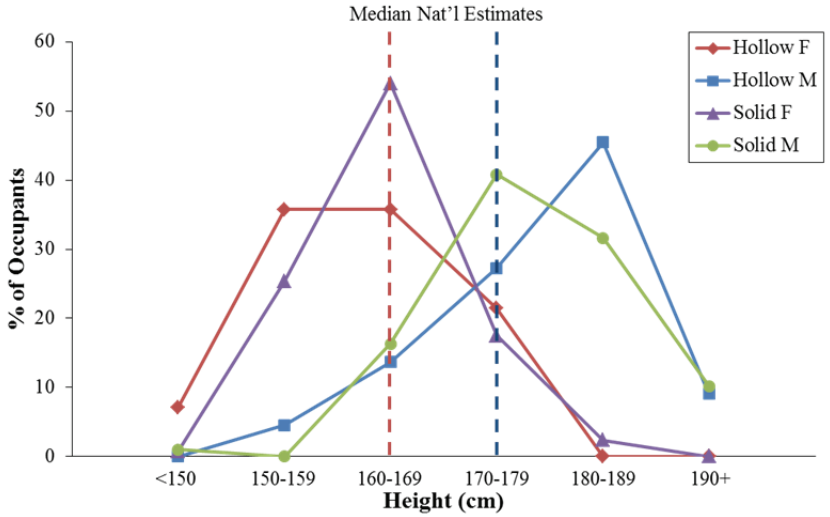

Figure 11: Height distributions shown as a percent of occupants in each category.

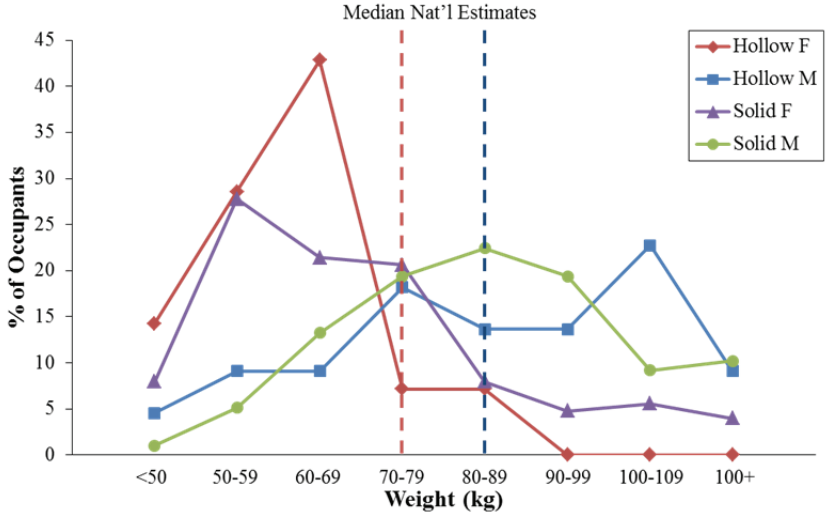

Figure 12: Weight distributions shown as a percent of occupants in each category.

A greater percentage of occupants with abdominal injuries to the hollow organs only were rear seat passengers (RSP) compared to any other occupant category (Figure 13). This was also true for right front passengers (RFP). Figure 14 shows that a greater percentage of occupants sustained solid only injuries compared to hollow only injuries in all seating positions. However, considering occupants sustaining AIS3+ hollow only or solid only abdominal injuries, the percentage of occupants that sustained hollow only injuries was higher for rear seat passengers and right front passengers than for drivers (Figure 14). A chi-square test (α=0.05) was performed on the driver, RFP, and rear seating positions for the Hollow and Solid categories. There was a significant relationship between the injury categories and seating positions (p=0.02).

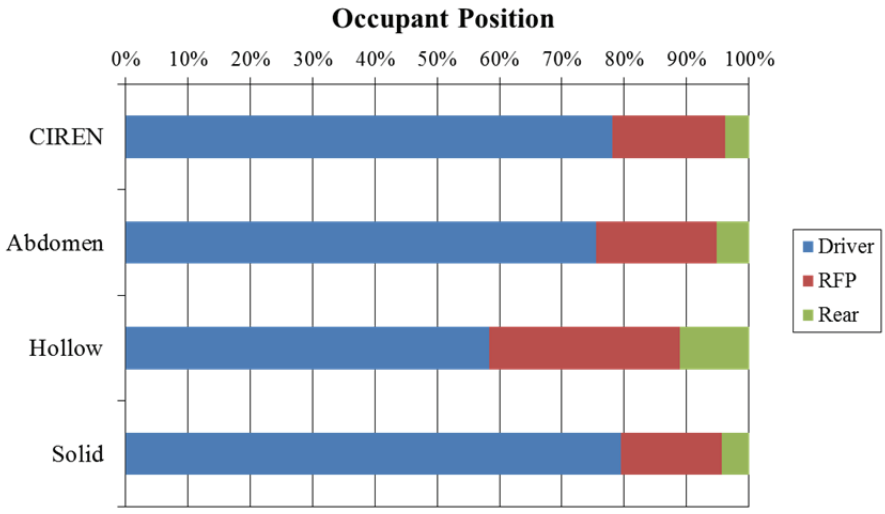

Figure 13: Occupant seating position distribution by category.

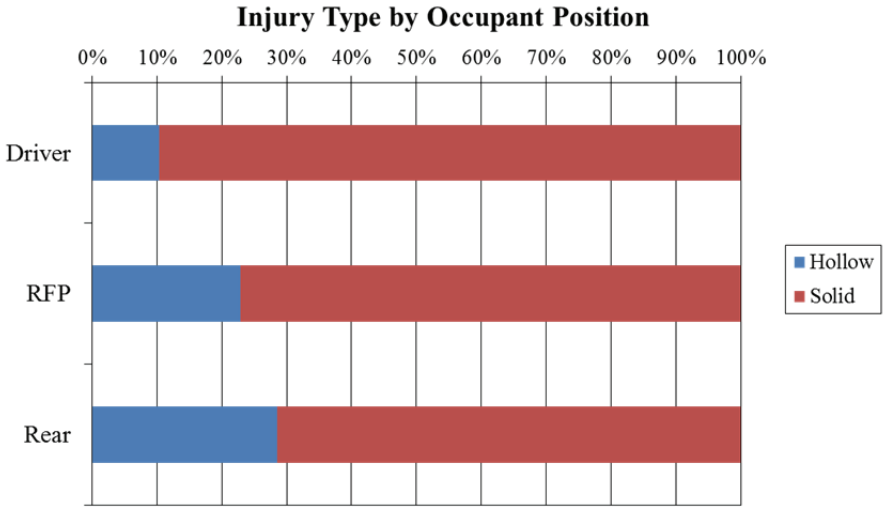

Figure 14: Occupant injury type by seating position for solid only and hollow only abdominal injuries.

Approximately 68% of occupants in the CIREN database (≥ 12 yo; non-pregnant occupants) were restrained using a lap-shoulder belt, lap belt, or shoulder belt only. In comparison, 52% of occupants with abdominal injuries to the solid organs only were belted with a lap or lap-shoulder belt, and 100% of occupants with abdominal injuries to the hollow organs only were restrained using a lap-shoulder belt (Figure 15).

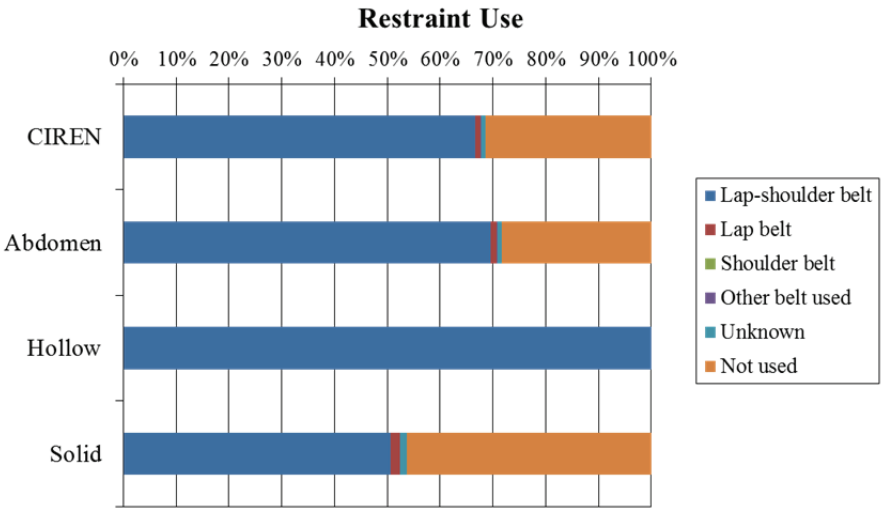

Figure 15: Occupant restraint use by category.

Figure 16 and Figure 17 show the distributions of crash severity by category for delta-V and BES. Case occupants in collisions with unlisted delta-V or BES were excluded. For reference, the number of cases with unlisted delta-V or BES in each category is included in Table 6. A greater percentage of occupants in the Hollow category were in collisions at a higher speed (> 50 kmph) compared to the other categories. The median delta-V for the Hollow category was 57 kmph, and the median delta-V for the Solid category was 47 kmph. The difference in delta-V was statistically significant between the Hollow and Solid categories ($p=0.01$) using the Mann-Whitney test ($\alpha=0.05$). Figure 18 shows the distribution of object struck by occupant category. A greater percentage of collisions in the Solid category were tree/pole impacts compared to the Hollow category.

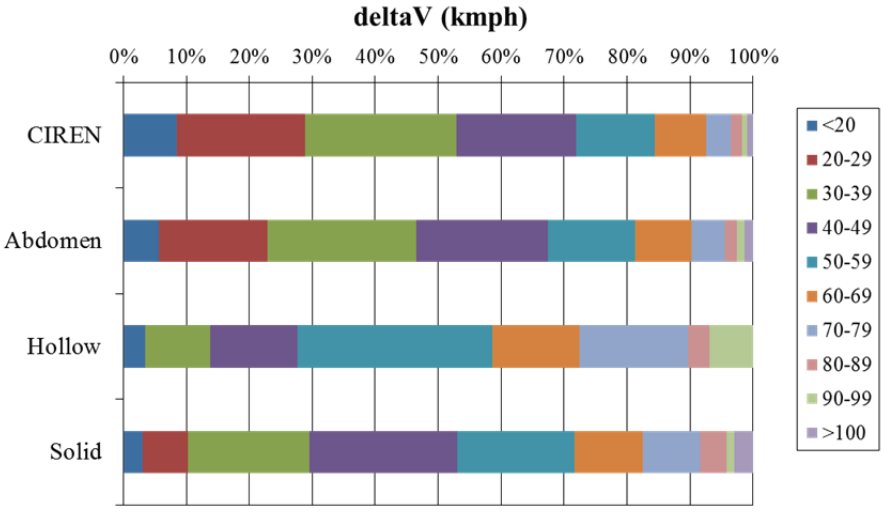

Figure 16: Crash severity (delta-V) by category. Unlisted cases excluded.

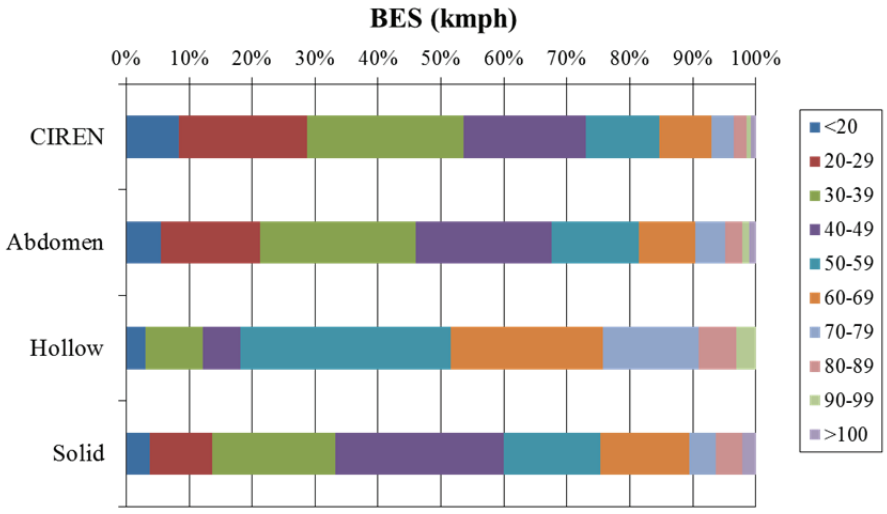

Figure 17: Crash severity (BES) by category. Unlisted cases excluded.

Table 6: Number of cases with unlisted crash severity.

Category	CIREN	Abdomen	Solid	Hollow
delta-V Unlisted	1340	535	63	7
BES Unlisted	818	310	39	3
Total Cases	4150	1892	229	36

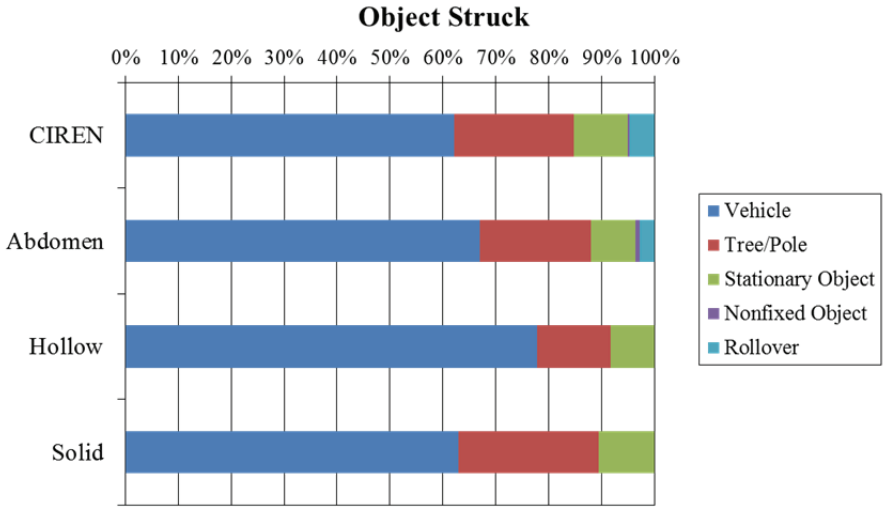

Figure 18: Object struck by category.

PDOF was examined for all occupants 12 years old or older in each injury category, with pregnant occupants excluded. Figure 19 shows each PDOF related to an injurious case in each category. This included any injury severity and all PDOF except those that were unlisted. Abdominal organ injuries sustained to the hollow organs only were almost entirely limited to impacts of ± 90°.

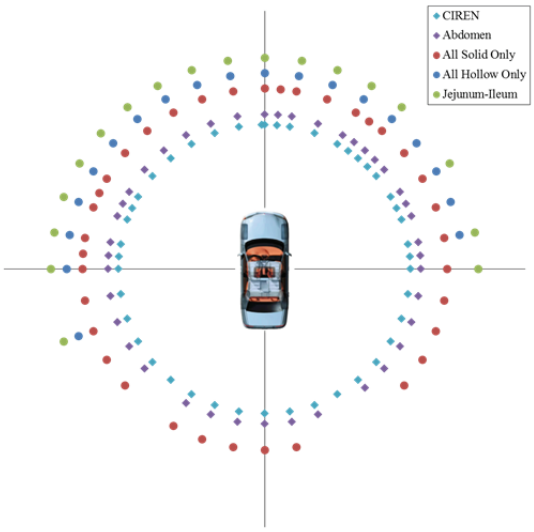

Figure 19: PDOF associated with injury occurrence in each category.

Injury distribution and source were assessed for all serious abdominal injuries to the hollow organs only or the solid organs only for occupants in frontal crashes. There were a total of 48 hollow only injuries and 323 solid only injuries. Table 7 summarizes the injury distribution in each category. Injuries to the jejunum-ileum comprised 56% of the hollow organ injuries, followed by colon injuries (38%). Injuries to the liver (53%) and the spleen (37%) were the most common injuries in the solid only category.

Table 7: Injury distribution for serious injuries to the hollow and solid organs.

Hollow			Solid		
Organ	N	%	Organ	N	%
Jejunum-Ileum	27	56	Liver	171	53
Colon	18	38	Spleen	119	37
Stomach	2	4	Kidneys	27	8
Duodenum	1	2	Pancreas	6	2
Total	48	100	Total	323	100

Figure 20 shows the injury source distribution for each category. Source was determined as either the source or the involved physical component (IPC) coded for each injury in the CIREN database. In the Hollow category, all occupants were restrained with a 3-pt. seatbelt, and 79% of the injuries were attributed to abdominal interaction with the belt restraint webbing or buckle. In the Solid category, 51% of the occupants were restrained with a 3-pt. seatbelt, and 2% of the occupants were restrained with a lap belt only. In this category, 29% of the injuries were attributed to the seatbelt. A greater percentage of injuries in the Solid category were attributed to the steering wheel (43%) compared to the seatbelt (29%). It is important to note that 79% of the occupants with solid only organ injuries were drivers, whereas 58% of occupants with hollow only injuries were drivers (Figure 13). Therefore, it was less likely for steering

wheel contact to be a possible source of injury for hollow only injuries than for solid only injuries due to occupant seating position. The other injury sources included the airbag and interior vehicle components.

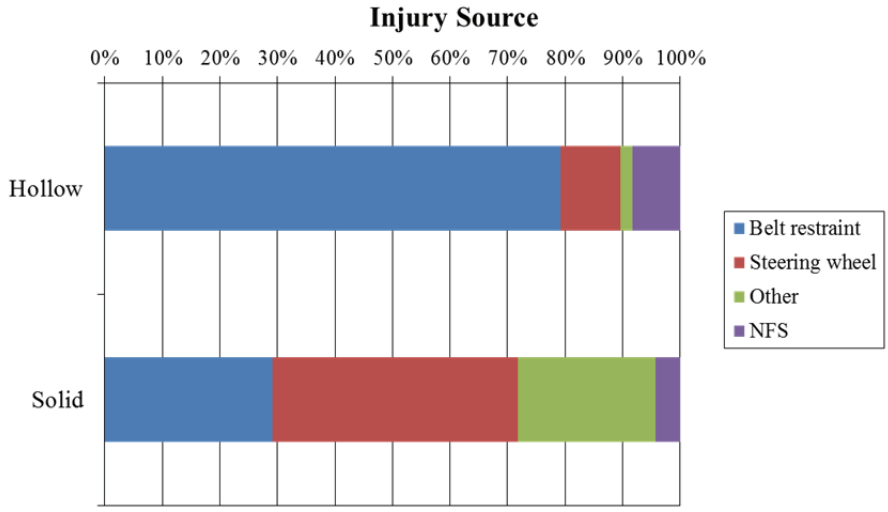

Figure 20: Injury source for the hollow only and solid only categories.

Jejunum-Ileum Injuries. There were 109 case occupants with jejunum-ileum injuries in the CIREN database with a total of 124 injuries to the jejunum or ileum. The concomitant abdominal injuries were identified for all 109 case occupants with jejunum-ileum injuries (Figure 21). Seventy-six occupants with jejunum-ileum injuries also had one or more abdominal skin contusions, and 33 occupants with jejunum-ileum injuries had no skin contusion. Other common injuries sustained by occupants with jejunum-ileum injuries were injuries to the colon (54 occupants), spleen (23 occupants), and liver (17 occupants).

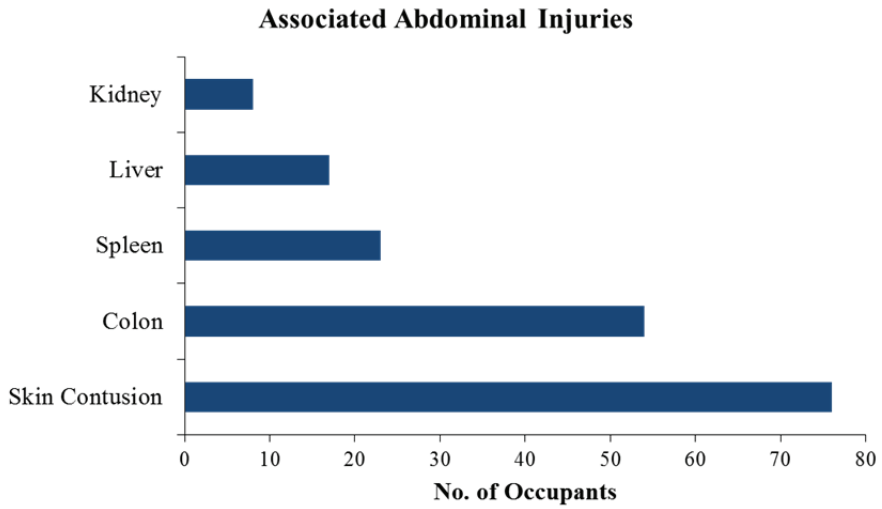

Figure 21: Number of occupants with jejunum-ileum injuries and associated abdominal injuries by type.

Occupants that sustained jejunum-ileum injuries with and without abdominal skin contusions were further examined to assess whether abdomen contact with the seatbelt was predominantly coded as the jejunum-ileum injury source when skin contusion was present. There were 88 jejunum-ileum injuries sustained by occupants that also sustained abdominal skin contusions, and 60% of these injuries were attributed to the seatbelt (Figure 22, left). Thirty-six injuries occurred in occupants that did not sustain skin contusion. The seatbelt was coded as the injury source for 36% of the injuries, and 25% of the injuries were attributed to contact with the steering wheel/rim (Figure 23, left). However, 82% of occupants without skin contusion were drivers (Figure 23, right), whereas 57% of occupants that sustained both jejunum-ileum injuries and skin contusions were passengers (Figure 22, right).

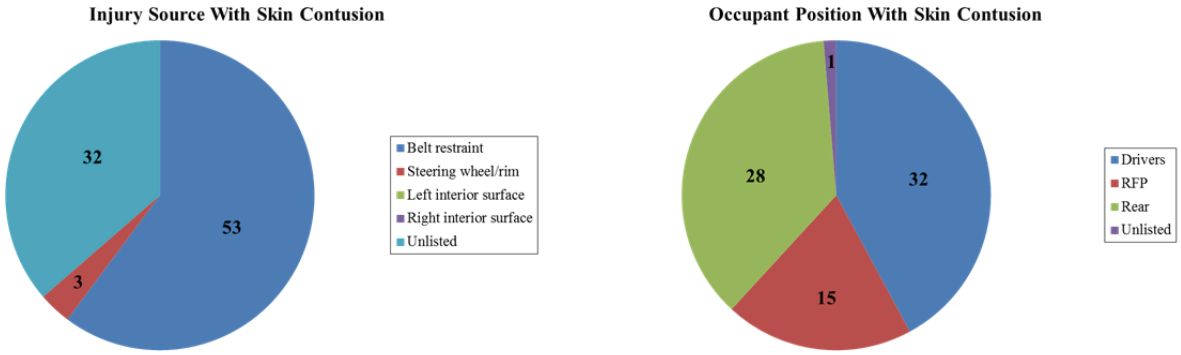

Figure 22: Injury source and position for occupants with jejunum-ileum injuries and skin contusion. Numbers indicate number of injuries (N=88) or occupants (N=76).

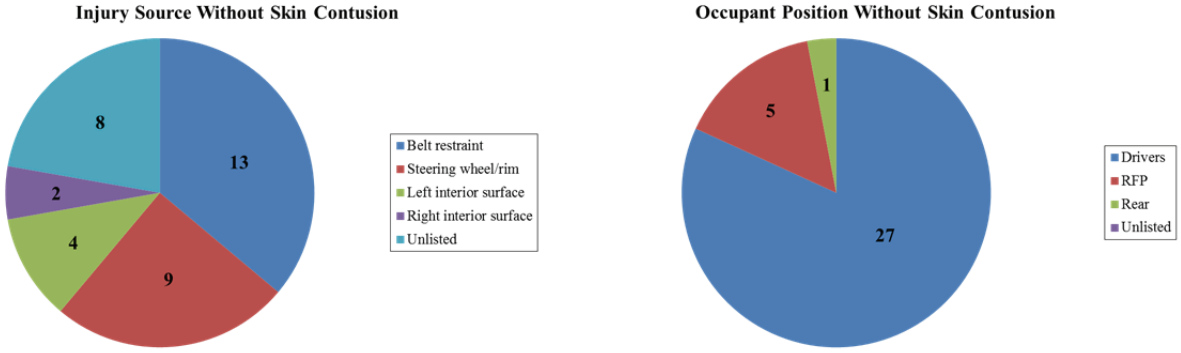

Figure 23: Injury source and position for occupants with jejunum-ileum injuries without skin contusion. Numbers indicate number of injuries (N=36) or occupants (N=33).

Occupants 12 years old or older with jejunum-ileum injuries accounted for 85 occupants and 96 injuries. The number of occupants with jejunum-ileum injuries by age group is shown in Figure 24. The distribution of occupants with hollow only or both hollow and solid abdominal injuries is identified for each age range. The age range with the greatest number of jejunum-ileum injuries was 20-29 years. No

considerable difference in the distribution of the number of occupants with hollow only injuries versus hollow and solid injuries was identified.

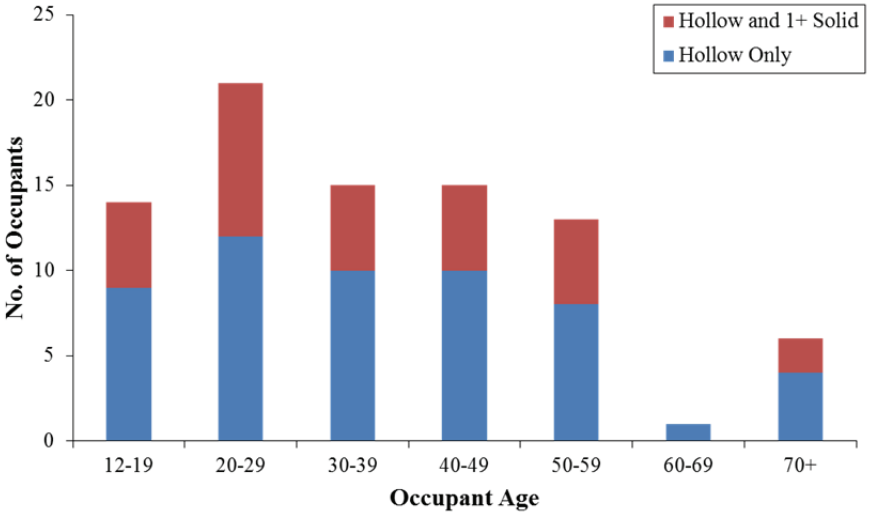

Figure 24: Number of occupants with jejunum-ileum injuries by age range.

No clear trends with gender, height, or weight were identified for occupants 12 years old or older with jejunum-ileum injuries. However, 59% of occupants with jejunum-ileum injuries were between 12 and 40 years old. Similar to the Hollow category in which 11% of occupants were rear seat occupants, a greater percentage (approximately 12%) of occupants with jejunum-ileum injuries were rear seat occupants compared to occupants in CIREN (4% rear seat occupants) and occupants with all abdominal injuries (5% rear seat occupants). The majority of occupants with jejunum-ileum injuries were restrained with a lap-shoulder belt (87%). Considering BES, 55% of cases with identified crash speeds were 50 kmph or greater (61% for delta-V). Male occupants with jejunum-ileum injuries had a higher median crash speed compared to females (Table 8). Only cases with known delta-V or BES were used. Delta-V was unlisted for 13 male and 13 female cases, and BES was unlisted for 6 male and 6 female cases. The object struck in 64% of the cases was another vehicle. The majority of case occupants that sustained jejunum-ileum injuries were in frontal crashes, with 80% of cases having a PDOF of ± 30°.

Table 8: Median crash speed for male and female occupants with jejunum-ileum injuries.

Category	Median Speed (kmph)
Delta-V Male	60
Delta-V Female	49
BES Male	54
BES Female	47

The jejunum-ileum injury distribution was assessed by severity using the OIS scale for 96 injuries sustained by occupants 12 years old or older (Figure 25). Lower severity injuries (OIS I and II) accounted for 40% of injuries with a specified injury severity level (93 injuries), and 42% of jejunum-ileum injuries were OIS III in severity. The distribution of occupant gender by jejunum-ileum injury severity was assessed for 93 injuries with a specified injury severity (Figure 26). Male occupants accounted for a greater percentage of higher severity injuries compared to female occupants.

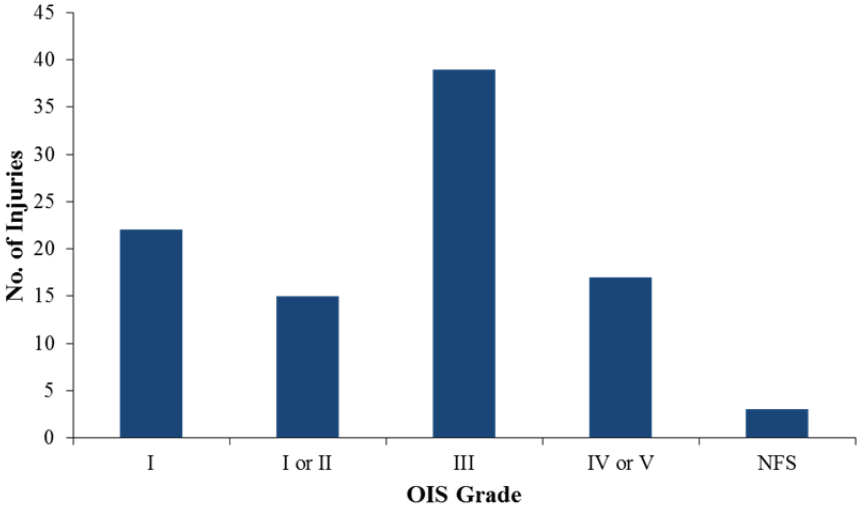

Figure 25: Jejunum-ileum injury distribution by severity (96 injuries).

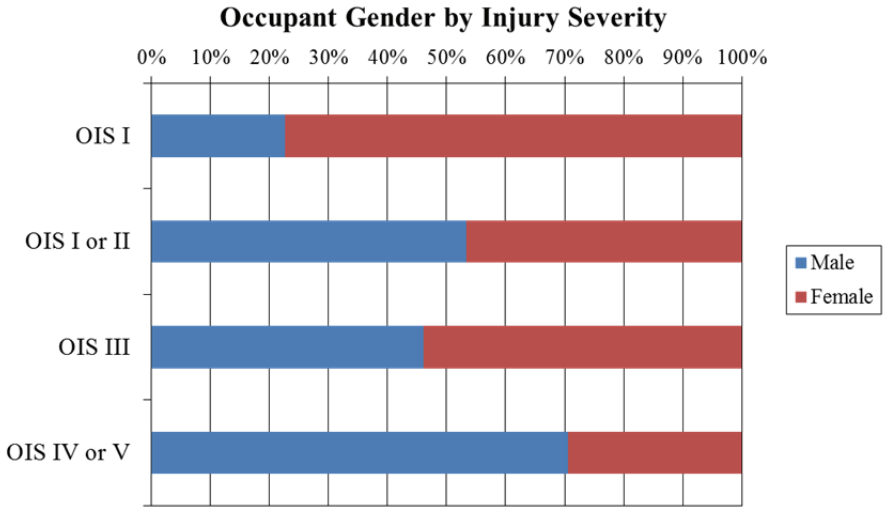

Figure 26: Occupant gender distribution by jejunum-ileum injury severity.

Injury severity was also assessed by occupant seating position (Figure 27). A greater percentage of occupants in the rear seating positions sustained higher severity injuries (OIS III+) compared to front seat

occupants. The injury source was more commonly attributed to the seatbelt for OIS III+ injuries (77%) than for lower severity injuries (57%) (Figure 28).

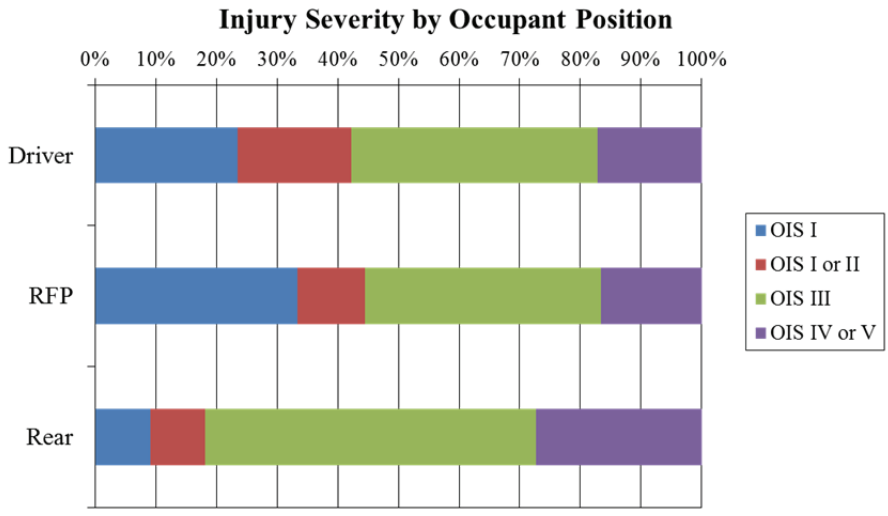

Figure 27: Injury severity distribution by occupant seating position for 93 jejunum-ileum injuries.

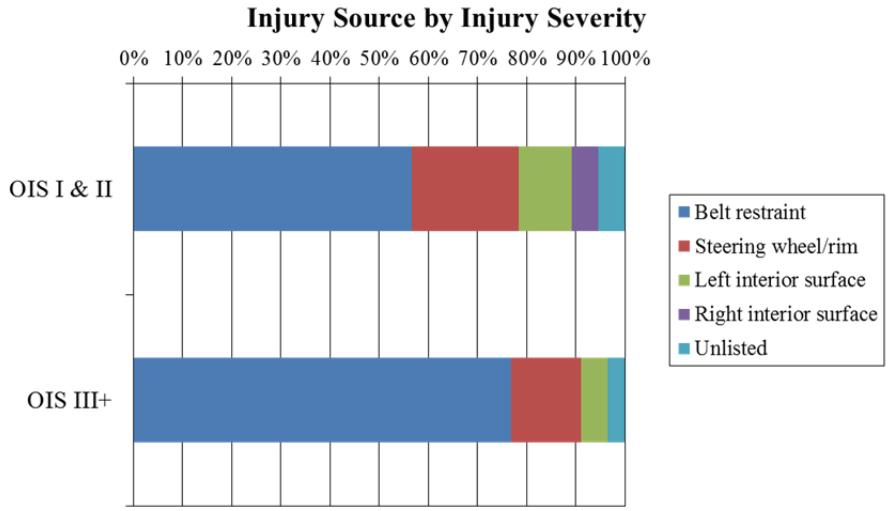

Figure 28: Injury source distribution by injury severity for 93 jejunum-ileum injuries.

Of the 85 occupants 12 years old or older with jejunum-ileum injuries, approximately 64% of occupants had abdominal injuries to the hollow organs only (Figure 29), and approximately half of those occupants only had jejunum-ileum injuries (Figure 30).

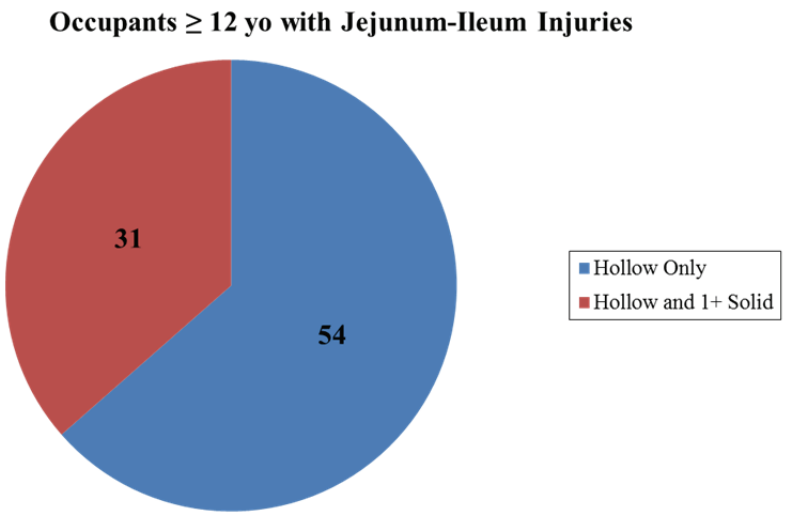

Figure 29: Distribution of hollow only injuries for occupants ≥ 12 yo with jejunum-ileum injuries.

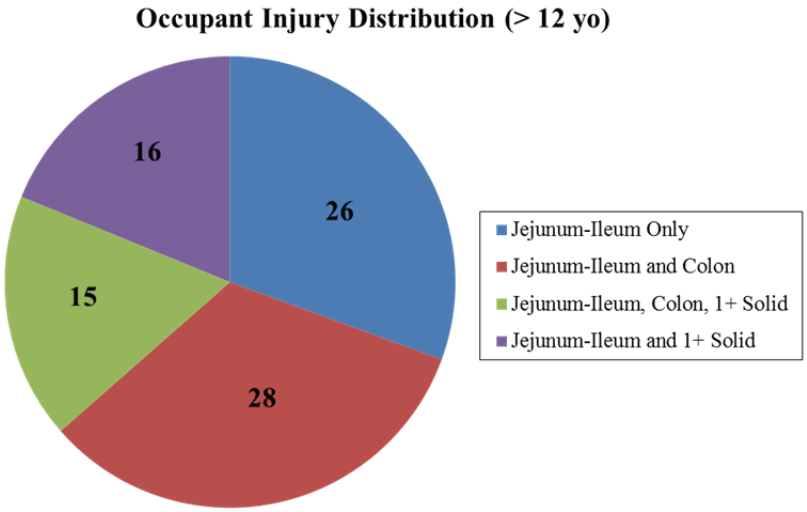

Figure 30: Distribution of abdominal injury type for occupants ≥ 12 yo with jejunum-ileum injuries.

Fifty-eight adult case occupants sustained jejunum-ileum injuries in frontal crashes (≥ 12 yo; PDOF ± 20°), and 48 of these occupants also sustained abdominal skin contusions or abrasions. Eight of these occupants were not restrained. Considering occupants 12 years old or older in frontal crashes with jejunum-ileum injuries (58 occupants), 24 occupants, or roughly 40%, sustained one or more rib fractures and 18 occupants, or roughly 30%, sustained two or more rib fractures. There was no clear association between jejunum-ileum injuries and the presence of rib fractures with increasing crash severity (Figure 31). The median speed for occupants with jejunum-ileum injuries and 1+ rib fractures was 52 kmph, using BES and excluding cases with unlisted BES. For occupants with jejunum-ileum injuries and no rib fractures, the median speed was 57 kmph.

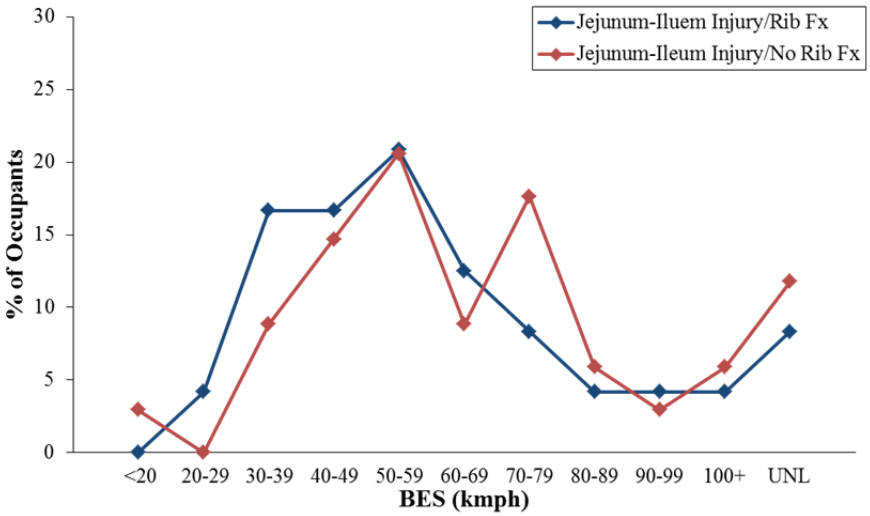

Figure 31: Percent of occupants with jejunum-ileum injuries with and without rib fractures at each speed.

Summary of Findings. Lap-shoulder belt interaction was found to be a common factor in hollow organ injury, which was typically associated with higher crash severity. Seventy-two percent of occupants with abdominal injuries to the hollow organs only (AIS3+) were in crashes above 50 kmph when delta-V was known. The hollow organs were more likely to be injured in a rear seat occupant than in a front seat occupant, with a greater percentage of rear seat occupants experiencing this type of injury than in any other category, although there are fewer rear seat occupants in general. Hollow organ injuries also occurred in a greater percentage of right front passengers compared to drivers. Jejunum-ileum injuries sustained by rear seat occupants were more often higher severity injuries than jejunum-ileum injuries sustained by front seat occupants. All occupants in frontal crashes with serious injuries to the hollow organs only were belted. The majority of the occupants with jejunum-ileum injuries exhibited abdominal contusions attributed to the lap belt, potentially implying improper belt use or submarining. No clear association was found between hollow organ injury and age or anthropometry, however there was some suggestion that shorter or more slender females might be at increased risk. Male occupants accounted for a greater percentage of OIS III+ jejunum-ileum injuries but were involved in more severe crashes overall based on the median crash speed for male occupants that sustained jejunum-ileum injuries. There was no clear association between occupants with jejunum-ileum injuries and the presence of rib fractures.

Case Analysis

The distributions of the height and weight of the case occupants selected for analysis with respect to the 58 case occupants with jejunum-ileum injuries (≥ 12 yo; PDOF ± 20°) are shown for females and males in Figure 32 and Figure 33, respectively. The median national estimates for height and weight (McDowell et al., 2008) are also shown.

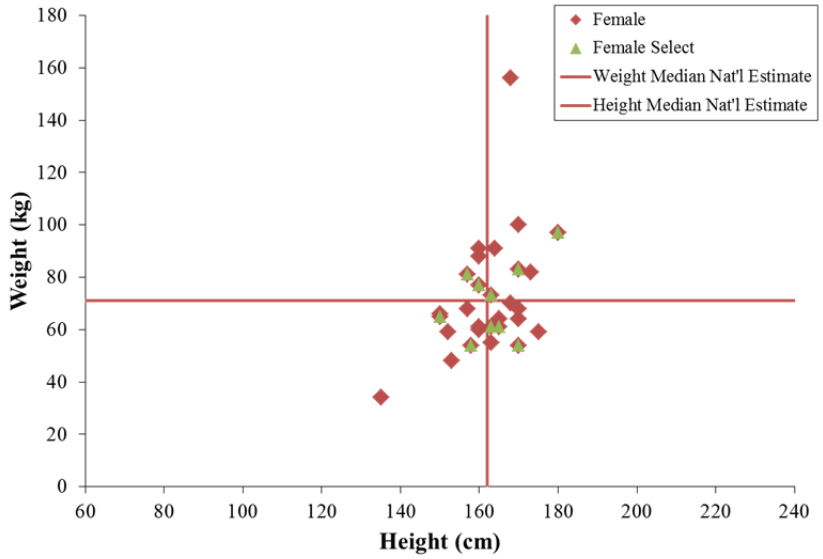

Figure 32: Weight and height of female occupants with jejunum-ileum injuries selected for analysis.

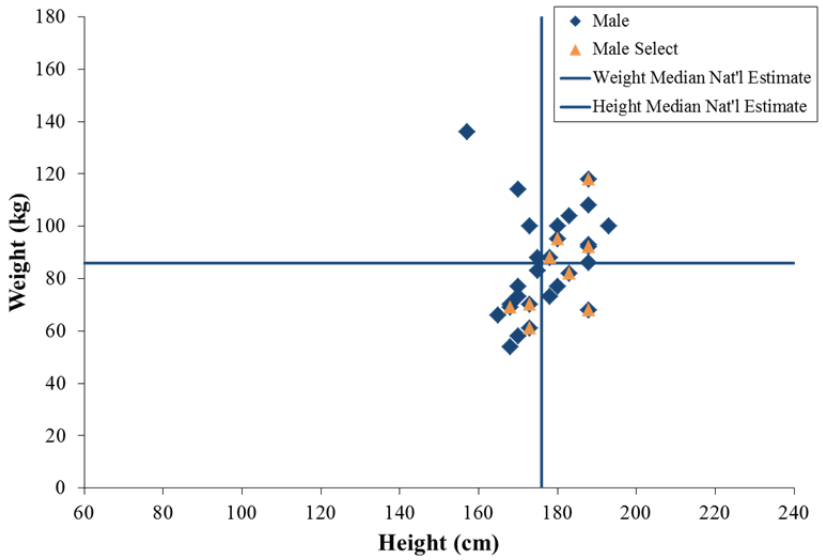

Figure 33: Weight and height of male occupants with jejunum-ileum injuries selected for analysis.

Case Summaries. Nineteen cases were analyzed in detail, and the relevant occupant, crash, and injury characteristics of each case are summarized in this section. Summaries for cases 1-10 describe female

occupants, and summaries for cases 11-19 describe male occupants. Cases are ordered arbitrarily within the gender groups. All occupants were using the lap-shoulder belt at the time of the collision, and in all cases with the exception of case 6, the frontal airbags deployed. Abdominal skin contusions were identified in 14 of the 19 cases. In the majority of the cases (17 out of 19), the jejunum or ileum injuries were attributed to abdominal contact with the seatbelt. Specific injury location is included for each of the cases when known. Injury location along the length of the jejunum is provided in reference to the ligament of Treitz, the suspensory ligament that connects the duodenum to the diaphragm at the junction of the distal duodenum and proximal jejunum.

Case 1: This case occupant was a female right front passenger with a normal BMI of 23.0 (height of 163 cm and weight of 61 kg) involved in a severe frontal impact into the right side of another vehicle. The case vehicle was a 2005 Buick LeSabre 4-door sedan, and the struck vehicle was a 2006 Ford Mustang coupe. The PDOF was 350°. The delta-V estimated for the impact was 36 kmph and was considered low compared to the distributed front end damage sustained by the case vehicle. The case occupant sustained abdominal injuries to only the hollow abdominal organs including hematomas of the cecum and sigmoid colon mesentery and a 3-mm full-thickness perforation of the jejunum 25 mm from the ligament of Treitz (AIS=3) with associated mesenteric hematoma. All injuries were attributed to lap-belt loading of the abdomen with a confidence level of certain. Abdominal skin contusions that were also evidenced with CT were high on the abdomen, above the iliac crests. The postulated mechanism for the jejunum perforation was compression and rate of compression.

Case 2: This case occupant was a female driver involved in a severe offset frontal impact with another vehicle that crossed the median of the roadway. The case vehicle was a 2003 Ford Explorer Sport Trac 4-door pickup truck that was impacted by a 2002 Ford Explorer 4-door sport utility vehicle. The PDOF was 0°, and the vehicle damage was distributed across the center and left of the front end of the case vehicle. The delta-V for the collision was 66 kmph. The case occupant had a height and weight of 170 cm and 83 kg and an overweight BMI equal to 28.7. The occupant sustained both solid and hollow abdominal organ injuries including a bladder rupture, minor lacerations of the liver and the spleen,

contusions of the transverse colon, and thickening of the wall of the proximal jejunum in two locations (AIS=2). The jejunum contusions were not high-ranking injuries for this occupant. The case review indicated that the injuries to the jejunum were probably due to loading from the seatbelt, however considerable contact with other interior vehicle components occurred with intrusion of the instrument panel (47 cm) and steering assembly (5 cm). The case occupant loaded the seatbelt, steering wheel airbag, instrument panel, knee bolster, toe pan, and brake pedal, sustaining severe head, thorax, pelvis, and lower extremity injuries.

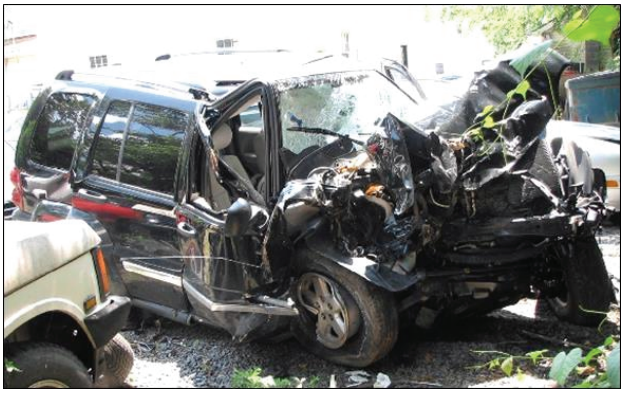

Case 3: This occupant was a female driver involved in a severe frontal impact into a tree > 10 cm in diameter. The case vehicle was a 2005 Jeep Liberty sport utility vehicle. The delta-V for the collision was 64 kmph. The PDOF was 10° with damage distributed across the center and right side of the front end of the vehicle. The case occupant had a height of 180 cm, weight of 97 kg, and BMI of 29.9, which was classified as overweight. The occupant sustained abdominal injuries to only the hollow organs, and all of the abdominal injuries were attributed to the seatbelt with a confidence level of certain. The injuries included a minor mesentery laceration and a laceration of the terminal ileum (AIS=2). The occupant sustained skin contusions across the lower abdomen that were attributed to the seatbelt. The occupant also sustained chest injuries attributed to the seatbelt and upper and lower extremity injuries that were attributed to contact with the instrument panel, knee bolster, and toe pan.

Case 4: This case occupant was a female driver with a height of 150 cm, weight of 65 kg, and an overweight BMI equal to 28.9. She was involved in a severe frontal impact with a large tree 90 cm in diameter that resulted in distributed front end damage to the case vehicle, a 2009 Hyundai Sonata 4-door sedan. The delta-V for the collision was 79 kmph. Abdominal injuries sustained by this occupant were solid and hollow organ injuries including spleen laceration and devascularization injuries (AIS=4), ascending and sigmoid colon lacerations, a mesentery contusion in the central abdominal region, and two jejunum perforations (AIS=2). The jejunum injuries included a devascularized segment of the proximal jejunum and a mid-jejunal perforation. Based on seatbelt webbing abrasions, the case occupant was considered to have heavily loaded the seatbelt with her upper torso and abdomen. The occupant also

loaded the airbag, knee bolster, brake pedal, and toe pan. The jejunum injuries were attributed to the seatbelt with a confidence level of probable. This occupant did not sustain abdominal skin contusions or rib fractures.

Case 5: This case occupant was a female right front passenger involved in a fatal frontal impact with a utility pole at 46 kmph. The case vehicle was a 1995 Oldsmobile 88 Royale 4-door sedan. The PDOF was 0° with vehicle damage to the right side of the front end. This was an older occupant of 75 years, with a height of 163 cm, weight of 73 kg, and BMI equal to 27.5, which was classified as overweight. The occupant sustained 10+ abdominal injuries to both the solid and hollow abdominal organs. All abdominal injuries were attributed to the seatbelt with a confidence level of certain. The occupant sustained an ileum contusion, mid-to-distal in location (AIS=2). She also sustained abdominal skin contusions attributed to the seatbelt. The case review suggested that the occupant may have been out-of-position with respect to the seatbelt at the time of the impact due to swerving of the vehicle prior to the collision with the utility pole. The occupant loaded the seatbelt, passenger airbag, instrument panel, and floor pan. The causes of death included a comorbidity of atherosclerotic heart disease, rib cage flail chest (10 rib fractures), and a diaphragm laceration.

Case 6: This occupant was a female right front passenger involved in a low-speed (delta-V of 13 kmph) frontal impact with another vehicle in an intersection. The case vehicle was a 1995 Toyota pickup that collided with a 1995 Ford Taurus station wagon. The case occupant had a normal BMI of 18.7, with a height of 170 cm and weight of 54 kg. The seat back of the case vehicle was not adjustable. The only injury that was sustained in the collision was a jejunum perforation 152 mm distal to the ligament of Treitz (AIS=3). This injury was attributed to abdominal contact with the seatbelt with a confidence level of certain. The occupant did not sustain abdominal skin contusions.

Case 7: This case occupant was a 73 year old female driver involved in a fatal frontal impact with another vehicle. The case vehicle was a 2002 Toyota Highlander 4-door sport utility vehicle, and the struck vehicle was a 2001 Mitsubishi Montero XLS 4-door sport utility vehicle. The delta-V for this impact was 71 kmph, with a PDOF of 10° and distributed damage to the front end of the case vehicle. The case occupant had an obese BMI equal to 30.1, a height of 160 cm, and weight of 77 kg. The abdominal injuries sustained by the case occupant were hollow organ injuries including a mesentery laceration, abdominal contusions, and a full-thickness jejunum laceration extending to the root of the mesentery (AIS=4). All abdominal injuries were attributed to abdominal contact with the seatbelt with a confidence level of certain. The occupant sustained skin contusions of the chest and lower abdomen that were attributed to the seatbelt. The case reviewers attributed the abdominal injuries to the high seatbelt forces expected of a high delta-V collision and not to improper seatbelt use. The occupant also loaded the knee bolster, pedals, and deployed frontal airbag. She sustained serious thoracic injuries including bilateral rib fractures with pneumothorax, transverse process fractures of the cervical and thoracic spine, and lower extremity injuries. Contributing factors to injury were the speed of the crash and the age of the occupant.

Case 8: This occupant was a female driver with a normal BMI of 22.4. Her height and weight were 165 cm and 61 kg, respectively. This case occupant was involved in a high-speed (delta-V of 81 kmph) frontal impact into a tree > 10 cm in diameter. The case vehicle was a 2006 Chevrolet Monte Carlo SS coupe. The damage to the vehicle was distributed over the center and right side of the front end. The occupant sustained abdominal injuries to the hollow organs only including a cecum laceration, multiple contusions of the sigmoid colon, and a distal ileum perforation (AIS=3). These injuries were attributed to abdomen contact with the seatbelt with a confidence level of certain. Abdominal skin contusions were present on the lower abdomen of the occupant. The mechanism for the ileum injury was coded as compression, with the high delta-V of the collision listed as a contributing factor for injury. Considerable occupant contact with interior vehicle components including the steering wheel rim, instrument panel, knee bolster, and pedals resulted in additional injuries to the spine and the extremities. This case occupant did not sustain any rib fractures in the collision.

Case 9: This case occupant was a female driver involved in a frontal collision with another vehicle. The case vehicle was a 2001 Chevrolet Monte Carlo 4-door sedan that was impacted by a 1991 Buick Regal 4-door sedan. The delta-V for the impact was 46 kmph, the PDOF was 340°, and the vehicle damage was distributed across the front end. The case occupant had a height of 158 cm, weight of 54 kg, and a normal BMI equal to 21.6. The abdominal injuries sustained in the collision were to the hollow organs and included a contusion of the mesentery of the right colon and a proximal jejunum perforation (AIS=3). The abdominal skin contusions were over the umbilicus of the occupant, high on the abdomen. The abdominal injuries were attributed to contact with the seatbelt with a confidence level of certain. The mechanism for the jejunum injury was coded as compression with a contributing factor of improper restraint use. The occupant also sustained 9 rib fractures on the right side of the thorax and 7 pelvis and lower extremity injuries. The other interior vehicle contacts included the knee bolster, toe pan, and pedals.

Case 10: This case occupant was a female driver with a height of 157 cm, weight of 81 kg, and an obese BMI of 32.9. She was involved in a severe frontal impact with another vehicle. The case vehicle was a 2005 Toyota Rav4 4-door 4x4 sport utility vehicle. The struck vehicle was a 1999 Plymouth Grand Voyager SE minivan. The delta-V was 65 kmph, the PDOF was 350°, and the damage to the case vehicle was distributed across the front end. The abdominal injuries sustained in the collision were to the hollow organs and included a serosal tear of the right anterior colon and a perforation of the mid-jejunum 1 cm in length (AIS=2) with associated mesenteric hematoma. The injuries were attributed to the seatbelt with a confidence level of certain. The occupant sustained multiple skin contusions high on the abdomen above the umbilicus and shear injuries to the subcutaneous tissue directly beneath the contusions. Other injuries were attributed to occupant contact with interior vehicle components including the steering wheel, deployed frontal airbag, knee bolster, pedals, and toe pan. The occupant did not sustain rib fractures in the collision.

Case 11: This case occupant was a male driver involved in a severe frontal impact with a tree > 10 cm in diameter. The case vehicle was a 2008 Acura TL. The delta-V for the collision was 71 kmph. The impact resulted in distributed damage to the front end of the case vehicle. The case occupant had a height of 178 cm, weight of 88 kg, and his BMI of 27.8 was classified as overweight. The case occupant sustained both solid and hollow abdominal organ injuries including a complete transection of the sigmoid colon (AIS=4), subcapsular hematomas surrounding the liver and spleen, mesentery contusions, and multiple areas of serosal tears of the jejunum and ileum (AIS=2). All abdominal injuries were attributed to the seatbelt with a confidence level of probable. The occupant sustained abdominal skin contusions low on the abdomen at the level of the iliac crests. The mechanism for the severe colon injury was coded as shear and attributed to the seatbelt. The occupant also loaded the instrument panel, knee bolster, and toe pan and sustained a sternum fracture, rib fracture, and upper and lower extremity injuries.

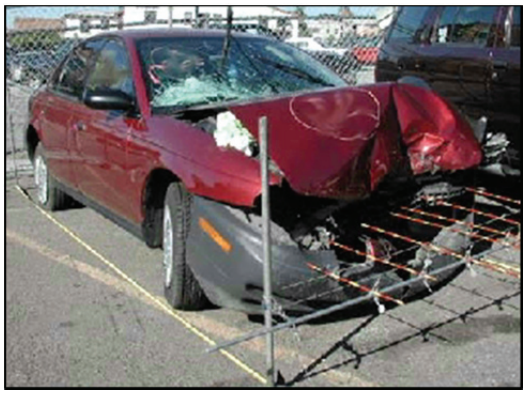

Case 12: This case occupant was a male right front passenger with a normal BMI of 24.5. His height and weight were 183 cm and 82 kg, respectively. The crash involved a full-frontal collision into a large boulder with a delta-V of 51 kmph. The case vehicle was a 1999 Saturn SL sedan with distributed front end damage resulting from the collision. The case occupant was asleep prior to the vehicle exiting the roadway. The abdominal injuries sustained in the collision were to both the solid and hollow abdominal organs and included an avulsion of the tip of the spleen, a sigmoid colon contusion, a laceration with deserosalization extending from the cecum to the ascending colon, and perforations of the jejunum 200 and 215 cm from the ligament of Treitz (AIS=3). All abdominal injuries were attributed to the seatbelt, and the jejunum injuries were attributed to the seatbelt with a confidence level of certain. The occupant sustained skin contusions to the left and right sides of the lower abdomen also attributed to the seatbelt. The occupant was positioned with the seat adjusted to the rear-most track position and the seat back reclined. The case review therefore suggested that the occupant loaded heavily into the seatbelt system, not making contact with the deployed frontal airbag due to the distance of the occupant from the instrument panel at the time of the collision. The lower extremities of the occupant loaded the lower right instrument panel. The occupant did not sustain any rib fractures.

Case 13: This occupant was involved in a severe frontal impact with another vehicle at a delta-V of 78 kmph. The case vehicle was a 2006 Toyota Scion TC hatchback, and the struck vehicle was a 2000 Dodge Grand Caravan. The PDOF of the impact was 10° and the resulting damage was distributed across the front end of the case vehicle. The case occupant had a height of 180 cm, weight of 95 kg, and BMI equal to 29.3, which was classified as overweight. The occupant sustained abdominal injuries to the hollow organs that included a complete transection of the colon at the recto-sigmoid junction (AIS=4), mesentery hematoma, a rectus abdominus rupture, and transections of the middle and distal jejunum (AIS=4). The abdominal injuries were attributed to abdomen contact with the seatbelt or steering wheel. The involved physical components for the jejunum injuries were coded as the seatbelt with a confidence level of probable and the steering wheel rim with a confidence level of possible. The case occupant also sustained bilateral abdominal skin contusions and shearing injuries in the lower left quadrant of the abdomen. These injuries were attributed to the seatbelt with a confidence level of certain. The mechanism for the jejunum injuries was coded as compression with contributing factors to injury including the high delta-V of the impact, as well as seatbelt interaction. The only other injury to the occupant was an upper extremity injury.

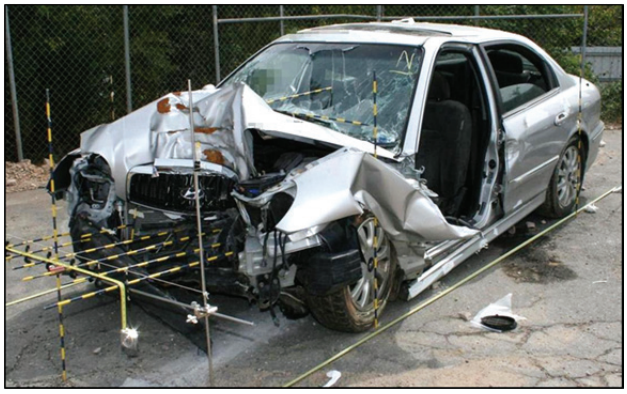

Case 14: This case occupant was a male seated in the left rear seat of a 2005 Hyundai Sonata involved in a severe frontal impact into a tree > 10 cm in diameter. The delta-V for the impact was 76 kmph, the PDOF was 0°, and the vehicle damage was distributed across the center and left side of the front end. The case occupant had a height of 173 cm, weight of 61 kg, and a normal BMI equal to 20.4. Abdominal injuries sustained in the collision were to the hollow organs and included Grade I duodenum and cecum deserosalization injuries and a Grade I deserosalization injury of the proximal jejunum 4 cm in length (AIS=2). All abdominal injuries were attributed to the seatbelt with a confidence level of certain. The occupant sustained multiple abdominal skin contusions above the level of the umbilicus that were attributed to the seatbelt. Rear seat back intrusion due to loading from unsecured trunk cargo may have compounded the loading of this occupant into the seatbelt and the driver seat back. The occupant sustained face, spine, and extremity injuries but did not sustain rib fractures in the collision.

Case 15: This case occupant was a male driver with a normal BMI of 24.4, height of 168 cm, and weight of 69 kg. The case vehicle was a 1999 Chevrolet S-10 pickup truck involved in a severe full-frontal collision into the right side of another vehicle. The delta-V for this collision was unavailable, and the BES was determined to be 77 kmph, which was considered to be reasonable but somewhat high for the impact. The PDOF was 350° with distributed front end vehicle damage. The abdominal injuries sustained in this collision were to the hollow organs and included serosal tears of the colon in two locations and jejunum tears in two locations (AIS=3). The occupant did not sustain abdominal contusions. Longitudinal intrusion equal to 17 cm affected the front plane of the case vehicle including the steering assembly, instrument panel, and toe pan. The abdominal injuries were attributed to the steering wheel rim with a confidence level of probable. The occupant sustained two right rib fractures that were attributed to the seatbelt or steering wheel rim contact and lower extremity fractures attributed to contact with the center instrument panel and toe pan.

Case 16: This case occupant was a male driver involved in a full-frontal impact with another vehicle with a delta-V of 59 kmph. The case vehicle was a 2007 Chevrolet Impala 4-door sedan that impacted a 2007 Toyota Yaris hatchback. The PDOF was 350° with distributed front end damage of the case vehicle. The occupant had a height of 188 cm, weight of 92 kg, and BMI of 26.0, which was classified as overweight. The abdominal injuries sustained by the occupant were to the hollow organs and included a left colon serosal tear, mesentery laceration, and mid-jejunum perforation (AIS=4) with associated mesenteric bleeding. The abdominal injuries were attributed to abdomen contact with the seatbelt with a confidence level of certain. The occupant sustained bilateral skin contusions high on the abdomen at the level of the umbilicus and above the ASIS. The occupant also sustained a chest skin contusion that was attributed to the seatbelt but did not sustain any rib fractures.

Case 17: This occupant was a male driver involved in a severe full-frontal impact with a tree that was 30 cm in diameter. The impact resulted in distributed front end vehicle damage. The case vehicle was a 1998 Nissan Sentra 4-door sedan. The delta-V for the impact was 54 kmph. The case occupant had a height of 173 cm, weight of 70 kg, and a normal BMI equal to 23.4. The case occupant fell asleep while driving and the vehicle exited the roadway. The abdominal injuries sustained in the collision were to the hollow organs and include a colon laceration (AIS=4), mesentery laceration, sigmoid colon and cecum contusions, and two devascularization injuries of the small bowel (AIS=4) – a 10-cm devascularization of the distal jejunum, and an 8-cm devascularization of the proximal ileum. All abdominal injuries were attributed to the seatbelt with confidence levels of certain and probable. The occupant additionally sustained bilateral skin contusions of the lower abdomen that were attributed to the seatbelt. The occupant sustained a chest contusion and a left clavicle fracture attributed to contact with the seatbelt, and the occupant contacted the toe pan and sustained multiple fractures of the foot.

Case 18: This case occupant was a male driver involved in a fatal full-frontal impact with vehicle size mismatch. The case vehicle was a 2005 Hyundai Accent hatchback that impacted a 2003 Ford Econoline van with a delta-V of 96 kmph. The collision resulted in distributed damage extending vertically over the entire front end of the case vehicle. The case occupant had a height of 188 cm, weight of 118 kg, and an obese BMI equal to 33.4. The abdominal injuries sustained in the collision were to the hollow organs and included a laceration of the sigmoid colon mesentery, a sigmoid colon laceration 4 cm in length, and a terminal ileum perforation (AIS=4) with associated mesenteric disruption. Intrusion of the vehicle steering assembly of 10 cm contributed to considerable occupant contact with the interior vehicle components including the seatbelt, steering column, knee bolster, and windshield. The ileum injury was associated with loading of the steering wheel with a confidence level of certain. The mechanism for injury was compression and rate of compression with contributing factors of high delta-V and vehicle intrusion. The causes of death for this occupant included a myocardium contusion and diaphragm rupture with herniation. No rib fractures were reported.

Case 19: This case occupant was a male driver with a normal BMI of 19.2, height of 188 cm, and weight of 68 kg. He was involved in a frontal impact with a PDOF of 340° into a stationary vehicle. The case vehicle was a 1999 Honda Accord EX 4-door sedan that impacted a 1990 Toyota Corolla DX sedan, resulting in distributed front end damage to the case vehicle. The delta-V for the collision was 49 kmph. The occupant sustained abdominal injuries to the hollow organs including a sigmoid colon laceration, lacerations to the small bowel mesentery and right colon mesentery, and perforations to the distal jejunum and proximal ileum (AIS=3). All abdominal injuries were attributed to the seatbelt, and the confidence level for the jejunum and ileum injuries was certain. Due to the impact, there was left instrument panel intrusion equal to 4 cm and considerable occupant contact with interior vehicle components. The occupant sustained no abdominal skin contusions in the collision.

Case Comparisons. The 19 cases with jejunum-ileum injury selected for analysis were further investigated by categorizing the seatbelt routing of the occupants as evidenced by abdominal skin contusions resulting from the collisions (Table 9). All occupants identified with lap-belt contusions high on the abdomen (5 occupants) sustained a jejunum injury at the location of the proximal or middle jejunum (Table 10). The majority of the case occupants with injuries to the distal jejunum or ileum also had lower abdominal contusions. Vehicle intrusion was a factor for three of the four injuries attributed to abdomen contact with the steering wheel. Two of these occupants had unspecified abdominal contusions, and two of these occupants did not have abdominal skin contusions. Out of the 19 cases that were analyzed, seven of the collisions were tree or pole impacts. Four of these occupants had lower abdominal contusions, and five occupants had distal injuries. Two occupants had proximal or mid- jejunum injuries.

The majority of the cases analyzed in detail (12/19 cases) had a delta-V greater than 56 kmph. Occupants with overweight or obese BMI and jejunum-ileum injuries were almost exclusively involved in crashes with speeds greater than 56 kmph (9/10 occupants), with a median speed of 69 kmph. Occupants with normal BMI classifications experienced a range of crash severities with a median speed of 51 kmph.

No clear association was found with rib fractures. The majority of the occupants analyzed had one or no rib fractures (13/19 occupants). Four case occupants had a high number of rib fractures (9+ fractures). These occupants were female, and two of the occupants were greater than 70 years old, both with fatal outcomes from the collisions.

Table 9: Abdominal skin contusions from select cases.

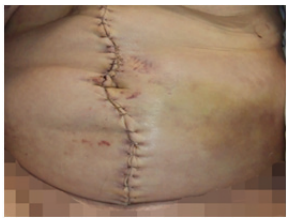		
Case 7	Case 10	Case 11
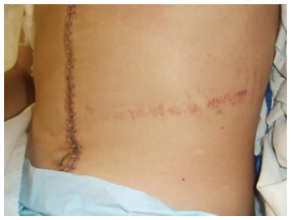	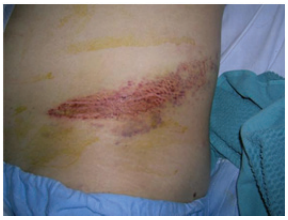	
Case 14	Case 16	Case 17

Table 10: Injury location and abdominal contusion assessment for each case.

Case	M/F	Stature	BMI	Pos.	ΔV	Jejunum-Ileum Injuries	AIS	IPC	Contusions
01	F	163	23.0	RFP	36	Jejunum perforation – proximal	3	Belt	Belt mark high
09	F	158	21.6	D	46	Jejunum perforation – proximal	3	Belt	Belt mark high
14	M	173	20.4	RSP	76	Jejunum serosal tear – proximal	2	Belt	Belt mark high
10	F	157	32.9	D	65	Jejunum perforation – middle	2	Belt	Belt mark high
16	M	188	26.0	D	59	Jejunum perforation – middle	4	Belt	Belt mark high
06	F	170	18.7	RFP	13	Jejunum perforation – proximal	3	Belt	No skin contusion
04	F	150	28.9	D	79	Jejunum devasc. – proximal Jejunum perforation – middle	2	Belt	No skin contusion
15	M	168	24.4	D	77	Jejunum tears NFS	3	SW	No skin contusion; Intrusion
19	M	188	19.2	D	49	Jejunum perforation – distal Ileum perforation – proximal	3	Belt	No skin contusion; Intrusion
18	M	188	33.4	D	96	Ileum perforation – terminal	4	SW	No skin contusion; Intrusion
02	F	170	28.7	D	66	Jejunum wall contusions – proximal	2	Belt/SW	Contusions NFS; Intrusion
13	M	180	29.3	D	78	Jejunum transections – mid-to-distal	4	Belt/SW	Contusions NFS
05	F	163	27.5	RFP	46	Ileum contusion – mid-to-distal	2	Belt	Contusions NFS
12	M	183	24.5	RFP	51	Jejunum perforation – middle	3	Belt	Low contusions
07	F	160	30.1	D	71	Jejunum laceration (massive)	4	Belt	Low contusions
11	M	178	27.8	D	71	Jejunum-ileum serosal tears	2	Belt	Low contusions
17	M	173	23.4	D	54	Jejunum devasc. – distal Ileum devasc. – proximal	4	Belt	Low contusions
08	F	165	22.4	D	81	Ileum perforation – distal	3	Belt	Low contusions
03	F	180	29.9	D	64	Ileum laceration – terminal	2	Belt	Low contusions

Stature units are cm; delta-V units are kmph; NFS is not further specified.

DISCUSSION

The CIREN case analysis conducted in this study supplemented the NASS/CDS dataset and previous literature data with detailed injury information and the association of occupant and crash characteristics with specific abdominal injuries. No clear trends with age or anthropometry were identified with the CIREN analysis. However, without controlling for crash severity, gender differences in injury patterns were found. Males comprised a greater percentage of occupants with abdominal injuries to the hollow organs only compared to the other categories, and males accounted for a greater percentage of occupants with higher severity jejunum-ileum injuries compared to females. Males, however, were typically involved in higher severity crashes. The median speed for adult male occupants with jejunum-ileum injuries was 60 kmph, whereas the median speed for females with jejunum-ileum injuries was 49 kmph. In general, a greater percentage of occupants with abdominal injuries to the hollow organs only were in higher severity collisions compared to the other categories in the CIREN database. The results of the NASS/CDS analysis also identified the median speed for AIS2+ abdominal injuries (39 kmph) as greater than the median speed for all occupants (17 kmph) (Gabler, 2013). Compared to the NASS/CDS results, higher median speeds were observed in the categories analyzed from the CIREN database, highlighting the distribution of the database toward more severe collisions overall.

A greater percentage of occupants with abdominal injuries to the hollow organs only were rear seat passengers compared to any other occupant category, and rear seat occupants with abdominal injuries were more likely to sustain a hollow injury than right front passengers or drivers. Additionally, a greater percentage of occupants in the rear seating positions sustained higher severity jejunum-ileum injuries (OIS III+) compared to front seat occupants. The studies by Lamielle et al. (2006) and Frampton et al. (2012) identified belted rear seat occupants as having a higher likelihood of sustaining abdominal injuries compared to belted front seat occupants. Frampton et al. (2012) also found an increased incidence of hollow organ injuries for rear seat occupants. Other studies did not assess both front and rear seat occupants. Although there are fewer rear seat occupants in general, further investigation of hollow organ injury occurrence in rear seat passengers is necessary to improve occupant protection in the rear seat.

The results of this study support a difference in primary injury mechanism for hollow and solid organ injuries. Compared to the incidence of seatbelt use in the CIREN database (68%), solid organ injury was associated with a reduced incidence of seatbelt use (52%), whereas hollow organ injury was associated with an increased incidence of seatbelt use (100%). All occupants with hollow only injuries were restrained, and a greater percentage of hollow only injuries in this study were attributed to abdominal contact with the seatbelt compared to solid only injuries. This was consistent with previous studies that identified a higher occurrence of hollow abdominal organ injury in belted compared to unbelted

occupants (Lamielle et al., 2006; Klinich et al., 2010). However, restraint loading remains an important component to solid organ injury mechanisms as well. Finally, a greater percentage of occupants than expected sustained injuries only to the hollow organs or to the jejunum-ileum without obtaining injuries to the solid organs. This result further supports a different mechanism of injury for the jejunum-ileum compared to the solid abdominal organs.

Skin contusion was a common concomitant injury for occupants with jejunum-ileum injuries, and these injuries were most often attributed to abdominal contact with the restraint system. Injury source was investigated in this analysis to identify whether abdomen contact with the seatbelt was predominantly coded as the jejunum-ileum injury source when skin contusion was present. The injury source for occupants with skin contusion was more commonly attributed to the belt than for occupants without skin contusion; however, drivers comprised a greater percentage of occupants without skin contusion, increasing the likelihood for steering wheel interaction in this category.

Injury locations along the length of the small intestine appeared to be associated with the locations of abdominal contusions that were attributed to the seatbelt. All occupants identified with seatbelt contusions high on the abdomen sustained a jejunum injury at the location of the proximal or middle jejunum. The majority of these injuries were perforations. It was likely that these occupants were either improperly belted at the time of the crash, indicating a direct loading mechanism that resulted in tear-type injuries, or that submarining occurred and the lap portion of the seatbelt ended up loading the abdomen. A plausible mechanism is local, direct compression by the seatbelt combined with areas of tension resulting from portions of the bowel being displaced by the belt, producing tearing injuries. A number of the case occupants with injuries to the distal jejunum or ileum also sustained lower abdominal contusions inferior to the umbilicus that were attributed to the seatbelt, potentially indicating a similar local mechanism for these injuries.

A number of case occupants sustained skin contusions at the level of the iliac crests, indicating that the belt may have properly engaged the pelvis throughout the crash event, or that the lap portion of the seatbelt was positioned over the pelvis at the onset of loading. Jejunum-ileum injuries sustained by these case occupants included mid-jejunum lacerations, jejunum and ileum devascularization injuries, and jejunum-ileum serosal tears. An example is case 17, where lower abdominal contusions implied proper seatbelt routing over the iliac crests at the onset of loading, yet the injuries sustained (devascularization injuries to the distal jejunum and proximal ileum without perforation) were consistent with an improperly belted occupant or occupant submarining. This could be an example of a distraction injury mechanism in which a properly routed seatbelt maintained the position of the occupant while the more mobile

abdominal contents such as the jejunum moved forward away from the spine, applying tension to the vasculature of the bowel at the tethered regions. Similarly, case occupant 11 had skin contusions below the abdomen that implied loading of the iliac crests by the lap portion of the belt, yet this case occupant sustained jejunum and ileum serosal tears. This was a high delta-V collision and the occupant had a BMI classified as overweight, supporting the plausibility of an inertia-based traction mechanism for the jejunum injuries sustained by this occupant.

Tension applied to the bowel and the connective tissues is a common factor for both proposed mechanisms: direct compression and displacement, and the distraction-based mechanism. Due to the convolutions along the length of the jejunum, axial tension or relative displacement between mobile and non-mobile portions of the structure may result in the straightening of the local curvature of the jejunum. This mechanism has been supported by preliminary investigations in which axial tension applied distal to the duodenum of *ex vivo* specimens resulted in damage to the jejunum. The role of the tethering mesentery and connective tissues in the loading applied to the bowel should be investigated further.

In addition to occupant contact with the seatbelt, the interaction of front seat occupants with the airbag may affect hollow organ injury patterns and mechanisms. In the current study, the frontal airbags deployed in all but one of the 19 cases considered for analysis. For occupants with intestinal injury and no skin contusions, the injury could potentially be attributed to a tension or distraction mechanism, or direct interaction of the abdomen with the airbag. Therefore, the timing of airbag deployment may have potentially important implications on the analysis of the injury mechanisms for front seat occupants. The timing of the airbag deployments was not considered in this analysis but could be identified for cases with available event data recorder information. This was not accounted for in the current study; therefore, these interactions should be addressed specifically in future analyses.

Overall, the characteristics associated with hollow organ injuries occurring in field accidents have a number of implications for future experimental testing conducted to examine clinically-relevant jejunum-ileum injuries and potential real-world mechanisms. The results of the CIREN analysis suggest that higher-energy seatbelt loading, possibly in conjunction with a more rotated pelvis characteristic of a rear seat occupant, or a submarining condition with the lap portion of the belt displacing into the abdomen should be considered for the study of jejunum injury in the cadaver model. Regional investigations of failure mechanisms such as the straightening of the local curvature of the jejunum would provide valuable insight into the way in which injuries occur and could be used to identify the loading thresholds for damaging the jejunum. Further, controlled experimental investigations are needed to determine the role of the spine, connective tissue tethering, and the contents of the bowel on the type and extent of the injuries

that are generated in these crash scenarios. Finite element model simulations could be used to examine the internal stress and strain responses to the loading conditions resulting in injury in real-world crashes, with implications for improving experimental design. However, limitations exist with current full-body finite element models, including an absence of local validation data, which is addressed further in subsequent chapters of this dissertation. The mechanisms expected to result in injury, such as high-energy restraint loading and the potential effects of seatbelt positioning and submarining, should be further investigated with whole-body testing to identify the injury thresholds for the hollow organs.

Injuries to the jejunum and ileum are difficult to detect clinically and can lead to patient morbidity with delays in diagnosis. Therefore, understanding the mechanisms of injury is not only important for injury mitigation in MVCs, but also for the implementation of strategies to improve patient triage based on crash and occupant characteristics such as abdominal contusions from seatbelt loading and the associated injury types and severities.

Limitations

Although the CIREN database combines the crash, occupant, and injury data required for this type of mechanistic injury analysis, the database includes only occupants with serious injuries, over-representing high severity collisions. This database is not a population-based sample, and therefore, no calculation or discussion of injury risk can be obtained from this analysis. Further, crash investigator and case assessor subjectivity may exist in the sources and mechanisms identified for each injury. A limited number of statistical comparisons were considered for this dataset as the purpose of this analysis was a mechanistic investigation of specific injuries. Additionally, the dataset used for detailed case analysis represents a small sample size, therefore limiting the statistical analyses possible for these comparisons. However, the trends identified with accident data analysis can be applied to the development of experimental protocols to investigate tissue tolerances and failure mechanisms based on the nature of injuries occurring in the field.

CONCLUSION

An analysis of the CIREN database was conducted to identify factors involved in hollow abdominal organ injuries sustained in MVCs, with a specific focus on jejunum and ileum injuries. The following characteristics were identified:

- Hollow organ injuries that were sustained by vehicle occupants in frontal crashes were associated with a high crash severity.
- The likelihood of sustaining hollow organ injury was greater for rear seat occupants compared to front seat occupants, and jejunum-ileum injuries sustained by rear seat occupants were often higher severity injuries than those sustained by front seat occupants.
- Lap-shoulder belt interaction was found to be a common factor in hollow organ injury. The majority of occupants with jejunum-ileum injuries also sustained abdominal contusions attributed to the seatbelt. Occupants with seatbelt contusions high on the abdomen typically sustained injuries to the proximal jejunum, whereas occupants with lower abdominal contusions sustained injuries to the distal jejunum and ileum.
- All occupants found in the CIREN database with abdominal injuries to only the hollow organs were restrained, whereas 52% of occupants with solid organ injury only were restrained. While interaction with the seatbelt remains a contributing factor in solid organ injury, this difference suggests that the mechanism of injury may be different for hollow and solid organ injuries.
- Local combined compression and tension is one possible mechanism for jejunum-ileum injuries associated with the seatbelt. For example, axial tension that results in the straightening of local curvature in combination with a lateral contact load applied due to lap-belt loading of the abdomen may generate local tearing injuries of the jejunum.

The interaction between the restraint system and the abdomen was characterized on a case-by-case basis to investigate potential local injury mechanisms. The correlations between seatbelt routing and injury type and location presented in this study have implications for future assessments of restraint system performance, including the effects of seatbelt fit. Classification of the environment in which these injuries occur in real-world crashes can be applied to the design of controlled experiments to further investigate hollow organ injury mechanisms and failure tolerances in crash-specific loading modes.

CHAPTER 3

Material Properties of the Post-Mortem Gastrointestinal Tract in High-Rate Equibiaxial Elongation

Dynamic equibiaxial tension tests were conducted on cruciate tissue samples obtained from the stomach, small intestine, and colon of four human cadavers to characterize the mechanical response and failure tolerance of these tissues. Samples were stretched to failure using a custom equibiaxial test device. Load, acceleration, sample thickness, and the displacement of optical markers on the sample surface were recorded throughout the duration of each test. The stress-strain response was quantified for 18 stomach samples, 20 small intestine samples, and 21 colon samples. Tests were conducted at an average maximum principal strain rate of 67.6 ± 20.5 s^{-1}. The average Green-Lagrange strain at failure ranged from 11% to 16% in the circumferential direction, and the average longitudinal strain at failure ranged from 12% to 14%. The average 2nd Piola Kirchhoff stress at failure ranged from 1.80 MPa for the stomach in the circumferential direction to 3.28 MPa for the small intestine in the longitudinal direction. Throughout the length of the digestive tract, the data indicated an increased resistance to stretch in the longitudinal direction with a greater average stress at failure and lower average strain at failure compared to the circumferential direction. Regional variations in material response were also quantified for the stomach and the colon. Data from this study characterize the biomechanical response of the human post-mortem gastrointestinal organs at strain rates expected to be experienced in motor vehicle collisions.

INTRODUCTION

The risk of serious injury in motor vehicle collisions (MVCs) is substantially reduced with the proper use of seatbelts (Klinich et al., 2010). However, clinical data and field accident analysis have indicated an increase in the occurrence of hollow visceral injury in belted occupants in MVCs (Anderson et al., 1991; Rutledge et al., 1991; Lamielle et al., 2006). Lamielle et al. (2006) reported that for belted occupants, abdominal organ injuries were more frequently hollow organ injuries (58%) compared to solid organ injuries (42%). Regional experimental studies have been conducted to investigate the overall response of the abdomen to seatbelt loading (Miller, 1989; Rouhana et al., 1989; Hardy et al., 2001a; Rouhana, 2002; Trosseille et al., 2002; Foster et al., 2006; Lamielle et al., 2008), and local failure response data have been quantified at the material and structural levels for the human liver and spleen (e.g. Sparks et al., 2007; Brunon et al., 2010; Kemper et al., 2010; Kemper et al., 2012). However, the tissue-level response to high-rate loading has not been investigated for the post-mortem hollow abdominal organs. Crash-induced injuries of the hollow organs include serosal tears, lacerations, perforations, and de-vascularization injuries (Appleby and Nagy, 1989; Munns et al., 1995; Carrillo et al., 1996; Shinkawa et al., 2004). These

failure modes may be associated with multiple types of loading; however, the purpose of this study was to characterize the biomechanical response of the hollow abdominal organs by quantifying the multidirectional stress and strain relationships of tissue samples tested to failure in equibiaxial tension.

Existing material properties data for the human post-mortem stomach, small intestine, and large intestine are limited to the uniaxial, quasi-static tensile response (Yamada, 1970; Egorov et al., 2002). Egorov et al. (2002) tested longitudinal and transverse tissue samples from each organ at a constant, quasi-static loading rate of 50 mm/min. The results indicated directional response variations for the small and large intestines, with a greater peak stress occurring in the longitudinal direction. No directional differences were reported for the stomach. Yamada (1970), citing Iwasaki (1953), reported directional and regional differences in stiffness for these tissues. A stiffer response was reported in the longitudinal direction for all regions of the small intestine, with the lowest ultimate strength and percent elongation occurring for the duodenum, followed by the jejunum and the ileum. Similarly, a stiffer response was reported for the large intestine in the longitudinal direction with a greater ultimate strength and lower ultimate elongation compared to the transverse direction. Regional differences were also identified for the large intestine including a lower ultimate elongation and a reduced tensile strength in the transverse direction for the descending colon compared to the other regions. For the human stomach, Yamada (1970), citing Nonogaki (1960) and Fukuyama (1961), reported a higher percent elongation in the transverse direction for all regions. The greatest ultimate strength and percent elongation were reported for the fundus, followed by the corpus and the antrum regions. All of these tests were conducted using quasi-static loading rates. Due to the viscoelastic nature of soft tissues, a different response is expected for tissue samples tested at the higher loading rates that would be experienced in MVCs. However, no data exist that characterize the dynamic response of the human gastrointestinal organs.

In this study, equibiaxial tension tests were conducted to address the limitations of uniaxial tension testing, despite the increased complexity of the multi-axial test configuration. In a uniaxial test, samples are typically elongated without constraint in the transverse direction. This affects the mechanical environment of the sample, resulting in a high strain, low stress material response. This would represent a considerable effect for the highly deformable membranous abdominal tissues such as the intestines. The mechanical environment of a planar biaxial test more accurately matches multi-axial loading and failure that may be occurring *in vivo*. Biaxial tests result in a high stress, low strain mechanical environment, yielding a stiffer response with less extensibility and higher ultimate stress than uniaxial testing (Lanir and Fung, 1974; Demer and Yin, 1983). Further, biaxial tests are necessary to determine the multidirectional stress and strain relationships that cannot be inferred from a single uniaxial test due to tissue anisotropy (Sacks, 2000). Therefore, dynamic equibiaxial tissue testing was conducted in this study

to define the high-rate, multidirectional material response and failure properties of the human post-mortem stomach, small intestine, and colon.

METHODOLOGY

Surrogate Characteristics

Equibiaxial tension tests were conducted on tissue samples obtained from the digestive tract of four fresh, never-frozen post-mortem human surrogates (PMHS). Donors were screened to avoid medical conditions that could potentially affect the material response of the abdominal soft tissues. All surrogates were male and had an average age of 76 years, average stature of 179 cm, and average mass of 93 kg (Table 11).

Table 11: PMHS characteristics.

Cadaver	Gender	Age	Stature (cm)	Mass (kg)
SM78	M	77	175	81
SM79	M	72	193	142
SM80	M	72	173	72
SM82	M	81	174	78
Average		76	179	93

Sample Preparation

The hollow abdominal organs that were tested in this study included the stomach, small intestine, and colon. Each organ has a thin (less than 5 mm), extensible wall structure comprised of four layers: an inner mucosa, submucosa, muscularis externa, and an outer serosa or adventitia (Ross and Pawlina, 2011). The stomach is divided into four anatomic regions: the cardia, the fundus, the corpus or body, and the pyloric antrum. The inner mucosal layer lining the stomach forms longitudinal folds, or rugae. Rugae are more prominent in the distal regions of the stomach and permit extension during filling. The small intestine is divided into three anatomic regions: the duodenum, the jejunum, and the ileum. The inner layers of the small intestine form transverse folds known as plicae circulares, and the lumen of the small intestine is lined with villi to increase surface area for absorption. The colon is divided into four anatomic regions: the ascending, transverse, descending, and sigmoid colon. Thin bands of muscle fibers known as teniae coli extend axially along the length of the colon. The segments of tissue forming the sections between the bands are known as haustra coli.

To harvest the tissues, the abdominal cavity of each PMHS was dissected and the digestive tract was excised intact. Each excised hollow organ was trimmed of all fat, mesentery, and peritoneal attachments without disrupting the outer layer of the tissue. The stomach was incised along the lesser curvature from the pyloric sphincter to the esophagus prior to obtaining tissue samples from the fundus, corpus, and antrum regions. Samples were obtained from the duodenum and jejunum-ileum of the small intestine and

the ascending, transverse, descending, and sigmoid colon of the large intestine. Samples were ordered from the proximal to the distal end of each organ.

The excised organs of each surrogate were divided into rectangular tissue sections devoid of visible inhomogeneities. The small intestine and colon tissue sections were opened along the mesenteric border aligned with the longitudinal axis of the organ. Each section was positioned on foam board backing with the serosa or adventitia exposed for stamping. A custom CNC-machined stamp was applied to the tissue using an arbor press. The stamp was designed to produce cruciate-shaped samples with four arm branches converging to form a 10-mm central square region of interest (ROI). Radiused edges between adjacent arm branches reduced stress concentrations at the edges of the ROI. The stamp was aligned with two co-linear arms oriented parallel to the visible longitudinal fiber direction of each tissue section or offset from the fiber direction by 22 degrees (Figure 34). The offset was selected to minimize error in material parameter determination when characterizing the response of the tissue (Lanir et al., 1996) and to prevent failure across the arm branches of the sample (Shah et al., 2006). Tests conducted in an offset configuration result in failure diagonally through the ROI of the sample, which yields additional useable response data for each test. Therefore, the majority of the samples were tested in the offset configuration, and a limited number of samples were tested in the aligned configuration for comparison. All samples were obtained with the layered wall structure intact.

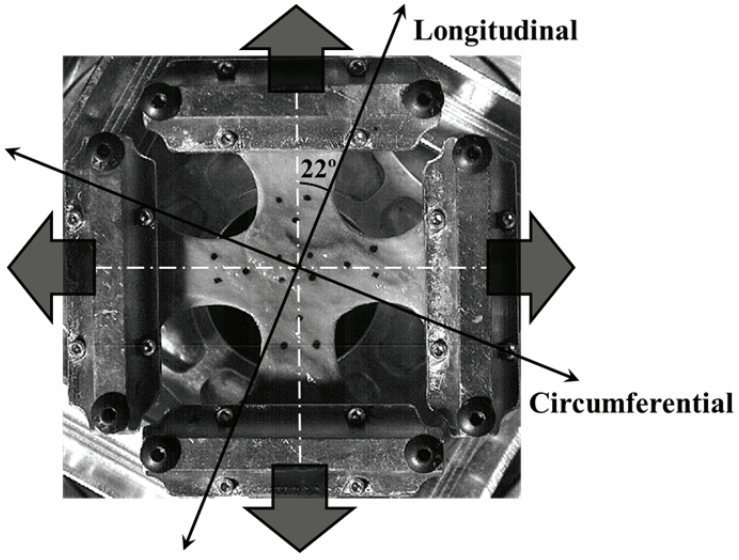

Figure 34: Sample alignment in an offset configuration.

Procurement to testing time was minimized for all tissue samples. Tissues were stored in saline-soaked gauze in airtight containers at 1°C between procurement and testing. Normal saline was used to maintain sample hydration during positioning and testing. All testing was conducted at ambient temperature.

Test Configuration

Biaxial testing was conducted using a custom test device designed to apply multidirectional strain to cruciate samples at high rates (Figure 35). A detailed description of the device is given by Mason et al. (2005). Sample arms were gripped in four low-mass tissue clamps designed to reduce inertial effects at less than 16 grams for each assembly. The upper and lower edges of each clamp were offset from one another, with knurled surfaces to limit slip at the interface between the tissue sample and the clamp. Threaded rods were used to mount each clamp to a corresponding lightweight carriage equipped with low-friction bearings riding on linear rails. Carriages were rigidly coupled to a central drive disk such that rotation of the disk resulted in simultaneous outward motion of the carriages.

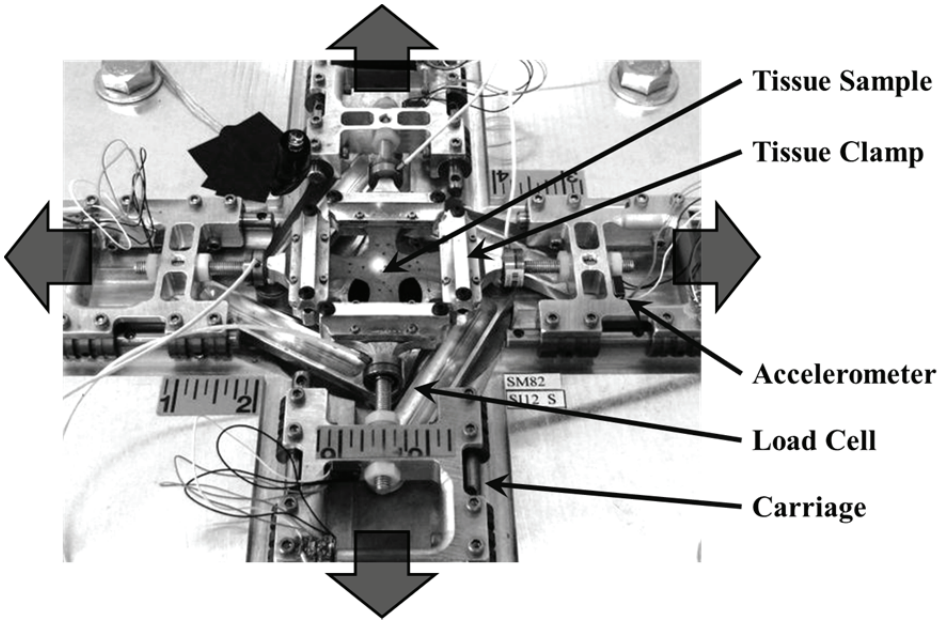

Figure 35: Biaxial tissue test device.

Rotation of the disk was generated by a hydraulic actuating mechanism rigidly linked to a lower carriage of the test device and loaded by a falling mass (Howes and Hardy, 2012). The cylindrical mass was suspended by a magnet and pulley system and released from a desired height within an acrylic drop tube. The mass was grounded to release the buildup of static discharge from sliding friction in the tube. The impact of the falling mass with the piston of a master hydraulic cylinder initiated the motion of a slave cylinder connected to the lower carriage of the test device by a mechanical linkage system. The bore ratio between the master and slave cylinders was selected to amplify the impact velocity at the slave piston. Piston velocity was altered by varying the drop height of the mass.

Vibration from the mass impact with the hydraulic cylinder was dampened by a sand-filled base beneath the drop tower designed with leather padding and a layer of polyurethane casting resin between the base

and the floor. The test device was supported by an isolated sand-filled base. All instrumentation mounts attached to the base were stabilized to eliminate independent oscillation. Vibration of the test device was assessed with a tri-axial accelerometer array (7264B-2000g, Endevco, CA) mounted to the base to verify that device motion was minimal (on average less than 2 g in any direction) for each test during the time window of interest. Data were captured using 20 ksps.

Miniature load cells (ELFF-T2E-100lb, Measurement Specialties, CA) were used to measure applied load at each tissue clamp. Miniature accelerometers (3038-500g, Measurement Specialties, CA) were mounted to each carriage for inertia compensation of the measured load. Laser displacement sensors (LK-G157, Keyence Corporation, NJ) mounted above and below the sample were used to obtain sample thickness in the ROI throughout the duration of each test. The lasers used the same wavelength but operated in phase opposition and therefore did not interfere with one another. Sample thickness was calculated using a calibrated difference in recorded measurement from the upper and lower sensors. All data were captured using 20 ksps. Overhead high-speed video (Phantom v9.1, Vision Research, NJ) recorded parallel to the sample surface was captured using 2500 fps. Video was recorded using a resolution of 800 x 800 pixels and an exposure of 200 μs, which provided optical data in the ROI of the sample at a resolution of 7 pixels per millimeter. The video and data acquisition for each test were synchronized using a voltage-regulated light source in-view of the overhead video.

Tissue samples were positioned in the test device with the inner mucosal layer in view of the high-speed video camera. Prior to positioning the sample, the carriage assemblies were adjusted to the inward position, and each clamp was adjusted using the threaded rods to ensure that all clamps were equidistant from the center of the test device. Samples were transferred to a foam block upon which the ROI was supported to ensure minimal deformation occurred during positioning. Sample arms were aligned with the centerline of each lower clamp and positioned maintaining equal arm length to the center of the ROI. Once aligned, the upper clamps were applied and tightened, and the foam support was removed from beneath the sample. To maintain repeatable initial conditions, the clamps were individually adjusted using the threaded rods to reduce any remaining slack in the sample. A pattern of 17 optical markers was applied to the sample surface using indelible ink. Samples were stretched at a target strain rate of 100 s^{-1} until complete transection occurred. This target rate was selected based on the results of Hardy et al. (2008), where the instantaneous strain rates in the cadaver aorta exceeded 50 s^{-1} in dynamic impact tests that simulated loading in MVCs.

Data Processing and Analysis

All data were zeroed at the time corresponding to the initiation of carriage movement determined from high-speed video analysis. Failure was defined as tear initiation identified using the high-speed video. All data were truncated at the time of tear initiation as the purpose of this work was to obtain response and tolerance to failure, and the subsequent tear propagation requires a more complex analysis. If a peak in the load-time history preceded visible tear initiation, data were then truncated at the time of peak load filtered using SAE J211 Channel Frequency Class (CFC) 600 Hz (SAE, 2007).

Multidirectional displacement data were obtained by tracking the position of five markers in the ROI (Figure 36) using motion analysis software (TEMA, Image Systems, Linköping, Sweden) employing a regional correlation method. Displacement data for each marker were input into LS-DYNA as boundary prescribed motion for five nodes. Each triad of nodes sectioned the ROI into four triangular shell elements. Green-Lagrange strain, maximum principal strain, and maximum shear strain were determined as the average value from each of the four elements solved at 0.05 ms time intervals.

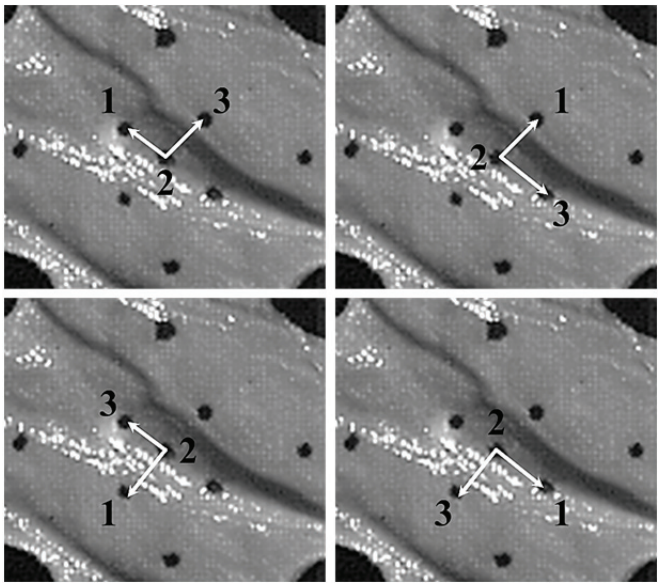

Figure 36: Optical marker triads in the ROI of a small intestine sample.

LS-DYNA was used to calculate strain for each of the tissue tests; however, the corresponding equations are included for completeness. Green-Lagrange strain for each element corresponds to the strain tensor (Eqn. 2) calculated from the deformation gradient computed for each triad (Eqn. 1). The stretch ratio (λ) and true strain (ε) were calculated from the Green-Lagrange strain (Eqn. 3). Maximum principal strain corresponds to the eigenvalues ($\lambda\pm$) of the Green-Lagrange strain tensor (Eqn. 4). The average maximum principal strain rate was calculated as the average of the time derivative of the maximum principal strain over the test duration.

$$\mathbf{F} = \left(\begin{bmatrix} X_1 & X_2 \\ Y_1 & Y_2 \end{bmatrix}_{t=1}\right)\left(\begin{bmatrix} x_1 & x_2 \\ y_1 & y_2 \end{bmatrix}_{t=0}\right)^{-1} \quad \text{Eqn. 1}$$

$$\mathbf{E} = \begin{bmatrix} E_{11} & E_{12} \\ E_{21} & E_{22} \end{bmatrix} = \frac{1}{2}(F^T F - I) \quad \text{Eqn. 2}$$

$$\varepsilon = \ln \lambda = \ln \sqrt{2E + 1} \quad \text{Eqn. 3}$$

$$\lambda_{\pm} = \frac{1}{2}\left[(E_{11} + E_{22}) \pm \sqrt{4E_{12}E_{21} + (E_{11} - E_{22})^2}\right] \quad \text{Eqn. 4}$$

Calculation of the load applied to the ROI in each direction was dependent on inertia compensation and scaling of the measured load. The effective mass used for inertia compensation was optimized for each of the four measured loads for each tissue test. The compensated load for each clamp was adjusted to the ROI by applying an assumption of a proportional transmission of load through each arm to the central region. A scaling ratio of the initial length of the ROI, obtained as the distance between the outer marker pairs, to the initial sample arm width in the same direction was applied to scale the normal load at each time step. The resulting values were taken as the load applied to the ROI. Two compensated loads in each direction were averaged to obtain the load-time histories in the X- and Y-directions.

True stress (S) was calculated by first determining changing cross-sectional area (A_n) for each sample. Laser thickness data filtered using SAE J211 CFC 180 Hz (SAE, 2007) was multiplied by the average ROI length, determined in each direction. In the event that the laser thickness data were confounded by sample surface inhomogeneities, an assumption of incompressibility (Poisson's ratio equal to 0.5) was used to calculate changing sample thickness by assuming volume conservation. The validity of this assumption was investigated by Shah et al. (2006) using samples from the cadaver aorta, although greater variability would be expected for gastrointestinal samples due to the presence of inhomogeneities on the upper and lower surfaces of the samples. However, for the colon samples tested in this study, no significant differences ($p=0.38$) were identified using the Student's t-test ($\alpha=0.05$) to compare the measured and calculated thickness at tissue failure for N=18 samples with available thickness data. Figure 37 shows example time-histories of the thickness of four colon samples.

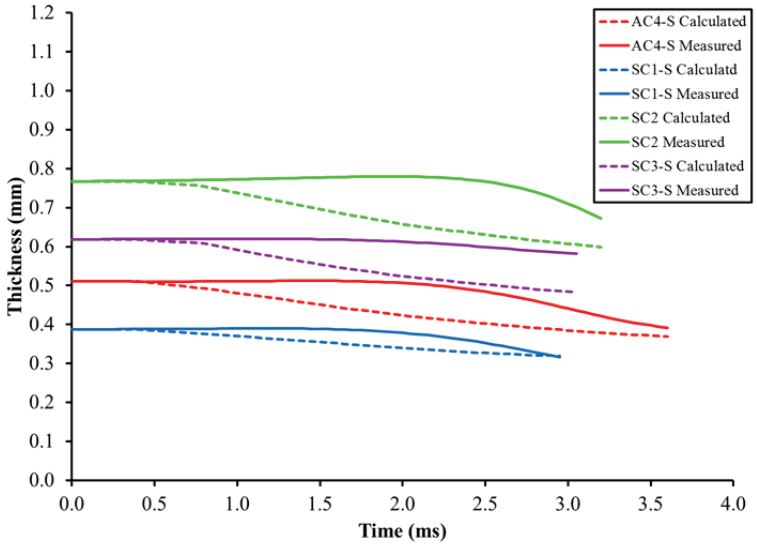

Figure 37: Examples of the measured and calculated thickness for the colon.

True stress (S) was calculated using the unfiltered load (P) applied to the region of interest in each direction divided by the appropriate cross-sectional area (Eqn. 5). 2nd Piola Kirchhoff stress (K) was determined using the unfiltered applied load (P), the initial cross-section (A_0), and the inverse of the stretch ratio (λ) (Eqn. 6). Stress data were filtered using SAE J211 CFC 600 Hz (SAE, 2007).

$$S = \frac{P}{A_{n_\perp}} \quad \text{Eqn. 5}$$

$$K = \frac{P}{A_{0_\perp}} * \frac{1}{\lambda_\parallel} \quad \text{Eqn. 6}$$

All strain and stress data from the offset tissue tests were transformed to align with the material axes of the tissue (Eqn. 7-Eqn. 10).

$$\varepsilon_x' = \frac{\varepsilon_x + \varepsilon_y}{2} + \frac{\varepsilon_x - \varepsilon_y}{2}\cos 2\theta + \frac{\gamma_{xy}}{2}\sin 2\theta \quad \text{Eqn. 7}$$

$$\varepsilon_y' = \frac{\varepsilon_x + \varepsilon_y}{2} - \frac{\varepsilon_x - \varepsilon_y}{2}\cos 2\theta - \frac{\gamma_{xy}}{2}\sin 2\theta \quad \text{Eqn. 8}$$

$$\sigma_x' = \frac{\sigma_x + \sigma_y}{2} + \frac{\sigma_x - \sigma_y}{2}\cos 2\theta + \tau_{xy}\sin 2\theta \quad \text{Eqn. 9}$$

$$\sigma_y' = \frac{\sigma_x + \sigma_y}{2} - \frac{\sigma_x - \sigma_y}{2}\cos 2\theta - \tau_{xy}\sin 2\theta \quad \text{Eqn. 10}$$

Within each region, the circumferential and longitudinal failure strains were compared using two-sample Student's t-tests assuming unequal variances (α=0.05). For regions with a small number of samples (e.g. N=3), it was assumed that the results would fit a normal distribution if a greater number of samples were tested from that region. Other regions with a greater number of samples passed the normality test, therefore supporting this assumption. However, for regions with a small number of samples, the p-value would only indicate significance if the standard deviation was very small. Single factor ANOVA (α=0.05) was used to compare failure strain between regions for each direction. Identical statistical comparisons were made for failure stress. Single factor ANOVA (α=0.05) was also used to compare the directional failure response between the organs of the digestive tract.

RESULTS

Dataset Summary

Approximately 150 dynamic equibiaxial tension tests were conducted on tissue samples harvested from four PMHS including 39 stomach tests, 72 small intestine tests, and 38 colon tests. An example test sequence is shown in Figure 38. Tests were included in the final dataset based on sample uniformity in the initial position and tear initiation away from the grip edges. The uniformity of the sample shape was assessed qualitatively and confirmed with optical measurements of arm width and length using an initial video still from each test. Samples were excluded from the dataset if any of the sample arms were a considerably different width or length compared to the other arm branches or if the centerlines of the sample arms were noticeably offset from one another in the X- and Y-directions. For each sample meeting the inclusion criteria, the stress and strain responses were determined.

The final dataset included 18 stomach tests, 20 small intestine tests, and 21 colon tests. The stress-strain results for each organ are presented in terms of the regional and directional differences in material response. The relative stiffness of the responses was assessed based on the values for stress and strain at tissue failure. These results were compared within each organ and throughout the length of the digestive tract.

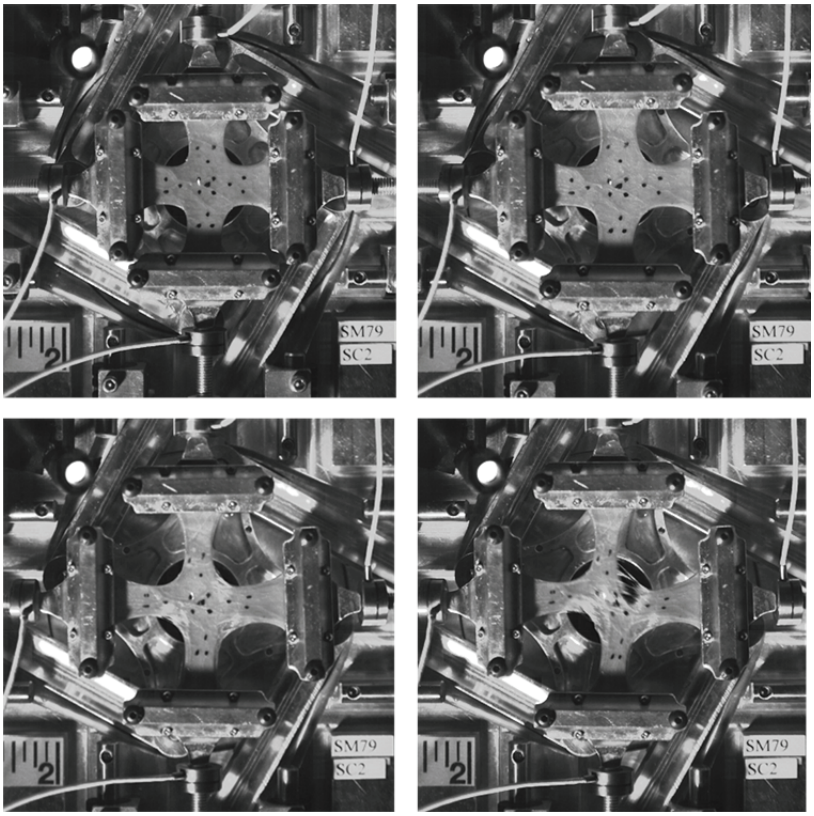

Figure 38: Video still images from an offset colon test with failure through the ROI.

Stomach Response Data

A total of 39 equibiaxial tension tests were conducted on stomach samples obtained from four PMHS. The final dataset for analysis included 18 stomach samples meeting inclusion criteria of sample uniformity and failure tear initiation at the edge of the ROI. Samples were obtained from each anatomic region of the stomach with the exception of the cardia, due to the small size of this region. The final dataset included 3 fundus samples, 10 corpus samples, and 5 antrum samples. The average maximum principal strain rate for all tests was 52.3 ± 14.3 s^{-1}. The average maximum principal strain at failure was 0.160 ± 0.052 for all samples. Maximum shear strain at failure was approximately 8-percent on average. Strain-time histories for each test are provided in the Appendix (Figure 47). The directional Lagrangian stress-strain response curves for all stomach samples are shown in Figure 39 and Figure 40. The aligned (N=6) and offset (N=12) samples are differentiated in Figure 39 and Figure 40; however, all samples were considered together for analysis due to the low sample size.

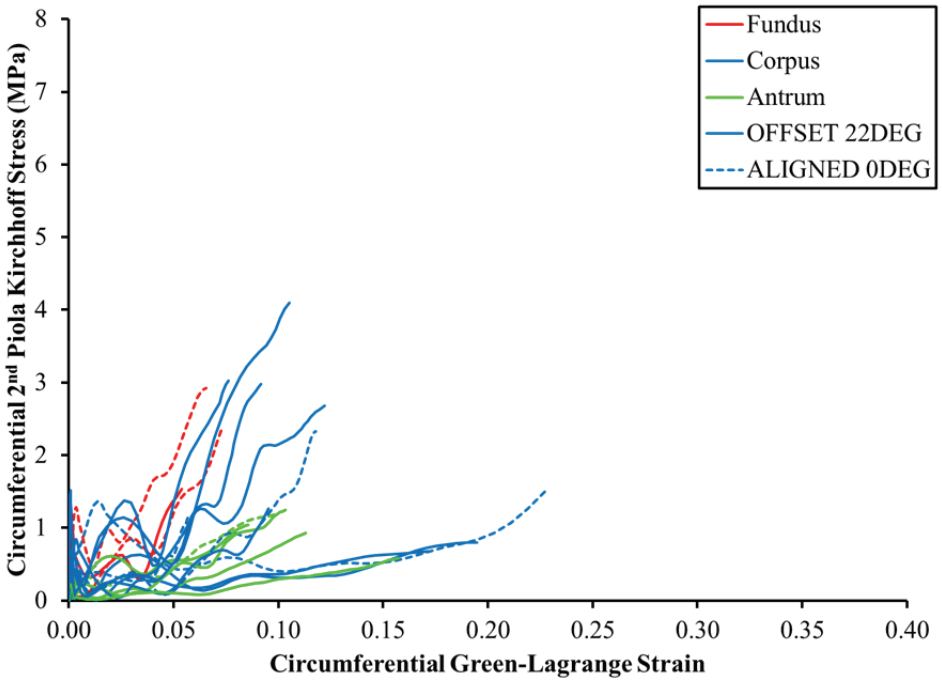

Figure 39: Circumferential stress-strain responses by region of the stomach.

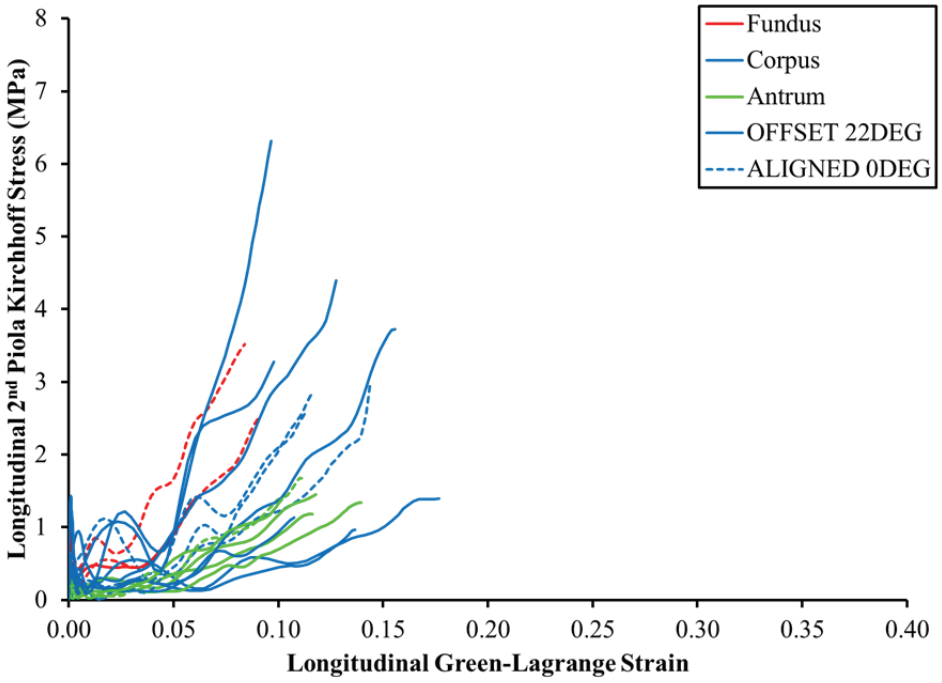

Figure 40: Longitudinal stress-strain responses by region of the stomach.

Overall, the strain at failure was approximately equal on average for the circumferential and longitudinal directions. The average Green-Lagrange strain at failure was 0.112 ± 0.048 in the circumferential direction and 0.117 ± 0.027 in the longitudinal direction. On average, the strain at failure was slightly greater in the longitudinal direction for each region of the stomach, though there were no significant differences by direction within each region (Table 12). There was a statistically significant difference in longitudinal strain at failure between regions of the stomach ($p=0.02$) as determined using single factor ANOVA (Table 14). Post hoc analyses using the Tukey-Kramer multiple comparisons test indicated that the longitudinal strain at failure for the fundus of the stomach was significantly lower than for the corpus region ($p<0.05$). No other comparisons were significant. The true strain results are provided in the Appendix (Table 25).

The average stress at failure was greater in the longitudinal direction for all regions of the stomach. In the circumferential direction, the average 2nd Piola Kirchhoff stress at failure was 1.80 ± 1.01 MPa for all samples, and the average stress at failure in the longitudinal direction was 2.45 ± 1.42 MPa. The differences in average directional stress at failure for the stomach were not significant overall ($p=0.12$); however, for the antrum of the stomach, the stress at failure was significantly greater in the longitudinal direction than in the circumferential direction ($p=0.02$) (Table 13). No significant differences in the average stress at failure were found between regions in either the circumferential ($p=0.10$) or the longitudinal direction ($p=0.13$) using single factor ANOVA (Table 14). The true stress results are provided in the Appendix (Table 26).

Table 12: Green-Lagrange strain at failure by region of the stomach.

Region	N	Circumferential Strain		Longitudinal Strain		p-value
		AVG	STDEV	AVG	STDEV	
Fundus	3	0.064	0.009	0.080	0.015	0.22
Corpus	10	0.126	0.055	0.127	0.026	0.95
Antrum	5	0.112	0.027	0.117	0.014	0.70
Total	18	0.112	0.048	0.117	0.027	0.71

Table 13: 2nd Piola Kirchhoff stress at failure by region of the stomach (MPa).

Region	N	Circumferential Stress		Longitudinal Stress		p-value
		AVG	STDEV	AVG	STDEV	
Fundus	3	2.26	0.70	2.49	1.04	0.77
Corpus	10	2.06	1.13	2.97	1.63	0.17
Antrum	5	1.00	0.27	1.41	0.18	**0.02**
Total	18	1.80	1.01	2.45	1.42	0.12

Table 14: ANOVA comparisons between regions of the stomach.

Parameter	Circumferential	Longitudinal
	p-value	p-value
Green-Lagrange Strain	0.14	**0.02**
True Strain	0.13	**0.01**
2nd Piola Kirchhoff Stress	0.10	0.13
True Stress	0.11	0.14

Small Intestine Response Data

The final dataset of small intestine samples included 20 tests. The majority of the samples were harvested from the jejunum, with one sample from the ileum. The regions were therefore grouped together for analysis. The directional Lagrangian stress-strain response curves are shown in Figure 41 and Figure 42. The aligned (N=4) and offset (N=16) sample groups are differentiated in Figure 41 and Figure 42; however, the aligned and offset samples were considered together for analysis due to the low sample size. The average maximum principal strain rate for all tests was 79.5 ± 21.3 s^{-1}. The average maximum principal strain at failure was 0.227 ± 0.063 for all samples. Maximum shear strain at failure was approximately 12-percent on average for the small intestine tests. Strain-time histories for each test are provided in the Appendix (Figure 48). The Lagrangian directional responses at failure are summarized in Table 15, and the true stress and strain results are provided in the Appendix (Table 27).The average Green-Lagrange strain at failure in the circumferential direction was 0.148 ± 0.061, and the average strain at failure in the longitudinal direction was 0.136 ± 0.047. The average 2nd Piola Kirchhoff stress at failure was 1.99 ± 1.19 MPa and 3.28 ± 1.54 MPa in the circumferential and longitudinal directions, respectively. The directional strains at failure were not significantly different (p=0.49); however, the stress at failure was significantly greater in the longitudinal direction (p=0.01).

Table 15: Lagrangian strain and 2nd Piola Kirchhoff stress (MPa) at failure for the small intestine.

N	Circumferential Strain		Longitudinal Strain		p-value
	AVG	STDEV	AVG	STDEV	
20	0.148	0.061	0.136	0.047	0.49
N	Circumferential Stress		Longitudinal Stress		p-value
	AVG	STDEV	AVG	STDEV	
20	1.99	1.19	3.28	1.54	**0.01**

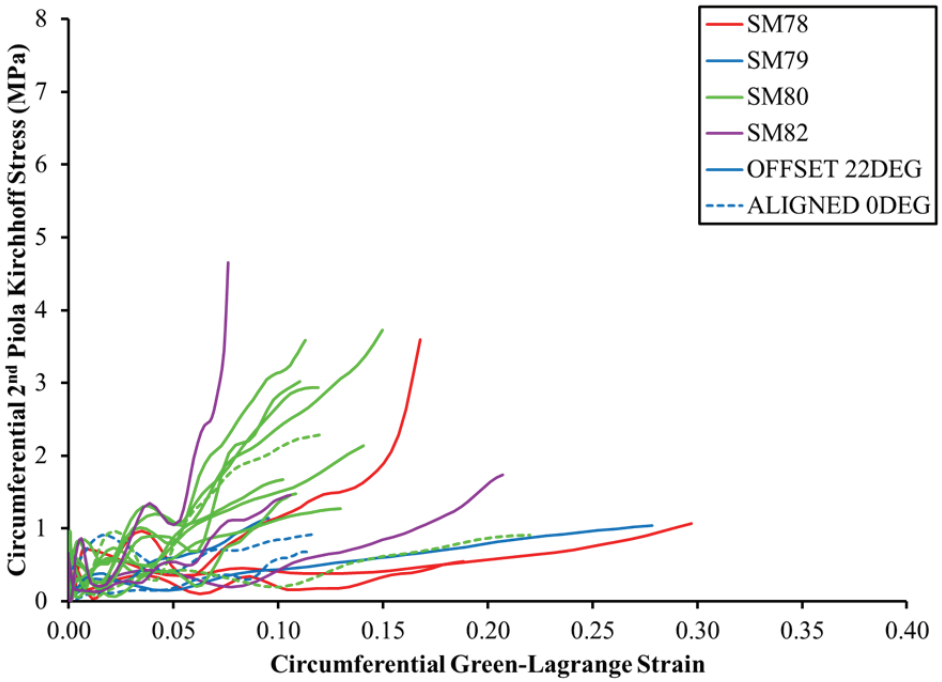

Figure 41: Circumferential stress-strain responses for the small intestine.

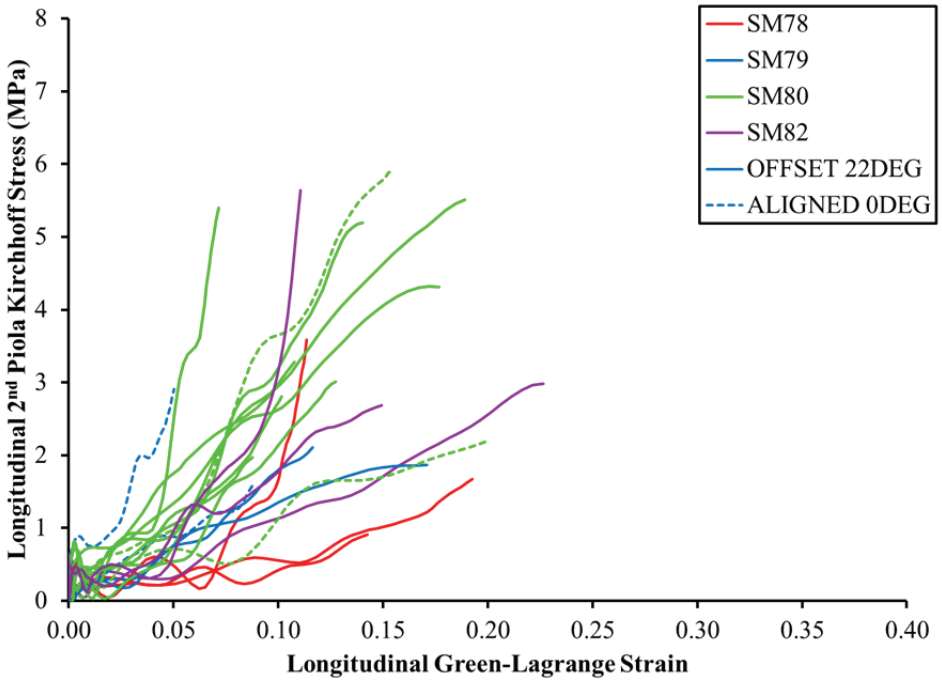

Figure 42: Longitudinal stress-strain responses for the small intestine.

Colon Response Data

A total of 38 equibiaxial tension tests were conducted on colon samples obtained from four PMHS. The final dataset consisted of 21 tests meeting inclusion criteria of sample uniformity in each direction and failure tear initiation at the edge of the ROI. The average maximum principal strain rate for all tests was 69.2 ± 16.0 s^{-1}. For the majority of the tests, the strain at failure was greater in the circumferential direction compared to the longitudinal direction. The average Green-Lagrange strain at failure was 0.158 ± 0.036 in the circumferential direction and 0.139 ± 0.039 in the longitudinal direction. The average 2nd Piola Kirchhoff stress at failure was 2.35 ± 1.37 MPa and 3.20 ± 1.51 MPa in the circumferential and longitudinal directions, respectively. The average maximum principal strain at failure was 0.207 ± 0.060, and the maximum shear strain at failure was approximately 10-percent on average for all tests.

The final dataset included 3 samples from the ascending colon, 4 from the transverse colon, 7 from the descending colon, and 7 from the sigmoid colon. Figure 43 and Figure 44 show the directional Lagrangian stress-strain response for each region of the colon. The aligned (N=7) and offset (N=14) sample groups are differentiated in Figure 43 and Figure 44. In general, the samples aligned with the long axis of the tissue showed a decreased stiffness in the circumferential direction compared to samples that were offset by 22 degrees. No clear trend was observed in the longitudinal direction. Due to the low sample size, the aligned and offset samples were considered together for the remainder of the analysis.

In all regions, the average strain at failure was greater in the circumferential direction than in the longitudinal direction. However, there were no statistically significant directional differences in strain at failure within each region (Table 16). Further, no statistically significant differences in strain were found between regions in either the circumferential ($p=0.34$) or the longitudinal direction ($p=0.59$) using single factor ANOVA (Table 18). Strain-time histories for each test are provided in the Appendix (Figure 49). Although no significant differences were found at failure between the regions, the grouping of the strain-time curves for the sigmoid colon suggested a variation in the response of this region compared to the ascending, transverse, and descending regions in both directions (Figure 49). The average stress at failure was greater in the longitudinal direction for all regions of the colon. No statistically significant differences were found in 2nd Piola Kirchhoff stress at failure by direction within each region (Table 17). There was a statistically significant difference in longitudinal stress at failure between regions of the colon ($p=0.01$) as determined by single factor ANOVA (Table 18). Post hoc analyses using the Tukey-Kramer multiple comparisons test indicated that the longitudinal stress at failure for the descending colon was significantly lower than for the sigmoid colon ($p<0.05$). No other comparisons were significant. The true stress and true strain results are provided in the Appendix (Table 28-Table 29).

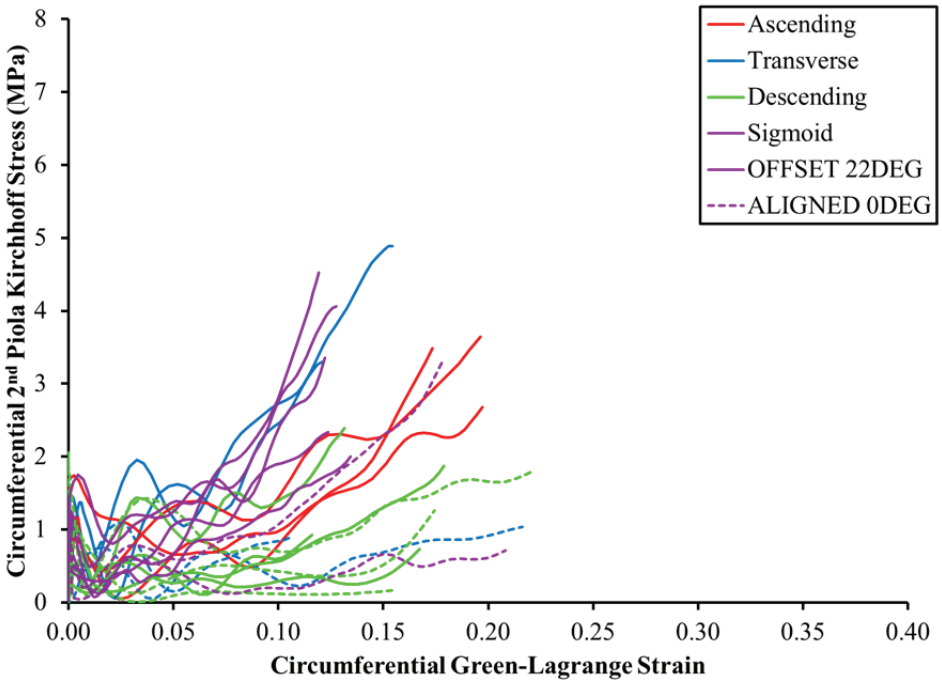

Figure 43: Circumferential stress-strain responses by region of the colon.

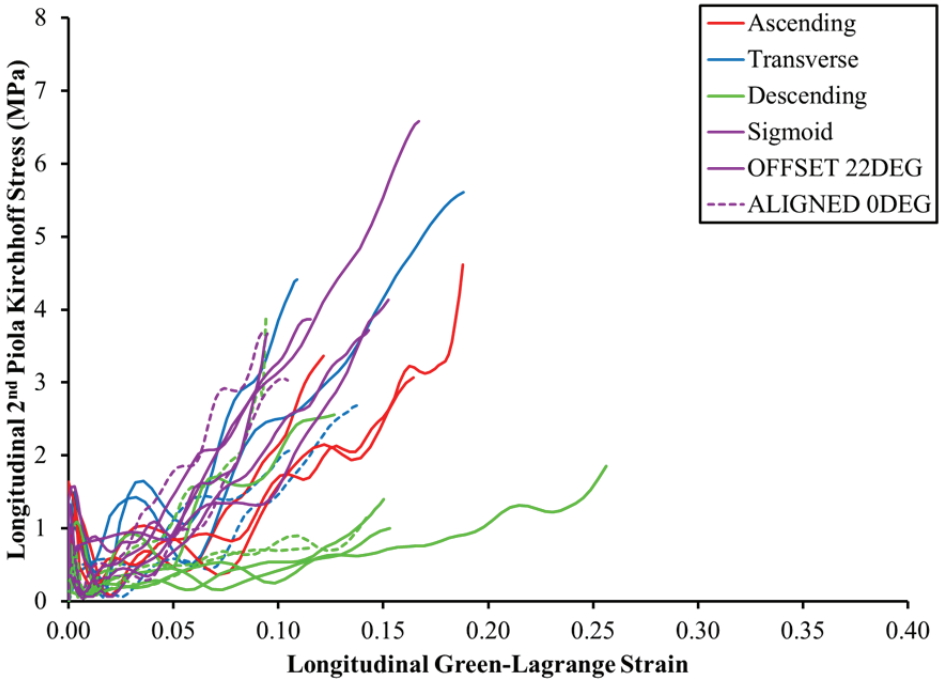

Figure 44: Longitudinal stress-strain responses by region of the colon.

Table 16: Green-Lagrange strain at failure by region of the colon.

Region	N	Circumferential Strain		Longitudinal Strain		p-value
		AVG	STDEV	AVG	STDEV	
Ascending	3	0.189	0.013	0.158	0.034	0.25
Transverse	4	0.149	0.049	0.135	0.038	0.67
Descending	7	0.163	0.034	0.148	0.052	0.54
Sigmoid	7	0.145	0.035	0.124	0.029	0.26
Total	21	0.158	0.036	0.139	0.039	0.11

Table 17: 2nd Piola Kirchhoff stress at failure by region of the colon (MPa).

Region	N	Circumferential Stress		Longitudinal Stress		p-value
		AVG	STDEV	AVG	STDEV	
Ascending	3	3.27	0.52	3.68	0.82	0.51
Transverse	4	2.53	1.92	3.70	1.61	0.39
Descending	7	1.31	0.77	1.80	1.10	0.35
Sigmoid	7	2.90	1.31	4.10	1.14	0.09
Total	21	2.35	1.37	3.20	1.51	0.06

Table 18: ANOVA comparisons between regions of the colon.

Parameter	**Circumferential**	**Longitudinal**
	p-value	p-value
Green-Lagrange Strain	0.34	0.59
True Strain	0.33	0.58
2nd Piola Kirchhoff Stress	0.07	**0.01**
True Stress	**0.05**	**0.03**

Organ Response Comparison

For all organs, failure occurred at approximately 14% strain on average. The colon had the greatest average strain at failure, followed by the small intestine and the stomach (Figure 45; Table 19). The average strain at failure was greater in the circumferential direction compared to the longitudinal direction for both the small intestine and the colon. For the stomach, the average strain at failure was approximately equal in both directions. No significant differences were found for directional strain at failure for each organ. However, there was a statistically significant difference in the strain at failure in the circumferential direction between organs as determined using single factor ANOVA ($p=0.01$) (Table 21). Post hoc analyses using the Tukey-Kramer multiple comparisons test indicated that the strain at failure in the circumferential direction was significantly lower for the stomach compared to the colon ($p<0.05$). No other comparisons were significant. The average stress at failure was on the order of 2 to 3 MPa for all organs in the circumferential and longitudinal directions, respectively. The average stress at failure was

greater in the longitudinal direction for each organ, though this result was not significant for the stomach or the colon (Figure 46; Table 20). For the small intestine, the stress at failure in the longitudinal direction was significantly greater than in the circumferential direction (p=0.01). No significant directional differences were found between organs using single factor ANOVA (Table 21).

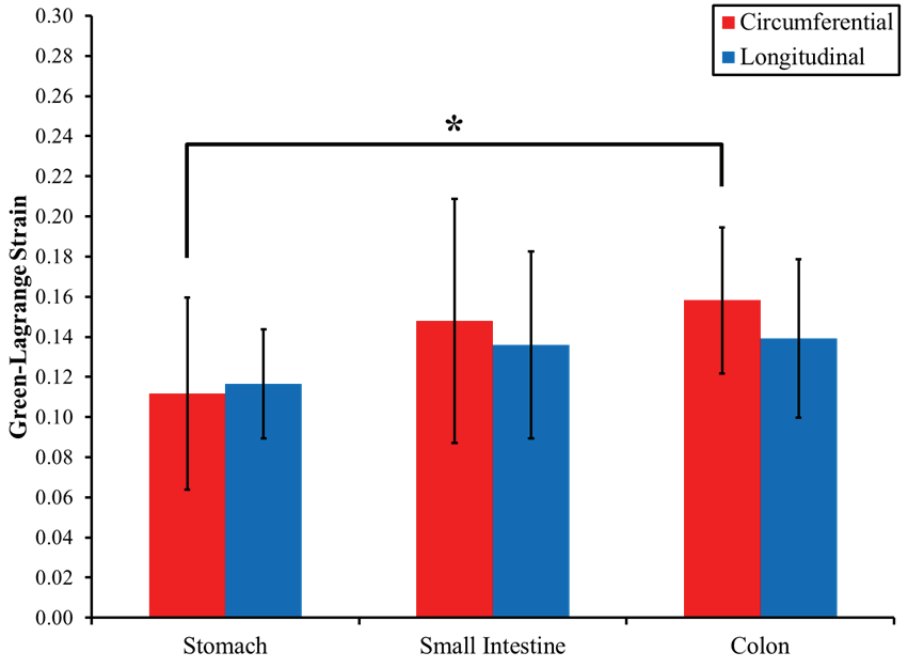

Figure 45: Average directional Green-Lagrange strain at failure by organ (*p<0.05).

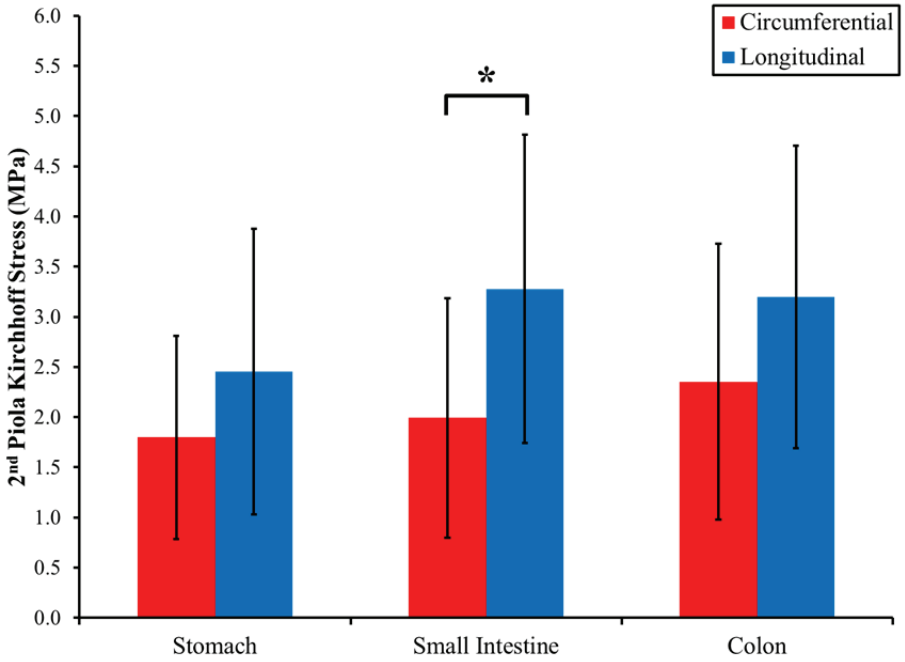

Figure 46: Average directional 2nd Piola Kirchhoff stress at failure by organ (*p=0.01).

Table 19: Directional Green-Lagrange strain at failure by organ.

Organ	N	Circumferential Strain		Longitudinal Strain		p-value
		AVG	STDEV	AVG	STDEV	
Stomach	18	0.112	0.048	0.117	0.027	0.71
Small Intestine	20	0.148	0.061	0.136	0.047	0.49
Colon	21	0.158	0.036	0.139	0.039	0.11

Table 20: Directional 2nd Piola Kirchhoff stress at failure by organ (MPa).

Organ	N	Circumferential Stress		Longitudinal Stress		p-value
		AVG	STDEV	AVG	STDEV	
Stomach	18	1.80	1.01	2.45	1.42	0.12
Small Intestine	20	1.99	1.19	3.28	1.54	**0.01**
Colon	21	2.35	1.37	3.20	1.51	0.06

Table 21: ANOVA comparisons between organs of the digestive tract.

Parameter	**Circumferential**	**Longitudinal**
	p-value	p-value
Green-Lagrange Strain	**0.01**	0.16
True Strain	**0.01**	0.17
2nd Piola Kirchhoff Stress	0.35	0.19
True Stress	0.22	0.24

DISCUSSION

Multidirectional stress-strain responses were quantified for dynamic equibiaxial tension tests conducted using post-mortem stomach, small intestine, and colon tissue samples. Directional differences in the material response were identified for each organ; however, for the majority of the comparisons the differences were not significant. In general, an increased resistance to stretch was observed in the longitudinal direction. A greater average stress at failure and lower average strain at failure occurred in the longitudinal direction compared to the circumferential direction for both the small intestine and the colon. For the stomach, the average strain at failure was similar in both directions, yet a greater stress at failure was observed in the longitudinal direction. The trends in directional material response identified in this study were similar to the results of uniaxial tension tests conducted at constant quasi-static strain rates (Yamada, 1970; Egorov et al., 2002). A decreased stiffness, or lower resistance to stretch, in the circumferential direction may be attributed to the physiologic need for expansion of the gastrointestinal organs in circumference during digestion. Further, for the colon, stretch in the longitudinal direction may be inhibited by the muscular teniae coli extending axially throughout the length of the large intestine. This is consistent with the findings of Egorov et al. (2002) in which an increase in stress occurred at a lower

percent strain for longitudinal teniae samples compared to longitudinal haustra samples and intact transverse samples.

Regional variations in mechanical response were observed in this study for the colon. On average, the strain at failure was greatest for the ascending colon, followed by the descending colon, transverse colon, and sigmoid colon for both the circumferential and longitudinal directions. These differences, however, were minimal and not significant. Average stress at failure for the descending colon was considerably lower than for the other regions. This result was only significant compared to the sigmoid colon in the longitudinal direction. Yamada (1970), citing Iwasaki (1953), also reported the lowest ultimate stress for the descending colon compared to the other regions of the large intestine. Despite similarities in wall structure between all regions of the colon, physiologic differences based on the composition of the intestinal contents at each stage of digestion and storage may contribute to the observed regional variations in mechanical response.

Regional response variations were also identified for the stomach; however, the unequal sample size from each region may have confounded the differences observed in this study. In both directions, the average strain at failure was greatest for the corpus, or body of the stomach, followed by the antrum and the fundus. This result was significant in the longitudinal direction where the strain at failure for the corpus was significantly greater than for the fundus. The body of the stomach likely undergoes greater expansion during filling compared to the proximal region, contributing to this result. Additionally, gastric wall structure varies between the regions of the stomach, with an increased prominence of rugae in the distal regions. Rugae allow for expansion of the stomach during filling; therefore, increased elongation is expected for regions of the stomach where rugae are present. In both the circumferential and longitudinal directions, a stiffer response was observed for the fundus samples compared to samples obtained from the antrum of the stomach. This result varied from the response reported by Yamada (1970), citing Nonogaki (1960) and Fukuyama (1961), which indicated a stiffer response for the pyloric region compared to the corpus and fundus regions. Due to the size of the samples tested in the current study, it is possible that the antrum samples were comprised of tissue from both the corpus and antrum regions. This may have affected the stiffness of the samples because the resistance to stretch is likely lower for the corpus region to accommodate the gastric contents during digestion. The response reported by Yamada (1970) for the pyloric region may have been obtained from samples of the thickened region of the pylorus adjacent to the pyloric sphincter, resulting in a greater stiffness for this region.

In this study, the variation in the hollow organ response to high-rate loading was identified throughout the length of the digestive tract. In both the circumferential and longitudinal directions, the intestinal strain at

failure was greater than the strain at failure for the stomach. This result was significant in the circumferential direction between the stomach and the colon. The need for expansion during digestion is likely greater for the intestines compared to the stomach, leading to increased stretch before failure for these organs. Shear strain was also greater for the small intestine and colon, indicating that an increased compliance of the tissue results in an increased propensity for shear in the sample. No significant differences in stress were identified between organs, though the average stress at failure was greater in both directions for the small intestine and colon compared to the stomach. Based on the values for stress and strain at tissue failure, the response data indicated the least resistance to stretch for the small intestine and colon in the circumferential direction and the greatest resistance to stretch for these tissues in the longitudinal direction. These trends are consistent with the patterns of expansion expected during digestion.

Egorov at al. (2002) also investigated the tensile response of the human stomach, small intestine, and large intestine, though those tests were conducted in uniaxial tension until failure at a quasi-static strain rate. The strain energy for the response of each organ was estimated to further compare the results of Egorov et al. (2002) and the results of the equibiaxial tests conducted in this study. The average stress-strain response for Egorov et al. (2002) was approximated assuming a linear ramp from the strain value where the stress increased to the peak in the stress response and the corresponding strain. The areas for the soft and stiff responses were also calculated. The soft response was approximated using one standard deviation below the average strain at the onset of stress and one standard deviation above the average strain at peak stress. Stress initiated at zero, and the terminal point was one standard deviation below the peak average response. The stiff response was approximated using one standard deviation above the average strain at the onset of stress and one standard deviation below the average strain at peak stress. Stress initiated at zero, and the terminal point was one standard deviation above the peak average response. For the equibiaxial tests conducted in this study, the area under the stress-strain curve was calculated for each test using Simpson's rule for integration. The average areas for the tests from each organ are summarized in Table 22-Table 24.

Table 22: Strain energy calculated for the stomach.

Stomach	Egorov et al. (2002)				Howes
	Soft	Average	Stiff		Average ± Stdev
	area, MPa	area, MPa	area, MPa		area, MPa
Circumferential	0.19	0.20	0.15		0.08 ± 0.04
Longitudinal	0.23	0.23	0.16		0.10 ± 0.05

Table 23: Strain energy calculated for the small intestine.

Small Intestine	Egorov et al. (2002)				Howes
	Soft	Average	Stiff		Average ± Stdev
	area, MPa	area, MPa	area, MPa		area, MPa
Circumferential	0.27	0.27	0.18		0.12 ± 0.06
Longitudinal*	0.20	0.15	0.01		0.19 ± 0.13

*Initial peak response

Table 24: Strain energy calculated for the colon.

Colon	Egorov et al. (2002)				Howes
	Soft	Average	Stiff		Average ± Stdev
	area, MPa	area, MPa	area, MPa		area, MPa
Circumferential	0.49	0.42	0.25		0.17 ± 0.10
Longitudinal*	0.34	0.36	0.28		0.18 ± 0.11

*Haustra samples (Egorov et al., 2002)

The results of Egorov et al. (2002) were reported as engineering stress and engineering strain. The average response for peak stress and failure strain ranged from 0.5 to 1.5 MPa and 1.39 to 2.06 strain, respectively. The average 2nd Piola Kirchhoff stress at failure for the equibiaxial tests in this study ranged from 1.80 to 3.28 MPa. The average Green-Lagrange strain at failure ranged from 0.112 to 0.158. The stress, and particularly the strain, at failure identified in each of the studies appear to indicate considerable differences in the material response. However, the comparison of the average strain energy for the equibiaxial tests to the range identified for Egorov et al. (2002) indicates less of a difference in the responses, suggesting greater overall similarity in the behavior of the tissues for both test modes.

Assumptions and Limitations

These tests were conducted using tissue samples harvested from four cadavers. Due to the limited number of samples overall, the samples from each surrogate were considered together for analysis. Variability between cadavers was not assessed but may have contributed to response variations within the organ groups. Additionally, the samples aligned with the material axes of the tissue and those offset from the long axis by 22 degrees were considered together for this analysis due to the low number of samples. A stiffer response was expected for the offset samples; however, this trend was only clearly observed in the circumferential direction for the colon. It is likely that additional regional differences in directional material properties would be apparent if the sample size within each region was increased and only the offset samples were considered for analysis.

Load was applied to the tissue samples a distance away from the ROI where stress and strain were calculated. In order to transfer the measured load to the ROI, assumptions of a uniform stress distribution

within the sample and a proportional transmission of load from the tissue clamps to the central region were applied. Small samples without visible defects were tested in an attempt to ensure that the samples were devoid of any large-scale inhomogeneities. Future work will include an assessment of the equality of the load distribution in each direction for the tissue samples. Additionally, load applied at the edge of each of the sample arms must propagate to the central region over time. It was assumed for these tests that the small size of the samples minimized the effect of load application a distance away from the ROI, and therefore an instantaneous transmission of load to the ROI occurred. However, the initial stress offset in the stress-strain response curves can be partially attributed to the load application and measurement at the edges of the arm branches of the sample before stretch occurred in the ROI. Additionally, a single value for effective mass was used for inertia compensation in each direction; however, the mass is not constant throughout the test, which can result in the onset of stress before deformation occurs.

For many of the samples, a peak in the load-time history occurred prior to the time of tear initiation identified using the high-speed video. This indicated that the sampling rate of the high-speed video was likely too low to capture the initiation of the tear for many of the samples for which the peak in the load-time history occurred between the last two frames of the video data. A peak in the load occurred earlier than one frame from the tear initiation in the video for a few of the samples from each organ. For these tests, it is probable that the tear initiated in a layer of the sample not visible from the high-speed video perspective. Additionally, stress-strain curves with changes in slope (but no peak in the load-time history) could indicate tear or compromise within the sample layers. Future tests using a greater video sampling rate or with both surfaces of the sample visible in the video could be used to investigate failure timing and tear initiation location.

The ability to obtain repeatable and uniform sample geometry for component-level tissue tests is confounded by the compliant nature of the tissue; however, shear strain was used to characterize this limitation. Uneven sample geometry, slip between sample layers, and rotation or vibration of the sample arms increases the shear strain. Shear strain was minimized in this study by maintaining short and equal sample arm length and ensuring even geometry for all four arms. The target maximum shear strain of ten-percent or less prior to tissue failure was considered reasonable for these tests, indicating that multi-axial stretch was achieved with minimal shear in the ROI.

The results of component-level tissue testing are only applicable *in vitro* and do not directly describe the *in vivo* response of the tissue. Although efforts were made to maintain repeatable initial test conditions for all samples, these conditions may not match the physiologic stress or strain state occurring *in vivo*. Additionally, differences in response between tissues with varying substructures, such as the visible folds

of plicae circulares of the small intestine samples compared to the relatively smooth surface structure of the colon samples, were not assessed separately in this analysis. The presence of mucosal folds on the sample surface likely indicates a difference in the initial strain state for these samples compared to samples without folds. The presence of folds also potentially indicates an increased propensity for stretch before failure for these sample layers, though the layered wall structure of the tissues was not considered independently. Further, the response of the tissue samples measured in a small central ROI may not be representative of the *in vivo* response of the whole organ (Sacks, 2000). Despite these limitations, acquiring equibiaxial response data contributes to material property validation at the component-level with an approach more representative of the complex, multi-axial behavior expected *in vivo*.

Applications

Experimental equibiaxial tests result in paired X- and Y-directional responses that cannot be separated for material parameter determination. However, the equibiaxial material responses quantified in this study can be applied using finite element simulation and optimization techniques to determine the material parameters to fit an existing constitutive representation of highly deformable materials. The results presented in this study can be further investigated with strain energy density function analysis using sample-specific finite element modeling of the equibiaxial tests.

CONCLUSION

Limited material properties data are available in the literature for the complex anatomical structures of the digestive system. Those data were typically obtained at quasi-static loading rates that are not representative of the dynamic loading rates experienced in MVCs. In this study, the material properties and failure thresholds of human post-mortem stomach, small intestine, and colon samples were obtained in equibiaxial stretch at high loading rates of approximately 70 s^{-1}. In blunt impacts, the abdominal tissues are likely loaded in a variety of modes; however, this study represents the first study to address the biaxial loading condition for the membranous abdominal tissues. These tests were designed to account for the anisotropic response of the material. The average Green-Lagrange strain at failure ranged from 0.112 ± 0.048 for the stomach in the circumferential direction to 0.158 ± 0.036 for the colon in the circumferential direction. The average 2nd Piola Kirchhoff stress at failure ranged from 1.80 ± 1.01 MPa for the stomach in the circumferential direction to 3.28 ± 1.54 MPa for the small intestine in the longitudinal direction. The overall stress-strain response for each organ indicated an increased resistance to stretch in the longitudinal direction compared to the circumferential direction, which is consistent with the expansion in circumference expected during digestion. Stress and strain response data quantified in this study provide new biomechanical data at loading rates useful for finite element impact simulations designed to evaluate crash-induced abdominal organ injury.

APPENDIX: Green-Lagrange strain-time histories and tabulated true stress and true strain results.

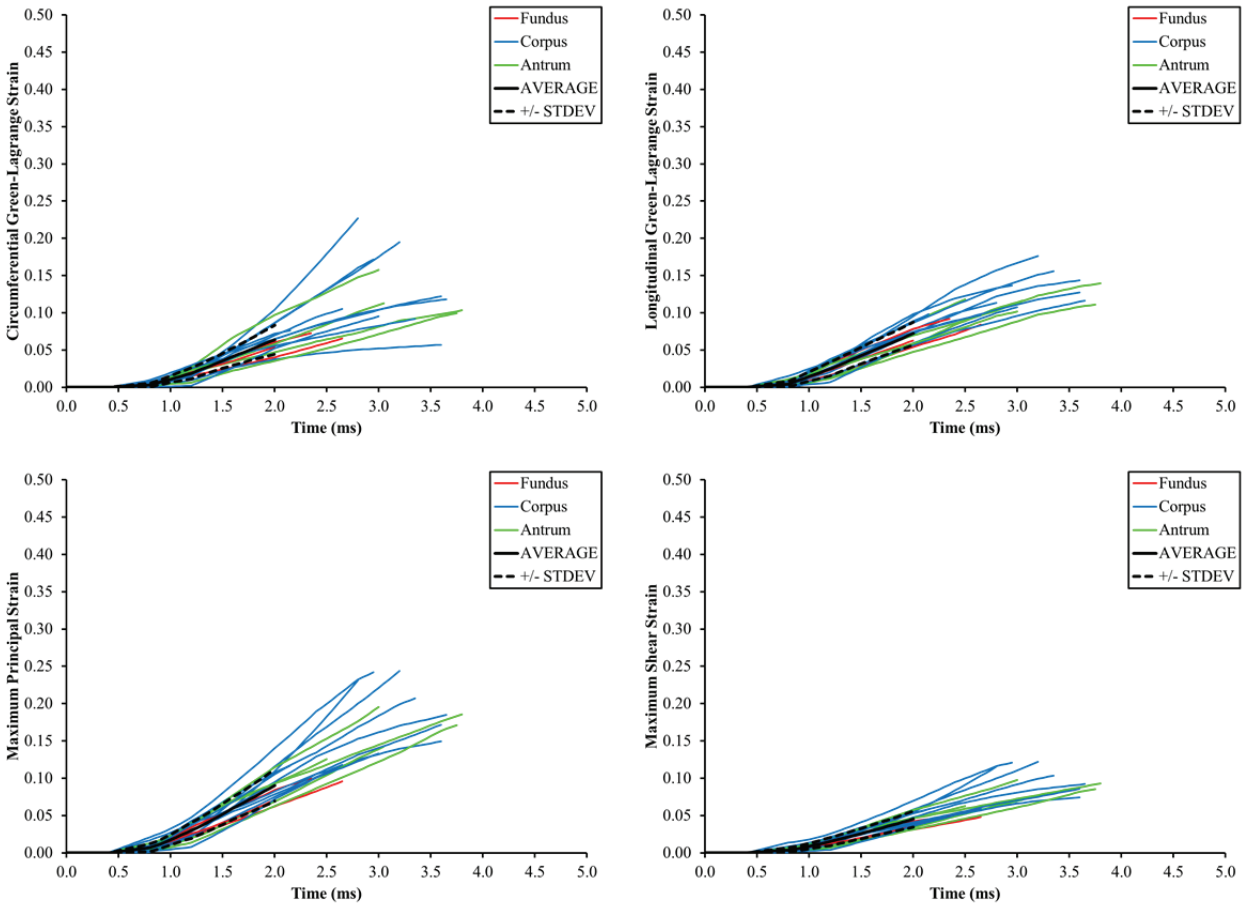

Figure 47: Green-Lagrange strain-time histories for 18 stomach samples.

Table 25: True strain at failure by region of the stomach.

Region	N	Circumferential Strain		Longitudinal Strain		p-value
		AVG	STDEV	AVG	STDEV	
Fundus	3	0.060	0.008	0.074	0.013	0.22
Corpus	10	0.111	0.043	0.113	0.020	0.88
Antrum	5	0.100	0.022	0.105	0.011	0.68
Total	18	0.099	0.038	0.104	0.022	0.64

Table 26: True stress at failure by region of the stomach (MPa).

Region	N	Circumferential Stress		Longitudinal Stress		p-value
		AVG	STDEV	AVG	STDEV	
Fundus	3	2.41	0.77	2.72	1.15	0.72
Corpus	10	2.30	1.31	3.39	1.99	0.17
Antrum	5	1.06	0.31	1.52	0.32	**0.05**
Total	18	1.97	1.16	2.76	1.72	0.12

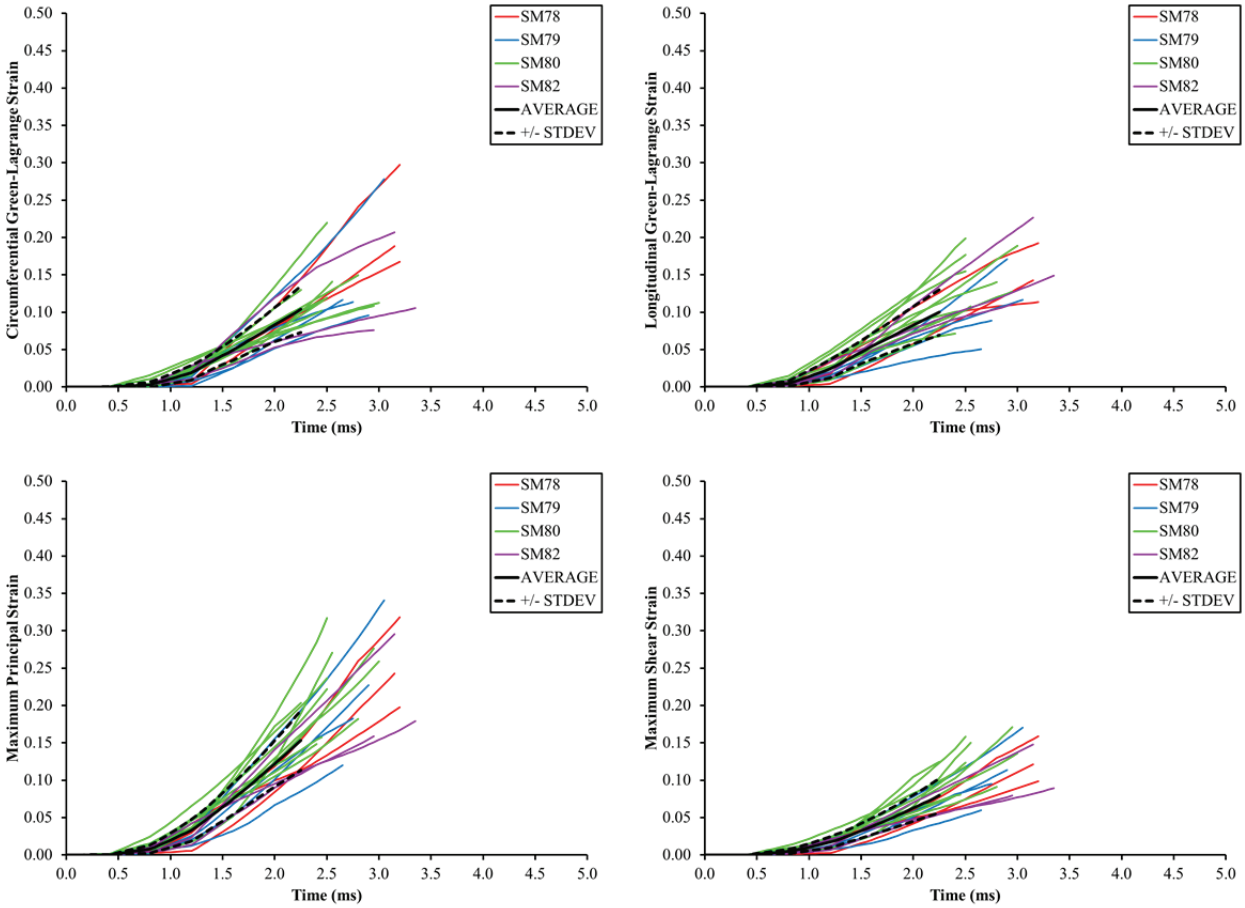

Figure 48: Green-Lagrange strain-time histories for 20 small intestine samples.

Table 27: True strain and true stress (MPa) at failure for the small intestine.

N	Circumferential Strain		Longitudinal Strain		p-value
	AVG	STDEV	AVG	STDEV	
20	0.127	0.044	0.119	0.037	0.50
N	Circumferential Stress		Longitudinal Stress		p-value
	AVG	STDEV	AVG	STDEV	
20	2.23	1.39	3.65	1.83	**0.01**

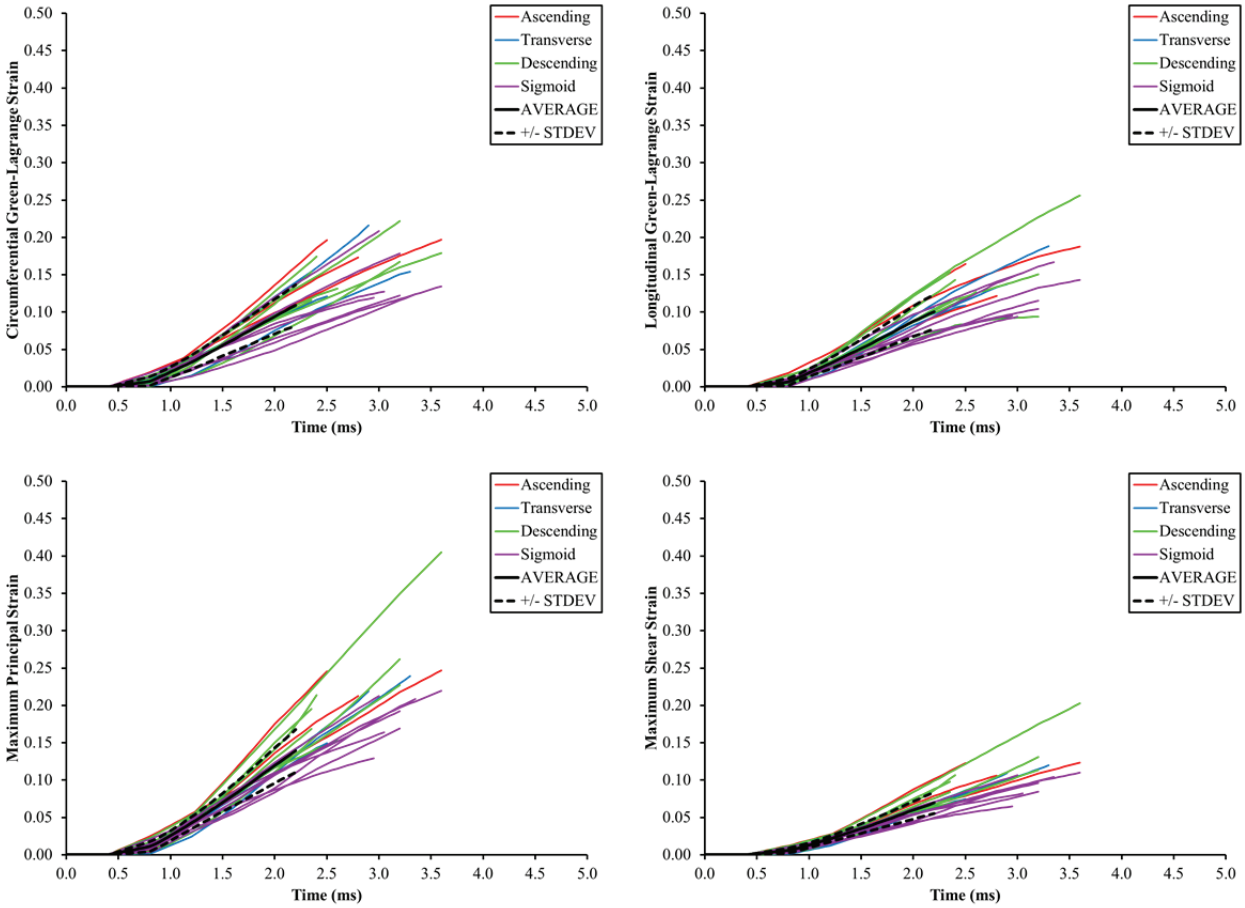

Figure 49: Green-Lagrange strain-time histories for 21 colon samples.

Table 28: True strain at failure by region of the colon.

Region	N	Circumferential Strain		Longitudinal Strain		p-value
		AVG	STDEV	AVG	STDEV	
Ascending	3	0.160	0.010	0.137	0.026	0.25
Transverse	4	0.130	0.037	0.119	0.029	0.67
Descending	7	0.141	0.026	0.129	0.038	0.50
Sigmoid	7	0.127	0.026	0.111	0.023	0.25
Total	21	0.137	0.027	0.122	0.030	0.10

Table 29: True stress at failure by region of the colon (MPa).

Region	N	Circumferential Stress		Longitudinal Stress		p-value
		AVG	STDEV	AVG	STDEV	
Ascending	3	4.14	0.84	4.49	1.33	0.73
Transverse	4	2.87	2.20	4.14	2.11	0.44
Descending	7	1.47	0.90	1.95	1.17	0.41
Sigmoid	7	3.39	1.55	4.74	1.87	0.17
Total	21	2.76	1.66	3.66	1.97	0.12

CHAPTER 4

Relative Position and Kinematics of the Thoracoabdominal Contents under Various Loading Scenarios

High-speed biplane x-ray was used to investigate the relative position and kinematics of the thoracoabdominal organs in response to blunt loading. The thoracic and abdominal organs of four post-mortem human surrogates were instrumented with radiopaque markers using a minimally invasive approach. Two cadavers were imaged in upright and inverted orientations, and the three-dimensional variation in the relative abdominal organ position between postures was quantified. These data were scaled and compared to positional MRI data from nine human subjects in seated postures and to the Global Human Body Models Consortium (GHBMC) 50th-percentile male model geometry. Each cadaver was then tested using crash-specific loading modes including frontal chest and abdominal impacts, as well as driver-shoulder seatbelt loading. Testing was conducted with each surrogate perfused, ventilated, and positioned in an inverted, fixed-back configuration. High-speed biplane x-ray was used to record the displacement of radiopaque internal organ markers throughout the tests. Marker positions were tracked using motion analysis software and projected into calibrated three-dimensional coordinates to obtain the marker positions and trajectories in response to blunt impact. Internal organ kinematics were quantified for the pericardium, lungs, diaphragm, liver, spleen, stomach, mesentery, and bony structures. These data can be used to better understand the interaction of anatomical structures during impact. Global response data in conjunction with local organ position and kinematics data can be applied to the development and validation of human body finite element models used to investigate injury mechanisms in motor vehicle collisions.

INTRODUCTION

Injuries to the thorax and abdomen are common consequences of motor vehicle collisions (MVCs). In frontal collisions, the chest is the most frequently injured body region at the AIS3+ severity level, and the prevalence of abdominal injuries increases with increasing injury severity (Elhagediab and Rouhana, 1998; Lee and Yang, 2002; Klinich et al., 2010). Numerous studies have investigated the response of the cadaver thorax and abdomen to blunt impact loading. Many organ injury mechanisms have been postulated for these regions; however, the internal organ kinematics of the thoracoabdominal contents in crash-specific loading scenarios have not been quantified. High-speed x-ray was used by Rouhana et al. (1986) to investigate the interface between the abdomen and impactor during blunt lateral impacts to New Zealand White rabbits. Additional studies investigating internal organ deformation or motion in response to loading have typically focused on a specific injury of interest, such as traumatic rupture of the aorta

(Hardy et al., 2008), or obtaining dynamic motion within a localized region such as the head (Hardy et al., 2007), cervical spine (Deng et al., 2000; Sundararajan et al., 2004), or knee (Tashman and Anderst, 2003). An understanding of the human internal organ response to regional abdominal loading would aid in the study of injury mechanisms by facilitating the design of better future experiments and the development of appropriate computational models to further investigate potential mechanisms including organ interaction, relative motion between structures, or stress-strain responses.

The use of full-body finite element (FE) models is becoming increasingly more prevalent for the evaluation of occupant protection in automotive environments (Yang et al., 2001). FE models of the human thorax have been continuously refined for the prediction of thoracic injury risk and the assessment of occupant restraint performance; yet experimental data are needed for the further development and validation of these models (Kent et al., 2008). Computational models have become of particular importance to abdominal organ injury mitigation because current anthropomorphic test devices lack the biofidelity, anatomical detail, and instrumentation to assess abdominal loading in simulated crash scenarios. However, existing models have typically been validated against external global loading conditions, with the local kinematics not specifically evaluated. As human body FE model complexity increases, local kinematics validation data at the organ level are needed to ensure accurate model response for the appropriate prediction of injury in simulated impacts.

The interpretation and translation of experimental results for use in FE model development and validation pose further challenges. FE model geometries are typically generated using human subject geometry obtained in the supine posture using imaging modalities such as computed tomography (CT) and magnetic resonance imaging (MRI). However, studies have shown postural variations in abdominal organ position of up to 40 mm for human subjects from the supine to the seated position (Beillas et al., 2009) and variations in organ location and morphology in the supine and seated postures for human subjects representing the 5^{th}, 50^{th}, and 95^{th}-percentile males and females (Hayes et al., 2013a; Hayes et al., 2013b). Additionally, FE model geometry does not correspond to the organ position and orientation present in cadavers during testing, and the relationship between cadaver organ geometry and FE model geometry is usually unknown. Variations between geometries could confound the ability to correlate injury prediction using models with organ damage that is observed in cadavers, resulting in discrepancies between the predicted areas of damage in the model and organ location in the cadaver.

The ways in which changes in posture affect the position of the internal organs, particularly the highly mobile and deformable abdominal contents, are important considerations for developing experimental test protocols. Traditionally, regional cadaver impact tests have been conducted with cadavers upright, or in a

nominal seated posture approximating the position expected of a vehicle occupant. Recent studies have conducted regional impact tests with the cadaver inverted in an attempt to adjust the relative positions of the internal organs into a more anatomical configuration (Hardy et al., 2006; Hardy et al., 2008). The rationale for inverting the cadaver is to counter post-mortem changes, including the lack of active musculature, by adjusting for the effect of gravity on these tissues. The results of the studies by Hardy et al. (2006; 2008) have shown that clinically-relevant internal organ injuries that had not been previously produced in a surrogate model can be generated by inverting the cadaver prior to impact, which alters the initial conditions of the test. Although these studies illustrate that cadaver organ position is critical to the occurrence and type of soft tissue damage induced during blunt impact, the effect of cadaver posture on organ position has not been quantified.

In this study, the three-dimensional variation in abdominal organ position was quantified in upright and inverted cadaver postures to improve the interpretation of both old and new experimental data for use in FE modeling. Knowledge of the relative position and orientation of the internal organs under different experimental conditions will aid in the translation of regional experimental data to impact simulations. In addition to appropriate organ position, correct model kinematics are necessary to investigate potential injury mechanisms related to organ interaction and relative motion between anatomic structures. In this study, impact loading was combined with high-speed biplane x-ray imaging to quantify internal organ kinematics in response to blunt impacts to the thorax and abdomen. This study was designed with the intent of providing data for FE model applications whereas previous experimental studies have been used retrospectively for model development or validation. Global force-deflection response data from this study can be used in conjunction with the local internal kinematics data to form an association between the internal and external responses. Further, the quantification of relative internal organ kinematics during blunt impact can be used to identify potential crash-induced injury mechanisms based on the structural interactions of the abdominal contents during impact.

METHODOLOGY

Surrogate Characteristics

Four unembalmed, previously frozen post-mortem human surrogates (PMHS) were instrumented in the thoracic and abdominal regions. Two PMHS were imaged in the abdominal region to examine the effects of posture on the relative position of the abdominal organs. All four PMHS were imaged using high-speed biplane x-ray to investigate internal organ motion in response to blunt impact. Table 30 summarizes the characteristics of each cadaver, and additional anthropometry measurements are included in Appendix A. All PMHS were male with an average age of 76 years, average stature of 180 cm, and average mass of 57

kg. The PMHS were selected to approximately match the 50th-percentile male in stature, with a lower mass to improve visibility using the imaging system.

Table 30: PMHS characteristics.

Test Region	PMHS	Gender	Age	Stature (cm)	Mass (kg)
Thorax	SM75	M	76	173	47
	SM81	M	72	188	54
Abdomen	SM72	M	73	185	53
	SM86	M	84	174	74
50th-Percentile*		M	38	175	77

*Schneider et al., 1983

Surrogate Preparation

Marker Placement. Radiopaque markers were implanted into skeletal structures and fixed within internal organs of the chest and abdominal cavities of each PMHS. This methodology is an extension of the techniques developed by Hardy et al. (2006; 2008). However, varying from the approach of Hardy et al. (2006; 2008), in this study the markers were fixed in locations throughout the organs of interest to obtain general organ kinematics for each test series. Markers were lead spheres applied with a minimally invasive approach to limit damage to the cadaver. Table 31 summarizes the instrumented organs and bony structures for each surrogate.

Table 31: Marker placement by organ for each PMHS.

Surrogate	SM75	SM81	SM72	SM86
Diaphragm	X	X	X	X
Pericardium	X			
Lungs	X			
Liver		X	X	X
Spleen				X
Stomach			X	X
Mesentery			X	X
Clavicle	X			
Spine	X	X	X	X
Sternum	X	X	X	X
Ribs	X	X		

All instrumentation was applied using sub-axillary and infra-xyphoid approaches. The thoracic cavity and mediastinum were accessed with a bilateral sub-axillary thoracotomy introducing minor damage to the lateral aspects of rib five. Markers 5 mm in diameter were sewn onto the right and left pericardium. Markers 2 mm in diameter were fixed in plastic helical anchors and inserted into the right and left lungs. The abdominal organs were accessed with a midline incision inferior to the xiphoid process. Markers 2 to

5 mm in diameter were stitched to the diaphragm, stomach, and mesentery (Figure 50). Diaphragm markers were positioned in an arc about the central tendon. Stomach markers were sewn into the body of the stomach, and mesentery markers were located along the jejunum. Circular washers of varying diameters were sewn to the stomach and mesentery with the lead spheres to aid in marker differentiation in two-dimensional x-rays.

Markers 2 mm in diameter were inserted and fixed within the parenchyma of the liver and the spleen. A small visceral incision and a custom guide tool were used to position the markers at the approximate mid-depth of the parenchyma of each organ. Markers were inserted into the liver to the right and left of the falciform ligament, spanning the width of the organ in the coronal plane. Due to organ size and location, markers were inserted into the parenchyma of the spleen in only two locations.

The bony structures of each surrogate were instrumented with 2-mm diameter markers. Skeletal markers affixed to the ribs, clavicles, and sternum were lead hemispheres mounted within brass washers. The skeletal structures were instrumented by first removing the soft tissue and periosteum at each marker location and drying the exposed bone before adhering marker assemblies directly to the bone. Marker triads were inserted into the vertebral bodies of each PMHS by drilling directly into the vertebrae in two locations. The triads served as fixed reference points for each surrogate. Marker positions within each organ and vertebral body were identified using supine anterior-posterior and lateral planar x-rays obtained prior to each test series (Figure 51).

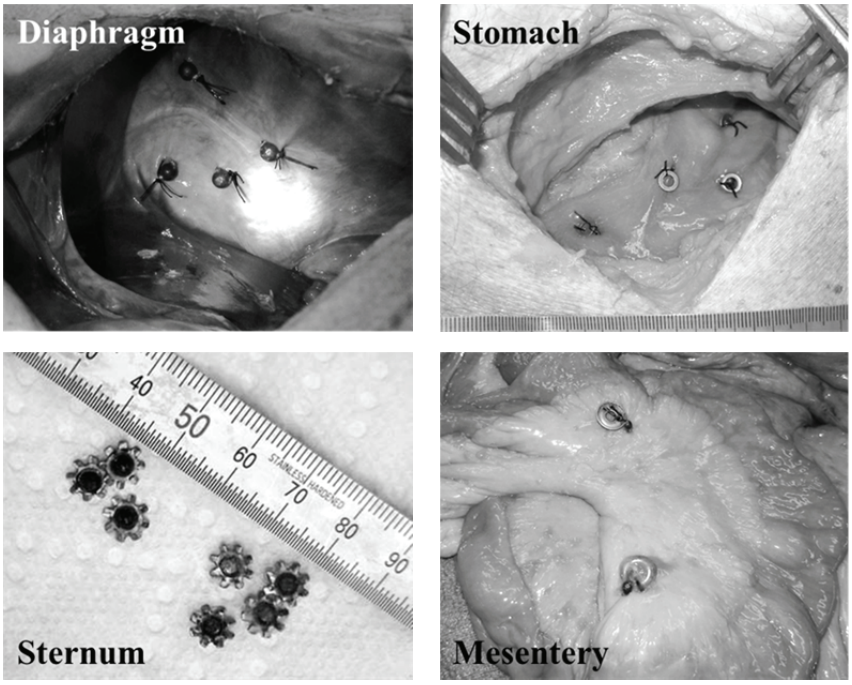

Figure 50: Radiopaque markers. §

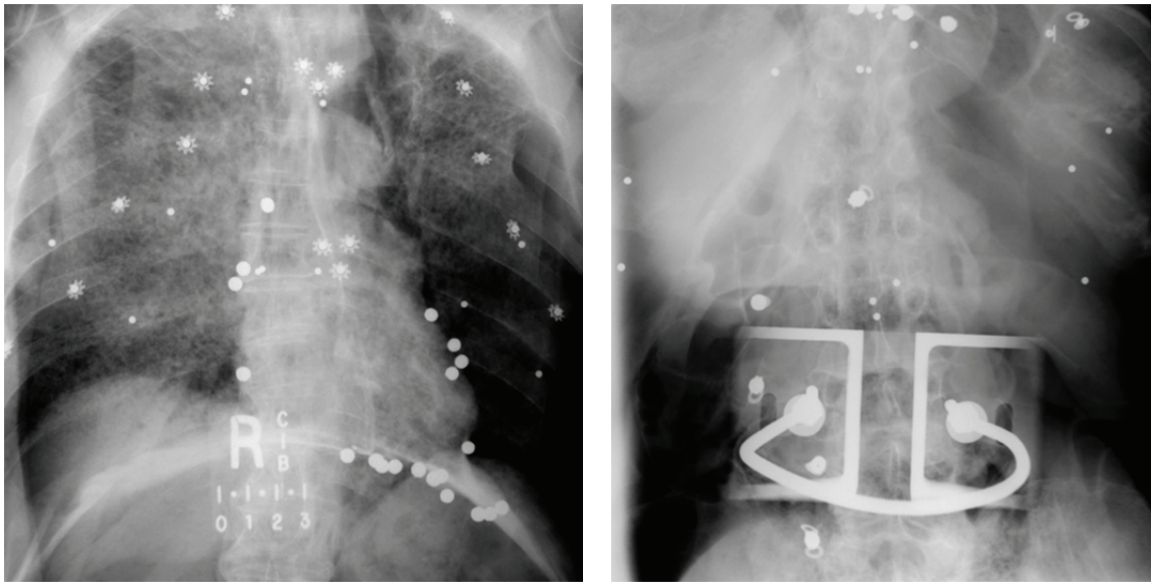

Figure 51: Supine planar x-rays of the instrumented cadaver thorax and abdomen. §

Spine Fixation. All tests in this study were conducted in a fixed-back configuration. The method of spine fixation was identical to that used by Foster et al. (2006) and Hardy et al. (2006; 2008). Rods were installed around the vertebrae in two locations (typically C5 and L3) using a minimally invasive approach through small dorsal incisions. The vertebrae were separated from the surrounding tissue with blunt dissection performed through the incisions at each location. The ventral aspect of each vertebra was detached from the surrounding tissue and vasculature with the exception of the anterior longitudinal ligament. The lateral processes at the location of the lumbar bracket were excised. Nylon webbing was inserted around the vertebrae and later used to position the PMHS using ratchet mechanisms. A 'U-shaped' rod was installed around the vertebrae, curving around the ventral surface of each vertebral body. Custom brackets were attached to each rod and tightened flush with the posterior aspect of the cadaver. The brackets were designed to mount to an acrylic support plate on a reinforced hanging fixture to maintain the position of the cadaver during imaging.

Physiologic Preparations. Traditionally, various procedures are implemented during PMHS preparation to improve the biofidelity of the test surrogates. In this study, each PMHS was prepared with bilateral ascending and descending perfusion entering into the neck and groin. Plastic tubing barbs were inserted and secured into the right and left common carotid arteries and jugular veins, as well as into the right and left femoral arteries and veins. 'T-shaped' compression fittings were attached to the tubing and barbs inserted into the vasculature in each location. For each surrogate, arterial and venous pressures were measured using Millar micro-tip pressure transducers. The transducers were fed to the heart, the liver via the vena cava, or the abdominal aorta using one branch of the 'T-shaped' fitting. The third branch of the

fitting was connected to the perfusion system, allowing fluid flow around the pressure transducer and through the vasculature. A centrifugal pump was used to perfuse the vasculature to near physiologic levels (7-14 kPa) with normal saline. Additionally, a tracheostomy was performed on each surrogate to provide access to the airways and lungs for inflation to 5-7 kPa immediately prior to impact.

Specific preparations were undertaken for surrogates tested in the abdominal region. The stomach of each PMHS was evacuated, sealed at the distal region, and filled with 500 mL of normal saline solution to simulate a more repeatable stomach configuration. Air introduced into the abdominal cavity during preparation was evacuated prior to closing the midline incision that provided access to the abdominal organs. Following closing, a port and vacuum tube were inserted into the lower left quadrant of the abdomen. This location was selected to prevent interaction with the impactor face during loading. Residual air in the abdominal cavity after closing was removed by pulling a vacuum through the port prior to testing.

Test Configurations

The test series in this study were categorized as either static positioning tests or dynamic impact tests. For all tests, each PMHS was imaged using a high-speed biplane x-ray system. The system consisted of two 80 kW x-ray generators and two 40-cm image intensifiers, each with a high-speed monochrome video camera (Phantom v9.1, Vision Research, NJ). The positions of the x-ray generators and image intensifiers were adjusted relative to the cadaver for each test. The operating values of the x-ray system were altered for each cadaver to obtain the best radiographic images of the implanted markers. High-speed video was recorded using a frame rate of 1000 to 1250 fps and an exposure of 200 μs. Visible light video (Phantom v9.1, Vision Research, NJ) was recorded from a lateral perspective for each of the dynamic tests.

All tests were conducted with the PMHS in a fixed-back configuration to prevent surrogate motion out of view of the x-ray system during the impact tests. To maintain spine position, surrogates were mounted to a stationary hanging fixture using the triangular spine brackets fixed around the vertebrae. The hanging fixture was a reinforced aluminum frame, and the spine brackets were designed to mate with a vertically-oriented acrylic support plate mounted to the frame. The positions of the cadaver and fixture were adjusted relative to the x-ray system for each test and relative to the impactor face for the dynamic tests.

Static Positioning Tests. Static tests were conducted using surrogates SM72 and SM86 to quantify the effects of cadaver orientation on the relative position of the abdominal organs. Images were obtained with each PMHS mounted to the support fixture in an upright posture, as well as following each stage of preparation: stomach filled to 500 mL, lungs ventilated, vacuum applied to the abdominal port, and the vasculature perfused to physiologic levels. The methods were applied in series such that the final stage of

preparation included the effects of each of the prior stages. The imaging procedure was repeated following each stage of preparation with the PMHS inverted. Marker locations in the final upright and final inverted positions were compared for each PMHS. Although implemented in both cadavers, the effects of each stage of the physiologic preparations were only quantified for SM86. Prior to altering the test position of each surrogate, imaging was performed using a distortion correction grid in each planar x-ray view. Each test had a unique calibration obtained using a rigid target frame imaged using the biplane x-ray system.

Dynamic Impact Tests. Tests were conducted using four PMHS that were subjected to four different fixed-back loading conditions as summarized in Table 32. Figure 52 shows a typical impact test configuration with the cadaver fixed in an inverted posture. Tests were conducted with the PMHS inverted with the purpose of adjusting the initial position of the thoracic and abdominal organs to a more anatomical configuration by reverting the effects of gravity on post-mortem soft tissue (Hardy et al., 2006; Hardy et al., 2008; Howes et al., 2013). Once positioned, the PMHS and the fixture were aligned with the linear impactor at the anatomic level of interest with the coronal plane of the PMHS parallel to the impactor face.

Impacts to the thorax and abdomen were designed based on the observations of Hardy et al. (2008) and Hardy et al. (2001a), respectively. The loading modes consisted of a 305-mm diameter, 37.5-kg rigid-disk impact at 6.7 m/s centered at the xiphoid process, a driver-side shoulder seatbelt applied at a target speed of 3.0 m/s, a 114-mm diameter, 32.2-kg cylinder impactor applied to the abdomen at 3.0 and 4.0 m/s without engaging the thorax, and a 25.4-mm diameter, 32.6-kg rigid-bar impact at 6.7 m/s centered at the mid-umbilicus (Table 32; Figure 53). The rigid-disk impact was intended to apply a distributed load to the thorax at a high impact severity to induce considerable motion of the internal organs. The peak loading rate of the seatbelt test was selected based on the results of Hardy et al. (2001a). Both thoracic tests were destructive; therefore, two PMHS were subjected to single thoracic loading modes. Each surrogate tested in the abdominal region was subjected to multiple impacts of increasing severity. The two initial abdominal impacts were non-injurious, designed to induce increasing magnitudes of organ motion within the abdominal cavity without engaging the thorax. The final test for each surrogate was designed as a destructive test to induce a considerable amount of marker excursion for the instrumented organs.

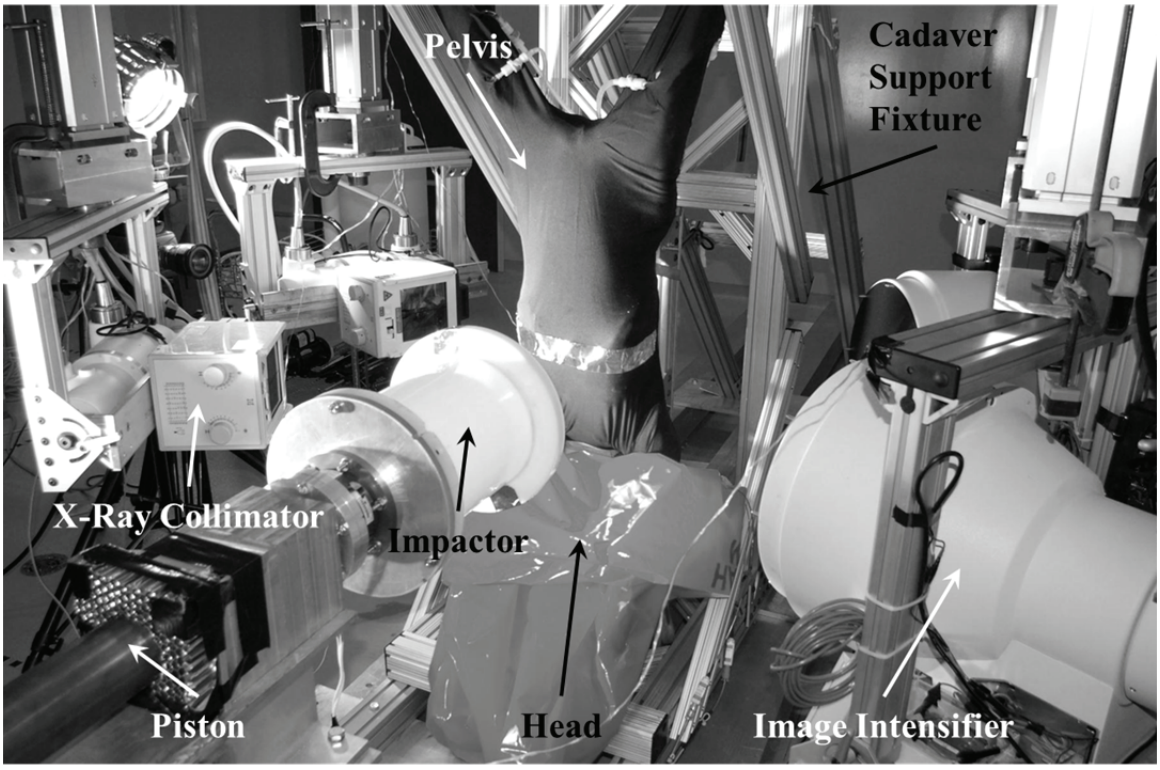

Figure 52: A typical frontal impact configuration using a 305-mm diameter impactor. §

Table 32: Test configurations.

PMHS	Region	Type	Location	Impactor Mass (kg)	Impactor Diameter (mm)	Target Velocity (m/s)	Nominal Stroke (mm)
SM75	Thorax	Rigid-Disk	Xiphoid Process	37.5	305	6.7	75
SM81	Thorax	Seatbelt	Driver-Shoulder	-	-	3.0	-
SM72	Abdomen	Cylinder	Mid-Umbilicus	32.2	114	3.0	50
		Cylinder	Mid-Umbilicus	32.2	114	4.0	50
		Rigid-Bar	Mid-Umbilicus	32.6	25.4	6.7	-
SM86	Abdomen	Cylinder	Mid-Umbilicus	32.2	114	3.0	50
		Cylinder	Mid-Umbilicus	32.2	114	4.0	50
		Rigid-Bar	Mid-Umbilicus	32.6	25.4	6.7	50

Rigid-Disk Impact at the Xiphoid Process
305-mm diameter impactor

Driver-Side Shoulder Seatbelt Test

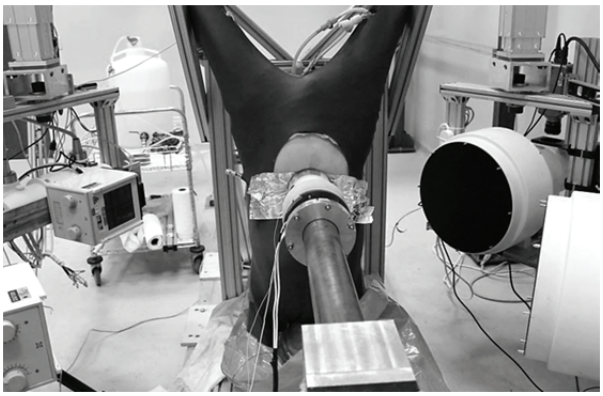

Cylinder Impact at the Mid-Umbilicus
114-mm diameter impactor

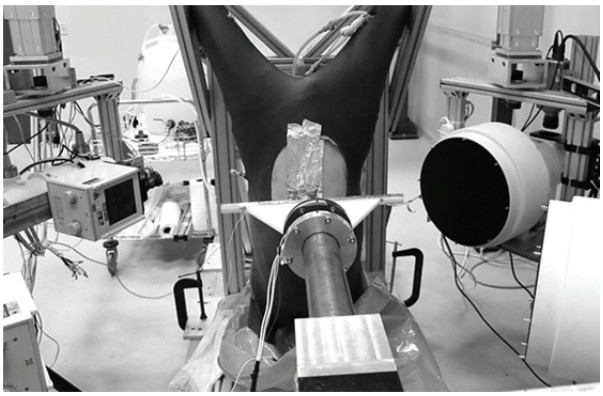

Rigid-Bar Impact at the Mid-Umbilicus
25.4-mm diameter impactor

Figure 53: Example test configurations for the four loading scenarios. §

For each impact test, the impactor decoupled from the piston rod prior to contact with the thorax or abdomen. The motion of the impactor was arrested after 75 mm of free-flight for the thoracic impact and 50 mm for the abdominal impacts by engaging Hexcel. Hexcel was engaged for an additional 25 mm for the thoracic impact for an overall impactor displacement of 100 mm. For the abdominal impacts, Hexcel was engaged for an additional 12 mm of travel for an overall impactor displacement of 62 mm for each impact. The SM72 rigid-bar impact test was the only test to deviate from the nominal piston stroke. A limited amount of Hexcel was engaged for this test and a greater overall impactor displacement resulted in maximal compression to the spine of the cadaver. Impact load and acceleration were measured using a 22.2-kN range load cell (1968-22.2kN, Denton, MI) and a 2000-g range accelerometer (7264B-2000g, Endevco, CA) for inertia compensation. Data were captured using 20 ksps.

The seatbelt apparatus was driven by a pneumatic linear impactor at a target peak belt speed of 3.0 m/s. A single strip of belt webbing was routed around the cadaver and through a system of rollers to the impactor face (Figure 54). The impactor was fired toward the posterior aspect of the cadaver and resulted in the

belt loading the anterior aspect of the cadaver from behind. Seatbelt webbing load cells (13.3-kN range) were located at the shoulder and anchor locations. Data were captured using 20 ksps. Lead markers were sewn onto the seatbelt webbing for x-ray tracking. Stripes marked on the webbing at 25.4-mm intervals indicated belt displacement in the visible light high-speed video.

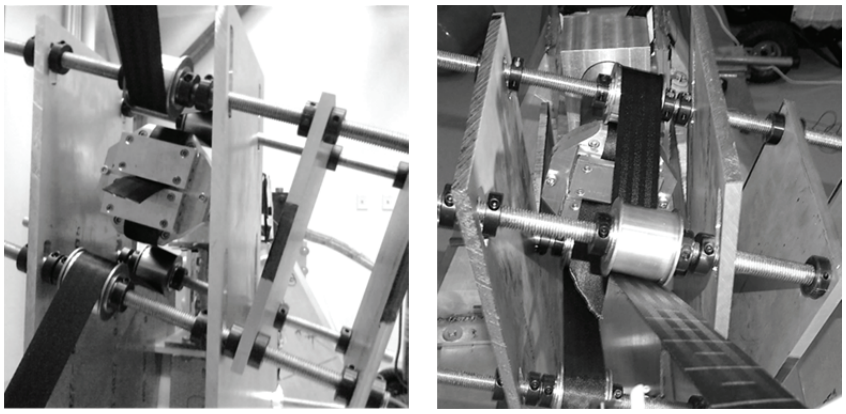

Figure 54: The seatbelt loading apparatus from lateral and superior perspectives. §

For each test configuration, distortion correction and calibration images were recorded using the x-ray system prior to altering the experimental setup.

Data Reduction and Analysis

Impact Response, Filtering, and Scaling. Impactor load, acceleration, velocity, and displacement, and arterial and venous pressures were quantified for each test. Measured acceleration was used for inertial compensation of the impactor load. Belt loads measured in two locations were summed for the seatbelt test. All loads were filtered and presented using SAE J211 Channel Frequency Class (CFC) 600 Hz and 180 Hz (SAE, 2007). Impactor speed and deflection were determined using the measured acceleration. For the seatbelt test, belt penetration was determined using visible light video for optical tracking of a three-dimensional seatbelt marker initially positioned approximately at the level of the xiphoid process. Belt speed was determined as the derivative of the seatbelt deflection measured at the xiphoid process. Belt speed and deflection were filtered using CFC 60 Hz. The rate of penetration of the seatbelt would vary at other contact locations, as the nature of the interaction is different and includes greater relative sliding away from the rib cage. Arterial and venous pressure-time histories were filtered using CFC 600 Hz. Peak results were tabulated for all tests.

Equal-stress/equal-velocity scaling (Eppinger, 1976) was used to scale the load and penetration for each test that resulted in injury to the cadaver. The results were scaled for the purpose of examining Injury Assessment Reference Values (IARVs) within the context of injury, and therefore, results from tests designed to be well below injury thresholds were not scaled. Equal-stress/equal-velocity scaling is a

volumetric scaling method assuming geometric similitude between subjects, as well as constant modulus of elasticity and constant density. This method assumes a linear relationship between the mass of each subject such that the mass scale factor is found by dividing the representative mass by the subject mass. Based on the assumption of constant density, the length scale factor is the mass ratio raised to the one-third power. To maintain constant modulus of elasticity, the load scale factor is equal to the square of the length scale factor. Peak load and peak penetration data are presented as both scaled and raw values.

Injury Criteria. Injury metrics were calculated using equal-stress/equal-velocity scaled data and peak response data. The representative mass used to scale the data was 78.2 kg, based on the mass of a Hybrid III 50th-percentile male dummy. Peak load was obtained prior to Hexcel contact for the impact tests and from scaling the summed load for the seatbelt test. Peak penetration was determined as the maximum of the double-integrated impactor acceleration data. Peak compression (Cmax) was obtained by dividing the raw peak penetration by the initial external anterior-posterior chest depth measured at the approximate level of the xiphoid process, or by the initial anterior-posterior abdominal depth measured at the level of the umbilicus, to the opposing spinous processes as determined via palpation. Peak penetration speed was determined as the maximum of the integrated impactor acceleration data. Peak response data were used to calculate impact energy (Fmax*Cmax) (Rouhana et al., 1987) and Abdominal Injury Criterion (Vmax*Cmax) (Rouhana et al., 1985). V*C was calculated from the penetration speed, determined from the differentiation of the penetration, and the compression.

Image Processing

Following each x-ray imaging sequence, distortion correction was applied to each planar view using a custom algorithm. Additionally, the three-dimensional relationship between the x-ray heads and the image intensifiers was calibrated, and the calibration was applied to each camera view using image enhancement and target tracking software (TEMA, Image Systems, Linköping, Sweden). For each test, marker locations were tracked in the planar views from both high-speed cameras, and the three-dimensional coordinates for each marker were determined as the intersection of ray projections of each point from the planar perspectives.

Coordinate System Transformation. The origin of the anatomic coordinate system for each cadaver corresponded to the anterior, superior aspect of T10 at the midline of the vertebra. Supine anterior-posterior and lateral planar x-rays of the spine, thorax, and abdominal region were used to determine the location of the spine marker triads fixed within the vertebrae with respect to the anatomic coordinate system. Marker locations obtained in three dimensions were transformed from the global positions to the anatomic coordinate system using the body-fixed basis in the spine. The approach was similar to the

methodology used by Padgaonkar (1976). For the seatbelt test, transverse plane rotation was used to translate global position data to the anatomic coordinate system. Transverse plane rotation was achieved by using laboratory references to identify the angle between the cadaver and the global coordinate system. Targets on bony landmarks were then used to translate the origin of the anatomic coordinate system to align with T10 as in the static positioning tests and the impact tests. All data were output in the anatomic coordinate system with the X-direction positive from posterior to anterior, the Y-direction positive from right to left, and the Z-direction positive from caudal to cranial. This coordinate system was selected such that marker motion in the anatomically cranial direction was positive.

Data Comparisons, Scaling, and Mapping. Organ position data from cadavers SM72 and SM86 in upright and inverted postures, and additional diaphragm position data from SM75 and SM81, were compared to human subject MRI data obtained in an upright seated posture (Beillas et al., 2009) and to the Global Human Body Models Consortium (GHBMC) model. The GHBMC model is a 50^{th}-percentile male, also positioned in an upright seated posture. Dimensions for each subject and model are included in Appendix B (Table 40).

Beillas et al. (2009) presented data from nine human subjects imaged in the sagittal plane using an upright MRI scanner. The subjects were positioned in an occupant posture using a custom seat with a seat back angle of 25 degrees from the vertical axis and a seat pan angle of 9 degrees from the horizontal axis. Scan data were acquired using 5 mm slices with a resolution of 256 x 256 pixels and a pixel size of 1.56 x 1.56 mm. Following scan data acquisition, a custom registration process was applied to deform a reference triangular mesh to match the imaging dataset for each human subject using a series of successive geometric transformations of the model. Data from the current study were mapped to each of the nine transformed models corresponding to each seated human subject as described herein. All data and models were translated and rotated to align with the origin of the anatomic coordinate system (the anterior-superior aspect of T10 at the midline) prior to comparison.

The data from each of the studies were scaled using two methods: equal-stress/equal-velocity scaling (Eppinger, 1976) and scaling by stature. To scale using the equal-stress/equal-velocity method, the mass scale factor was first found by dividing the representative mass of the GHBMC model (78.5 kg) by the subject mass. Based on the assumption of constant density, the length scale factor was defined as the mass ratio to the one-third power. The length scale factor was applied to the data in the X-, Y-, and Z-directions. The data were also separately scaled by stature, with the scale factor determined as the ratio of the GHBMC model height (1.75 m) to the subject height, and applied in all three dimensions. Scale factors are provided in Appendix B (Table 41).

Diaphragm and liver position for each cadaver in the upright and inverted postures was compared to the GHBMC model using the scaled and non-scaled data. Internal organ markers for each cadaver were mapped to a corresponding node on the model. Nodes were selected in reference to marker positions identified using supine anterior-posterior and lateral planar x-rays, in conjunction with pre-test images captured during marker placement. Therefore, the nodes were selected functionally and not in reference to marker position relative to T10. For the liver, nodes corresponding to the marker locations were related to the model surface on two sides. Node positions were found along the diaphragmatic surface of the liver, and then projected along the Z-direction to the appropriate height within the structure. Nodes were selected to match marker placement in the sagittal plane by approximating the mid-depth of the liver parenchyma in each location. For the human subjects, only diaphragm marker positions were compared. The same procedure was used to map the diaphragm marker positions in the cadavers to corresponding nodes of the human subject mesh. A set of nodes was selected in reference to the marker positions from each cadaver using one of the human subject mesh geometries. Identical node numbers were then used to compare cadaver marker position to each human subject.

The X-, Y-, and Z-directional differences of the PMHS marker positions from the corresponding mesh nodes were determined for each marker in both the upright and inverted cadaver postures. Differences were then averaged in each direction for all subject comparisons to each cadaver organ, and the standard deviations were calculated. The vector magnitude from each marker-to-node comparison was averaged for all of the markers in each organ.

Motion Analysis. For each of the dynamic tests, marker trajectories were obtained in three-dimensions using the target tracking software. Not all targets were visible in both planar views for every test, and some targets were only in view for portions of the tests due to the limited viewing area of the image intensifiers. No attempt was made to fill gaps in the three-dimensional motion analysis data. Coordinate system transformation was applied to transform all marker positions to the anatomic coordinate system. All tests were fixed-back tests such that the vertebral body marker triads were stationary within the fixed spine; however, in some of the tests, minimal spine motion occurred during peak penetration. Any global motion of the spine markers that occurred was subtracted from the global motion of the internal organ markers following transformation to the anatomic coordinate system. Marker trajectories were filtered using a 50 Hz 4^{th} order Butterworth filter, corresponding to a (pseudo) Channel Frequency Class 30 Hz filter (Hardy et al., 2001b). This filter profile was found not to alter the peak deflections while preserving all important shape characteristics.

RESULTS

Static Positioning Tests

Effects of Preparation. The change in position of the internal organs at each stage of preparation was quantified in the upright posture for SM86 (Figure 55-Figure 57; Appendix B, Table 44-Table 48). Due to the limited viewing area of the image intensifiers and the larger size of this cadaver, only the diaphragm and liver markers were within the viewing range with the PMHS upright. For these organs, the predominant change in marker position during preparation was caudal in direction, with an average magnitude of change of 23 mm in the superior-inferior direction for all markers from the initial to the final position. Filling the stomach resulted in the greatest lateral change of 7 mm in the Y-direction on average, and ventilation had the greatest effect in the Z-direction with an average change of 13 mm.

The change in position of the internal organs at each stage of preparation was also quantified for SM86 in the inverted posture with an average change in position between the initial and final conditions of 11 mm (Figure 55-Figure 57; Appendix B, Table 49-Table 52). The initial state for the inverted cadaver was with a known stomach volume of 500 mL. For the inverted orientation, ventilation and perfusion had the greatest effects on marker position. In general, markers shifted anterior and superior with ventilation and vacuum application and posterior and inferior with perfusion. However, a different pattern was observed for markers implanted in the right lobe of the liver, which moved inferior with ventilation of the lungs. Vacuum application resulted in an anatomically cranial shift in marker position toward the diaphragm with the PMHS inverted. It should be noted that the changes due to cadaver preparation were small in comparison to the changes in position occurring from the upright to the inverted postures.

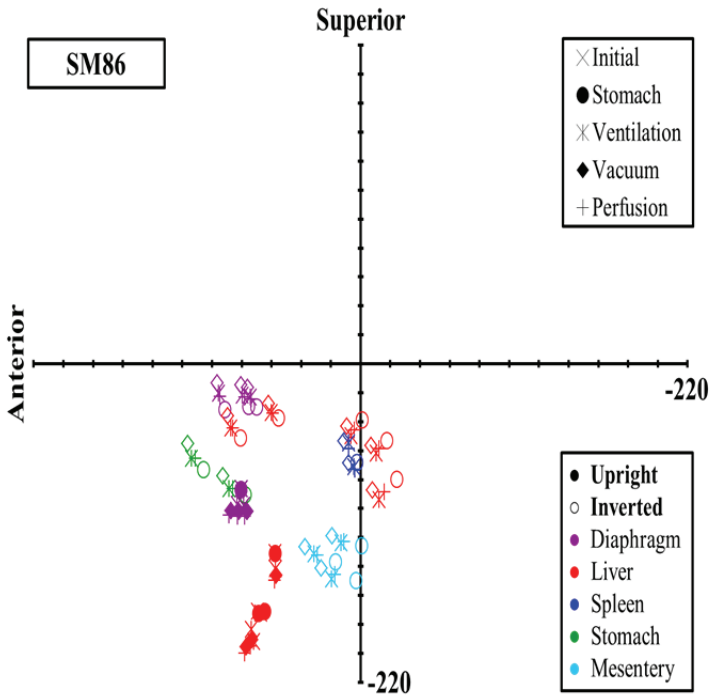

Figure 55: Change in marker position in the sagittal plane during preparation. Scale is mm. Data are not scaled.

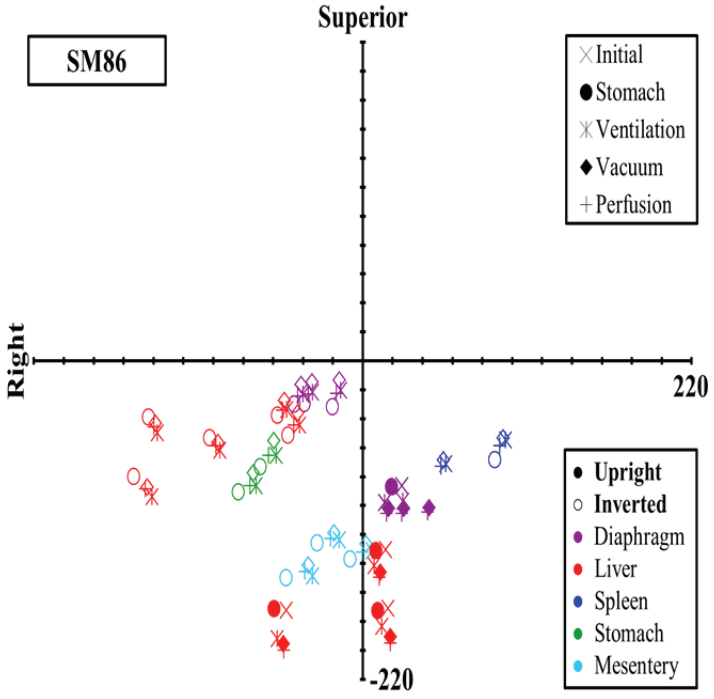

Figure 56: Change in marker position in the coronal plane during preparation. Scale is mm. Data are not scaled.

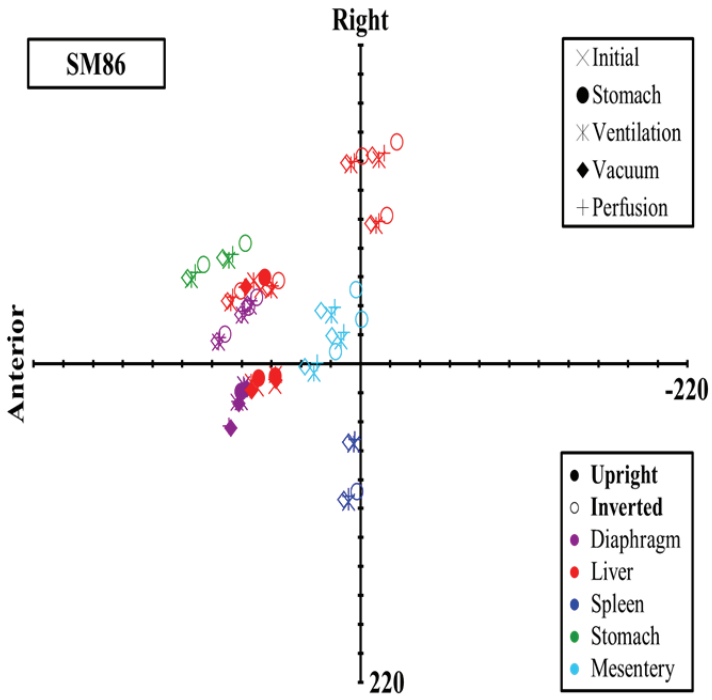

Figure 57: Change in marker position in the transverse plane during preparation. Scale is mm. Data are not scaled.

Effects of Posture. The marker positions in the final upright and final inverted orientations were directly compared for each cadaver (SM72 and SM86) with no scaling applied (Figure 58). Position data for each test are tabulated in Appendix B (Table 42-Table 52). Compared to the upright position, when inverted the organs shifted cranially and the separation between markers in the Z-direction decreased. In the inverted posture, all markers in the diaphragm and liver fell within 66 to 81 mm of one another in the Z-direction, whereas in the upright orientation, the most cranial and caudal markers of the diaphragm and liver ranged from 95 mm to 169 mm in separation in the Z-direction. In the transition from the upright to inverted posture, there was a lateral shift in diaphragm position to the opposite side of the midline for both PMHS. The relative change in position of the diaphragm markers, determined as the average of the vector magnitudes calculated for each marker from the upright to the inverted posture, was 106 mm. The relative change in liver marker position from the upright to the inverted posture was 137 mm, on average.

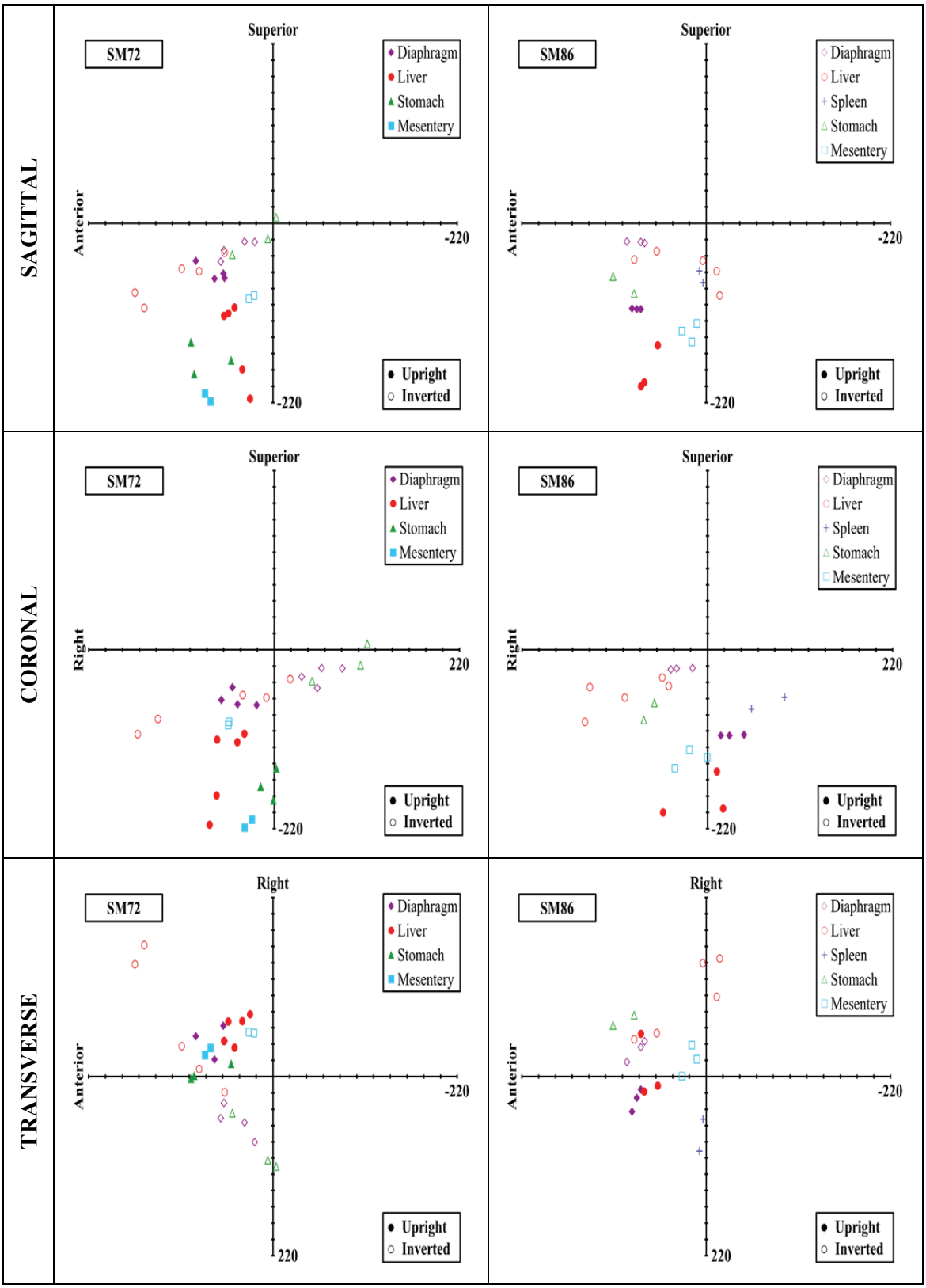

Figure 58: Upright and inverted marker positions with the origin at T10.

Scale is mm. Data are not scaled.

Table 33 lists the magnitude and direction of the change in marker position that occurred in the transition from the upright to the inverted posture. Marker displacement varied in magnitude and direction within an organ. For example, Table 33 shows for SM72 that the change in position of liver markers 03 and 05 was anterior and superior in direction for both markers but was considerably greater in magnitude for marker 05. In the lateral direction, displacement was 31 mm toward the left for liver marker 03 and 85 mm toward the right for liver marker 05. Alternatively, the displacement of liver marker 04 was in the same direction as 05, but with differences in magnitude of 2, 15, and 17 mm in the X-, Y-, and Z-directions, respectively. The separation between both pairs of markers shortened in the Z-direction and increased in the X- and Y-directions when inverted. Additionally, the vector magnitudes between marker pairs differed for the upright and the inverted postures. For example, the vector magnitude between liver markers 03 and 05 was 108 mm in the upright position and 141 mm in the inverted position. The vector magnitude between liver markers 04 and 05 was 38 mm in the upright position and 32 mm when inverted.

Table 33: Directional differences in marker position from the upright to the inverted posture.

	Marker	X (mm)	Y (mm)	Z (mm)
SM72	Diaphragm01	-29.6	100.9	-1.0
	Diaphragm02	-0.4	95.0	28.7
	Diaphragm03	-24.0	100.0	44.5
	Diaphragm04	-47.9	101.5	45.2
	Liver01	11.6	54.6	67.1
	Liver02	29.7	34.5	54.7
	Liver03	55.5	30.5	54.8
	Liver04	128.1	-69.9	94.0
	Liver05	126.5	-85.2	111.4
	Stomach01	-101.6	108.0	153.6
	Stomach02	-1.5	60.9	129.4
	Stomach03	-87.9	103.5	166.3
	Mesentery01	-52.5	-28.3	115.9
	Mesentery02	-51.7	-18.5	130.0
SM86	Diaphragm01	6.2	-61.0	82.3
	Diaphragm02	-4.8	-62.7	82.3
	Diaphragm03	-4.4	-59.4	81.2
	Liver01	11.8	-64.3	150.5
	Liver02	1.2	-65.0	115.3
	Liver03	-73.9	-86.9	154.6

Considering the liver of both cadavers, with the PMHS in the upright posture the position of the liver markers covered a greater range in the superior-inferior direction and less in the anterior-posterior and lateral directions compared to the inverted posture (Table 34). For SM72 the difference in the Z-direction

between the most cranial and most caudal markers was 112 mm in the upright posture versus 68 mm in the inverted posture. The range in the Y-direction between the furthest lateral markers was 41 mm versus 181 mm for the upright and inverted postures, respectively. This range accounts for the furthest separation between markers in each direction, which may not be the separation between the same two markers in all directions.

Table 34: Range covered by the liver markers.

PMHS	Posture	X (mm)	Y (mm)	Z (mm)
SM72	Upright	31.1	41.2	111.9
	Inverted	107.0	181.0	67.6
SM86*	Upright	20.1	71.0	50.6
	Inverted	82.0	93.6	11.3

*Only liver makers 01, 02, and 03 included.

Data Comparisons. Data for the comparisons between the cadavers, human subjects, and model are summarized in Appendix B (Table 53-Table 55). The overall vector magnitude between the PMHS diaphragm and the human subject diaphragm was lower for the inverted cadaver posture compared to the upright cadaver posture (Table 53). For equal-stress/equal-velocity scaled data, the difference in magnitude was 73 mm on average for the inverted diaphragm and 106 mm on average for the upright diaphragm. Differences in the Y-direction (right-left) were generally greater than differences in the X-direction (posterior-anterior) for both postures. On average, the Z-directional differences were equal in magnitude for the upright and inverted postures, but opposite in direction (± 27 mm for equal-stress/equal-velocity scaled data).

Similar trends were found when comparing the diaphragm and liver position for the PMHS and the GHBMC model (Table 54-Table 55). For both organs, the mean distance between the PMHS and model was lower on average for the inverted cadaver posture compared to the upright posture. On average, the directional differences were considerably greater for the upright posture compared to the inverted posture for the diaphragm in all directions and for the liver in the Z-direction.

Scaling the data using the different metrics did not result in considerable differences. Stature scaled data showed similar trends compared to the equal-stress/equal-velocity scaled data. However, for the stature scaled data, the average mean distances between the cadaver organs and the human subject and model organs were generally slightly lower for both PMHS postures compared to the equal-stress/equal-velocity scaled data. This was also true for the Z-directional differences in organ position.

Impact Response

Eight tests were conducted using four whole human cadavers. Response parameters and calculated injury metrics for each impact test are included in Table 35, Table 37, and Table 38. Results are presented as the peak response and as the arrested response, corresponding to the peak response prior to the impactor contact with the Hexcel. Peak results for the seatbelt test are presented in Table 36. Tabulated data were filtered using CFC 600 Hz unless otherwise specified. Response-time histories from each test are provided in Appendix C (Figure 75-Figure 82). The load-penetration response curves for each test are shown in Figure 59-Figure 62. The vertical line (denoted Hexcel Contact) indicates the degree of chest deflection or abdominal penetration at the time of Hexcel contact for each impact. Corridors are shown in Figure 60 for single diagonal seatbelt loading (Kent et al., 2004) and in Figure 62 for free-back rigid-bar tests at 6 m/s (Hardy et al., 2001a).

Table 35: Response data for the SM75 thoracic rigid-disk impact test.

Parameter	Arrested/Peak	CFC	Units	Raw	Scaled
Penetration Speed	Peak Response	-	m/s	6.57	-
Penetration	Hexcel Contact	-	mm	76.94	91.17
	Peak Response	-	mm	108.96	129.11
Impactor Load (Fmax)	Hexcel Contact	600Hz	kN	3.62	5.08
Arterial Pressure	Hexcel Contact	600Hz	kPa	32.14	-
	Peak Response	600Hz	kPa	40.74	-
Venous Pressure	Hexcel Contact	600Hz	kPa	74.91	-
	Peak Response	600Hz	kPa	74.91	-
Compression (Cmax)	-	-	-	0.43	-
Energy (Fmax*Cmax)	-	600Hz	N	1.54	2.17
AIC (Vmax*Cmax)	-	-	m/s	2.81	-
V*C	-	-	m/s	1.78	-

Table 36: Peak results for the SM81 driver-side shoulder seatbelt test.

Parameter	CFC	Units	Raw	Scaled
Penetration Speed	60Hz	m/s	3.31	-
Penetration	60Hz	mm	119.63	135.35
Shoulder Load	600Hz	kN	2.58	3.30
Anchor Load	600Hz	kN	2.23	2.85
Summed Load	600Hz	kN	4.81	6.16
Arterial Pressure	600Hz	kPa	105.93	-
Venous Pressure	600Hz	kPa	83.62	-
Compression (Cmax)	-	-	0.50	-
Energy (Fmax*Cmax)	600Hz	N	2.39	3.06
AIC (Vmax*Cmax)	60Hz	m/s	1.64	-
V*C	-	m/s	1.08	-

Table 37: Response data for the SM72 abdominal impact tests.

				SM72-1	SM72-2	SM72-3	
Parameter	**Arrested/Peak**	**CFC**	**Units**	**Raw**	**Raw**	**Raw**	**Scaled**
Penetration Speed	Peak Response	-	m/s	3.03	4.20	6.64	-
Penetration	Hexcel Contact	-	mm	51.55	57.69	108.35	123.35
	Peak Response	-	mm	60.40	75.52	124.55	141.79
Impactor Load (Fmax)	Hexcel Contact	600Hz	kN	0.68	1.02	10.44	13.53
Arterial Pressure	Hexcel Contact	600Hz	kPa	7.15	7.77	37.39	-
	Peak Response	600Hz	kPa	10.76	17.47	47.19	-
Venous Pressure	Hexcel Contact	600Hz	kPa	12.43	20.66	46.54	-
	Peak Response	600Hz	kPa	15.05	31.69	-	-
Compression (Cmax)	-	-	-	0.37	0.46	0.76	-
Energy (Fmax*Cmax)	-	600Hz	N	0.25	0.47	7.98	10.34
AIC (Vmax*Cmax)	-	-	m/s	1.12	1.95	5.07	-
V*C	-	-	m/s	1.13	1.45	3.36	-

Table 38: Response data for the SM86 abdominal impact tests.

				SM86-1	SM86-2	SM86-3	
Parameter	**Arrested/Peak**	**CFC**	**Units**	**Raw**	**Raw**	**Raw**	**Scaled**
Penetration Speed	Peak Response	-	m/s	4.28	3.50	6.70	-
Penetration	Hexcel Contact	-	mm	48.00	69.46	65.12	66.33
	Peak Response	-	mm	71.28	84.09	82.26	83.79
Impactor Load (Fmax)	Hexcel Contact	600Hz	kN	0.83	0.82	2.05	2.12
Arterial Pressure	Hexcel Contact	600Hz	kPa	34.77	47.44	54.46	-
	Peak Response	600Hz	kPa	62.62	74.19	122.06	-
Venous Pressure	Hexcel Contact	600Hz	kPa	0.95	2.85	0.84	-
	Peak Response	600Hz	kPa	5.39	5.96	10.37	-
Compression (Cmax)	-	-	-	0.33	0.39	0.38	-
Energy (Fmax*Cmax)	-	600Hz	N	0.28	0.32	0.79	0.82
AIC (Vmax*Cmax)	-	-	m/s	1.43	1.38	2.58	-
V*C	-	-	m/s	0.98	1.04	1.89	-

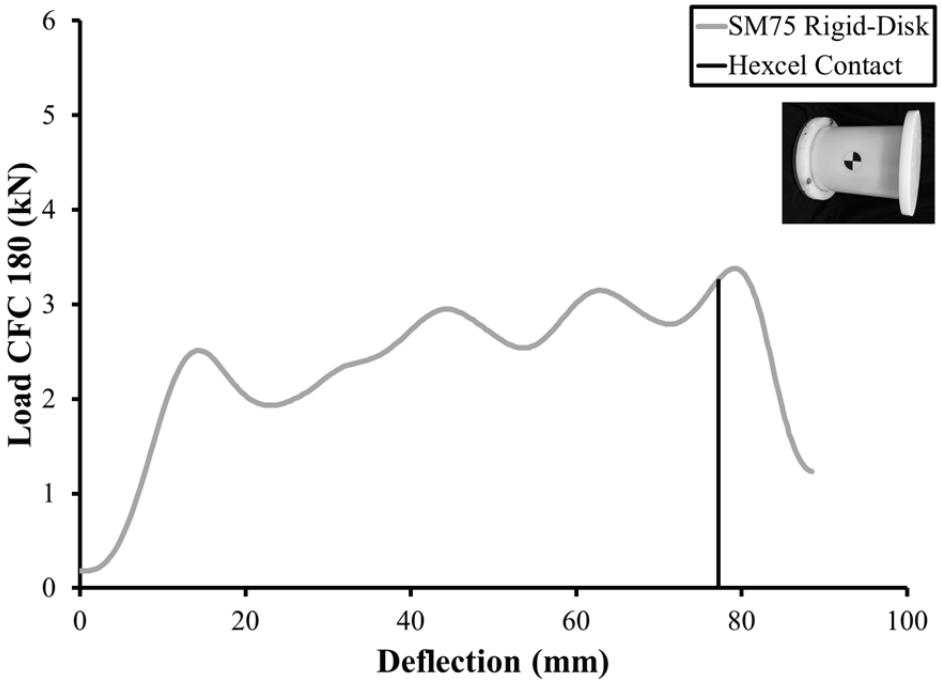

Figure 59: Force-deflection response for the 6.7 m/s thoracic rigid-disk impact.

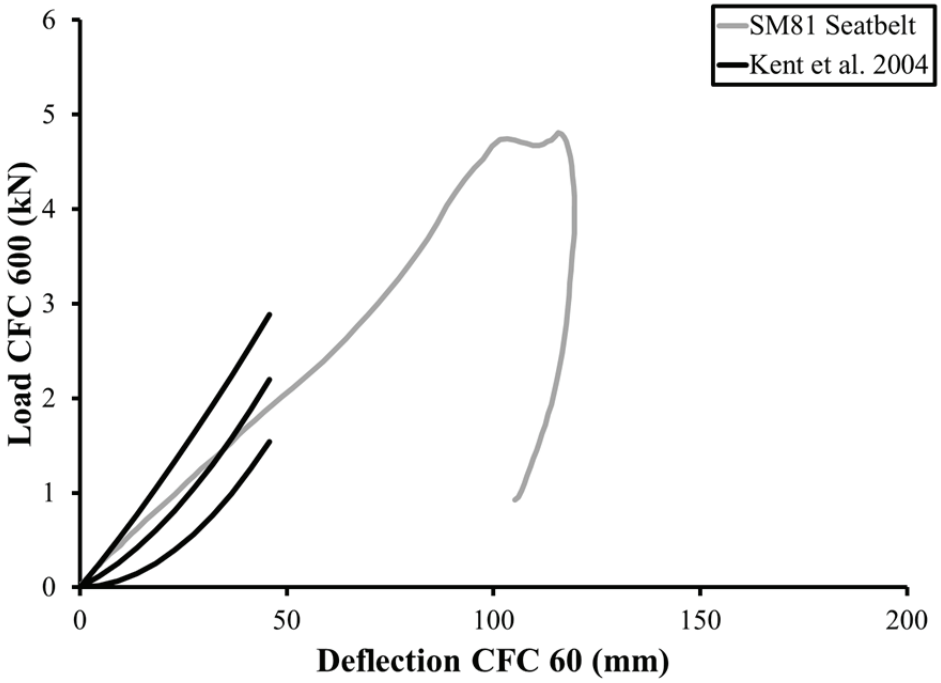

Figure 60: Force-deflection response for the 3.0 m/s seatbelt test.

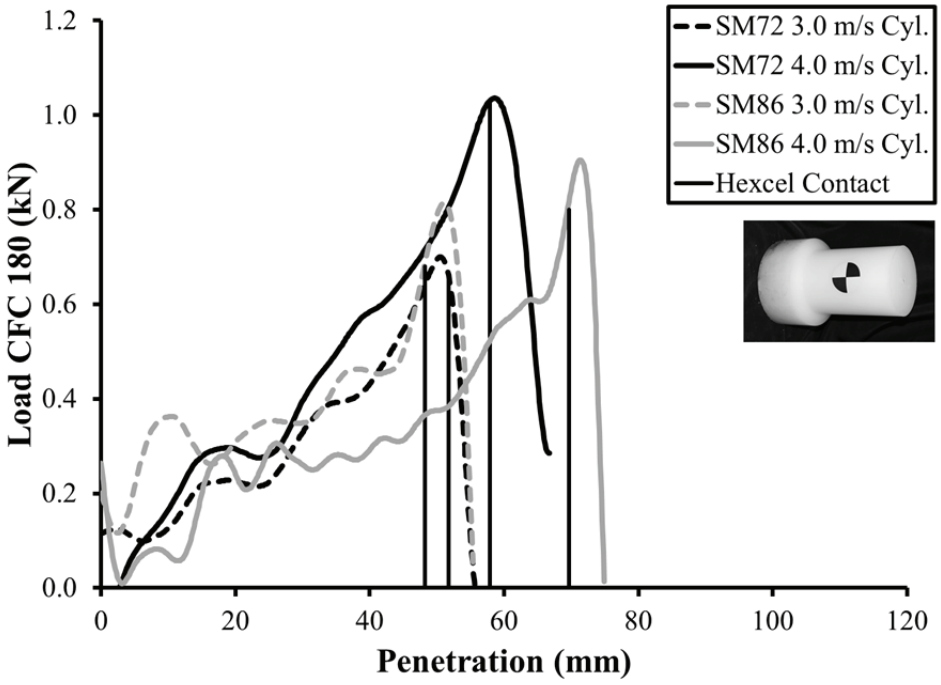

Figure 61: Load-penetration response for the abdominal cylinder impacts at 3.0 m/s and 4.0 m/s.

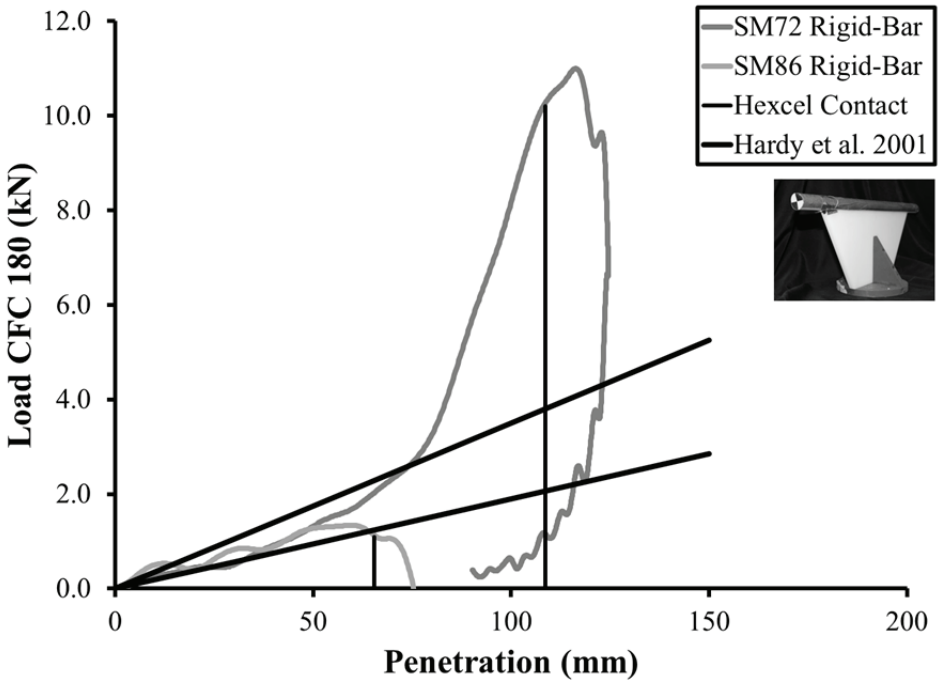

Figure 62: Load-penetration response for the 6.7 m/s abdominal rigid-bar impacts.

Injury Response

The thoracic rigid-disk impact, seatbelt test, and abdominal rigid-bar impacts generated damage to the cadavers. A summary of the autopsy findings for each cadaver is included in Table 39. The main findings were multiple rib fractures in all test series, as well as sternum fractures occurring in the thoracic rigid-disk impact test and seatbelt test. The seatbelt test also resulted in a left clavicle fracture and a myocardial tear in the right ventricle.

Table 39: Summary of autopsy findings.

Test	Surrogate	Findings	AIS*	MAIS*
Thorax Rigid-Disk	SM75	Multiple bilateral rib fractures/flail chest	5	**5**
		Sternum fracture	2	
Seatbelt	SM81	Multiple bilateral rib fractures	5	**6**
		Sternum fracture	2	
		Left clavicle fracture	2	
		Rupture of right ventricle	6	
Abdomen Rigid-Bar	SM72	Multiple rib fractures ≥ 3 ribs	3	**3**
Abdomen Rigid-Bar	SM86	Multiple rib fractures ≥ 3 ribs	3	**3**

*Gennarelli and Wodzin (Eds.), 2005

Kinematic Responses

A subset of marker trajectories for each test is included in this section. All trajectories were filtered using a 50 Hz 4th order Butterworth filter, or pseudo SAE J2ll CFC 30 Hz. All trajectories are provided in sagittal, coronal, and transverse planes using the anatomic coordinate system (X-direction positive posterior-to-anterior, Y-direction positive right-to-left, and Z-direction positive caudal-to-cranial) with the origin at the anterior-superior aspect of T10 at the midline of the vertebra. A slight delay in the onset of marker motion relative to impactor contact with the thorax or abdomen occurred for each test. Visual interpretation of the organ motion indicated that the soft tissues in the direct path of the impact followed the trajectory of the seatbelt or the impactor. Tissues lateral, superior, or inferior to the impactor were displaced outward away from the path of the impact.

Thoracic Impact. Still images from the high-speed video and a corresponding x-ray image sequence from the thoracic rigid-disk impact are included in Appendix D (Figure 83) and Appendix E (Figure 87), respectively. Motion analysis data were obtained for 88.8 ms. Figure 63-Figure 65 show trajectories for the diaphragm, pericardium, lungs, and sternum markers. Additional marker trajectories for the skeletal markers are included in Appendix F (Figure 91). Initial positions in anatomic coordinates are included in Appendix F (Table 56), as well as peak marker excursion, calculated as the absolute value of the maximum excursion in each direction.

In response to the impact, the sternum, diaphragm, and pericardium markers showed a pronounced superior and posterior trajectory at the onset of loading (Figure 63). The dominant motion of the sternum and the diaphragm was in the right posterior direction with a linear trajectory (Figure 65). However, the motion of the sternum markers was at a steeper angle toward the right compared to the diaphragm. Motion patterns of the markers sewn to the pericardial sac indicated a widening of the pericardium during loading. Markers to the right and left of the midline moved toward the respective lateral sides before motion occurred in a largely posterior trajectory (Figure 65). Pericardium motion was more circular on the right side of the heart, where the initial position was closer to the midline compared to the pericardium markers to the left of the heart (Figure 64-Figure 65). The circular patterns of the pericardium markers to the left of the heart were elongated similar to the diaphragm marker trajectories as both sets of markers initiated approximately equidistant from the midline (Figure 65). In general, markers in the lungs followed inconsistent trajectories that appeared to be dependent on marker location.

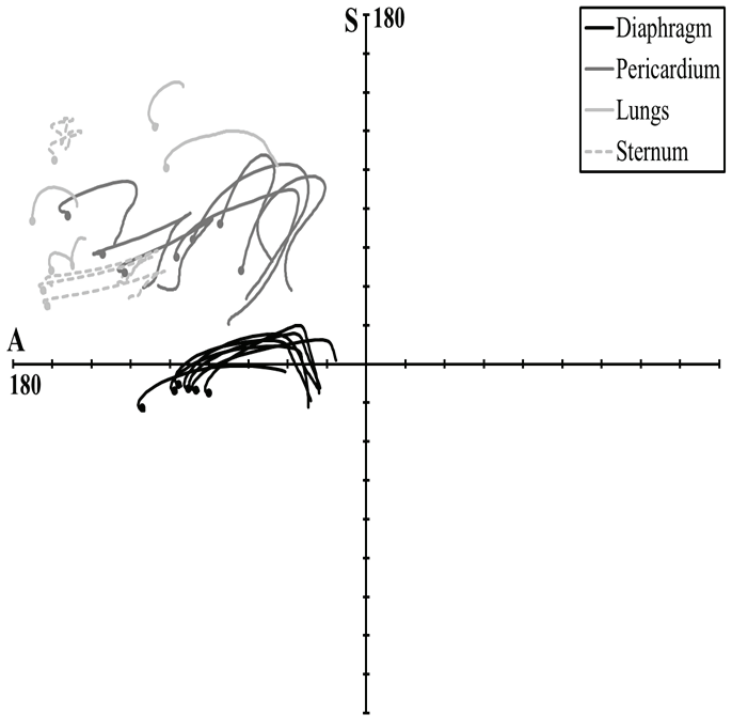

Figure 63: Marker trajectories in the sagittal plane for the SM75 thoracic rigid-disk impact at 6.7 m/s. § Circles identify initial position. Scale is mm.

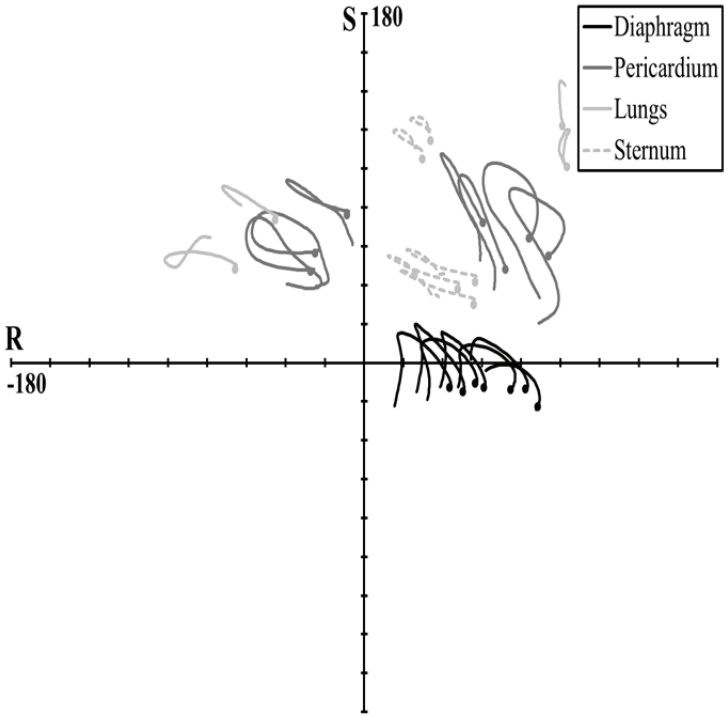

Figure 64: Marker trajectories in the coronal plane for the SM75 thoracic rigid-disk impact at 6.7 m/s. § Circles identify initial position. Scale is mm.

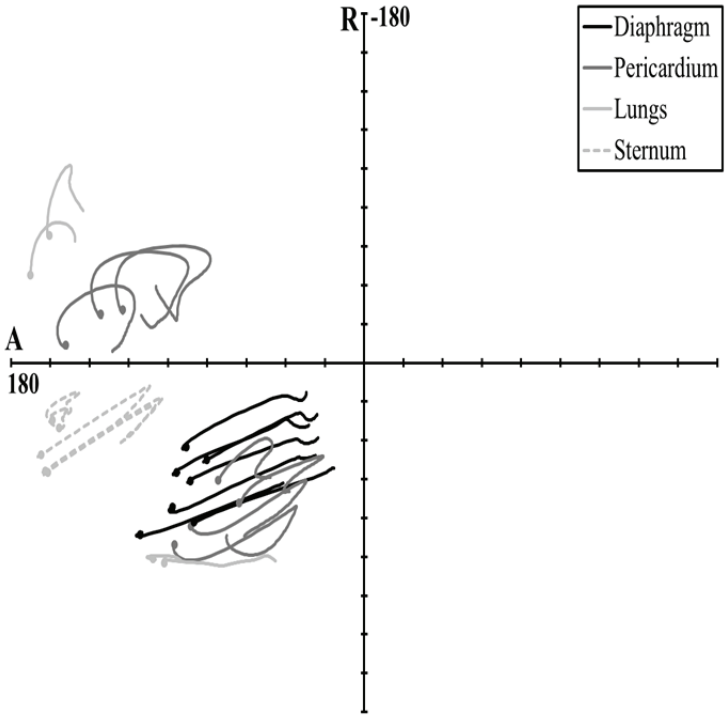

Figure 65: Marker trajectories in the transverse plane for the thoracic rigid-disk impact at 6.7 m/s. § Circles identify initial position. Scale is mm.

Seatbelt Loading. Still images from the high-speed video and a corresponding x-ray image sequence from the seatbelt test are included in Appendix D (Figure 84) and Appendix E (Figure 88), respectively. Motion analysis data were obtained for up to 67.2 ms. Initial marker position and peak excursion are tabulated in Appendix F (Table 57). In general, marker trajectories closely followed the path of the seatbelt (Figure 66-Figure 68). The motion was anterior to posterior with an approximately linear trajectory directed caudally and toward the right lateral side. Motion of the liver and diaphragm was similar with the exception of the more pronounced lateral trajectory of the liver markers (Figure 67). Diaphragm markers initially located to the left of the belt moved toward the left lateral side before following the path of the seatbelt toward the right (Figure 68). Bony markers at the xiphoid process followed a considerably steeper trajectory in the inferior-posterior direction compared to the soft tissue markers (Figure 66). It should be noted that the onset of marker motion for the focal seatbelt loading was delayed relative to the timing of the belt engaging the thorax for markers further from the anterior aspect of the cadaver.

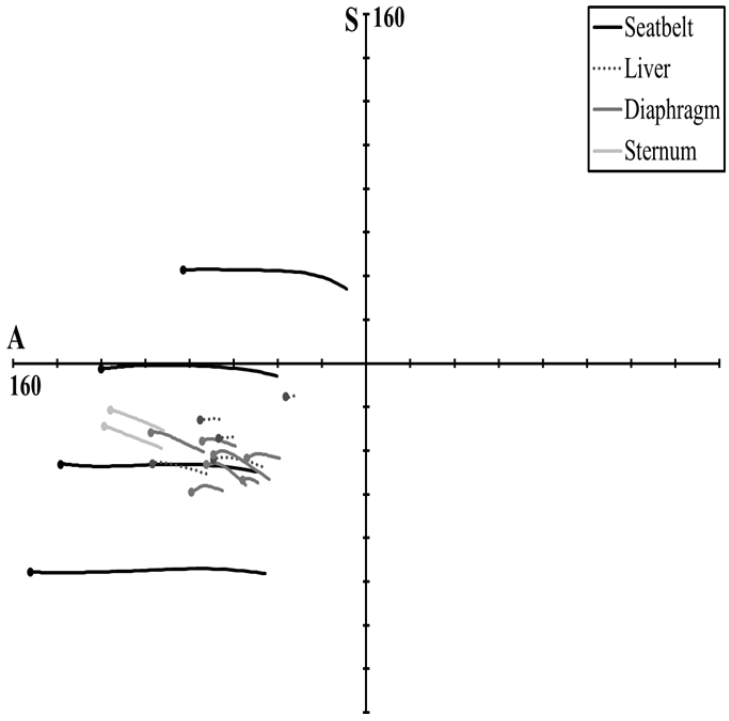

Figure 66: Marker trajectories in the sagittal plane for the SM81 seatbelt test at 3.0 m/s. § Circles identify initial position. Scale is mm.

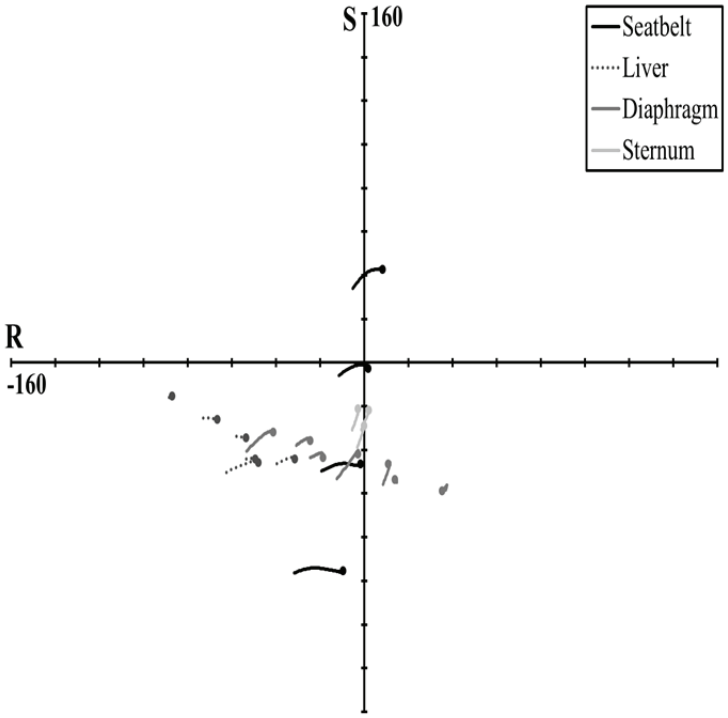

Figure 67: Marker trajectories in the coronal plane for the SM81 seatbelt test at 3.0 m/s. § Circles identify initial position. Scale is mm.

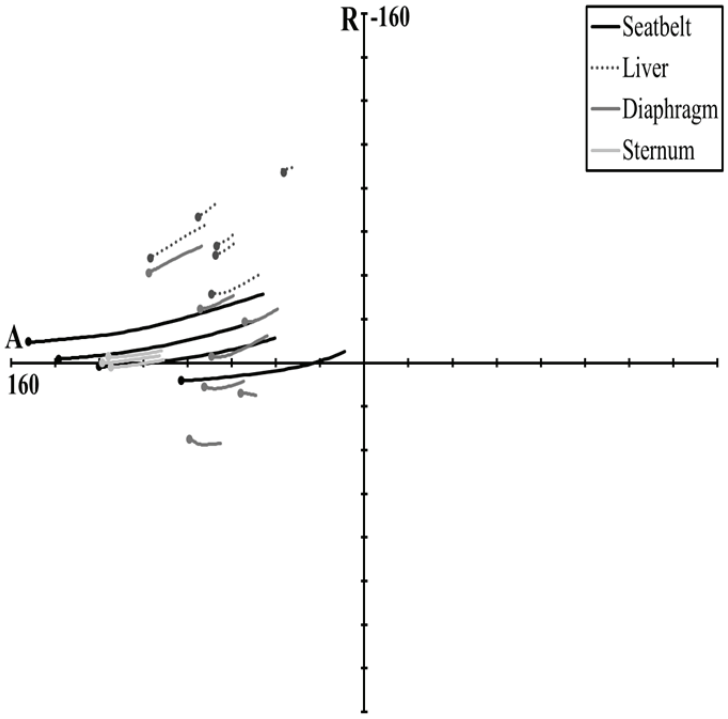

Figure 68: Marker trajectories in the transverse plane for the SM81 seatbelt test at 3.0 m/s. § Circles identify initial position. Scale is mm.

Abdominal Impacts. Still images from the high-speed video and corresponding x-ray image sequences from the abdominal impact tests are included in Appendix D (Figure 85-Figure 86) and Appendix E (Figure 89-Figure 90), respectively. Motion analysis data for the initial 100 ms of example abdominal impacts are presented in Figure 69-Figure 74. Individual plots for each impact are included in Appendix F (Figure 92-Figure 94). Additional marker data including tracking intervals, initial positions, and peak excursions are included in Appendix F (Table 58-Table 63).

All abdominal impacts occurred at the level of the mid-umbilicus of the inverted cadaver, resulting in anatomically cranial and anterior marker motion at the onset of loading. Marker trajectories generally continued in repeatable looping patterns, following the initial anterior, superior motion with motion toward the posterior, inferior aspect of the cadaver. The trajectories of markers to the right and left of the midline initiated toward the respective lateral side. Induced marker motion continued well beyond the time of peak impactor displacement for all impacts.

Marker trajectories for the 3.0 m/s cylinder impact to SM72 are shown in Figure 69-Figure 71. Marker patterns for the 3.0 m/s and 4.0 m/s cylinder impacts to SM72 were similar (Appendix F, Figure 92). The main distinctions of the 4.0 m/s test included a slight shift in the initial position of the markers and more pronounced trajectories in the 4.0 m/s test with roughly the same patterns as in the 3.0 m/s test. Little diaphragm motion occurred during these impacts. The markers of the diaphragm moved in tight circular patterns with a slight anterior-superior trajectory initially, followed by an arc in the left posterior to right anterior direction. The liver markers moved in a distinct arc to the right before continuing posterior and inferior from the initial position. Markers in the right lobe of the liver showed greater excursion than the markers in the left lobe, but the patterns were similar for all liver markers. Stomach and mesentery motion occurred in less defined patterns, first shifting superior and anterior before arcing toward the left, inferior, posterior region.

With some variability, the results from SM72 were replicated in the 3.0 m/s and 4.0 m/s cylinder impacts to SM86 (Appendix F, Figure 93). The diaphragm patterns were similar; however, the arcing liver marker motion occurred with a less defined pattern for SM86. Spleen motion in SM86 was in an elongated arc in the left, inferior, posterior direction. Hollow organ motion occurred in a similar elongated arc directed both inferiorly and posteriorly from the initial marker positions.

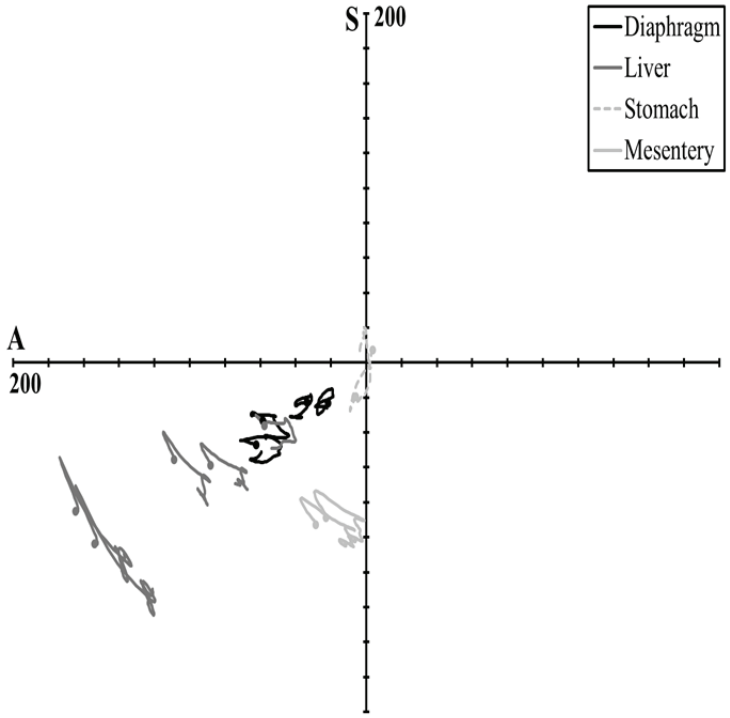

Figure 69: Marker trajectories in the sagittal plane for the SM72 cylinder impact at 3.0 m/s. § Circles identify initial position. Scale is mm.

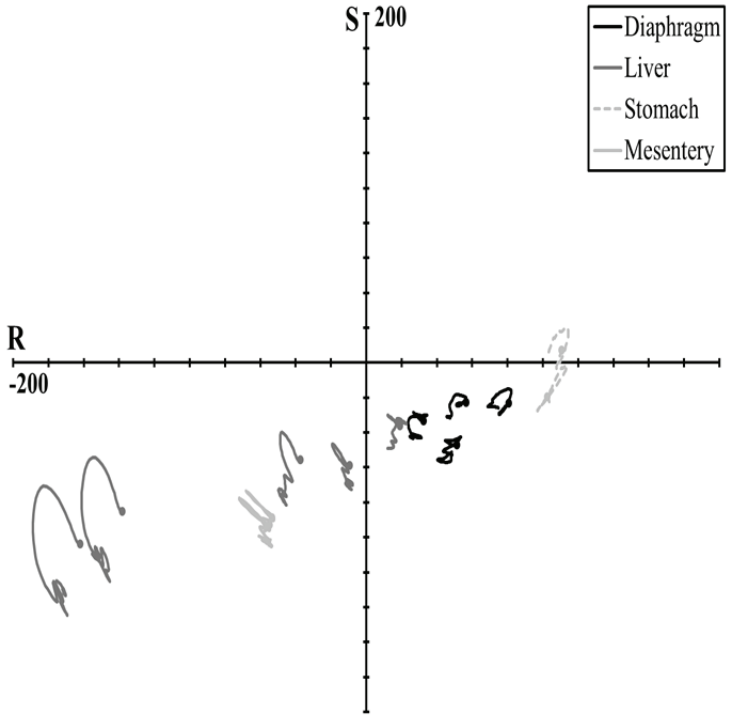

Figure 70: Marker trajectories in the coronal plane for the SM72 cylinder impact at 3.0 m/s. § Circles identify initial position. Scale is mm.

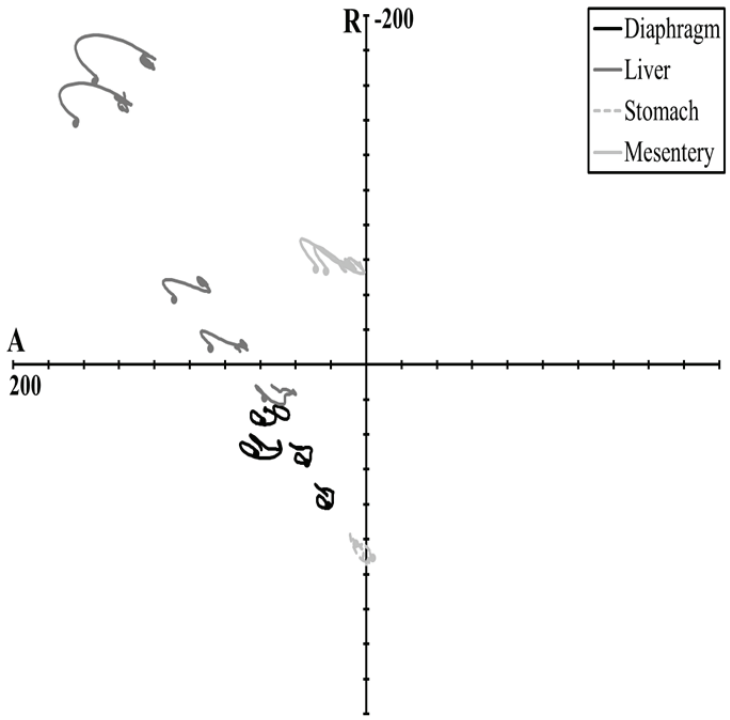

Figure 71: Marker trajectories in the transverse plane for the SM72 cylinder impact at 3.0 m/s. § Circles identify initial position. Scale is mm.

Rigid-bar impacts to SM72 and SM86 produced comparable patterns of internal organ motion with generally greater excursion occurring in SM72, shown in Figure 72-Figure 74. For each test, the stomach, liver, and diaphragm trajectories were similar, looping from the initial position in a superior, inferior, and then anterior pattern. The initial marker positions with respect to T10 varied for each cadaver, and marker motion was generally toward the right in SM72 but occurred in both directions for markers in SM86. Markers implanted in the parenchyma of the spleen in SM86 showed an elongated anterior to posterior trajectory toward the left inferior aspect of the cadaver (Appendix F, Figure 94). Mesentery markers moved in elongated posterior-inferior trajectories, toward the right in SM72 and toward the left in SM86.

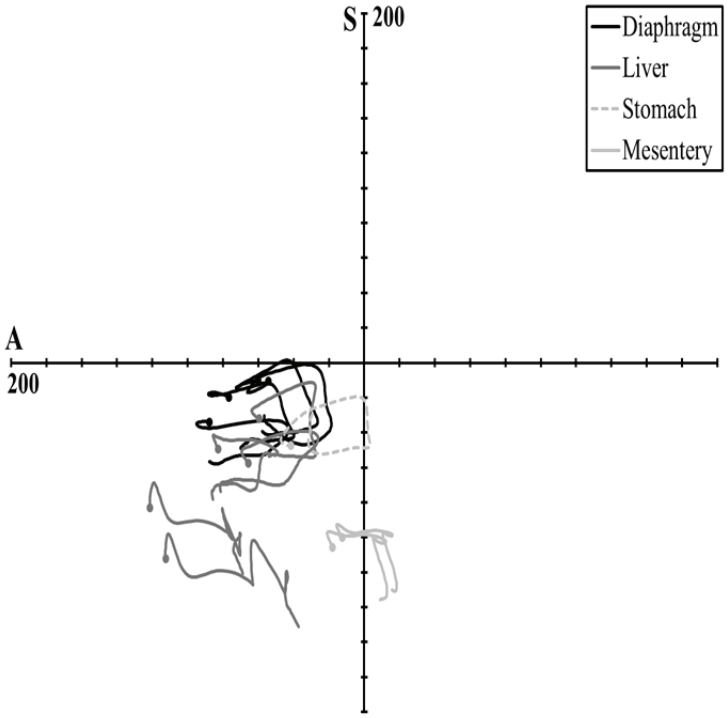

Figure 72: Marker trajectories in the sagittal plane for the SM72 rigid-bar impact at 6.7 m/s. § Circles identify initial position. Scale is mm.

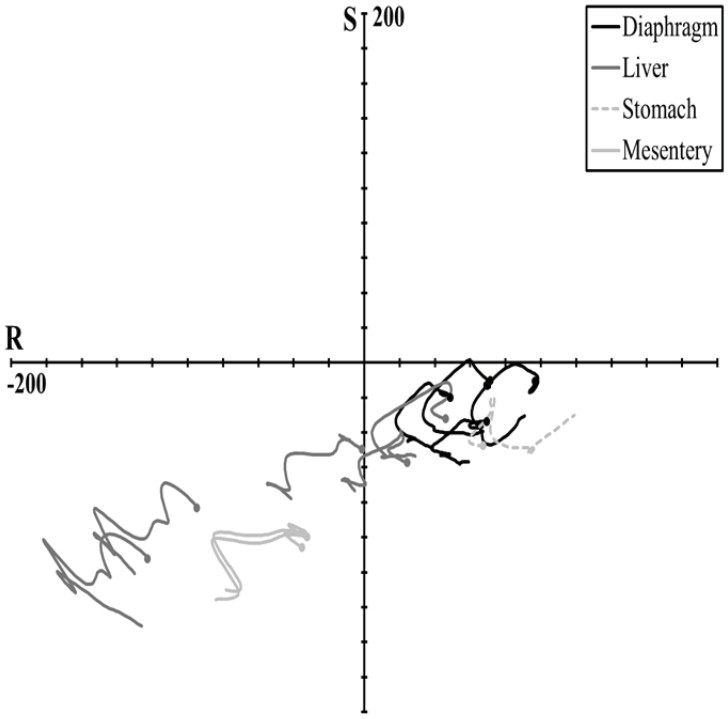

Figure 73: Marker trajectories in the coronal plane for the SM72 rigid-bar impact at 6.7 m/s. § Circles identify initial position. Scale is mm.

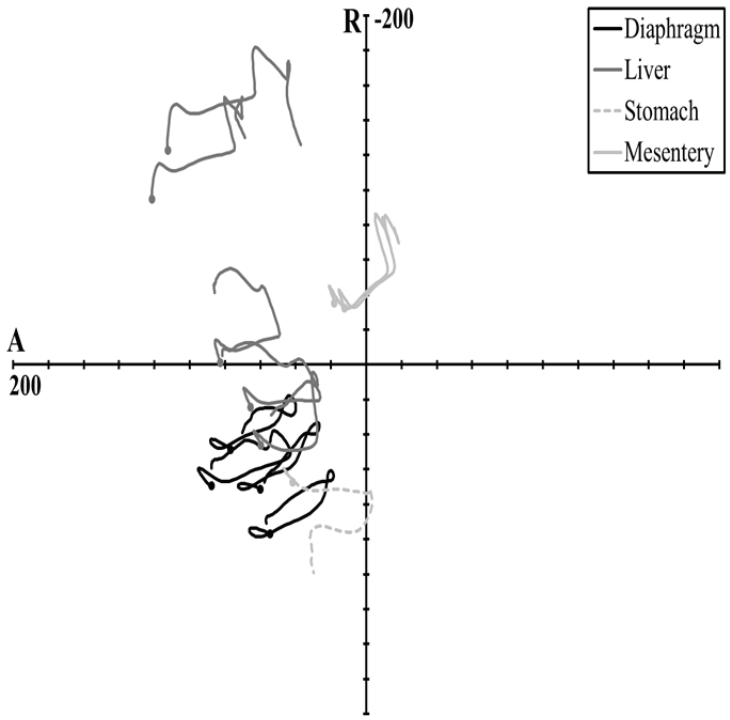

Figure 74: Marker trajectories in the transverse plane for the SM72 rigid-bar impact at 6.7 m/s. § Circles identify initial position. Scale is mm.

DISCUSSION

The primary objective of this study was to combine blunt impact loading with high-speed biplane x-ray imaging to quantify internal organ position and kinematics for use in computational model analysis. Four cadavers were tested using frontal impacts of varying severity and seatbelt loading to induce internal organ motion in the thoracic and abdominal cavities. To improve the interpretation of experimental data obtained in this study, the effects of cadaver orientation on the relative position of the internal organs were quantified for two cadavers. Organ position, marker trajectories, and relative organ displacements generated during impact give an indication of internal organ motion and interaction that may form the basis for further investigation of crash-induced injury mechanisms for the abdominal organs.

Static Positioning Tests

Two factors influencing relative abdominal organ position in the cadaver were investigated in this study: the effects of preparation techniques commonly applied during experimental testing to improve the biofidelity of the test surrogate, and the effects of cadaver orientation in upright and inverted postures. The change in organ position with each stage of cadaver preparation resulted in a relatively small effect of 11 to 20 mm overall from the initial to the final conditions. Although preparation had a minimal influence on the position of the abdominal organs, the aspects of cadaver preparation have a potentially large effect

on the dynamic response of the abdomen. For abdominal impact testing, the boundary conditions and general coupling between organ systems are important to both the mechanical and damage responses of the cadaver. These conditions influence which structures are loaded and how the load propagates within the abdominal region. For example, surrogate preparation techniques that introduce air into the abdominal cavity can reduce organ coupling while increasing relative position changes. The results of this study suggest that evacuation of intra-abdominal air not only removes this compressible component from the abdomen, but alters relative organ position to potentially reduce the gaps between organs, which would improve coupling during loading. Additionally, perfusion has long been considered important to creating more life-like turgor of the solid organs to obtain clinically-relevant damage responses during impact. Researchers should continue to implement preparation techniques to improve the biofidelity of the cadaver response to impact; however, it is important to consider the implications of each of these methods on test outcomes when developing experimental protocols and interpreting test results.

Compared to the effects of preparation, cadaver posture had a much larger influence on the relative position of the abdominal organs. The difference in diaphragm position in the upright and inverted postures was 106 mm on average. This change was similar in magnitude to the mean total excursion of the diaphragm during deep respiration (103 ± 22 mm) published by Wade (1954) for an erect posture. The change in liver marker position from the upright to the inverted posture was 137 mm on average. This was considerably greater than the physiologic motion of the liver, reported by Suramo et al. (1984) as 55 mm during deep breathing. The changes in position of the cadaver diaphragm and liver from the upright to the inverted posture were considerably greater than the variations in organ position for human subjects in the supine and seated postures (Beillas et al., 2009).

Intuitive changes in organ position were observed with the effect of gravity in the upright orientation compared to the inverted posture. With the cadaver upright, an increase in separation of the relative marker positions occurred in the vertical direction, and the organs were drawn caudally. This represents a considerable effect, particularly on the positions of the diaphragm and the liver. Further, the separation between the liver and the diaphragm in the upright position likely indicates the presence of trapped air beneath the diaphragm, which would reduce coupling during impact. When inverted, the cadaver diaphragm shifted cranially and the mobile abdominal contents shortened in the Z-direction, spreading laterally. For both PMHS, the diaphragm position shifted to the opposite side of the midline in the transition from the upright to the inverted posture. In addition to compression by the mobile abdominal contents, the position of the diaphragm was likely affected by the change in position of the thoracic contents when inverted.

Based on the tethering and attachments of the organs and the relative changes in proximity of the instrumented abdominal contents in each posture, it is likely that changes in organ shape also occurred with cadaver inversion. For example, variations in marker displacement magnitude and direction in the transition from the upright to the inverted posture occurred between markers fixed within the parenchyma of the liver. This indicates important differences in potentially both the shape and the position of the organs between the two experimental conditions. Other studies have shown variations in organ morphology in the transition from the supine to the seated posture, with the greatest deviations occurring in the geometry of the liver (Hayes et al., 2013a). Although the variations in morphology support the likelihood of shape changes occurring in this study, the variations in organ shape with changes in posture are small compared with subject-to-subject variability (Beillas et al., 2009) and compared to the changes in relative marker positions in the upright and inverted postures. Overall, altering the posture of the cadaver would affect the initial and boundary conditions of an impact test, which has been shown to be critical to the reproduction of clinically-relevant injuries and injury mechanisms in the laboratory (Hardy et al., 2008).

Despite the importance of considering the implications of both cadaver preparation and posture on the mechanical and damage responses generated during impact, biovariability has the largest overall effect on relative organ position and the comparison between cadavers and human subjects. Individual variations in organ size and position have been shown to be greater than the effects of subject posture on organ position (Beillas et al., 2009). In this study, comparison of the diaphragm position between inverted and upright for all four PMHS to all nine of the human subjects indicated an essentially equal but opposite difference in position in the superior-inferior direction. Therefore, compared to the human subjects, the PMHS diaphragm was not a better match in either orientation. However, compared to the GHBMC model, which was derived from one exemplar human subject geometry, the average cadaver organ position compared better with the PMHS inverted.

As supine MRI is sometimes used to generate occupant FE model geometry, the considerable variability in internal organ position in the cadaver compared to the supine or seated human subject confounds the ability to correlate experimental observations in cadaver tests with injury prediction using FE model simulations. Previous studies have shown a variation in liver position of 40 mm in the Z-direction for human subjects in the supine and seated postures (Beillas et al., 2009). In this study, the mean difference in organ position between cadavers and human subjects was on the order of 100 mm. In combination with the effects of biovariability, particularly in abdominal morphology, these variations in organ position may be the basis for discrepancies between experimental results and model output.

This situation is further confounded by post-mortem changes in the cadaver and the subsequent effect of gravity relative to the position and posture of the cadaver. Ideally, monitoring and adjusting experimental conditions using a combination of surrogate orientation, perfusion, and evacuation of intra-abdominal air would improve comparisons between cadaver test results and FE model output. The results of this study provide context for the consideration of the effects of each of these parameters on experimental results when developing test protocols. Whether tests are designed with the intent of investigating injury mechanisms or providing data for modeling applications, it is suggested that researchers keep these phenomena in mind when interpreting test results and comparing them to FE model simulations. Adjustment of model geometry (subject-specific modeling) or impact conditions (impact location with respect to an organ position) might be possible to improve comparisons between simulations and experimental tests, but require some knowledge of organ position. Knowledge of organ position seems therefore critical for future studies where tests are conducted with the intent of providing data for model development or validation. However, the results of this study provide context for the interpretation of past experimental test results where organ position was unknown. This has important implications as these studies are often used to validate the performance of FE models.

As the use of FE models increases for the investigation of crash-induced injuries and mechanisms, data for the validation of model performance becomes increasingly important. Limitations will continue to exist when using cadavers to investigate human subject response and tolerance; however, this study was aimed at reducing the limitations between the comparison of experimental results obtained using PMHS to the output of FE models developed using human subject geometry. Without considering and possibly adjusting for these differences, injury prediction using FE models might not correlate with the damage observed in cadavers that results from regional impacts.

Impact Response

Thoracic Loading. The rigid-disk impact to the cadaver thorax resulted in a peak deflection of 109 mm with a peak load of 3.62 kN. The high-energy impact with considerable chest deflection resulted in bilateral compromise of the rib cage with multiple bilateral rib fractures and flail chest. Oscillations in the relative plateau of the force-deflection response (Figure 59) can be attributed to the increasing number of rib fractures as the impactor loaded the thorax. The 3.0 m/s seatbelt test resulted in a peak deflection of 120 mm with considerable belt interaction with the thorax. The force-deflection response for the seatbelt test initiated within the corridor developed by Kent et al. (2004) for single diagonal seatbelt loading tests performed on the bench top (Figure 60). The direct interaction of the belt with the rib cage in this study resulted in thoracic damage associated with severe or possibly even fatal injury in a vehicle occupant.

Abdominal Impacts. Two instrumented cadavers were tested using frontal impacts of varying severity to induce internal organ motion and interaction within the abdominal cavity. The cylinder impact tests were designed as low-energy tests to induce organ motion and resulted in an approximate peak load of 1 kN. By design, the impactor was arrested with Hexcel contact after 50 mm of penetration into the abdomen. Figure 61 shows this for the 3.0 m/s tests; however, for the 4.0 m/s tests, contact with the Hexcel occurred after a greater penetration into the abdomen. The position of the cadavers relative to the impactor face was not adjusted between the two cylinder impact tests. Therefore, any abdominal compression or shift of the tissues that was not restored following the 3.0 m/s tests contributed to the increased abdominal penetration that occurred before the impactor was arrested in the 4.0 m/s tests. This effect was greater for SM86, which had increased mass at the midsection compared to SM72.

The rigid-bar impact test conditions were different for the two cadaver tests. The SM72-3 rigid-bar impact was the only test to deviate from the nominal stroke of 50 mm before Hexcel contact. A limited amount of Hexcel was engaged for this impact, and a greater overall impactor displacement in this test resulted in impactor contact with the spine of the cadaver. The test conditions for the SM86-3 rigid-bar impact were identical to the cylinder impacts. The marked difference in the load-penetration response shown in Figure 62 for these impacts was largely a result of the variation in test conditions. However, both load-penetration curves initiated within the corridor for the Hardy et al. (2001a) free-back rigid-bar tests conducted at 6 m/s, indicating that the responses of the fixed-back tests were similar to the free-back responses up to approximately 50 mm of penetration into the abdomen. The load-penetration response for SM72-3 then increased in stiffness compared to the corridor, due to the high compressive loads resulting from maximal compression of the tissues against the spine.

Internal Organ Kinematics

Thoracic Loading. The rigid-disk impact to the thorax was designed to apply a symmetric, distributed loading that engaged the clavicles and the anterior aspect of the entire rib cage. This test configuration is substantially different from the typical localized impacts to the thorax traditionally used for FE model validation. In general, the markers exhibited predictable trajectories. However, markers implanted in the highly deformable soft tissue of the lungs moved in less defined patterns than the diaphragm and pericardium markers, which moved with very similar trajectories.

For the rigid-disk impact, the transverse perspective showed that the sternum and diaphragm markers were initially positioned to the left of the spine and moved with a linear trajectory toward the right, posterior aspect, which is counterintuitive to some extent. Still images and FARO laser scans of the PMHS and impactor surface recorded prior to impact indicated a greater protrusion of the left aspect of

the rib cage of this cadaver. Therefore, the impactor engaged the left side of the thorax first, driving tissues toward the right at the onset of loading. Further, FARO laser scans indicated that the center of the impactor was slightly biased toward the right side of the thorax. This information explains the nature of the target motion, and emphasizes the need to assess the initial impact conditions using techniques such as x-ray, still images, and FARO laser scan data to provide computational model developers with an indication of the orientation of the experimental setup.

For the seatbelt test, marker motion for the diaphragm and the liver was similar with an anterior to posterior trajectory that was directed slightly caudally throughout the test. Differences appeared in the coronal plane where some lateral and inferior motion of the diaphragm markers was observed, and the liver motion toward the right lateral side was more pronounced. Given that the diaphragm markers were located close to the midline of the cadaver, less lateral movement for these markers was expected compared to markers implanted into the parenchyma of the more mobile liver. The xiphoid process moved with a more caudal trajectory than the soft tissue markers as the seatbelt compressed and rotated the rib cage.

A clear difference in internal organ motion occurred in response to distributed loading compared to direct interaction of the thorax with the seatbelt. The initial trajectory of the internal organ markers in the thoracic rigid-disk impact was directed away from the impactor face (posteriorly and laterally) as tissues were compressed, whereas the internal organ kinematics in the seatbelt test closely matched the path of the belt as it loaded the thorax.

Abdominal Impacts. Each abdominal impact produced characteristic looping patterns in the soft tissues. At the onset of loading, marker motion was in the anatomically cranial and anterior directions. The trajectory of the impactor, however, was in the posterior direction, perpendicular to the coronal plane of the cadaver. The counterintuitive motion of the markers occurred as the impactor displaced soft tissues in the path of the impact, resulting in upward and outward trajectories that were opposite of the motion of the impactor for markers that were anatomically superior to the impact location.

Markers implanted in the liver to the left of the falciform ligament and markers sewn to the central tendon of the diaphragm moved in comparable patterns, likely due to the tethering of the liver to the diaphragm by the coronary ligament and the attachment of both structures to the anterior abdominal wall. Greater lateral motion of markers implanted in the right lobe of the liver can be attributed to the greater variation in position of the right lobe in comparison with the left, due to the size of the right lobe and the lack of ligamentous attachments to the anterior abdominal wall. Due to the small size and location of the spleen,

loading during impact was minimal, and therefore, motion patterns did not change considerably in response to the different impact scenarios.

Considerable variability existed in the initial positions and resulting trajectories of the stomach and mesentery markers for each of the cadavers. For example, the markers for surrogate SM72 were sewn into the body of the stomach and located in the left upper quadrant of the abdomen. The stomach of SM86 spanned a larger area of the abdomen, and therefore markers appeared to the right of the midline. Differences in initial position and marker patterns between cadavers can be attributed to variations in anatomy, structure, and mass distribution for the PMHS undergoing similar cylinder and bar impacts. SM72 was greater in stature and of a lower mass than SM86, resulting in generally greater marker excursion for the same impact energy. Further, the use of a vacuum to evacuate residual air from the abdominal cavity prior to impact removed a considerable amount of air in some cases. The removal of air from the abdominal cavity likely increased the organ system coupling for these impacts.

Limitations

Static Positioning Tests. The results of this study are limited by the use of only two PMHS for organ position comparison between postures. Similarly, organ position data were available for only four cadavers for comparison to the human subjects and the GHBMC model. Although statistical tests could not be applied to these data, the results of this study have important implications for interpreting and comparing experimental results to FE model output, and should be considered by investigators when deciding how to position and set the posture of a cadaver for testing.

Application of a limited number of targets in each organ prevented marker confusion when imaging the entire abdominal region. However, this reduced the amount of data obtained from a particular organ. Further, not all markers were visible in both planar views for every test due to the limited viewing area of the image intensifiers. This was particularly true for the upright test using SM86 in which the anatomical separation of the organs of interest forced markers outside of the viewing range. The close proximity of the abdominal organs with the PMHS in the inverted posture increased the number of markers visible using the biplane x-ray system.

Although the marker positions can be related back to bony landmarks using planar supine pre-test and post-test x-rays, the precise local anatomical position of the markers relative to each organ is unknown. In future studies, this information can be obtained from CT scans of the instrumented PMHS. These data would allow for better selection of specific points within the model geometry for direct comparison to the anatomical position of the markers. Additionally, spine posture varied between the human subjects and the cadavers. The PMHS spine was arbitrarily straightened during positioning and mounting to the

support fixture. Differences in posture confounded the ability to project the PMHS marker positions to the human subjects in the Z-direction.

Tremendous biovariability exists across human subjects and therefore PMHS as well. In itself, this confounds the ability to compare the results of a minimal number of cadaver tests to the output from FE models that are generated using exemplar human subject geometry. Within this study, the BMI of the cadavers, human subjects, and GHBMC model varied greatly. This variation was largely reflected in differences in abdominal morphology and abdominal thickness. Scaling assuming geometric similitude does not capture this variation in regional geometry, particularly for the soft tissues of the abdomen.

Dynamic Impact Tests. These impacts were conducted using four PMHS with a target height and weight matching or less than the 50th-percentile male height and weight. Cadavers were selected to be less than 78 kg to improve marker viewing capability using the biplane x-ray system. Variations in organ size and position within the thorax or abdominal cavity may vary considerably between the cadavers used for this study and existing FE models. Therefore, direct application of these data with regard to initial marker and organ position relative to model position should be cautioned.

Two cadavers were tested using repeated abdominal impacts of low but increasing energy. The initial impacts were designed to load only the abdominal tissues and to avoid engaging the lower aspects of the rib cage. Prior studies have applied multiple abdominal impacts to single surrogates and verified little change in the mechanical response with repeated tests (Hardy et al., 2001a). The use of multiple impacts in the current study was justified as the tests were designed to induce internal organ motion, and the primary objective was not the investigation of injury responses.

Tests were conducted in fixed-back configurations to prevent motion of the cadaver out of the viewing range of the x-ray system. Elimination of the whole-body acceleration that would occur in a free-back test results in a load-penetration response for the fixed-back tests that falls below accepted corridors for free-back abdominal impact tests (Hardy et al., 2001a). The free-back test configuration is more representative of the loading experienced by vehicle occupants; however, previous studies have shown approximately 1.5 mm of spine motion at peak penetration in free-back high-rate seatbelt tests (Foster et al., 2006). Therefore, restricting the spine motion in the fixed-back configuration likely had only a small effect on the overall motion of the internal organs up to the point of peak penetration of the impactor.

In preparation for the thoracic impact, the bilateral aspects of rib five were compromised to allow access to the pericardium and lungs. Although this should not have had a considerable effect on the impact response of the thorax, the local load distribution was likely altered slightly. Damage to the abdomen

during preparation was minimal; however, the density of the lead sphere markers was slightly greater than the density of the tissues, resulting in local increases in density at the implanted marker locations. As this study was focused on relative motion of the internal organs and not the local strain response of the tissues, the difference in density had little influence on the results. Further, in comparison of pre-test and post-test planar x-rays, implanted targets were shown to maintain relative position within the tissue.

Several of the tests conducted in this study were designed to be below the injury thresholds of the cadaver. The tests designed to cause injury resulted in substantial injury to the cadaver. Therefore, with the exception of the myocardial tear in the seatbelt test, the similar injury patterns and associated range of injury metrics limits the ability to assess the predictive value of the calculated metrics for these few tests having a variety of loading scenarios.

Not all marker positions could be identified and tracked in each view for the entirety of each test. This was due, in part, to the anatomical separation of organs of interest forcing markers outside of the viewing range. Markers were also obscured by portions of the test fixture, particularly in the seatbelt test configuration. Certain markers were difficult to discern through fat or other anatomic structures. No attempt was made to fill gaps in the kinematics data, though these gaps typically occurred at the onset of loading or at the end of the tests.

The use of close-proximity vertebral body markers to rotate and translate global position data to the anatomic coordinate system could introduce error in marker position. Although this does not contribute to intrinsic marker tracking error, errors in vertebral body marker position would be exaggerated when using the relatively small body-fixed basis to align the dispersed tracking data. This error would appear as differences in target trajectory. To assess this variation, a different method of transverse plane rotation was applied to the data using laboratory reference points to identify the angle between the anatomic and global coordinate systems (Howes et al., 2012). Comparison of the results indicated the equivalence of the two methods and the robustness of the approach applied in this study.

The results of the static positioning tests highlighted the variability in cadaver organ position relative to human subject geometry that is typically used to develop FE models. Based on these differences, the direct comparison of the internal organ kinematics data reported for four cadavers in this study to FE model response under the same impact conditions should be cautioned. In the absence of subject-specific modeling, model response should not be expected to directly replicate the organ kinematics presented in this study; however, the general trends in the model responses should be similar to the cadaver impact responses.

CONCLUSION

Static tests were conducted to quantify the three-dimensional variation in organ position in the cadaver. Cadaver preparation techniques resulted in relatively small position changes (11 to 20 mm overall). Researchers should continue to implement these methods due to the potentially large functional effects on the dynamic response of the abdomen. The changes in organ position in the upright and inverted cadaver postures represented a considerably larger effect than preparation techniques. In the upright posture, abdominal organ position was drawn caudally, whereas in the inverted posture the organs shifted cranially relative to T10. The inverted posture was associated with an average difference in diaphragm position of 106 mm compared to the upright posture. In relation to the organ position of seated human subjects, the mean distance magnitude between the diaphragm positions was on the order of 70 to 100 mm, and ± 27 mm in the vertical direction, as compared to the cadaver. Compared to the GHBMC model, the inverted cadaver was the best match for the diaphragm and the liver positions in the superior-inferior direction. Knowledge of the relative position and orientation of the internal organs under these different conditions aids in the interpretation and comparison of experimental data with FE modeling results used for injury prediction.

High-speed biplane x-ray was used to quantify internal organ kinematics in response to blunt loading for eight impact tests conducted using four whole post-mortem human surrogates. Visual interpretation of the motion patterns of the thoracic and abdominal organs indicated characteristic looping patterns of implanted markers in response to blunt impact and linear marker displacement in response to shoulder seatbelt loading. The patterns largely demonstrated an intuitive result as the markers moved as one would anticipate in response to the specific loading scenarios. The results of this study provide organ kinematics data useful for human body finite element model development or validation. Quantification of the kinematics response of individual organs in blunt impact can be used to drive future research in the investigation of internal organ injury mechanisms in automobile collisions.

APPENDIX A: PMHS anthropometry measurements.

Measurement	Location	SM75	SM81	SM72	SM86
Stature	Left	172.7	188.0	183.0	174.0
	Right	174.0		186.0	173.0
	Average	173.4		184.5	173.5
Shoulder Height		147.3	160.0	164.5	150.5
Waist Height	Left	97.0	104.1	118.0	103.0
	Right	96.5	104.1	117.0	102.0
Vertex to Pubic Symphysis Length		82.0	83.8	81.0	88.0
Vertex to Trochanter Length	Left	80.8	58.9	75.5	88.0
	Right			75.0	
Head Breadth		14.5	15.2	14.1	15.0
Head Anterior to Posterior Depth		18.9	18.8	18.2	16.5
Head Vertex to Chin Length		21.8	24.6	25.1	22.0
Neck Circumference		30.5	35.6	44.0	44.0
Chest Breadth	Axilla	26.4	27.7	31.0	32.0
	Nipple Line	26.4	28.7	28.0	30.0
	Sub-Sternum	27.4	29.2	27.0	32.5
Chest Depth	Axilla	20.8	21.8	19.0	20.0
	Nipple Line	22.9	23.1	21.0	22.5
	Sub-Sternum	21.8	22.1	21.0	24.5
Chest Circumference	Axilla	83.8	88.9	87.5	95.0
	Nipple Line	85.1	91.4	87.0	104.0
	Sub-Sternum	85.1	88.3	84.5	101.0
Interscye Breadth		26.7	30.5	33.0	28.0
Scye Circumference	Left	36.8	40.6	43.5	45.0
	Right			40.0	48.0
Shoulder Breadth		30.0	33.0	38.5	37.0
Shoulder to Elbow Length	Left	40.6	39.9	43.0	39.0
	Right			44.0	39.0
Elbow to Fingertip Length	Left	48.3	Amputated	59.3	47.0
	Right			59.3	47.0
Bicep Circumference	Left	20.3	21.6	20.3	27.0
	Right			21.0	26.0
Elbow Circumference	Left	22.9	20.3	23.5	24.5
	Right			25.0	28.0
Forearm Circumference	Left	17.8	22.9	18.5	23.0
	Right			21.0	23.5
Wrist Circumference	Left	16.5	Amputated	17.0	16.0
	Right			17.8	17.0
Waist Breadth		29.2	27.7	27.0	38.0
Waist Depth		14.0	17.8	13.0	19.0
Waist Circumference		76.2	85.1	71.0	94.0

Measurement	Location	SM75	SM81	SM72	SM86
Hip Breadth		29.2	30.5	31.0	36.0
Buttock Depth		15.7	17.8	15.0	18.0
Buttock Circumference		78.7	83.8	86.0	95.5
Thigh Circumference	Left	36.8	43.2	39.5	44.0
	Right			42.0	44.0
Lower Thigh Circumference	Left	27.9	30.5	30.3	34.0
	Right			33.8	34.5
Knee Circumference	Left	34.3	33.0	34.0	36.0
	Right			39.0	35.0
Tibia Height	Left	41.9	47.5	54.5	42.0
	Right	43.2	47.5	55.0	42.0
Calf Circumference	Left	24.1	25.4	27.3	28.0
	Right	24.1	26.7	29.0	29.0
Ankle Height	Left	10.2	6.4	10.0	8.5
	Right			10.0	9.0
Ankle Circumference	Left	20.3	19.1	26.0	19.5
	Right			24.5	19.0
Foot Breadth	Left	8.6	7.6	9.8	10.0
	Right	9.1		9.0	10.0
Foot Length	Left	24.1	24.1	28.0	25.5
	Right	23.9	23.6	28.5	25.5

APPENDIX B: Static positioning test data.

Table 40: Subject characteristics.

Subject	Gender	Age	Stature (m)	Mass (kg)	BMI	Sub-Sternum			
						Breadth (mm)		Depth (mm)	
						Supine	Seated	Supine	Seated
M01*	Male	29	1.75	70.0	22.9	323	290	198	193
M02*	Male	32	1.91	88.0	24.1	334	325	224	240
M03*	Male	29	1.75	64.0	20.9	302	307	198	187
M04*	Male	26	1.69	60.0	21.0	307	311	194	198
M05*	Male	26	1.81	80.0	24.4	304	288	231	241
M06*	Male	37	1.83	82.0	24.5	322	313	239	240
F01*	Female	41	1.74	68.0	22.5	273	276	192	175
F02*	Female	42	1.72	64.0	21.6	276	279	205	191
F03*	Female	34	1.62	53.0	20.2	282	295	188	186
SM72	Male	73	1.85	53.0	15.5	270	-	210	-
SM86	Male	84	1.74	74.0	24.4	325	-	245	-
SM75§	Male	76	1.73	47.0	15.7	274	-	218	-
SM81§	Male	72	1.88	54.0	15.3	292	-	221	-
Model	Male	-	1.75	78.5	25.6	-	345	-	230

*Data from Beillas et al., 2009

§Data from Howes et al., 2012

Table 41: Scale factors.

Subject	Equal-Stress/Equal-Velocity			Stature Scaling		
	X	Y	Z	X	Y	Z
M01	1.039	1.039	1.039	1.000	1.000	1.000
M02	0.963	0.963	0.963	0.916	0.916	0.916
M03	1.070	1.070	1.070	1.000	1.000	1.000
M04	1.094	1.094	1.094	1.036	1.036	1.036
M05	0.994	0.994	0.994	0.967	0.967	0.967
M06	0.986	0.986	0.986	0.956	0.956	0.956
F01	1.049	1.049	1.049	1.006	1.006	1.006
F02	1.070	1.070	1.070	1.017	1.017	1.017
F03	1.140	1.140	1.140	1.080	1.080	1.080
SM72	1.140	1.140	1.140	0.946	0.946	0.946
SM86	1.020	1.020	1.020	1.006	1.006	1.006
SM75	1.186	1.186	1.186	1.012	1.012	1.012
SM81	1.133	1.133	1.133	0.931	0.931	0.931
Model	1.000	1.000	1.000	1.000	1.000	1.000

Table 42: SM72 upright positions (mm).

Marker	X	Y	Z
Diaphragm01	92.0	-49.6	-46.2
Diaphragm02	59.0	-62.5	-61.9
Diaphragm03	57.7	-43.6	-67.4
Diaphragm04	69.6	-20.7	-68.4
Liver01	46.1	-35.6	-103.2
Liver02	58.4	-43.8	-113.4
Liver03	53.4	-67.8	-110.4
Liver04	36.6	-68.2	-179.0
Liver05	27.3	-76.8	-215.1
Stomach01	97.8	2.6	-146.3
Stomach02	49.9	-15.8	-168.3
Stomach03	94.0	-1.0	-185.6
Mesentery01	81.3	-26.4	-208.8
Mesentery02	74.5	-35.0	-218.8

Table 43: SM72 inverted positions (mm).

Marker	X	Y	Z
Diaphragm01	62.4	51.3	-47.2
Diaphragm02	58.6	32.5	-33.2
Diaphragm03	33.7	56.4	-22.9
Diaphragm04	21.7	80.8	-23.2
Liver01	57.7	19.0	-36.1
Liver02	88.1	-9.3	-58.7
Liver03	108.9	-37.3	-55.6
Liver04	164.7	-138.1	-85.0
Liver05	153.8	-162.0	-103.7
Stomach01	-3.8	110.6	7.3
Stomach02	48.4	45.1	-38.9
Stomach03	6.1	102.5	-19.3
Mesentery01	28.8	-54.7	-92.9
Mesentery02	22.8	-53.5	-88.8

Table 44: SM86 upright initial (mm).

Marker	X	Y	Z
Diaphragm01	-	-	-
Diaphragm02	-	-	-
Diaphragm03	80.1	26.1	-86.5
Liver01	69.3	16.9	-171.3
Liver02	57.5	15.2	-130.6
Liver03	67.0	-51.2	-172.3

Table 46: SM86 upright stomach filled (mm).

Marker	X	Y	Z
Diaphragm01	-	-	-
Diaphragm02	-	-	-
Diaphragm03	80.2	19.4	-87.5
Liver01	68.5	10.3	-172.7
Liver02	57.1	9.1	-131.5
Liver03	64.3	-59.1	-171.5

Table 45: SM86 upright ventilation (mm).

Marker	X	Y	Z
Diaphragm01	-	-	-
Diaphragm02	83.1	26.9	-97.2
Diaphragm03	78.5	14.9	-98.1
Liver01	73.5	12.7	-183.4
Liver02	57.2	7.5	-141.9
Liver03	72.0	-57.0	-191.9

Table 47: SM86 upright vacuum (mm).

Marker	X	Y	Z
Diaphragm01	87.4	44.4	-101.8
Diaphragm02	81.8	27.6	-101.9
Diaphragm03	76.3	17.3	-102.2
Liver01	73.2	18.6	-190.9
Liver02	56.9	11.7	-146.0
Liver03	77.0	-52.9	-195.7

Table 48: SM86 upright perfusion (mm).

Marker	X	Y	Z
Diaphragm01	88.3	43.3	-104.9
Diaphragm02	82.9	26.4	-105.5
Diaphragm03	77.8	16.1	-105.8
Liver01	74.2	18.4	-195.2
Liver02	57.9	11.3	-149.7
Liver03	78.0	-52.6	-200.3

Table 49: SM86 inverted initial (mm).

Marker	X	Y	Z
Diaphragm01	91.2	-20.2	-32.0
Diaphragm02	75.1	-38.8	-29.9
Diaphragm03	69.8	-45.7	-30.4
Liver01	80.4	-50.0	-51.5
Liver02	54.8	-56.9	-37.9
Liver03	-1.2	-143.1	-39.1
Liver04	-18.0	-102.2	-53.5
Liver05	-24.6	-153.1	-80.4
Stomach01	105.3	-68.3	-73.5
Stomach02	77.4	-82.9	-90.9
Spleen01	-	-	-
Spleen02	2.2	88.5	-68.7
Mesentery01	16.6	-8.2	-137.4
Mesentery02	-1.0	-30.3	-126.3
Mesentery03	2.8	-50.9	-150.2

Table 50: SM86 inverted ventilation (mm).

Marker	X	Y	Z
Diaphragm01	95.5	-14.6	-20.7
Diaphragm02	79.4	-33.4	-22.0
Diaphragm03	74.2	-39.8	-23.2
Liver01	87.1	-42.1	-44.4
Liver02	60.0	-50.6	-34.1
Liver03	6.3	-137.3	-49.7
Liver04	-10.5	-95.5	-61.7
Liver05	-12.5	-140.9	-94.0
Stomach01	113.8	-57.9	-65.3
Stomach02	88.4	-71.1	-86.5
Spleen01	4.4	55.8	-71.3
Spleen02	8.0	95.6	-54.8
Mesentery01	31.4	6.5	-131.4
Mesentery02	13.0	-15.7	-123.7
Mesentery03	19.4	-33.5	-149.0

Table 51: SM86 inverted vacuum (mm).

Marker	X	Y	Z
Diaphragm01	96.5	-15.6	-13.2
Diaphragm02	80.5	-33.8	-14.6
Diaphragm03	76.0	-41.2	-16.6
Liver01	89.4	-43.3	-36.2
Liver02	62.0	-52.2	-27.5
Liver03	9.1	-138.7	-43.2
Liver04	-7.0	-96.8	-56.7
Liver05	-7.9	-144.1	-87.5
Stomach01	116.3	-59.5	-55.1
Stomach02	92.6	-73.1	-77.6
Spleen01	8.1	54.2	-68.5
Spleen02	11.0	94.1	-53.3
Mesentery01	37.5	2.4	-126.4
Mesentery02	19.2	-19.2	-118.9
Mesentery03	26.6	-36.5	-141.4

Table 52: SM86 inverted perfusion (mm).

Marker	X	Y	Z
Diaphragm01	94.5	-17.7	-22.6
Diaphragm02	78.1	-36.3	-23.2
Diaphragm03	73.4	-43.4	-24.6
Liver01	86.0	-45.9	-44.7
Liver02	59.0	-53.7	-34.4
Liver03	4.0	-139.5	-45.7
Liver04	-12.4	-98.0	-58.8
Liver05	-15.9	-145.2	-88.8
Stomach01	111.2	-62.8	-65.4
Stomach02	86.0	-75.5	-86.4
Spleen01	3.7	52.4	-73.2
Spleen02	7.9	91.8	-58.9
Mesentery01	29.2	-0.3	-132.2
Mesentery02	11.3	-21.5	-123.1
Mesentery03	17.3	-38.7	-145.7

Table 53: Comparison of cadaver marker position to human subject nodes for the diaphragm (mm).

NO SCALING																
Cadaver	Inverted Diaphragm								Upright Diaphragm							
	Mean Distance		X-Difference		Y-Difference		Z-Difference		Mean Distance		X-Difference		Y-Difference		Z-Difference	
	AVG	STD	AVG	STD	AVG	STD	AVG	STD	AVG	STD	AVG	STD	AVG	STD	AVG	STD
72	36.8	16.1	-0.7	15.8	7.4	9.9	-25.0	24.7	113.7	13.7	-26.2	13.7	106.7	11.4	4.4	26.9
75	68.0	15.3	-49.5	10.3	-2.1	7.0	-41.9	22.4								
81	59.9	13.7	-27.1	13.2	47.3	8.2	-9.3	22.4								
86	115.3	13.9	-42.8	14.5	99.4	7.6	-31.3	23.6	80.3	16.0	-43.8	12.8	38.4	7.1	50.7	23.6
TOTAL	**67.5**	**31.5**	**-29.3**	**23.9**	**32.9**	**40.1**	**-27.8**	**25.8**	**99.4**	**22.1**	**-33.7**	**15.9**	**77.4**	**35.4**	**24.2**	**34.3**
EQUAL-STRESS/EQUAL-VELOCITY SCALING																
Cadaver	Inverted Diaphragm								Upright Diaphragm							
	Mean Distance		X-Difference		Y-Difference		Z-Difference		Mean Distance		X-Difference		Y-Difference		Z-Difference	
	AVG	STD	AVG	STD	AVG	STD	AVG	STD	AVG	STD	AVG	STD	AVG	STD	AVG	STD
72	36.9	15.9	-5.1	17.2	2.4	9.7	-23.3	26.0	124.8	13.9	-34.1	14.6	115.7	11.2	10.2	28.4
75	80.7	14.7	-64.5	10.4	-9.7	7.2	-42.1	23.4								
81	65.2	14.6	-34.2	14.0	49.7	8.2	-6.0	23.3								
86	119.2	15.0	-42.8	14.9	103.0	8.7	-33.4	24.5	81.6	16.3	-43.9	13.1	40.8	8.3	50.2	24.5
TOTAL	**73.1**	**33.0**	**-36.4**	**26.8**	**30.7**	**44.5**	**-27.1**	**27.5**	**106.3**	**26.2**	**-38.3**	**14.7**	**83.6**	**38.7**	**27.3**	**33.3**
STATURE SCALING																
Cadaver	Inverted Diaphragm								Upright Diaphragm							
	Mean Distance		X-Difference		Y-Difference		Z-Difference		Mean Distance		X-Difference		Y-Difference		Z-Difference	
	AVG	STD	AVG	STD	AVG	STD	AVG	STD	AVG	STD	AVG	STD	AVG	STD	AVG	STD
72	38.1	16.4	1.4	15.0	10.2	10.9	-26.6	24.2	110.2	14.3	-22.7	13.1	104.1	12.3	1.2	26.4
75	68.7	15.0	-50.8	9.9	-2.9	7.2	-41.6	22.1								
81	58.2	13.8	-22.8	12.6	46.9	9.0	-12.2	22.0								
86	115.4	14.0	-43.5	14.4	99.4	7.8	-31.0	23.2	81.0	15.8	-44.5	12.6	38.0	7.4	51.4	23.2
TOTAL	**67.7**	**14.0**	**-28.3**	**14.4**	**33.4**	**7.8**	**-28.7**	**23.2**	**97.7**	**20.8**	**-32.0**	**16.8**	**75.8**	**34.6**	**22.7**	**35.3**

Table 54: Comparison of cadaver marker position to GHBMC model nodes for the diaphragm (mm).

NO SCALING																
Cadaver	Inverted Diaphragm								Upright Diaphragm							
	Mean Distance		X-Difference		Y-Difference		Z-Difference		Mean Distance		X-Difference		Y-Difference		Z-Difference	
	AVG	STD	AVG	STD	AVG	STD	AVG	STD	AVG	STD	AVG	STD	AVG	STD	AVG	STD
72	31.2	8.2	12.1	14.5	-5.4	6.1	25.4	4.9	110.3	13.8	-13.3	7.9	93.9	7.8	54.7	17.3
75	16.6	3.2	-16.0	3.3	-3.2	2.2	0.0	2.9								
81	42.0	3.8	-2.6	8.7	25.3	2.4	32.6	3.0								
86	89.1	6.9	-21.6	3.3	85.1	6.3	14.8	1.4	102.4	2.4	-22.6	3.0	24.1	5.3	96.8	1.8
TOTAL	**41.8**	**27.8**	**-6.3**	**16.0**	**21.2**	**37.0**	**17.4**	**13.3**	**106.9**	**10.7**	**-17.3**	**7.7**	**64.0**	**37.8**	**72.8**	**25.6**
EQUAL-STRESS/EQUAL-VELOCITY SCALING																
Cadaver	Inverted Diaphragm								Upright Diaphragm							
	Mean Distance		X-Difference		Y-Difference		Z-Difference		Mean Distance		X-Difference		Y-Difference		Z-Difference	
	AVG	STD	AVG	STD	AVG	STD	AVG	STD	AVG	STD	AVG	STD	AVG	STD	AVG	STD
72	36.2	8.1	6.0	16.9	-13.2	4.6	29.8	6.4	121.6	12.7	-23.1	9.8	100.1	5.8	63.3	18.7
75	35.4	3.0	-32.6	3.3	-13.1	2.2	2.4	3.2								
81	48.5	3.4	-11.2	9.9	25.8	4.2	38.5	3.2								
86	90.2	6.7	-23.3	3.5	85.8	6.1	15.3	1.4	104.6	2.3	-24.3	2.9	23.5	5.0	98.9	1.8
TOTAL	**50.2**	**22.9**	**-15.0**	**18.3**	**16.4**	**41.0**	**20.7**	**14.9**	**114.3**	**12.9**	**-23.6**	**7.1**	**67.3**	**41.2**	**78.5**	**23.2**
STATURE SCALING																
Cadaver	Inverted Diaphragm								Upright Diaphragm							
	Mean Distance		X-Difference		Y-Difference		Z-Difference		Mean Distance		X-Difference		Y-Difference		Z-Difference	
	AVG	STD	AVG	STD	AVG	STD	AVG	STD	AVG	STD	AVG	STD	AVG	STD	AVG	STD
72	30.2	8.7	14.5	13.7	-2.5	6.9	23.7	4.4	106.1	14.2	-9.6	7.3	91.5	8.7	51.4	16.7
75	17.8	3.2	-17.0	3.3	-3.8	2.2	0.1	2.9								
81	39.4	3.9	1.9	8.0	25.1	1.6	29.6	2.9								
86	89.4	6.8	-22.1	3.4	85.3	6.3	15.0	1.4	103.0	2.4	-23.1	3.0	23.9	5.2	97.4	1.8
TOTAL	**41.3**	**27.8**	**-5.0**	**17.3**	**21.9**	**36.5**	**16.4**	**12.1**	**104.8**	**10.3**	**-15.4**	**9.0**	**62.6**	**36.8**	**71.1**	**27.3**

Table 55: Comparison of cadaver marker position to GHBMC model nodes for the liver (mm).

NO SCALING																
Cadaver	Inverted Liver								Upright Liver							
	Mean Distance		X-Difference		Y-Difference		Z-Difference		Mean Distance		X-Difference		Y-Difference		Z-Difference	
	AVG	STD	AVG	STD	AVG	STD	AVG	STD	AVG	STD	AVG	STD	AVG	STD	AVG	STD
72	83.6	63.5	-68.2	68.3	31.4	19.7	21.7	7.6	111.3	19.6	2.0	15.1	24.3	46.0	98.1	27.5
86	58.0	9.4	13.6	20.6	51.3	13.4	8.6	9.2	149.3	28.5	-17.7	28.3	-14.4	21.7	145.2	24.2
TOTAL	**70.8**	**44.8**	**-27.3**	**64.2**	**41.4**	**19.0**	**15.2**	**10.5**	**125.6**	**29.0**	**-5.4**	**21.5**	**9.8**	**41.7**	**115.8**	**34.5**
EQUAL-STRESS/EQUAL-VELOCITY SCALING																
Cadaver	Inverted Liver								Upright Liver							
	Mean Distance		X-Difference		Y-Difference		Z-Difference		Mean Distance		X-Difference		Y-Difference		Z-Difference	
	AVG	STD	AVG	STD	AVG	STD	AVG	STD	AVG	STD	AVG	STD	AVG	STD	AVG	STD
72	101.9	75.9	-84.3	74.5	40.6	30.5	31.2	10.3	131.1	25.0	-4.2	13.8	32.5	43.9	118.3	34.4
86	60.0	9.5	13.1	21.5	53.2	13.0	9.7	9.5	152.9	29.0	-19.1	28.4	-14.2	20.9	148.8	24.8
TOTAL	**81.0**	**55.6**	**-35.6**	**72.8**	**46.9**	**23.1**	**20.4**	**14.7**	**139.3**	**26.9**	**-9.8**	**20.0**	**15.0**	**42.5**	**129.7**	**33.2**
STATURE SCALING																
Cadaver	Inverted Liver								Upright Liver							
	Mean Distance		X-Difference		Y-Difference		Z-Difference		Mean Distance		X-Difference		Y-Difference		Z-Difference	
	AVG	STD	AVG	STD	AVG	STD	AVG	STD	AVG	STD	AVG	STD	AVG	STD	AVG	STD
72	76.9	58.6	-62.0	66.0	27.9	15.6	18.0	6.8	103.9	17.7	4.4	15.7	21.1	46.8	90.3	24.8
86	58.6	9.4	13.5	20.8	51.8	13.3	9.0	9.3	150.4	28.7	-18.1	28.3	-14.3	21.5	146.3	24.4
TOTAL	**67.8**	**40.7**	**-24.3**	**60.9**	**39.9**	**18.6**	**13.5**	**9.0**	**121.4**	**31.5**	**-4.0**	**22.5**	**7.8**	**41.5**	**111.3**	**36.9**

APPENDIX C: Impact response curves.

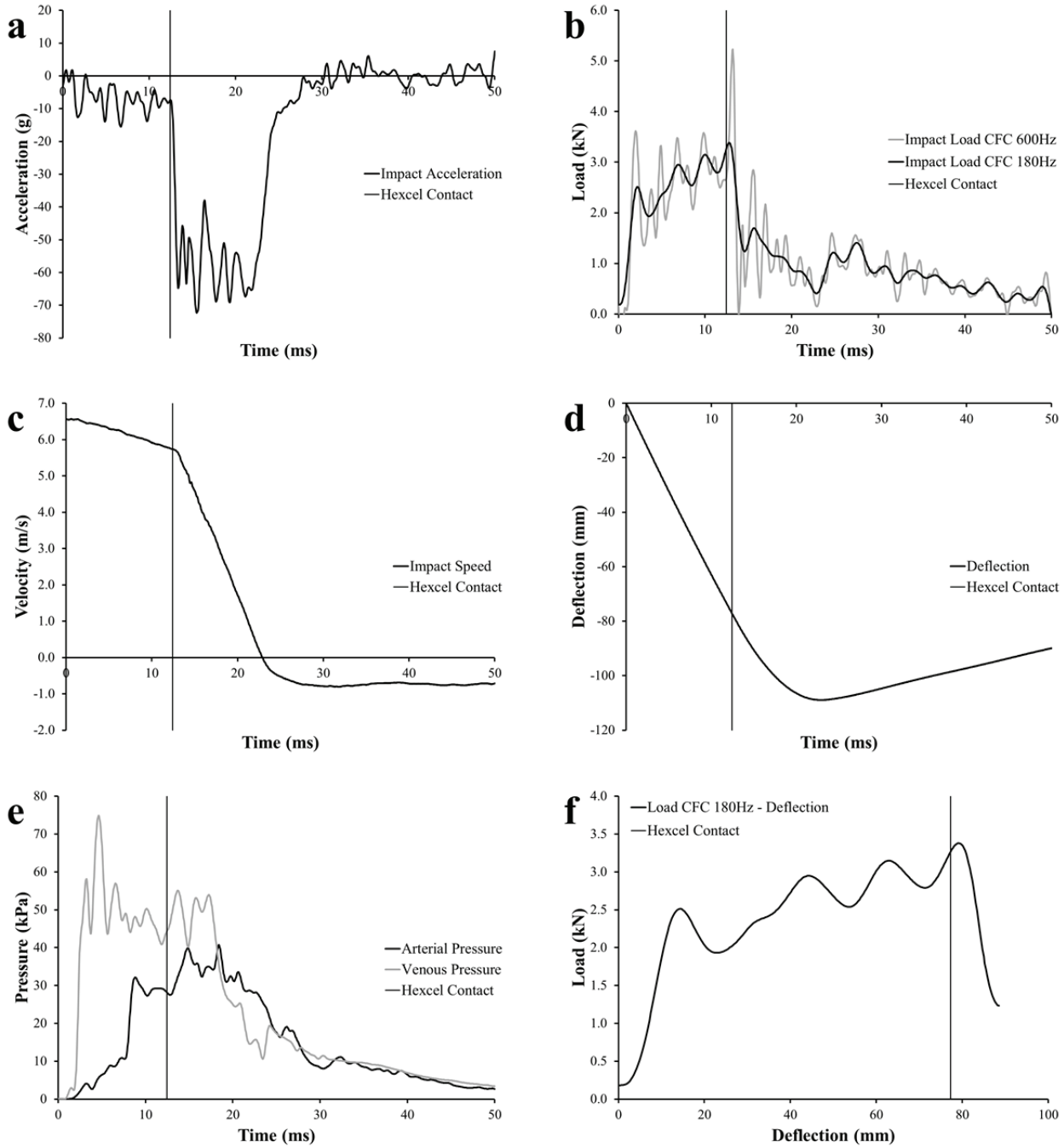

Figure 75: Impact response data for the thoracic rigid-disk impact to SM75 at 6.7 m/s. §

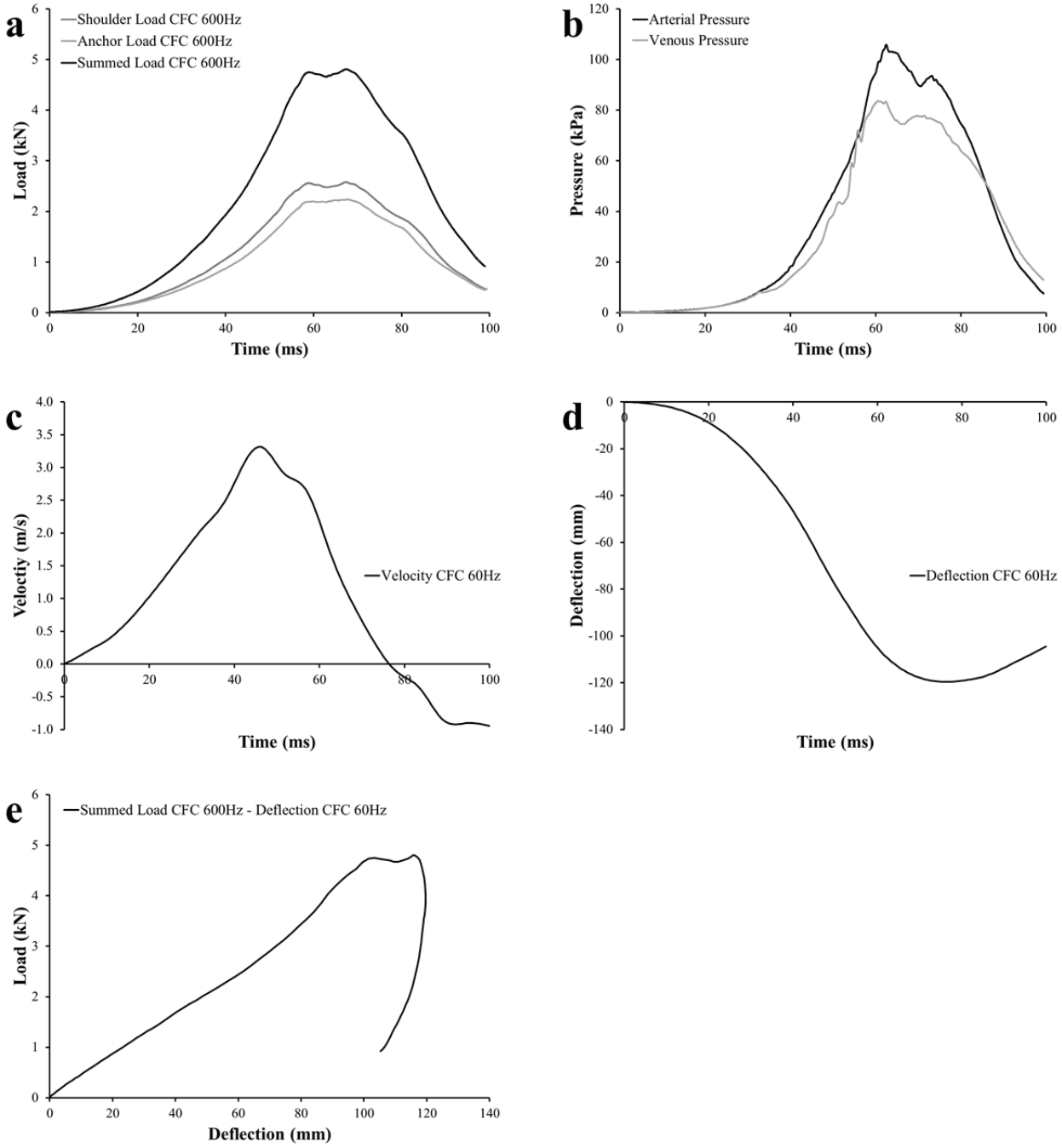

Figure 76: Response data for the 3.0 m/s seatbelt test using SM81. §

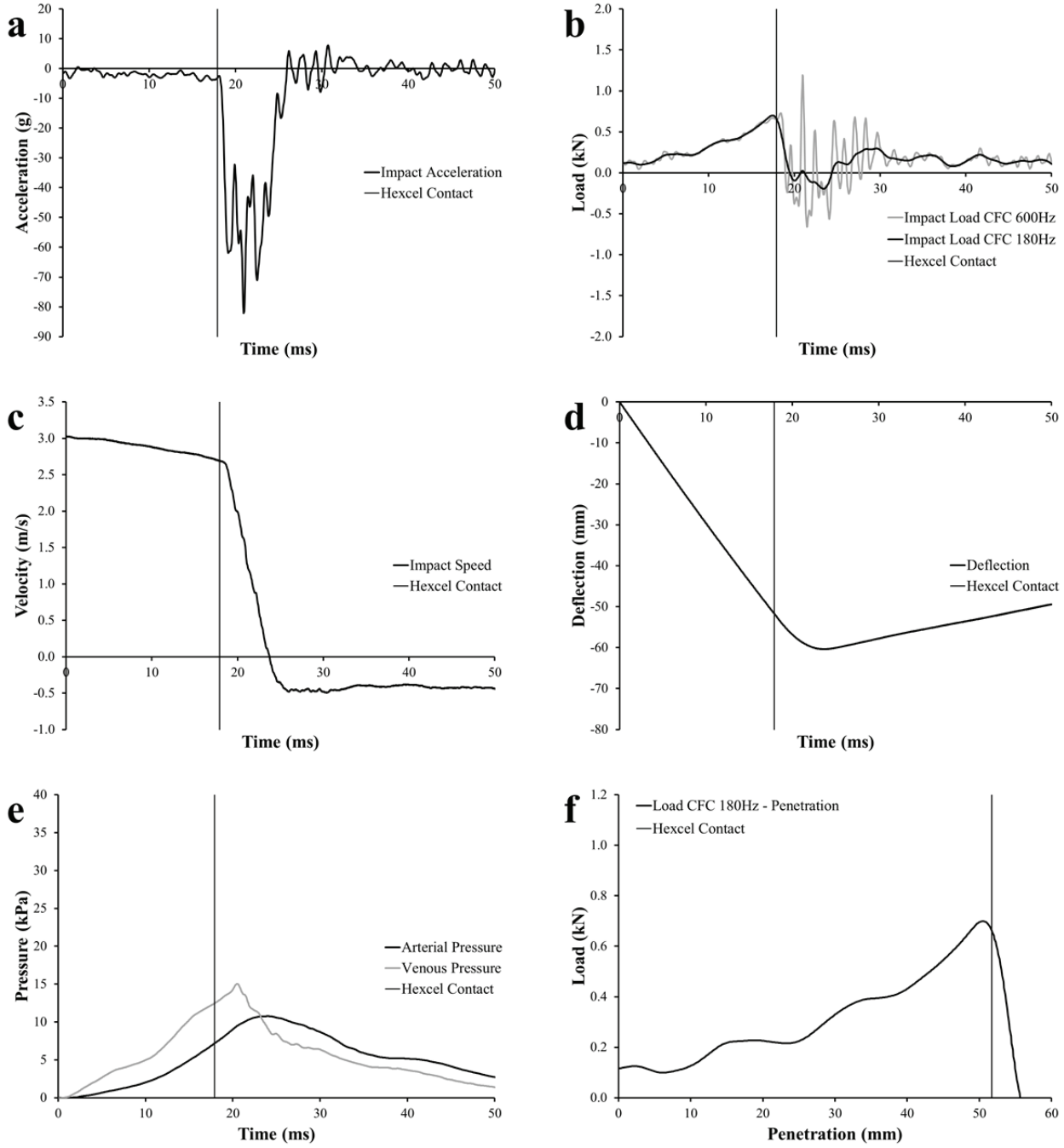

Figure 77: Impact response data for the cylinder impact to SM72 at 3.0 m/s (Test ID: 72-1). §

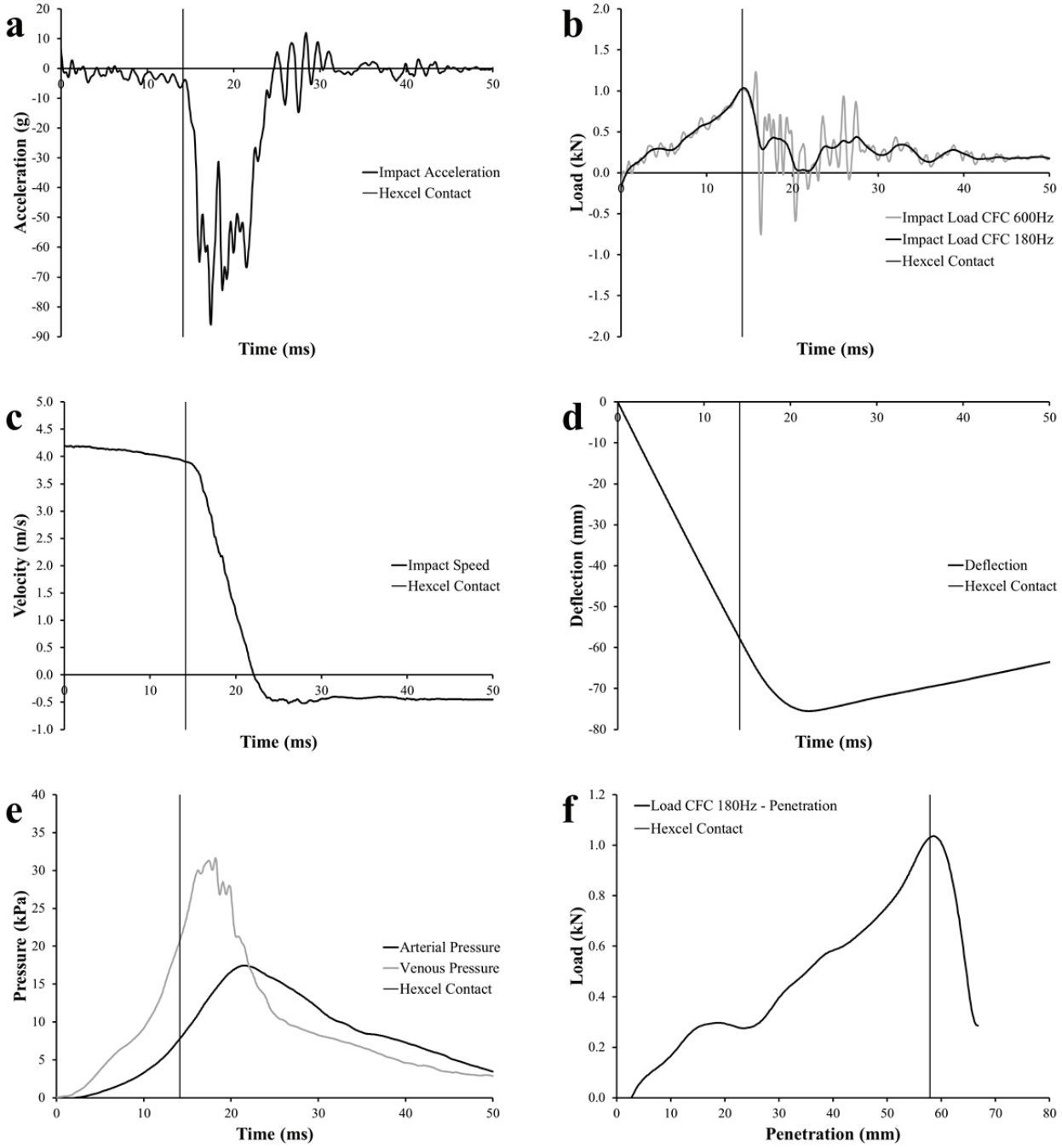

Figure 78: Impact response data for the cylinder impact to SM72 at 4.0 m/s (Test ID: 72-2). §

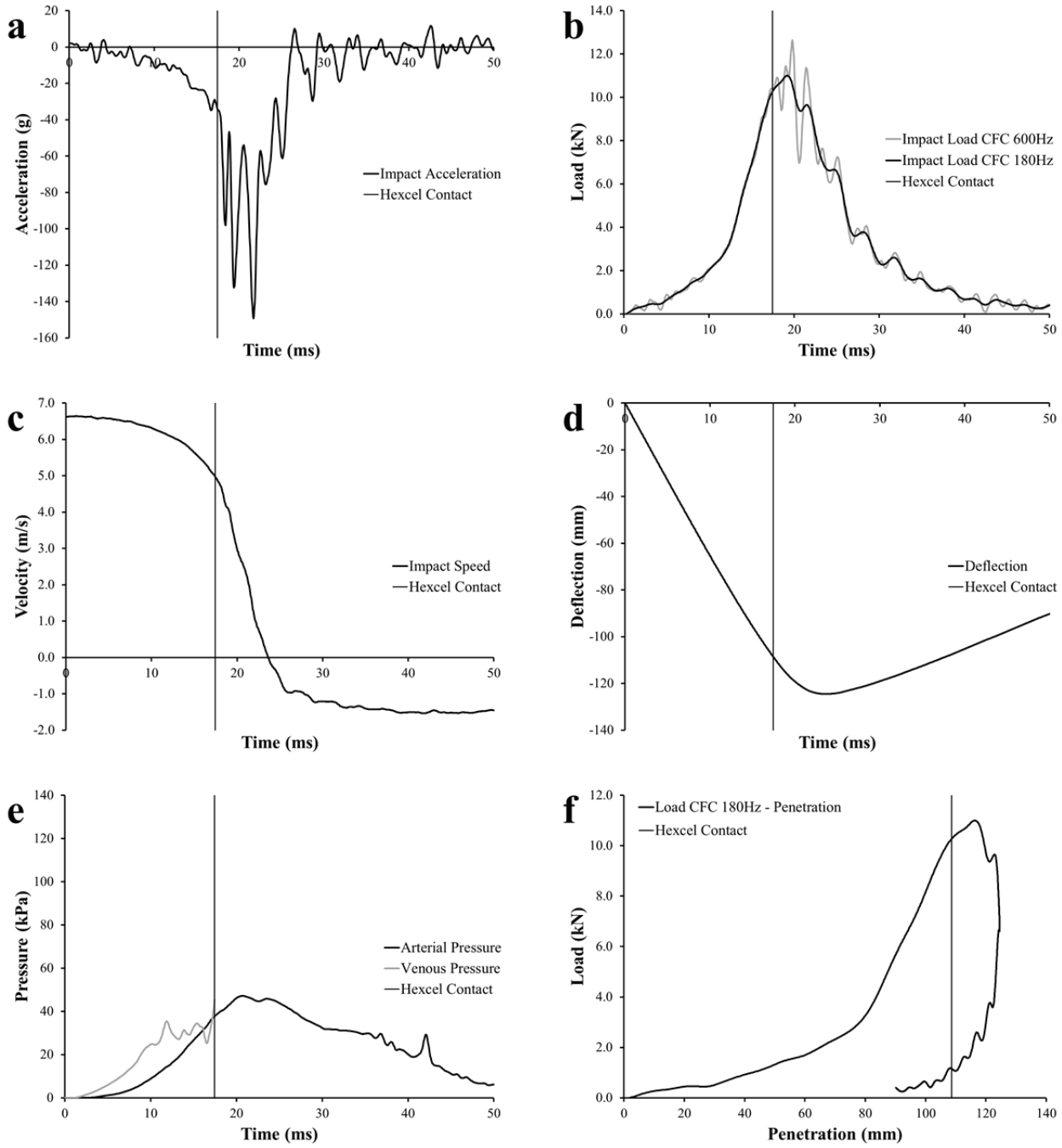

Figure 79: Impact response data for the rigid-bar impact to SM72 at 6.7 m/s (Test ID: 72-3). §

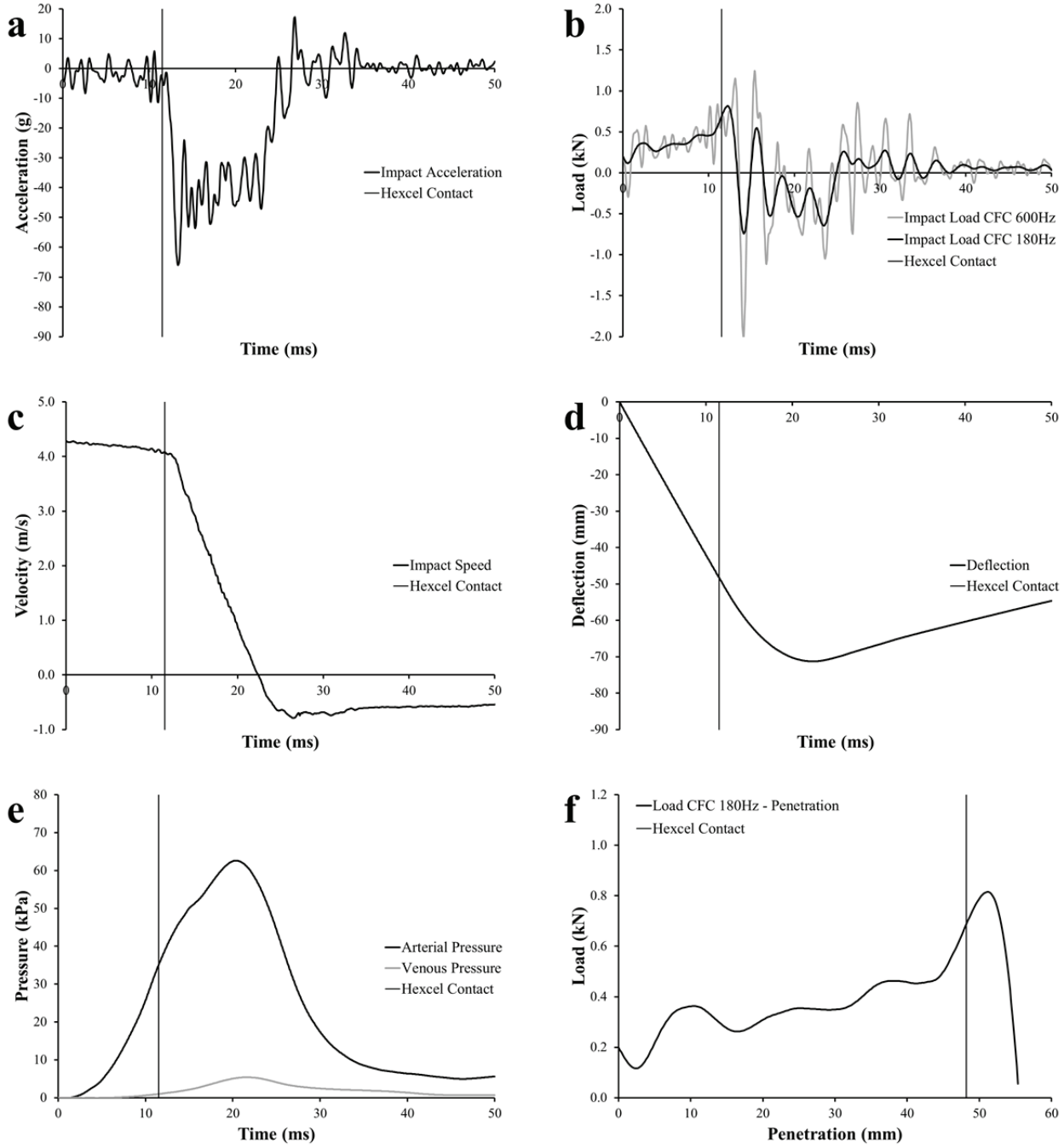

Figure 80: Impact response data for the cylinder impact to SM86 at 3.0 m/s (Test ID: 86-1). §

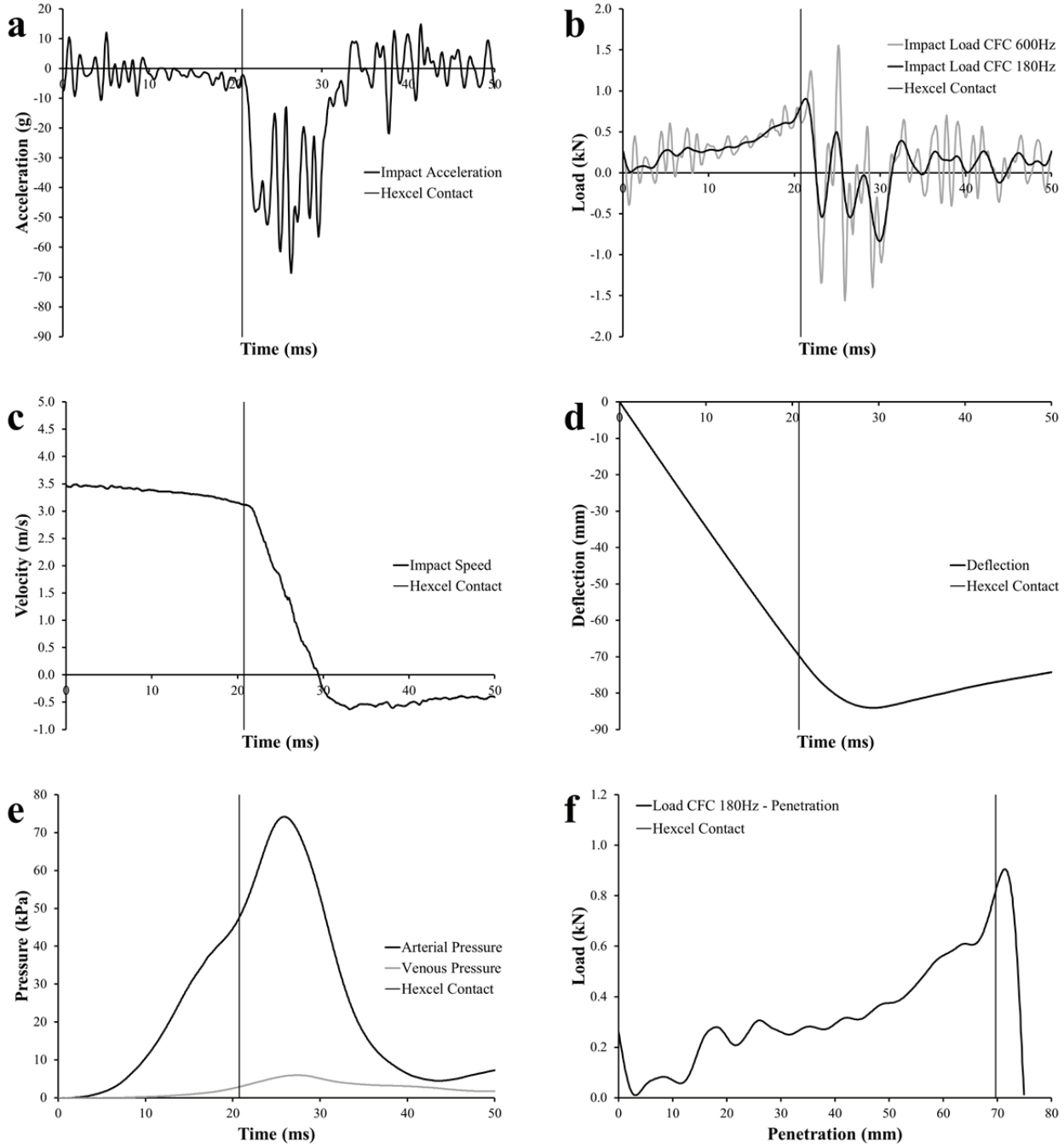

Figure 81: Impact response data for the cylinder impact to SM86 at 4.0 m/s (Test ID: 86-2). §

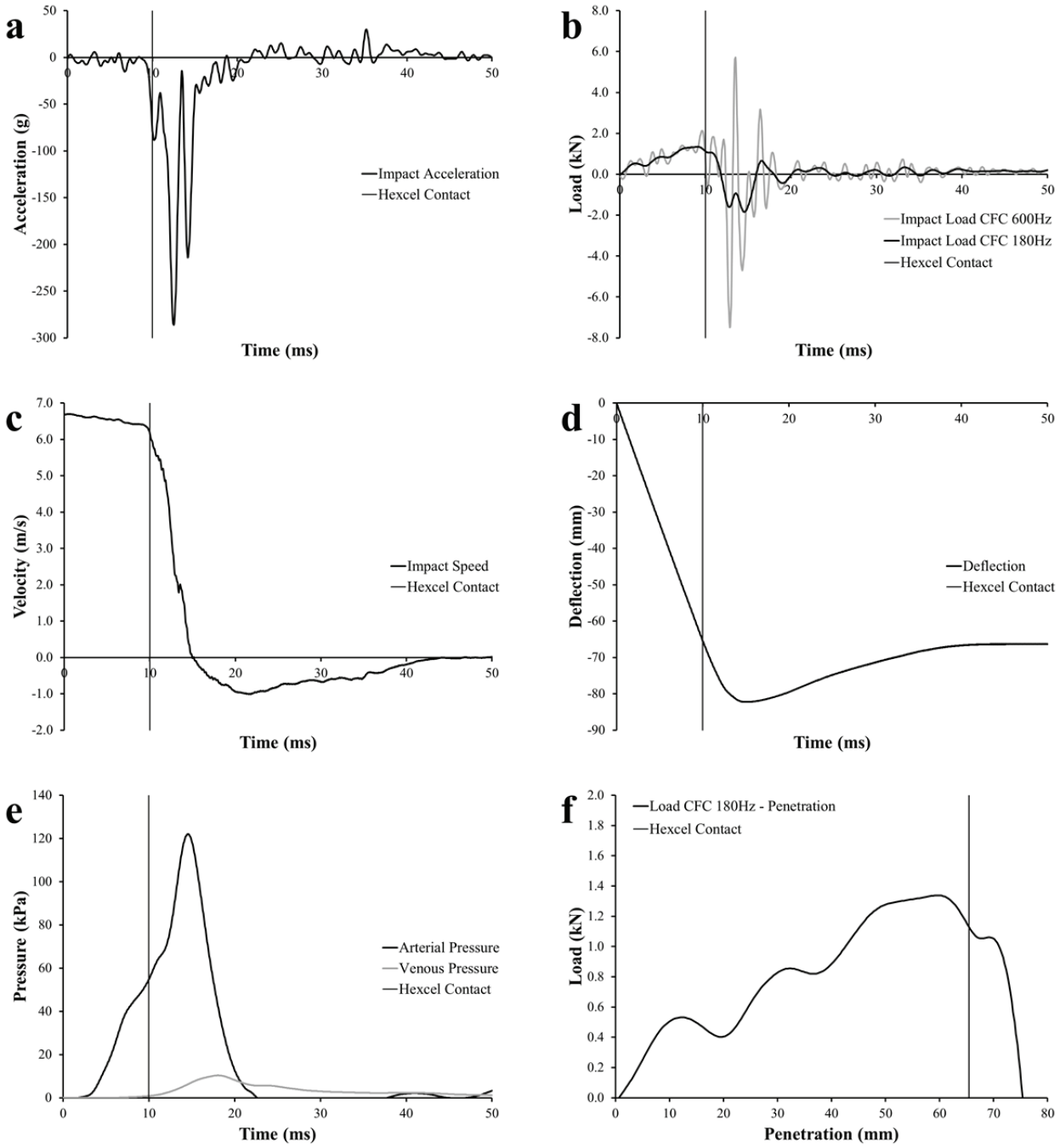

Figure 82: Impact response data for the rigid-bar impact to SM86 at 6.7 m/s (Test ID: 86-3). §

APPENDIX D: High-speed video sequences.

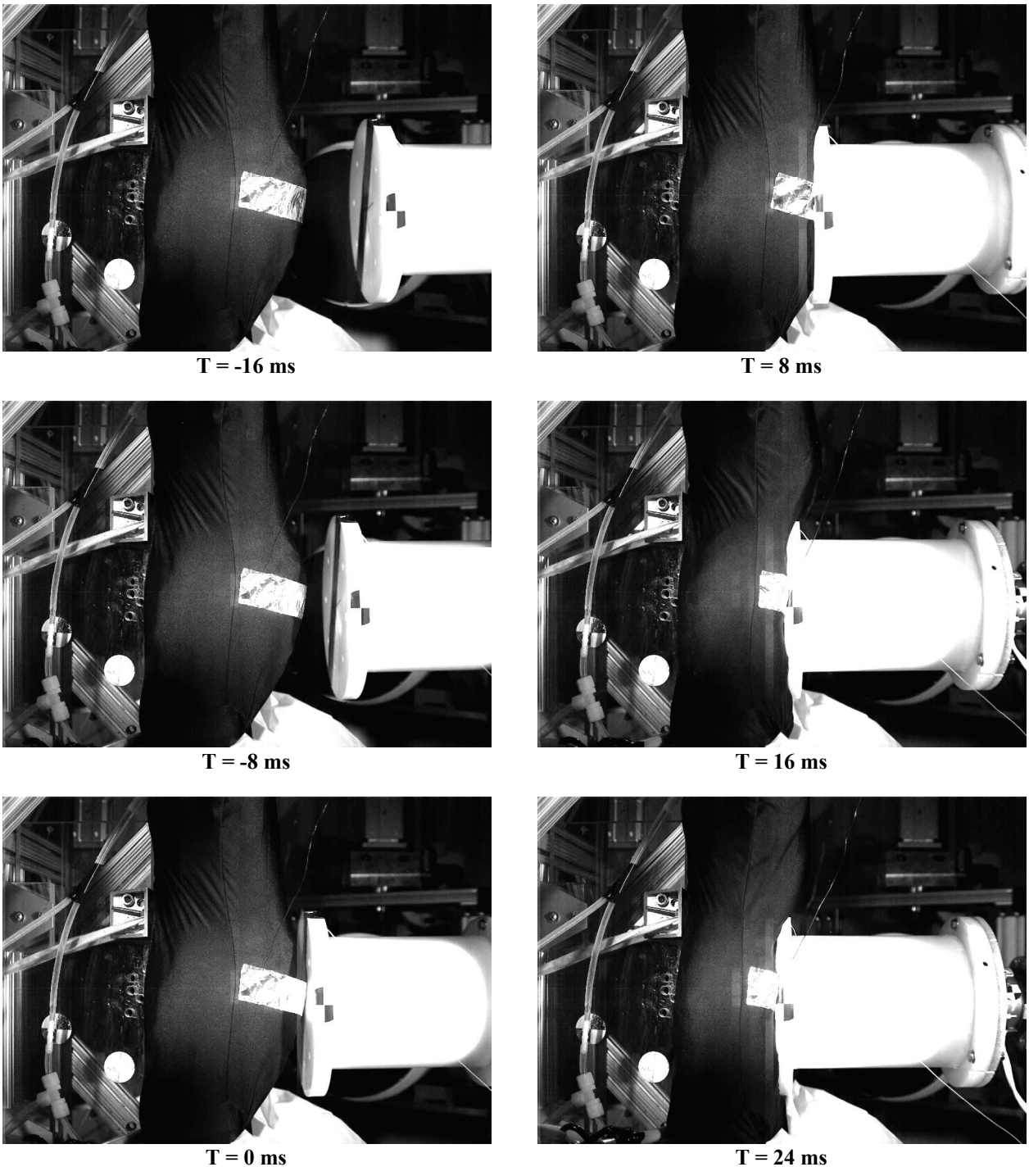

Figure 83: Thoracic rigid-disk impact image sequence from the lateral perspective. §

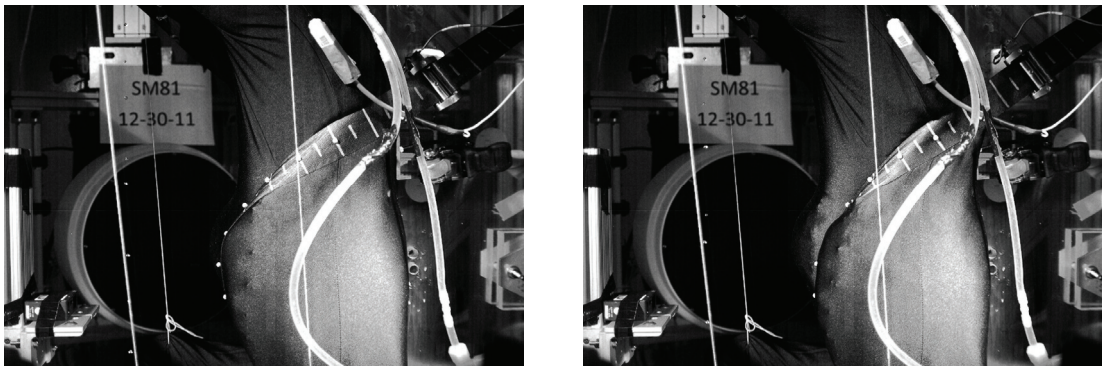

T = 0 ms **T = 32 ms**

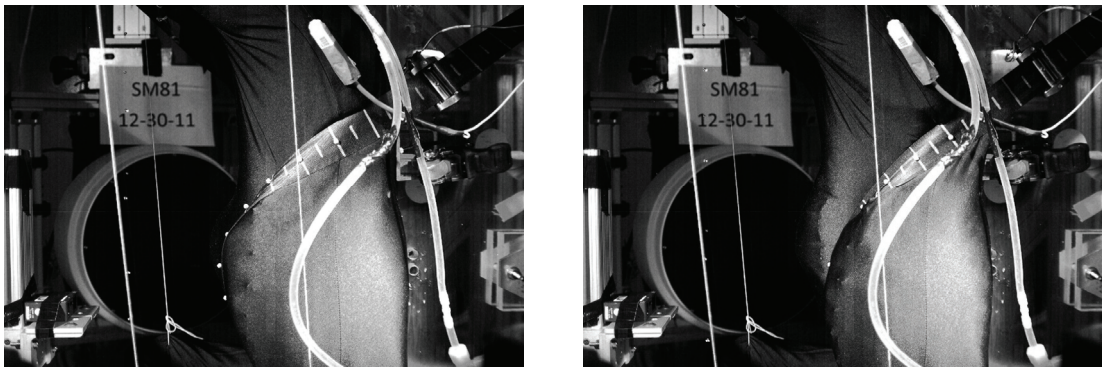

T = 8 ms **T = 40 ms**

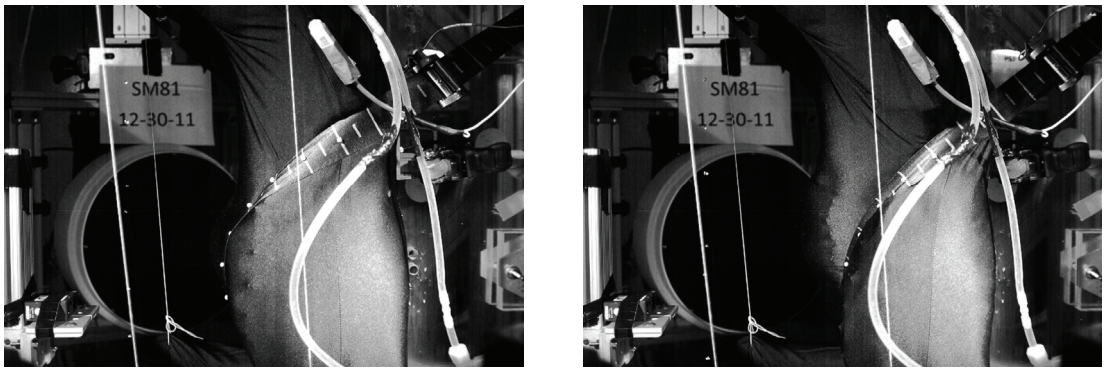

T = 16 ms **T = 48 ms**

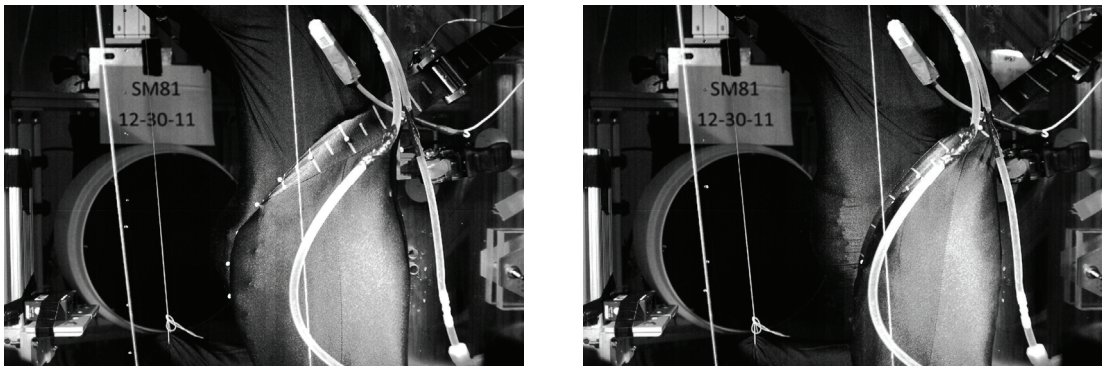

T = 24 ms **T = 56 ms**

Figure 84: Seatbelt loading image sequence from the lateral perspective. §

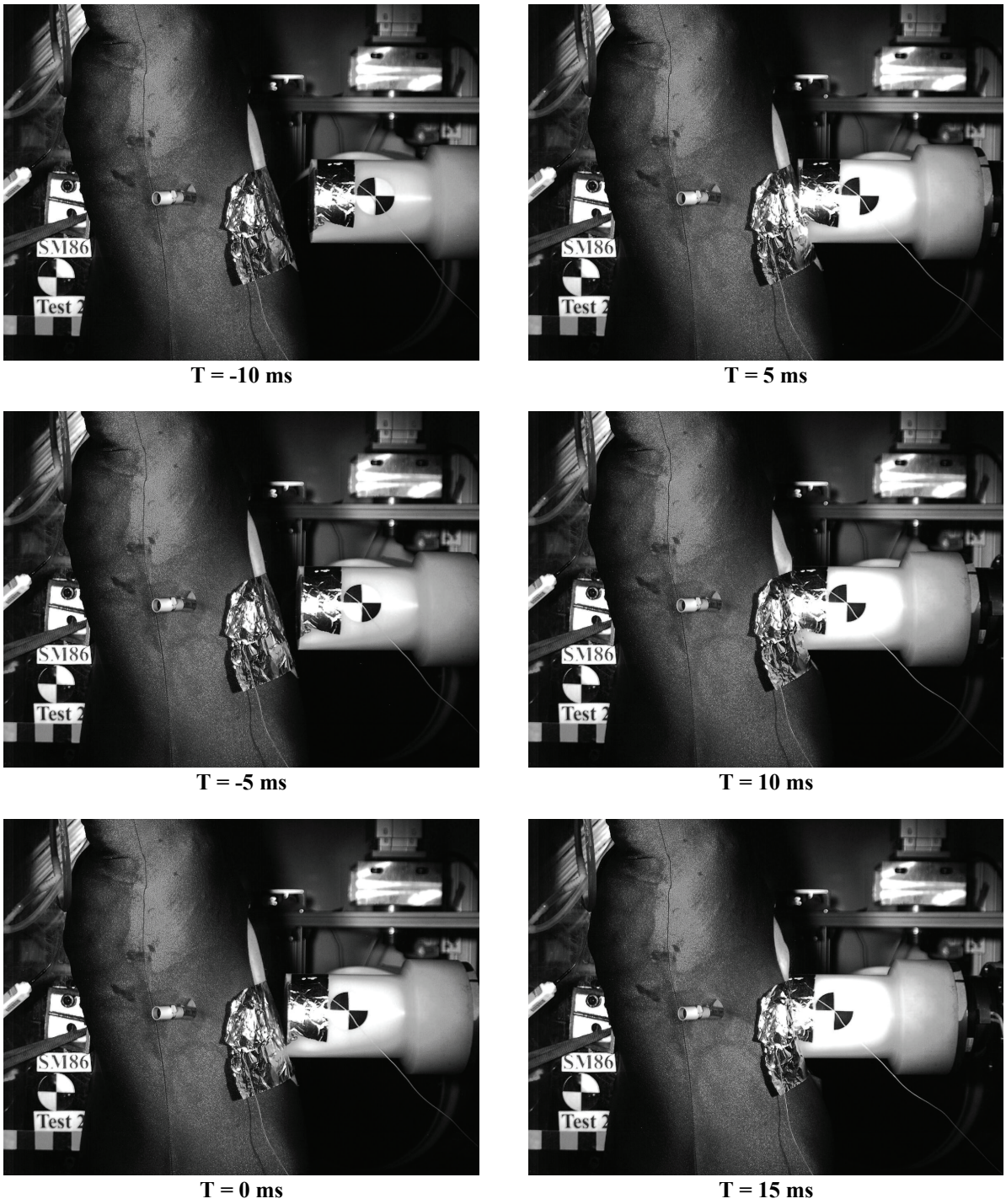

Figure 85: Example of a 4.0 m/s cylinder impact sequence from the lateral perspective for SM86. §

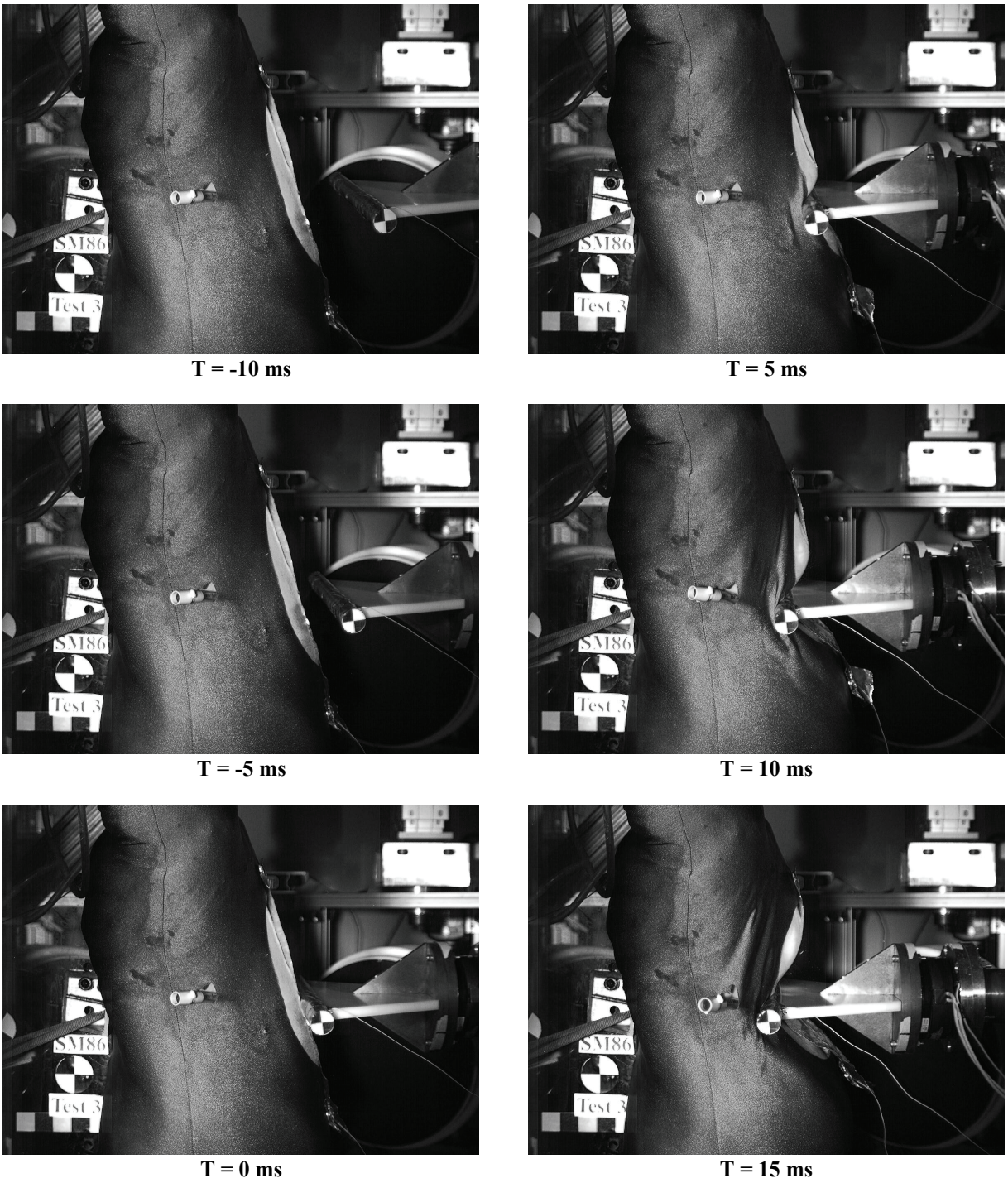

Figure 86: Example of a rigid-bar impact image sequence from the lateral perspective for SM86. §

APPENDIX E: High-speed x-ray image sequences.

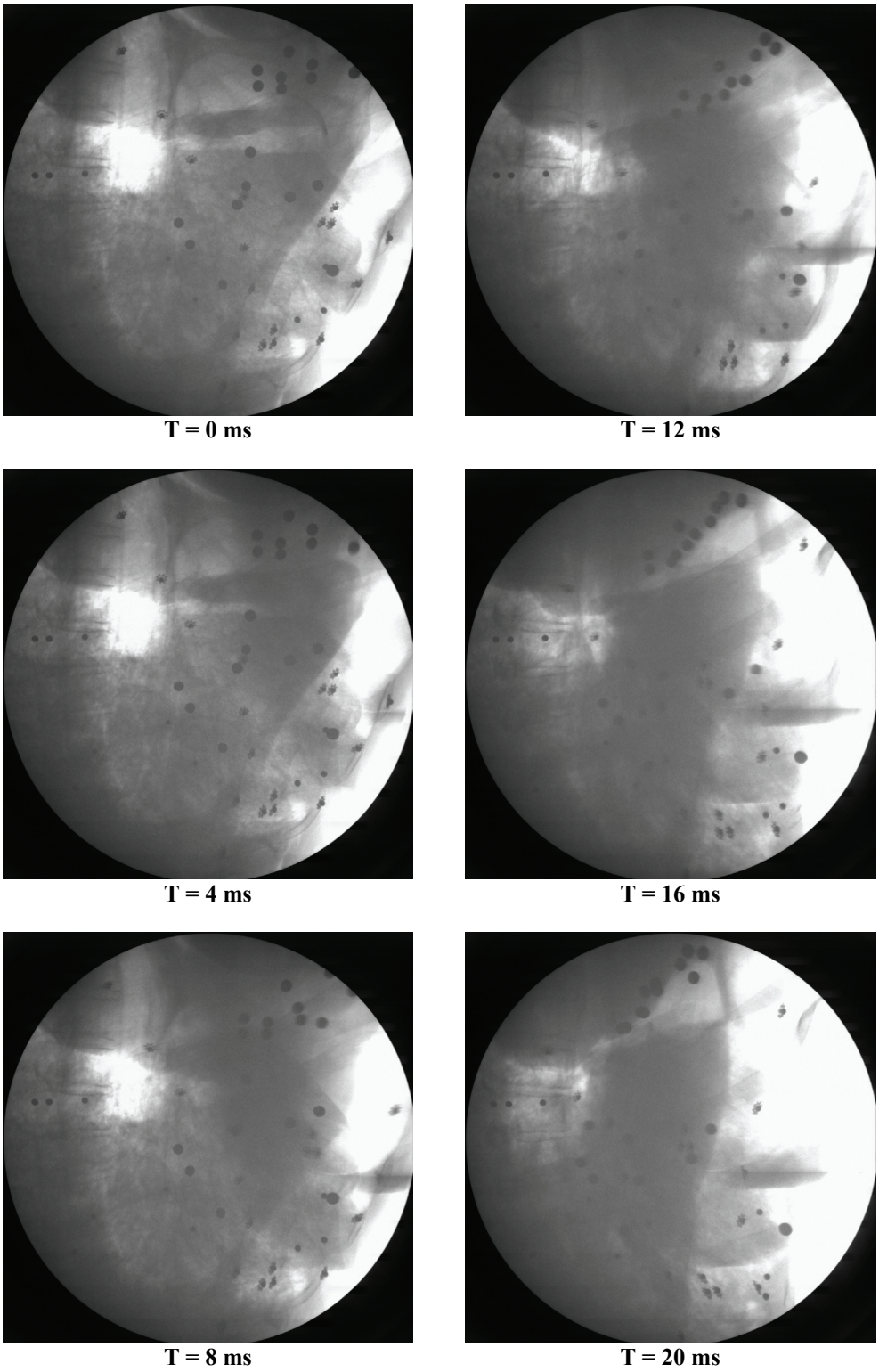

Figure 87: Thoracic rigid-disk impact x-ray image sequence. §

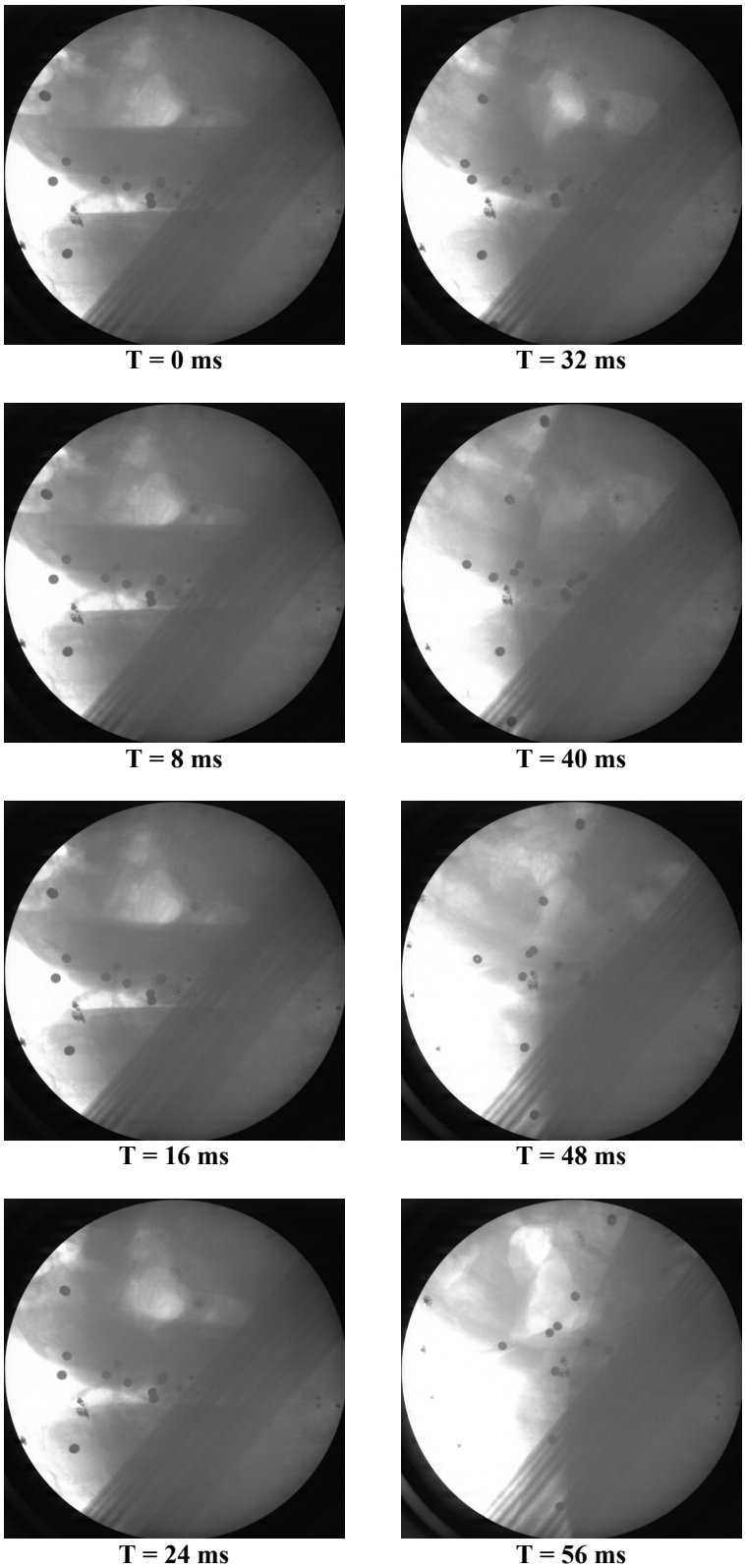

Figure 88: Seatbelt loading x-ray image sequence. §

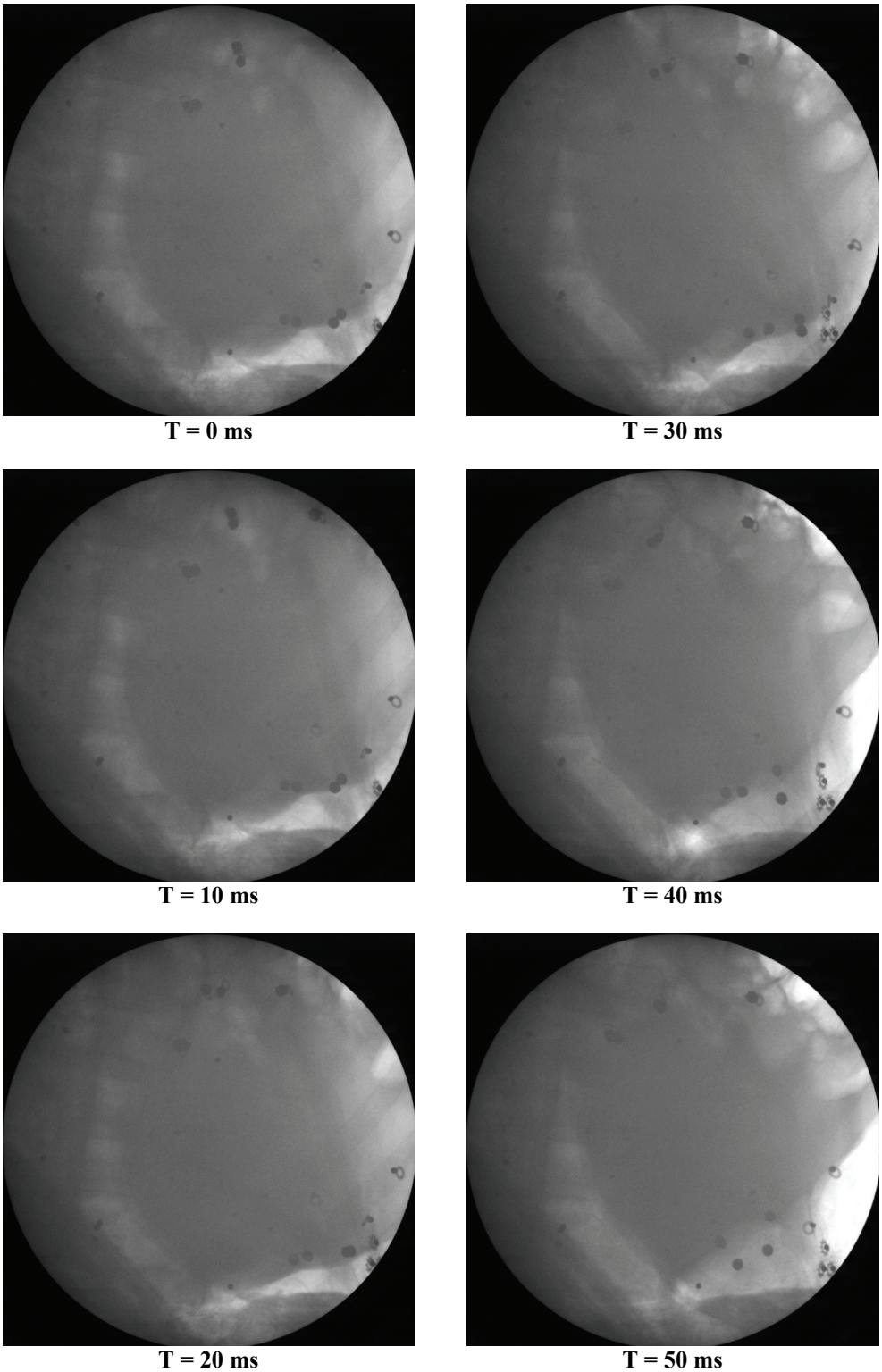

Figure 89: Example of a 4.0 m/s cylinder impact x-ray image sequence from SM72. §

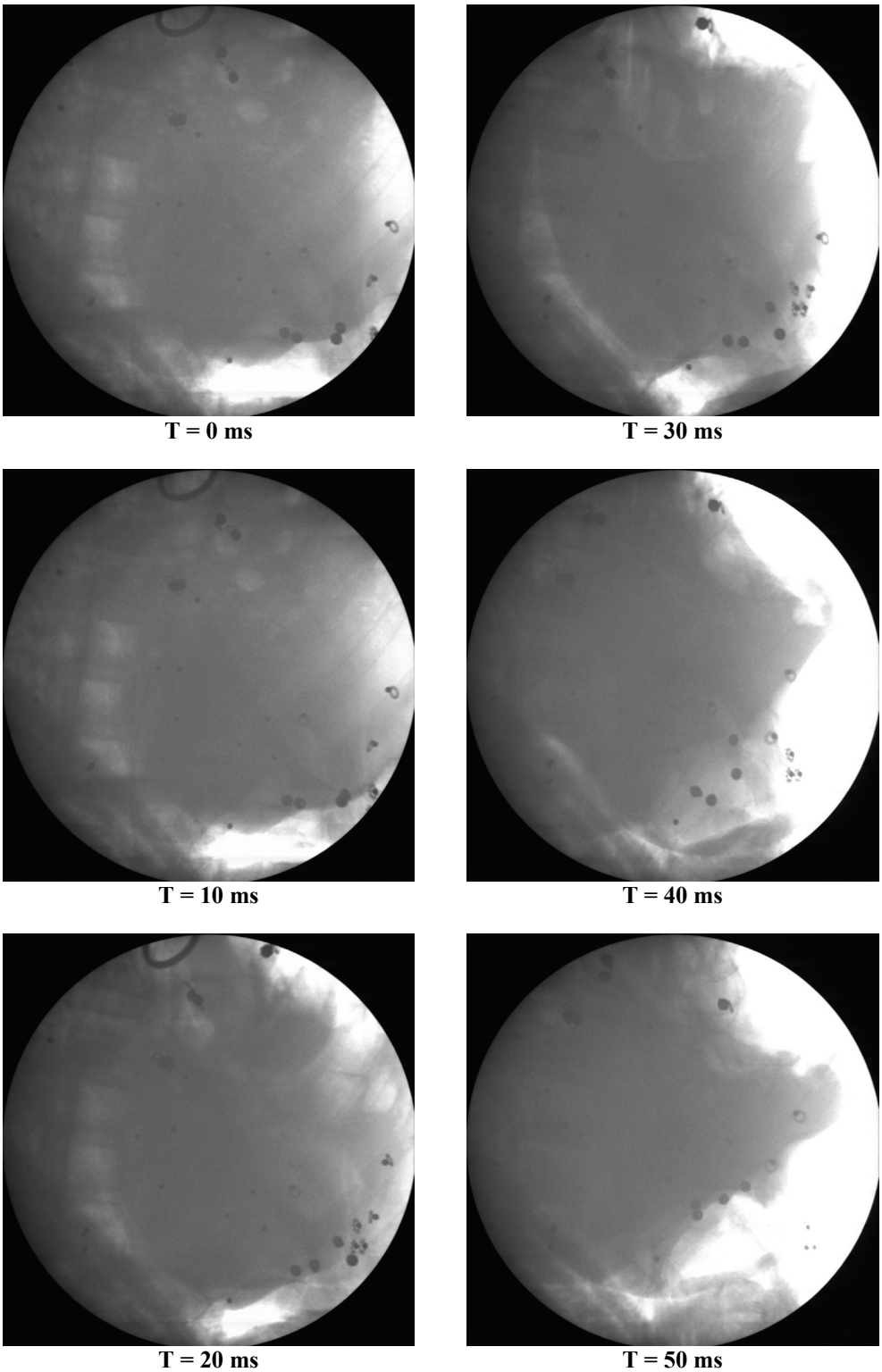

Figure 90: Example of a 6.7 m/s rigid-bar impact x-ray image sequence from SM72. §

APPENDIX F: Kinematic response data.

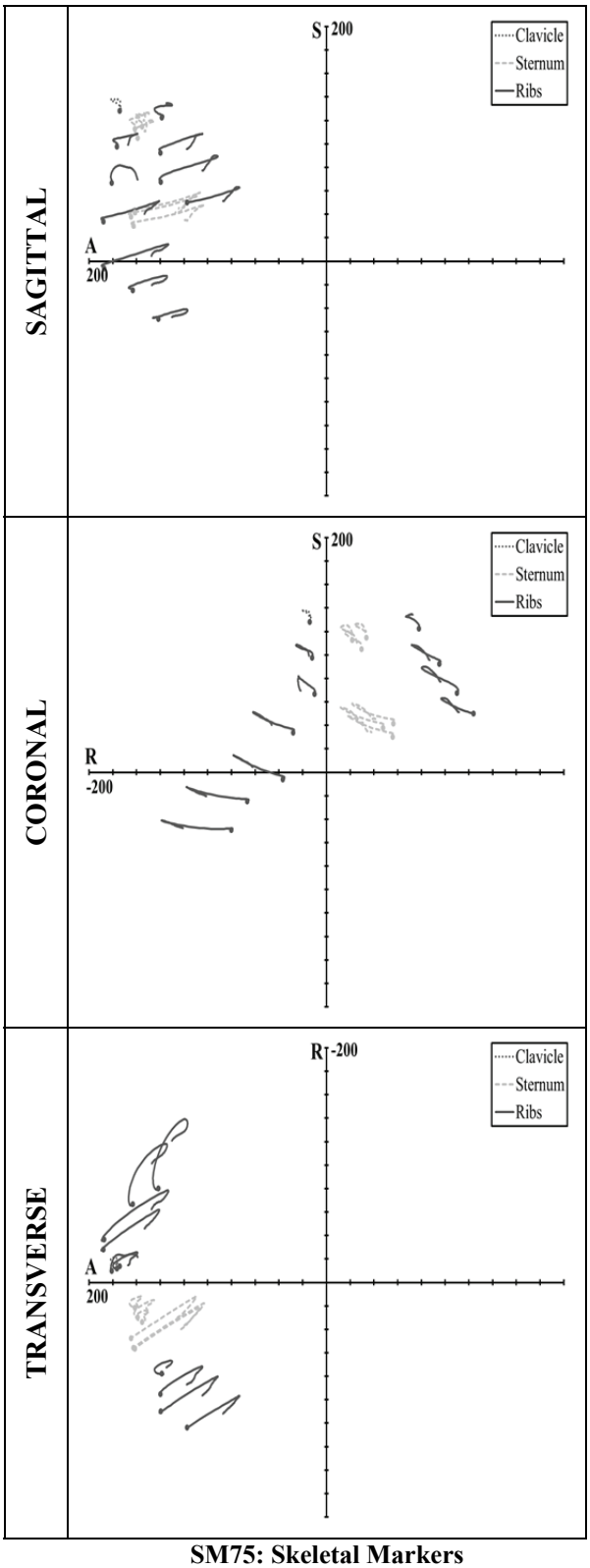

SM75: Skeletal Markers

Figure 91: Trajectories for the thoracic rigid-disk impact. Circles identify initial position. Scale is mm. §

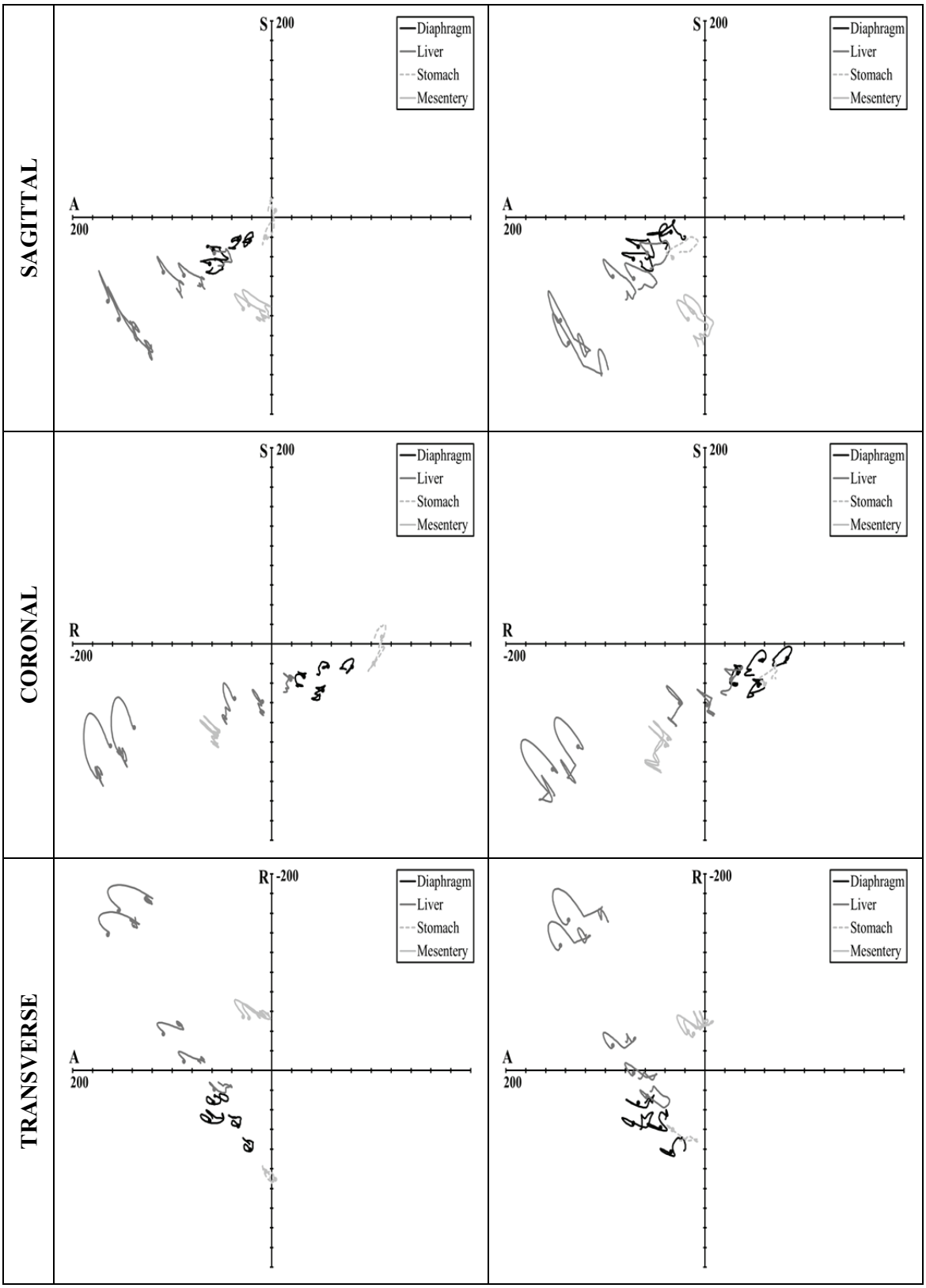

SM72-1: Cylinder 3.0 m/s **SM72-2: Cylinder 4.0 m/s**

Figure 92: Trajectories for the SM72 cylinder impacts. Circles identify initial position. Scale is mm. §

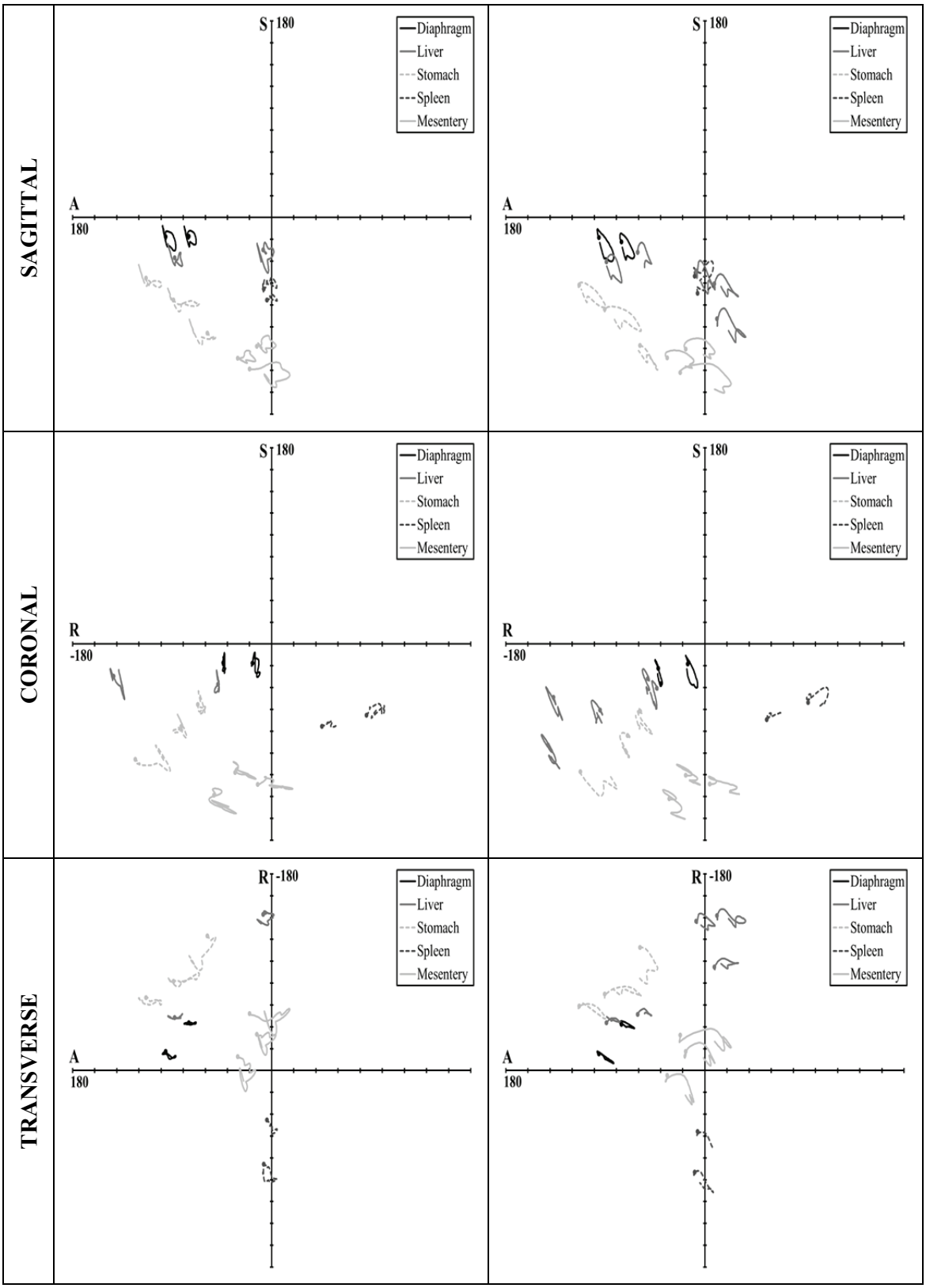

Figure 93: Trajectories for the SM86 cylinder impacts. Circles identify initial position. Scale is mm. §

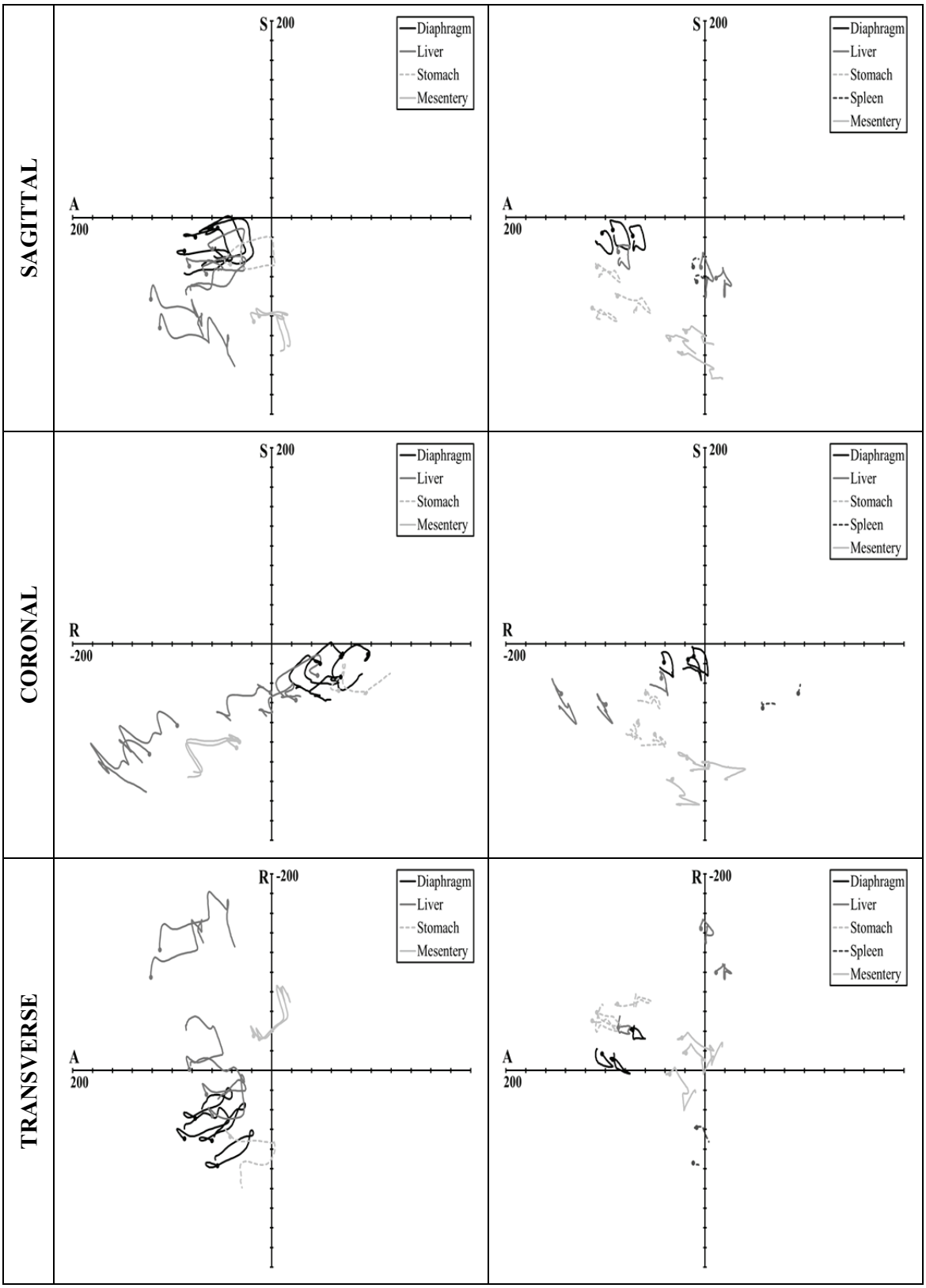

Figure 94: Trajectories for the 6.7 m/s rigid-bar impacts. Circles identify initial position. Scale is mm. §

Table 56: Tracking intervals, initial positions, and excursions for the SM75 6.7 m/s rigid-disk impact.

SM75		Interval (ms)		Initial Position (mm)			Peak Excursion (mm)		
Organ	**Marker**	**Begin**	**End**	**X**	**Y**	**Z**	**X**	**Y**	**Z**
Clavicle	C01	0.0	88.8	174.1	-14.0	128.2	7.8	7.1	9.9
Diaphragm	D01	0.0	40.0	71.2	77.8	-13.4	67.1	18.5	36.8
	D02	0.0	44.8	86.8	82.1	-13.6	71.5	27.8	26.0
	D06	0.0	55.2	80.4	50.1	-14.8	56.3	24.2	34.7
	D07	0.0	56.0	90.8	43.5	-12.6	61.3	28.1	28.0
	D08	0.0	52.8	95.6	56.6	-10.6	67.3	27.5	22.7
	D09	0.0	52.0	88.7	60.8	-12.7	65.2	22.1	28.3
	D10	0.0	49.6	97.7	74.4	-13.8	73.0	26.7	23.0
	D11	0.0	35.2	114.3	88.5	-22.6	73.0	26.4	21.6
Lungs	P01	0.0	47.2	170.3	-45.4	73.8	22.8	26.9	17.2
	P02	0.0	76.0	160.5	-65.8	48.2	17.1	35.8	16.7
	P03	0.0	32.0	133.1	-95.4	74.4	0.8	23.6	12.9
	P04	0.0	48.0	87.7	101.9	136.8	5.9	11.6	21.6
	P05	0.0	43.2	107.7	101.0	122.1	14.4	1.6	23.2
	P06	0.0	88.8	101.9	103.3	101.0	56.6	3.8	19.2
Pericardium	H02	0.0	88.8	152.3	-9.0	76.3	35.3	30.8	17.9
	H03	0.0	88.8	134.4	-25.1	56.4	44.7	32.1	21.4
	H04	0.0	88.8	123.2	-27.3	46.9	44.7	32.8	27.8
	H06	0.0	88.8	74.5	60.3	72.0	27.7	21.2	35.6
	H07	0.0	88.8	88.2	84.1	64.2	58.7	23.4	38.8
	H08	0.0	88.8	96.7	93.9	54.9	62.2	19.9	34.9
	H10	0.0	88.8	63.7	72.0	48.3	42.7	23.9	48.4
Ribs	R02	0.0	65.6	141.7	-80.2	-49.3	24.7	58.8	8.3
	R03	0.0	66.4	163.2	-66.8	-24.9	29.0	51.4	12.4
	R04	0.0	68.8	187.3	-36.8	-6.1	54.2	41.7	20.6
	R05	0.0	68.8	187.8	-28.1	33.6	47.2	33.8	17.7
	R06	0.0	77.6	180.9	-10.0	66.8	21.8	14.0	14.8
	R07	0.0	77.6	176.6	-12.0	97.5	17.4	13.6	11.1
	R08	0.0	52.8	138.6	77.8	122.3	8.7	11.1	12.4
	R09	0.0	79.2	139.8	95.0	92.5	35.3	23.3	16.0
	R10	0.0	79.2	139.7	110.0	67.6	48.1	29.8	22.3
	R11	20.8	79.2	117.4	123.8	50.1	44.1	27.2	13.0
Sternum	S01	0.0	88.8	155.4	33.6	114.6	6.0	10.1	12.1
	S02	0.0	88.8	161.3	21.7	112.5	5.9	9.8	13.0
	S03	0.0	88.8	159.1	29.6	104.9	13.8	14.7	15.2
	S04	0.0	88.8	161.3	56.5	41.6	54.8	34.8	16.8
	S05	0.0	88.8	164.7	47.5	38.0	55.3	35.5	17.2
	S06	0.0	88.8	162.5	55.8	30.1	59.7	38.1	17.8

Table 57: Tracking intervals, initial positions, and excursions for the SM81 3.0 m/s seatbelt test.

SM81		Interval (ms)		Initial Position (mm)			Peak Excursion (mm)		
Organ	**Marker**	**Begin**	**End**	**X**	**Y**	**Z**	**X**	**Y**	**Z**
Belt	B01	0.0	63.2	152.2	-9.7	-95.5	106.3	21.9	1.4
	B02	0.0	64.0	138.4	-1.8	-46.3	89.1	17.5	3.5
	B03	0.0	64.0	120.0	1.7	-2.7	79.7	13.1	3.0
	B04	34.4	67.2	82.9	8.2	42.7	74.1	13.5	8.7
Liver	L01	0.0	42.4	67.4	-49.4	-44.3	9.0	5.9	0.4
	L02	0.0	42.4	66.9	-53.6	-34.4	8.0	5.4	0.9
	L03	0.0	45.6	75.3	-66.6	-25.8	9.3	7.4	0.4
	L04	0.0	39.2	36.6	-87.1	-15.2	5.0	3.1	1.1
	L06	0.0	52.0	69.3	-31.5	-44.1	22.1	9.3	3.1
	L08	0.0	52.0	96.9	-48.0	-45.9	25.3	15.4	4.9
Diaphragm	D01	0.0	52.8	79.2	35.2	-58.8	14.1	2.3	2.7
	D02	0.0	49.6	72.4	10.9	-46.3	17.8	2.4	9.5
	D03	0.0	44.8	56.0	13.9	-53.6	7.0	0.9	1.2
	D04	0.0	53.6	69.2	-2.8	-41.8	25.3	9.5	11.3
	D05	0.0	48.0	74.4	-24.5	-35.6	15.2	6.3	2.3
	D06	0.0	52.8	97.6	-41.2	-31.7	23.9	12.2	8.8
	D07	0.0	49.6	54.1	-18.7	-43.6	14.8	5.8	2.2
Sternum	S01	0.0	44.0	118.7	0.0	-28.8	26.0	3.2	10.0
	S02	0.0	44.0	114.7	2.1	-21.7	23.9	3.4	9.1
	S03	0.0	44.0	116.0	-2.8	-21.3	24.1	2.8	9.5

Table 58: Tracking intervals, initial positions, and excursions for the SM72 3.0 m/s cylinder impact.

SM72-1		Interval (ms)		Initial Position (mm)			Peak Excursion (mm)		
Organ	**Marker**	**Begin**	**End**	**X**	**Y**	**Z**	**X**	**Y**	**Z**
Diaphragm	D01	0	100	62.4	51.3	-47.2	14.2	11.0	9.8
	D02	0	100	58.6	32.5	-33.2	14.7	8.8	10.0
	D03	0	100	33.7	56.4	-22.9	9.6	11.0	8.8
	D04	0	100	21.7	80.8	-23.2	7.1	12.1	8.1
Stomach	G01	0	100	-3.8	110.6	7.3	7.6	7.4	12.7
	G02	0	100	48.4	45.1	-38.9	21.4	13.7	8.8
	G03	0	100	6.1	102.5	-19.3	8.5	11.1	17.9
Liver	L01	0	100	57.7	19.0	-36.1	17.6	7.0	12.9
	L02	0	100	88.1	-9.3	-58.7	20.6	9.9	14.1
	L03	0	100	108.9	-37.3	-55.6	20.3	12.5	25.9
	L04	0	100	164.7	-138.1	-85.0	31.6	23.1	40.4
	L05	0	100	153.8	-162.0	-103.7	34.2	26.7	41.0
Mesentery	M01	0	100	48.9	-7.1	-134.6	36.6	21.6	20.2
	M02	0	100	92.5	-94.0	-147.5	36.8	38.3	20.1
	M03	0	100	52.6	-60.3	-125.8	29.9	22.5	20.7
	M04	0	100	28.8	-54.7	-92.9	22.2	17.3	15.3
	M05	0	100	22.8	-53.5	-88.8	21.7	14.6	15.3

Table 59: Tracking intervals, initial positions, and excursions for the SM72 4.0 m/s cylinder impact.

SM72-2		Interval (ms)		Initial Position (mm)			Peak Excursion (mm)		
Organ	**Marker**	**Begin**	**End**	**X**	**Y**	**Z**	**X**	**Y**	**Z**
Diaphragm	D01	0	180	71.8	53.7	-42.1	19.5	11.0	12.3
	D02	0	180	67.1	33.0	-29.6	15.9	7.9	12.9
	D03	0	180	44.5	57.9	-16.8	13.4	17.8	15.7
	D04	0	180	34.0	82.5	-14.5	14.4	14.5	12.0
Stomach	G02	0	180	32.5	59.9	-40.8	25.5	13.5	21.0
Liver	L01	0	180	58.1	26.1	-35.9	22.6	12.6	20.3
	L02	0	180	71.8	2.3	-61.9	23.3	21.4	24.4
	L03	0	180	92.5	-25.5	-60.1	22.8	28.7	32.2
	L04	0	180	145.3	-127.3	-104.7	36.9	28.6	44.4
	L05	0	180	137.1	-153.1	-127.7	51.0	31.7	40.3
Mesentery	M01	11	180	17.1	7.6	-145.5	25.6	22.5	24.8
	M02	0	180	63.1	-82.9	-175.5	31.7	43.0	16.8
	M03	0	180	21.5	-44.5	-145.5	21.3	28.6	28.3
	M04	0	180	16.9	-39.6	-103.3	20.1	20.4	31.9
	M05	0	180	11.4	-37.2	-96.6	19.8	23.0	34.8

Table 60: Tracking intervals, initial positions, and excursions for the SM72 6.7 m/s rigid-bar impact.

SM72-3		Interval (ms)		Initial Position (mm)			Peak Excursion (mm)		
Organ	**Marker**	**Begin**	**End**	**X**	**Y**	**Z**	**X**	**Y**	**Z**
Diaphragm	D01	0	180	87.6	69.2	-33.9	44.7	31.3	24.0
	D02	0	180	76.8	48.7	-20.0	36.9	30.8	28.9
	D03	0	180	60.1	71.3	-10.2	33.6	37.9	31.1
	D04	0	180	54.4	96.7	-10.5	35.8	35.9	36.3
Stomach	G02	0	180	41.6	67.3	-47.5	45.0	57.3	33.2
Liver	L01	0	180	59.6	46.1	-31.9	34.0	41.8	22.4
	L02	0	180	65.7	24.2	-57.3	39.6	36.9	18.8
	L03	0	180	82.7	-1.2	-49.5	33.6	53.8	30.1
	L04	0	180	121.4	-94.9	-83.1	53.9	58.3	43.0
	L05	0	180	112.3	-122.8	-112.3	76.6	59.1	42.6
Mesentery	M03	0	56	23.4	-39.4	-155.9	47.3	41.0	26.7
	M04	0	73	18.1	-35.3	-105.8	31.0	51.0	29.9
	M05	0	70	12.4	-32.4	-99.9	30.9	52.9	30.9

Table 61: Tracking intervals, initial positions, and excursions for the SM86 3.0 m/s cylinder impact.

SM86-1		Interval (ms)		Initial Position (mm)			Peak Excursion (mm)		
Organ	**Marker**	**Begin**	**End**	**X**	**Y**	**Z**	**X**	**Y**	**Z**
Diaphragm	D01	0	110	95.8	-17.4	-17.6	9.1	6.8	12.7
	D03	0	110	75.0	-43.9	-17.3	6.7	2.9	10.7
Liver	L05	0	110	87.9	-48.6	-36.8	7.1	3.3	12.8
	L07	0	110	7.6	-143.0	-29.4	9.5	13.7	34.2
Stomach	G10	0	110	113.5	-66.8	-55.5	14.1	7.0	16.7
	G11	0	110	88.8	-81.7	-75.4	23.3	10.8	19.8
	G12	28	108	58.2	-123.4	-105.6	16.4	37.2	24.5
Spleen	N15	0	74	4.4	45.4	-75.4	9.3	12.5	4.7
	N16	0	110	7.1	85.6	-65.2	11.9	16.4	14.4
Mesentery	M20	0	110	30.8	-12.7	-128.6	16.2	38.5	6.8
	M21	0	110	13.4	-33.0	-117.7	17.2	28.0	9.6
	M22	0	110	19.9	-52.2	-138.5	36.2	34.7	18.8

Table 62: Tracking intervals, initial positions, and excursions for the SM86 4.0 m/s cylinder impact.

SM86-2		Interval (ms)		Initial Position (mm)			Peak Excursion (mm)		
Organ	**Marker**	**Begin**	**End**	**X**	**Y**	**Z**	**X**	**Y**	**Z**
Diaphragm	D01	0	130	95.9	-15.4	-18.4	13.5	8.9	21.9
	D03	0	130	75.5	-42.1	-22.4	11.7	3.7	16.4
Liver	L05	0	130	89.1	-43.6	-40.7	14.0	7.8	19.0
	L06	0	88	60.7	-51.6	-31.8	12.3	5.0	13.8
	L07	0	130	8.0	-136.8	-48.9	17.0	8.6	20.8
	L08	0	130	-8.4	-94.9	-60.6	21.7	7.7	11.7
	L09	0	100	-11.0	-141.9	-92.5	25.9	10.5	21.7
Stomach	G10	0	130	113.8	-59.0	-61.6	23.9	11.6	20.8
	G11	0	130	90.6	-69.9	-83.9	33.0	8.7	20.2
	G12	31	130	58.6	-112.6	-117.0	15.8	35.4	22.5
Spleen	N15	0	56	6.6	55.9	-69.4	13.5	14.5	6.6
	N16	0	130	9.2	93.2	-53.8	16.7	18.4	13.8
Mesentery	M20	0	130	34.1	4.4	-128.6	24.1	28.1	9.2
	M21	0	130	17.3	-17.3	-120.5	26.2	16.8	9.9
	M22	0	130	22.3	-32.4	-142.0	45.9	22.0	18.6

Table 63: Tracking intervals, initial positions, and excursions for the SM86 6.7 m/s rigid-bar impact.

SM86-3		Interval (ms)		Initial Position (mm)			Peak Excursion (mm)		
Organ	**Marker**	**Begin**	**End**	**X**	**Y**	**Z**	**X**	**Y**	**Z**
Diaphragm	D01	0	105	92.5	-11.2	-12.7	17.0	14.4	19.6
	D03	0	105	72.5	-41.1	-18.6	12.4	9.3	14.9
	D04	25	105	103.4	-17.0	-15.7	10.7	13.4	21.4
Liver	L05	0	105	87.0	-43.9	-34.9	12.0	11.2	17.5
	L07	0	105	3.9	-144.2	-50.6	12.3	14.9	30.8
	L08	0	105	-11.3	-99.5	-61.5	15.2	8.8	19.3
Stomach	G10	0	105	108.4	-59.3	-50.1	23.4	14.2	15.6
	G11	0	105	87.9	-67.5	-79.9	33.5	11.5	17.2
	G12	0	105	77.0	-103.7	-116.8	39.2	42.7	20.7
	G13	13	105	113.2	-50.6	-92.0	25.0	13.5	14.7
Spleen	N15	0	50	8.3	57.9	-65.4	12.2	14.8	6.8
	N16	0	27	11.6	93.9	-50.2	5.4	2.0	8.7
Mesentery	M20	0	105	35.4	3.8	-124.1	26.0	36.7	14.0
	M21	0	105	19.0	-18.0	-116.4	27.6	21.8	14.3
	M22	0	105	23.0	-33.0	-138.4	40.5	27.2	27.1

CHAPTER 5

Summary

The research described in this dissertation generated novel biomechanical data that contributes to the field of injury biomechanics with the characterization of abdominal injury mechanisms in motor vehicle collisions and the quantification of the local tissue tolerance and regional response of the abdomen in crash-specific loading modes. The methodologies, results, and implications of each of the studies included in this dissertation are summarized herein.

Field accident data from the Crash Injury Research and Engineering Network (CIREN) database were analyzed to determine the occupant and crash characteristics associated with moderate and serious hollow abdominal organ injuries occurring in motor vehicle collisions (MVCs). Based on this analysis, 19 cases in the CIREN database with a jejunum-ileum injury were investigated to further examine potential hollow organ injury mechanisms, resulting in the following conclusions:

- In frontal crashes with adult occupants, no clear association was found between hollow organ injury incidence and age or anthropometry,
- Hollow organ injuries were associated with high crash severity; 58% of all occupants that sustained AIS3+ abdominal injuries to the hollow organs only were involved in crashes with a delta-V above 50 kmph,
- The percentage of abdominal injuries attributed to the hollow organs was higher for rear seat occupants compared to right front passengers or drivers,
- Lap-shoulder seatbelt interaction was a common factor for hollow organ injury. Compared to the incidence of seatbelt use in the CIREN database (68%), solid organ injury was associated with reduced restraint use (52%), whereas hollow organ injury was associated with increased seatbelt use (100%),
- The majority of occupants with jejunum-ileum injuries also sustained abdominal skin contusions attributed to the seatbelt. Occupants with seatbelt contusions high on the abdomen, suggesting improper seatbelt routing or submarining, typically sustained injuries to the proximal jejunum, whereas occupants with lower abdominal skin contusions sustained injuries to the distal jejunum and ileum.

The association between injury location and seatbelt routing found in this analysis supports a localized mechanism for hollow organ injury. For example, axial tension that results in the straightening of local curvature in combination with a lateral contact load applied due to lap-belt loading of the abdomen may

generate local tearing injuries of the jejunum. The classification of the environment in which these injuries occur can be applied to the design of controlled experiments to further investigate injury mechanisms, determine failure tolerances, and evaluate safety technologies.

Dynamic equibiaxial tension tests were conducted on tissue samples obtained from the human post-mortem stomach, small intestine, and colon to characterize the material properties and failure tolerance of these tissues. Tests were conducted using a custom equibiaxial device designed to apply high-rate multidirectional stretch to cruciate samples. The samples were oriented with the material axes of the tissue aligned with the stretching axes or offset from the stretching axes by 22 degrees. Samples were stretched to failure at a target strain rate of 100 s^{-1}. Regional and directional variations in material response were quantified, resulting in the following conclusions:

- The average Green-Lagrange strain at failure for all organs ranged from 11% to 16% in the circumferential direction and 12% to 14% in the longitudinal direction,
- Average stress at failure was greater in the longitudinal direction for all organs. The average 2nd Piola Kirchhoff stress at failure was on the order of 2 MPa for all organs in the circumferential direction and 3 MPa for all organs in the longitudinal direction,
- The data indicated an increased resistance to stretch in the longitudinal direction compared to the circumferential direction, which is consistent with the expansion in organ circumference that is expected during digestion,
- Trends indicating regional variations within organs and throughout the length of the digestive tract were identified; however, in general the material properties were not significantly different between the stomach, small intestine, and colon.

The material response and failure thresholds of the stomach, small intestine, and colon were quantified at strain rates relevant to abdominal loading in MVCs. The equibiaxial response data quantified in this study contribute to material property validation data for these organs at the component-level with an approach representative of the complex, multi-axial mechanical behavior expected *in vivo*.

The effects of cadaver orientation on the relative position of the abdominal organs of two cadavers were quantified with the cadavers in upright and inverted postures, resulting in the following conclusions:

- Cadaver preparation had a minimal influence on the position of the abdominal organs (11 to 20 mm overall); however, the boundary conditions and coupling between organ systems affected by these techniques have a potentially large effect on the dynamic response of the abdomen,

- Cadaver posture had a much larger influence on the relative position of the abdominal organs, with an average difference in diaphragm position in the upright and inverted postures of 106 mm,
- The position of the inverted cadaver diaphragm compared better to the Global Human Body Models Consortium (GHBMC) 50^{th}-percentile male model geometry; however, cadaver diaphragm position did not compare better to the human subject diaphragm in either posture.

Knowledge of the relative position and orientation of the internal organs under different experimental conditions will aid in the interpretation of regional experimental data and the correlation of experimental results to impact simulations used for the prediction of injury.

High-speed biplane x-ray imaging was used to investigate the relative kinematics of the thoracic and abdominal organs of four cadavers in response to eight crash-specific loading modes including blunt abdominal and thoracic impacts and driver-shoulder seatbelt loading, resulting in the following conclusions:

- Internal organ motion in response to blunt loading indicated that the soft tissues in the direct path of the impact followed the trajectory of the seatbelt or the impactor. Tissues lateral, superior, or inferior to the impactor were displaced outward away from the path of the impact,
- A clear difference in internal organ motion occurred in response to distributed thoracic loading compared to direct interaction of the thorax with the seatbelt,
- Abdominal impacts of varying severity produced characteristic looping patterns of the soft tissues.

Global force-deflection response data can be used in conjunction with the local internal kinematics data from this study to form an association between the internal and external responses. Quantification of the kinematics response of individual organs can be used to drive future research for the investigation of internal organ injury mechanisms for crash-induced loading. These data can be applied to validate internal organ motion generated in human body finite element model simulations used to assess occupant safety in motor vehicle collisions.

CONTRIBUTIONS TO THE FIELD

The research described in this dissertation is intended to be published in scientific journals and refereed proceedings as summarized in Table 64. Portions of this research were presented at scientific conferences as described in Table 65, and the honors received for this research are summarized in Table 66.

Table 64: Publication plan for research in this dissertation.

Ch.	Title	Publication
2	Abdominal Injury Patterns and Mechanisms Identified with CIREN Case Analysis	*Transportation Safety J* §
		J of Trauma §
3	Material Properties of the Post-Mortem Colon in High-Rate Equibiaxial Elongation	*Biomed Sci Instrum,* 48: 171-178, 2012
	Dynamic Material Properties of the Post-Mortem Human Colon	*IRCOBI Proceedings:* 124-132, 2013
	Material Properties of the Post-Mortem Gastrointestinal Tract in High-Rate Equibiaxial Elongation	*J of Biomechanics* §
4	Kinematics of the Thoracoabdominal Contents under Various Loading Scenarios	*Stapp Car Crash J,* 56: 1-48, 2012
	The Effects of Cadaver Orientation on the Relative Position of the Abdominal Organs	*Annals Adv Automot Med,* 57: 209-223, 2013
-	Impact and Injury Response of the Abdomen	*Accidental Injury: Biomechanics and Prevention*

§Publications currently in preparation.

Table 65: Additional presentations of research.

Ch.	Topic	Conference
3	Dynamic Material Properties of the Abdominal Organs	Rocky Mountain Bioengineering Symposium, 2012
		The Ohio State University Injury Biomechanics Symposium, 2012
		ASME Summer Bioengineering Conference, 2012*
		Biomedical Engineering Society Annual Meeting, 2012*
		International Research Council on Biomechanics of Injury, 2013
4	Relative Position and Kinematics of the Thoracoabdominal Organs	Biomedical Engineering Society Annual Meeting, 2012
		Stapp Car Crash Conference, 2012
		Association for the Advancement of Automotive Medicine, 2013

*Poster presentations.

Table 66: Honors received for research in this dissertation.

Year	Award
2012	John Paul Stapp Award Stapp Car Crash Journal and Conference
2012	First Place, Student Paper Award Stapp Car Crash Journal and Conference
2012	Dr. Margaret H. Hines Award for Best Oral Presentation The Ohio State University Injury Biomechanics Symposium
2012	First Place, Best Paper Award Rocky Mountain Bioengineering Symposium
2011	Runner-up, International Student Safety Technology Design Competition Enhanced Safety of Vehicles

REFERENCES

Anderson, P. A., Rivara, F. P., Maier, R. V., and Drake, C. (1991). The epidemiology of seatbelt-associated injuries. *The Journal of Trauma and Acute Care Surgery,* 31(1), 60-67.

Appleby, J. P., and Nagy, A. G. (1989). Abdominal injuries associated with the use of seatbelts. *The American Journal of Surgery,* 157(5), 457-458.

Ball, C. G., Feliciano, D. V., and Mattox, K. L. (2010). Combined splenectomy and nephrectomy for trauma: morbidity, mortality, and outcomes over 30 years. *The Journal of Trauma and Acute Care Surgery,* 68(3), 519-521.

Beillas, P., Lafon, Y., and Smith, F. W. (2009). The effects of posture and subject-to-subject variations on the position, shape and volume of abdominal and thoracic organs. *Stapp Car Crash Journal,* 53, 127-154.

Bondy, N. (1980). Abdominal injuries in the national crash severity study. *National Center for Statistics and Analysis Collected Technical Studies,* 2*,* 59-80.

Brunon, A., Bruyere-Garnier, K., and Coret, M. (2010). Mechanical characterization of liver capsule through uniaxial quasi-static tensile tests until failure. *Journal of Biomechanics,* 43(11), 2221-2227.

Carrillo, E. H., Somberg, L. B., Ceballos, C. E., Martini Jr, M. A., Ginzburg, E., Sosa, J. L., and Martin, L. C. (1996). Blunt traumatic injuries to the colon and rectum. *Journal of the American College of Surgeons,* 183(6), 548-553.

Cavanaugh, J. M., Nyquist, G. W., Goldberg, S. J., and King, A. I. (1986). Lower abdominal tolerance and response. Proc. 30th Stapp Car Crash Conference, 41-63.

Christmas, A. B., Wilson, A. K., Manning, B., Franklin, G. A., Miller, F. B., Richardson, J. D., and Rodriguez, J. L. (2005). Selective management of blunt hepatic injuries including nonoperative management is a safe and effective strategy. *Surgery,* 138(4), 606-611.

Demer, L. L., and Yin, F. C. (1983). Passive biaxial mechanical properties of isolated canine myocardium. *The Journal of Physiology,* 339(1), 615-630.

Deng, B., Begeman, P. C., Yang, K. H., Tashman, S., and King, A. I. (2000). Kinematics of human cadaver cervical spine during low speed rear-end impacts. *Stapp Car Crash Journal,* 44, 171-188.

Egorov, V. I., Schastlivtsev, I. V., Prut, E. V., Baranov, A. O., and Turusov, R. A. (2002). Mechanical properties of the human gastrointestinal tract. *Journal of Biomechanics,* 35(10), 1417-1425.

Elhagediab, A. M., and Rouhana, S. W. (1998). Patterns of abdominal injury in frontal automotive crashes. ESV Paper No. 98-S1-W-26.

Eppinger, R. H. (1976). Prediction of thoracic injury using measurable experimental parameters. Proc. 6th International Technical Conference on Experimental Safety Vehicles, 770-779. U.S. Department of Transportation, Washington, D.C.

Fabian, T. C., and Bee, T. K. (2008). Liver and Biliary Tract. In D. V. Feliciano, K. L. Mattox, and E. E. Moore (Eds.), *Trauma, 6th Edition* (pp. 637-660). New York: The McGraw-Hill Companies, Inc.

Foster, C. D., Hardy, W. N., Yang, K. H., King, A. I., and Hashimoto, S. (2006). High-speed seatbelt pretensioner loading of the abdomen. *Stapp Car Crash Journal,* 50, 27-51.

Frampton, R., and Lenard, J. (2009). The potential for further development of passive safety. *Annals of Advances in Automotive Medicine,* 53, 51-60.

Frampton, R., Lenard, J., and Compigne, S. (2012). An in-depth study of abdominal injuries sustained by car occupants in frontal crashes. *Annals of Advances in Automotive Medicine,* 56, 137-149.

Fukuyama, Y. (1961). Age changes of the strength for tension of human gastric walls. *Journal of the Kyoto Prefectural University of Medicine,* 69, 261-268.

Gabler, H. C. (2013). Analysis of Abdominal Injuries in Frontal Crashes: Task Report. CIB Report Number 2013-021, Virginia Tech-Wake Forest University, Center for Injury Biomechanics, Blacksburg, VA.

Gartner, L. P., and Hiatt, J. L. (2006). *Color Atlas of Histology: Fourth Edition.* Baltimore: Lippincott Williams & Wilkins.

Gennarelli, T. A. and Wodzin, E. (Eds.) (2005). Abbreviated Injury Scale 2005, Update 2008. Barrington, IL: Association for the Advancement of Automotive Medicine.

Guyton, A. C., and Hall, J. E. (2000). *Textbook of Medical Physiology: Tenth Edition.* Philadelphia: WB Saunders Company.

Hardy, W. N., Schneider, L. W., and Rouhana, S. W. (2001a). Abdominal impact response to rigid-bar, seatbelt, and airbag loading. *Stapp Car Crash Journal,* 45, 1-31.

Hardy, W. N., Foster, C. D., Mason, M. J., Yang K. H., King, A. I., and Tashman, S. (2001b). Investigation of head injury mechanisms using neutral density technology and high-speed biplanar x-ray. *Stapp Car Crash Journal,* 45, 1-32.

Hardy, W. N., Shah, C. S., Kopacz, J. M., Yang, K. H., Van Ee, C. A., Morgan, R., and Digges, K. (2006). Study of potential mechanisms of traumatic rupture of the aorta using insitu experiments. *Stapp Car Crash Journal,* 50, 247-266.

Hardy, W. N., Mason, M. J., Foster, C. D., Shah, C. S., Kopacz, J. M., Yang, K. H., King, A. I., Bishop, J., Bey, M., Anderst, W., and Tashman, S. (2007). A study of the response of the human cadaver head to impact. *Stapp Car Crash Journal,* 51, 17-80.

Hardy, W. N., Shah, C. S., Mason, M. J., Kopacz, J. M., Yang, K. H., King, A. I., Van Ee, C. A., Bishop, J. L., Banglmaier, R. F., Bey, M. J., Morgan, R. M., and Digges, K. H. (2008). Mechanisms of traumatic rupture of the aorta and associated peri-isthmic motion and deformation. *Stapp Car Crash Journal,* 52, 233-265.

Hardy, W. N., Howes, M. K., Kemper, A. R., and Rouhana S. W. (2013). Impact and Injury Response of the Abdomen. In N. Yoganandan and J. W. Melvin (Eds.), *Accidental Injury: Biomechanics and Prevention.* New York: Springer-Verlag. In-press.

Hayes, A. R., Gayzik, F. S., Moreno, D. P., Martin, R. S., and Stitzel, J. D. (2013a). Comparison of organ location, morphology, and rib coverage of a midsized male in the supine and seated positions. *Computational and Mathematical Methods in Medicine,* Article ID 419821.

Hayes, A. R., Gayzik, F. S., Moreno, D. P., Martin, R. S., and Stitzel, J. D. (2013b). Abdominal organ location, morphology, and rib coverage for the 5th, 50th, and 95th percentile males and females in the supine and seated posture using multi-modality imaging. *Annals of Advances in Automotive Medicine,* 57, 111-121.

Holbrook, T. L., Hoyt, D. B., Eastman, A. B., Sise, M. J., Kennedy, F., Velky, T., Conroy, C., Pacyna, S., and Erwin, S. (2007). The impact of safety belt use on liver injuries in motor vehicle crashes: the importance of motor vehicle safety systems. *The Journal of Trauma and Acute Care Surgery,* 63(2), 300-306.

Howes, M. K., and Hardy, W. N. (2012). Material properties of the post-mortem colon in high-rate equibiaxial elongation. *Biomedical Sciences Instrumentation*, 48, 171-178.

Howes, M. K., Gregory, T. S., Beillas, P., and Hardy, W. N. (2012). Kinematics of the thoracoabdominal contents under various loading scenarios. *Stapp Car Crash Journal,* 56, 1-48.

Howes, M. K., and Hardy, W. N. (2013). Dynamic material properties of the post-mortem human colon. Proc. 2013 International Research Council on Biomechanics of Injury, 124-132.

Howes, M. K., Beillas, P., and Hardy, W. N. (2013). The effects of cadaver orientation on the relative position of the abdominal organs. *Annals of Advances in Automotive Medicine,* 57, 209-223.

Hurtuk, M., Reed II, R. L., Esposito, T. J., Davis, K. A., and Luchette, F. A. (2006). Trauma surgeons practice what they preach: the NTDB story on solid organ injury management. *The Journal of Trauma and Acute Care Surgery,* 61(2), 243-255.

Iwasaki, T. (1953). Study on the strength of the human intestinal walls. *Journal of the Kyoto Prefectural University of Medicine,* 52, 673-702.

Kemper, A. R., Santago, A. C., Stitzel, J. D., Sparks, J. L., and Duma, S. M. (2010). Biomechanical response of human liver in tensile loading. *Annals of Advances in Automotive Medicine,* 54, 15-27.

Kemper, A. R., Santago, A. C., Stitzel, J. D., Sparks, J. L., and Duma, S. M. (2012). Biomechanical response of human spleen in tensile loading. *Journal of Biomechanics,* 45(2), 348-355.

Kemper, A. R., Santago, A. C., Stitzel, J. D., Sparks, J. L., and Duma, S. M. (2013). Effect of strain rate on the material properties of human liver parenchyma in unconfined compression. *Journal of Biomechanical Engineering.* In-press.

Kent, R., Lessley, D., and Sherwood, C. (2004). Thoracic response to dynamic, non-impact loading from a hub, distributed belt, diagonal belt, and double diagonal belts. *Stapp Car Crash Journal,* 48, 495-520.

Kent, R., Murakami, D., and Kobayashi, S. (2008). Frontal thoracic response to dynamic loading: the role of superficial tissues, viscera, and the rib cage. *International Journal of Crashworthiness,* 13, 289-300.

Kerdok, A. E., Ottensmeyer, M. P., and Howe, R. D. (2006). Effects of perfusion on the viscoelastic characteristics of liver. *Journal of Biomechanics,* 39(12), 2221-2231.

Klinich, K. D., Flannagan, C. A. C., Nicholson, K., Schneider, L. W., and Rupp, J. D. (2010). Factors associated with abdominal injury in frontal, farside, and nearside crashes. *Stapp Car Crash Journal*, 54, 73-91.

Lamielle, S., Cuny, S., Foret-Bruno, J. Y., Petit, P., Vezin, P., Verriest, J. P., and Guillemot, H. (2006). Abdominal injury patterns in real frontal crashes: influence of crash conditions, occupant seat and restraint systems. *Annals of Advances in Automotive Medicine,* 50, 109-124.

Lamielle, S., Vezin, P., Verriest, J. P., Petit, P., Trosseille, X., and Vallancien, G. (2008). 3D deformation and dynamics of the human cadaver abdomen under seatbelt loading. *Stapp Car Crash Journal,* 52, 267-294.

Lanir, Y., and Fung, Y. C. (1974). Two-dimensional mechanical properties of rabbit skin-II. experimental results. *Journal of Biomechanics,* 7(2), 171-182.

Lanir, Y., Lichtenstein, O., and Imanuel, O. (1996). Optimal design of biaxial tests for structural material characterization of flat tissues. *Journal of Biomechanical Engineering,* 118(1), 41-47.

Lee, J. B., and Yang, K. H. (2001). Development of a finite element model of the human abdomen. *Stapp Car Crash Journal,* 45, 1-22.

Lee, J. B., and Yang, K. H. (2002). Abdominal injury patterns in motor vehicle accidents: a survey of the NASS database from 1993 to 1997. *Traffic Injury Prevention,* 3(3), 241-246.

Loftis, K. L., Weaver, A. A., and Stitzel, J. D. (2011). Investigating the effects of side airbag deployment in real-world crashes using crash comparison techniques. *Annals of Advances in Automotive Medicine,* 55, 81-90.

MacKenzie, E. J., and Fowler, C. J. (2008). Epidemiology. In D. V. Feliciano, K. L. Mattox, and E. E. Moore (Eds.), *Trauma, 6th Edition* (pp. 25-40). New York: The McGraw-Hill Companies, Inc.

Mason, M. J., Shah, C. S., Maddali, M., Yang, K. H., Hardy, W. N., Van Ee, C. A., and Digges, K. (2005). A new device for high-speed biaxial tissue testing: application to traumatic rupture of the aorta. *SAE Transactions,* 114(6), 743-757.

Mays, E. T. (1966). Bursting injuries of the liver: a complex surgical challenge. *Archives of Surgery,* 93(1), 92-106.

McDowell, M. A., Fryar, C. D., Ogden, C. L., and Flegal, K. M. (2008). Anthropometric reference data for children and adults: United States, 2003-2006. U.S. Department of Health and Human Services, Centers for Disease Control and Prevention, National Center for Health Statistics.

Miller, M. A. (1989). The biomechanical response of the lower abdomen to belt restraint loading. *The Journal of Trauma and Acute Care Surgery,* 29(11), 1571-1584.

Moore, E. E., Cogbill, T. H., Malangoni, M. A., Jurkovich, G. J., Champion, H. R., Gennarelli, T. A., McAninch, J. W., Pachter, H. L., Shackford, S. R., and Trafton, P. G. (1990). Organ injury scaling, II: pancreas, duodenum, small bowel, colon, and rectum. *Journal of Trauma,* 30(11), 1427-1429.

Moore, K. L., and Agur, K. M. R. (2002). *Essential Clinical Anatomy: Second Edition.* Philadelphia: Lippincott Williams & Wilkins.

Munns, J., Richardson, M., and Hewett, P. (1995). A review of intestinal injury from blunt abdominal trauma. *Australian and New Zealand Journal of Surgery,* 65(12), 857-860.

NHTSA. (2010). Crash Injury Research and Engineering Network Coding Manual. U.S. Department of Transportation. National Highway Traffic Safety Administration.

Nonogaki, F. (1960). Study on the strength of the human gastric wall. *Journal of the Kyoto Prefectural University of Medicine,* 67, 1140-1144.

Nusholtz, G., and Kaiker, P. (1994). Abdominal response to steering wheel loading. Proc. 14th International Technical Conference on Enhanced Safety of Vehicles, 118-127. U.S. Department of Transportation, Washington, D.C.

Padgaonkar, A. J. (1976). Validation study of a three-dimensional crash victim simulator for pedestrian-vehicle impact. Doctor of Philosophy: Mechanical Engineering, Wayne State University.

Peitzman, A. B., Ford, H. R., Harbrecht, B. G., Potoka, D. A., and Townsend, R. N. (2001). Injury to the spleen. *Current Problems in Surgery,* 38(12), 932-1008.

Ross, M. H., and Pawlina, W. (2011). *Histology: A Text and Atlas: with Correlated Cell and Molecular Biology: Sixth Edition.* Baltimore: Lippincott Williams & Wilkins.

Rouhana, S. W., Lau, I. V., and Ridella, S. A. (1985). Influence of velocity and forced compression on the severity of abdominal injury in blunt, nonpenetrating lateral impact. *Journal of Trauma,* 25(6), 490-500.

Rouhana, S. W., Ridella, S. A., and Viano, D. C. (1986). The effect of limiting impact force on abdominal injury: a preliminary study. Proc. 30th Stapp Car Crash Conference, 65-79.

Rouhana, S. W. (1987). Abdominal injury prediction in lateral impact - an analysis of the biofidelity of the Euro-SID abdomen. Proc. 31st Stapp Car Crash Conference, 95-104.

Rouhana, S. W., Viano, D. C., Jedrzejczak, E. A., and McCleary, J. D. (1989). Assessing submarining and abdominal injury risk in the Hybrid III family of dummies. Proc. 33rd Stapp Car Crash Conference, 257-279.

Rouhana, S. W. (2002). Biomechanics of Abdominal Trauma. In A. M. Nahum and J. W. Melvin (Eds.), *Accidental Injury: Biomechanics and Prevention, 2nd Edition* (pp. 405-453). New York: Springer.

Rutledge, R., Thomason, M., Oller, D., Meredith, W., Moylan, J., Clancy, T., Cunningham, P., and Baker, C. (1991). The spectrum of abdominal injuries associated with the use of seat belts. *The Journal of Trauma and Acute Care Surgery,* 31(6), 820-826.

Sacks, M. S. (2000). Biaxial mechanical evaluation of planar biological materials. *Journal of Elasticity and the Physical Science of Solids,* 61, 199-246.

Saladin, K. S. (2008). *Human Anatomy: Second Edition*. New York: The McGraw-Hill Companies, Inc.

Schmitt, K. U., and Snedeker, J. G. (2006). Kidney injury: an experimental investigation of blunt renal trauma. *Journal of Trauma,* 60(4), 880-884.

Schmitt, K. U., Varga, Z., and Snedeker, J. G. (2006). Comparing the biomechanical response of human and porcine kidneys to blunt trauma. *Journal of Trauma,* 60(4), 885-887.

Schneider, L., Robbins, D., Pflueg, M., and Snyder, R. (1983). Development of anthropometrically based design specifications for an advanced adult anthropomorphic dummy family. Contract No. DTNH22-80-C-07502, University of Michigan Transportation Research Institute, Ann Arbor, MI.

Shah, C. S., Hardy, W. N., Mason, M. J., Yang, K. H., Van Ee, C. A., Morgan, R., and Digges, K. (2006). Dynamic biaxial tissue properties of the human cadaver aorta. *Stapp Car Crash Journal,* 50, 217-246.

Shinkawa, H., Yasuhara, H., Naka, S., Morikane, K., Furuya, Y., Niwa, H., and Kikuchi, T. (2004). Characteristic features of abdominal organ injuries associated with gastric rupture in blunt abdominal trauma. *The American Journal of Surgery,* 187(3), 394-397.

Society of Automotive Engineers. (1980). Standard J224 Collision Deformation Classification. Warrendale, PA.

Society of Automotive Engineers. (2007). Standard J211/1 Instrumentation for Impact Test - Part 1 - Electronic Instrumentation. Warrendale, PA.

Sparks, J. L., Bolte, J. H., Dupaix, R. B., Jones, K. H., Steinberg, S. M., Herriott, R. G., Stammen, J., and Donnelly, B. R. (2007). Using pressure to predict liver injury risk from blunt impact. *Stapp Car Crash Journal,* 51, 401-433.

Sundararajan, S., Prasad, P., Demetropoulos, C. K., Tashman, S., Begeman, P. C., Yang, K. H., and King, A. I. (2004). Effect of head-neck position on cervical facet stretch of post mortem human subjects during low speed rear end impacts. *Stapp Car Crash Journal,* 48, 331-372.

Suramo, I., Paivansalo, M., and Myllyla, V. (1984). Cranio-caudal movements of the liver, pancreas and kidneys in respiration. *Acta Radiologica: Diagnosis,* 25(2), 129-131.

Tashman, S., and Anderst, W. (2003). In-vivo measurement of dynamic joint motion using high speed biplane radiography and CT: application to canine ACL deficiency. *Journal of Biomechanical Engineering,* 125, 238-245.

Trosseille, X., Le-Coz, J. Y., Potier, P., and Lassau, J. P. (2002). Abdominal response to high-speed seatbelt loading. *Stapp Car Crash Journal,* 46, 71-79.

Viano, D. C., Lau, I. V., Asbury, C., King, A. I., and Begeman, P. C. (1989). Biomechanics of the human chest, abdomen, and pelvis in lateral impact. Proc. 33rd Annual Meeting of the Association for the Advancement of Automotive Medicine, 367-382.

Wade, O. L. (1954). Movements of the thoracic cage and diaphragm in respiration. *Journal of Physiology,* 124, 193-212.

Yaguchi, M., Omoda, Y., Ono, K., Masuda, M., and Onda, K. (2011). Traffic accident analysis towards the development of an advanced frontal crash test dummy indispensable for further improving vehicle occupant protection performance. ESV Paper No. 11-0221.

Yamada, H. (1970). *Strength of Biological Materials.* F. G. Evans (Ed.). Baltimore: Williams & Wilkins.

Yang, K. H., Hu, J., White, N. A., King, A. I., Chou, C. C., and Prasad, P. (2001). Development of numerical models for injury biomechanics research: a review of 50 years of publications in the Stapp car crash conference. *Stapp Car Crash Journal,* 50, 429-490.

Yoganandan, N., Pintar, F. A., Gennarelli, T. A., and Maltese, M. R. (2000). Patterns of abdominal injuries in frontal and side impacts. *Annals of Advances in Automotive Medicine,* 44, 17-36.